



Università degli Studi di Cagliari

DOTTORATO DI RICERCA

Scienze e Tecnologie della Terra e dell' Ambiente
Ciclo XXX

TITOLO TESI

ASSESSMENT METHODOLOGY OF PERMEABILITY IN A GRANITIC
AQUIFER IN A PILOT BASIN IN THE SOUTH OF SARDINIA (ITALY)

Settore scientifico disciplinare di appartenenza
GEO/05

Presentata da:	Sonia Aldana
Coordinatore Dottorato:	Prof. Aldo Muntoni
Tutor:	Prof. Giorgio Ghiglieri Prof.ssa Stefania Da Pelo
Co- Tutor:	Dott.ssa Maria Teresa Melis

Esame finale anno accademico 2016 – 2017
Tesi discussa nella sessione d' esame marzo 2018

ABSTRACT

Groundwater circulation in fractured hard rocks aquifer (HRA) is an essential element in the fields of water supply, environment and geotechnics. The fracture properties, as orientation, size, abundance, and quality, influence the circulation of water. The geometry of the fractures makes the hydrogeological environment anisotropic and heterogeneous. Hence, defining the geological model is fundamental to understand spatial variability of permeability, and to define hydrogeological features of the aquifers. The present work aimed to develop a methodology to assess the permeability on crystalline rocks. As a pilot site, the Masoni Ollastru River basin (12,5 km²) in the South of Sardinia was considered.

The reconstruction of the fracture network required a multiscale characterisation using field measurements and digital photogrammetry. The fractures field survey consisted in recording the features of discontinuities. The digital photogrammetry workflow produced a high resolution DEM (5m), orthophotos, digital stereo pairs, and a lineaments map.

For each 11 geomechanical stations, the set of joints was characterized and the permeability was calculated applying the Darcy's cubic law (three dimensional Darcy's law or only cubic law) for each set. Spatial distribution of fracture properties was evaluated to approach the heterogeneity of the medium. For this purpose, two different scenarios in the geological conceptual model were evaluated: the first one concerns a stratiform aquifer with a sub-horizontal and sub-vertical fissured layer in the paleo-weathering profile of the granites; the second one regards valley incision by differential erosion determined by structural features (fractures density). The layer of unconsolidated alterite above the granitic paleo-weathering profile is thin and seems to represent the deeper level where the rocks are less weathered and fractured. Probably, the significant erosion of the large part of the saprolite is related to an uplift after Pliocene time.

The permeability calculated with the cubic law was in a range of 10^{-8} to 10^{-2} m/s; the highest values are conditioned by the fractures aperture in the surface. According to the geological conceptual model, density and aperture of fractures decreases with depth, thus also permeability. The applied multi-phase methodology with a multiscale approach allowed to provide a hydrogeological conceptual model in a HRA.

ACKNOWLEDGEMENTS

I am deeply grateful with the University of Cagliari because with the scholarship it gave the opportunity to grow as a professional and person.

My tutors and my partners in the department were a huge support and made me feel welcome. Thanks to everybody who supported me specially in the difficult periods.

Cagliari, Sardinia,
Sonia Aldana

Contents

ABSTRACT	I
ACKNOWLEDGEMENTS	II
1 INTRODUCTION	13
1.1 <i>Hard rock in hydrogeological context</i>	13
1.2 <i>Relevance of studying HRA</i>	13
1.3 <i>Relevance of studying HRA in Sardinia</i>	17
2 LITERATURE REVIEW	18
2.1 <i>Permeability in hard rock aquifers</i>	18
2.1.1 Darcy's law in three dimensions	18
2.1.2 HRA as a stratiform aquifer paleo-weathering profile	21
2.2 <i>FACTORS AFFECTING THE PERMEABILITY IN HARD ROCK AQUIFERS.</i>	25
2.2.1 Rock type	25
2.2.2 Discontinuities	25
2.2.3 Orientation or attitude	31
2.2.4 Discontinuities Spacing	36
2.2.5 The fracture abundance	38
2.2.6 Persistence	40
2.2.7 Fracture endings	42
2.2.8 Aperture	42
2.2.9 Roughness	45
2.2.10 Weathering	48
2.2.11 Filling	48
2.2.12 Groundwater	50
2.2.13 Number of sets	51
2.3 <i>WATER BUDGET</i>	52
2.3.1 ESTIMATION OF WATER BUDGET	53
2.3.2 Hydrologic modeling	54
2.3.3 Methods to predict runoff in ungauged streams	56
2.3.4 Interpolation meteorological and climatological parameters	60
2.3.5 CLIMATIC FEATURES	62
3 STUDY AREA	68
3.1 <i>GEOGRAPHIC ASSESSMENT</i>	68
3.1.1 Meteo-climatic context	68
3.2 <i>GEOLOGICAL ASSESSMENT</i>	70
3.2.1 STRATIGRAPHY	70
3.2.2 GEOMORPHOLOGY	75
3.2.3 HYDROGEOLOGY	77
4 MATERIALS AND METHODS	78
4.1 <i>METHODOLOGICAL APPROACH</i>	78
4.2 <i>Evaluation of permeability in fractured granitic rocks.</i>	79
4.2.1 Assessment of rock mass properties	81
4.2.2 Lineaments map	85

4.2.3	Calculation of hydraulic permeability with the three dimensional anisotropic Darcy's law	91
4.2.4	Spatial distribution of sets and parameters. _____	91
4.3	<i>Methodology to estimate the Water budget in the ungauged Masoni Ollastru Basin.</i> _____	91
4.3.1	Basin delimitation _____	93
4.3.2	Precipitation interpolation _____	95
4.3.3	Temperature interpolation _____	102
4.3.4	Estimation of Evapotranspiration and Aridity index _____	104
4.3.5	Slope Coefficient map _____	104
4.3.6	Land cover Coefficient map _____	105
4.3.7	Permeability Coefficient map _____	106
4.3.8	The parametric runoff coefficient (C_k) calculation. _____	107
4.3.9	Water balance to MORB basin _____	108
4.3.10	Streamflow measurement _____	109
5	RESULT _____	113
5.1	<i>PERMEABILITY IN GRANITIC WATERSHED</i> _____	113
5.1.1	Sets of Lineaments _____	121
5.1.2	Spatial distribution of fractures and lineaments. _____	129
5.1.3	Distribution of fracture properties _____	131
5.1.4	Permeability. _____	141
5.2	<i>Water budget in the ungauged Masoni Ollastru Basin.</i> _____	144
5.2.1	Basin delimitation _____	144
5.2.2	Precipitation interpolation _____	144
5.2.3	Temperature interpolation _____	147
5.2.4	Estimation of Evapotranspiration and Aridity index _____	149
5.2.5	Mean Annual Effective Precipitation (P_{Aef}) _____	151
5.2.6	Slope coefficient map _____	151
5.2.7	Land use or vegetation map _____	152
5.2.8	Permeability Coefficient map _____	153
5.2.9	Runoff coefficient calculation _____	153
5.2.10	Mean Annual Potential Effective infiltration calculated from the Water Balance _____	155
5.2.11	Streamflow _____	156
6	DISCUSSION _____	160
7	CONCLUSION _____	164
8	REFERENCES _____	165

List of figures

Figure 1	Range of value of permeability modified from Freeze and Cherry, (1979)	15
Figure 2	Two dimensional diagram for the computation of permeability tensor from fracture geometry (from (Király 1971)	19
Figure 3	A conceptual model of a paleo-weathering profile in hard rocks showing the layers of the stratiform aquifer (Lachassagne et al. 2011). The figure shows a weathering profile of a granite compute by (from top to base): unconsolidated alterite (scapolite), fissured layer and fresh basement. The fissured layer has most of the aquifers (80%-90%).	22
Figure 4	Biotite alteration	24
Figure 5	Deformation parameters, stress and fissuration in an isotropic rock like granite (Wyns et al. 2015a)	24
Figure 6	The difference in size between the main types of discontinuities (Palmström 2015).	27
Figure 7	Diagram of classification of discontinuities proposed by the British Geological Survey (Gillespie et al. 2011).	28
Figure 8	Influence of the angle of the drill core and the fracture sets (Palmström, Sharma and Saxena 2001).	29
Figure 9	Block diagram showing the geomechanical properties of the fractures that are relevant in a hydrogeological characterisation.	30
Figure 10	Plane orientation. (a) The terminology used to describe a measure the attitude of a plane. The horizontal angles are the strike (ϑ) and the dip direction (α), the vertical angle is the dip (ψ). (b)The intersection of the plane with the southern hemisphere of a sphere delineating a circle. The strike the dip direction and dip are also represented on the hemisphere. (c) Projection of the intersection of the plane and southern hemisphere on the circle. (d) Circle with the projection of a plane like a great circle, the strike and the dip direction are perpendicular. Modified from Wyllie and Mah (2004)	32
Figure 11	(a) Representation of the angles used to describe the attitude of a line. (b) Representation of a line a semi-sphere (lower hemisphere). The intersection with the surface of the semi-sphere is a point called pole. Modified from Wyllie and Mah (2004)	32
Figure 12	(a) Lambert equal area net or Schmidt net, polar and equatorial projections. (b) Equal-area equatorial net for plotting poles and great circles. Modified from Wyllie and Mah (2004)	32
Figure 13	(a) Reference sphere with the representation of a plane striking 130° and dipping 50° . (b) Representation of measurement of the strike in an equal area net. (c) Representation of the measurement of the dip of a plane and the pole to the plane. (d) Great circle and pole to a plane with 130° strike and 50° dip. Modified from Wyllie and Mah (2004)	33
Figure 14	Representation of planes and their respective poles in a sphere.	34
Figure 15	Calculation of true spacing for planar discontinuities using the angles ϑ or α and the apparent spacing.	36
Figure 16	a) Fairly evenly spaced distribution. b) Clustered distribution. (c) Random distribution. (d) Combination of distributions. From (Priest & Hudson 1976)	38
Figure 17	Calculation of mean distance or mean spacing for a set of planar discontinuities in the X direction (normal to the mean fracture plane.	39
Figure 18	Computation of fracture spacing and frequency in the X direction normal to the mean fractures plane by Müller (took from Király 1969).	40
Figure 19	Determination of the average length for a set of fractures by Pahl (1981)	41
Figure 20	Example of a rock mass with long and continuous vertical joints and short not connected horizontal joints, leading to relatively high vertical permeability (Atkinson, 2000)	41
Figure 21	Block diagram showing the mechanical aperture and the hydraulic aperture.	43
Figure 22	(a) The Measure feeler gauge has steel blades of different thickness to measure the gap between two parts. The 25 blades in carbon steel set taper from 1mm wide down to 0.04mm and 76mm long. (b) Calliper	43
Figure 23	Comparison of real mechanical aperture with theoretical hydraulic apertures. The mismatch is caused by flow losses due to tortuosity and surface roughness. Took from Olsson and Barton (2001)	44
Figure 24	Roughness profiles and the corresponding range of JRC (joint roughness coefficient) values (ISRM, 1981).	46
Figure 25	The practical measurement of joint surface smoothness (from Milne, Germain and Potvin, 1992)	47

Figure 26	Profile used in the survey by Beer, Stead, and Coggan (2002) and the histogram of the distribution of the JRC values assigned by 123 people. Took from Beer, Stead, and Coggan (2002).	47
Figure 27	Classification of filling of discontinuities according to filling components and filling type by the BGS (Gillespie et al. 2011).	49
Figure 28	Effect of number of joints on the appearance of rock mass (ISRM, 1981).	51
Figure 29	Examples of block shapes depending on the fractures pattern (Dearman, 1991) and main type of blocks (Palmström 1996).	52
Figure 30	Schematic hydrologic cycle	53
Figure 31	Types of hydrological models.	55
Figure 32	Spatial configurations (a) hypothetical catchment in the plan (XY) view, (b) Tin discretisation (c) rectangular grid discretisation, (d) planes and channel segment (e) Explicit discretisation of depth (Z) and (f) separation of depth into unsaturated and saturated.	55
Figure 33 a)	Geological sketch map of the Variscan basement of Sardinia. In orange the Corsica-Sardinia Batholith (modified from Cuccuru et al. 2015). The Leni River basin recharge area is over the Intrusive unit of Villacidro, the main unit that outcrops in the Masoni Ollastru river basin. b) Schematic representation of the percentage deviation (PD) of C_s and C_k in 30 watersheds (modified from Ghiglieri et al. 2014). The PD in Leni River basin is -12.5%, and for the other granitic areas of Sardinia the PD is between 1.5% and 30%.	59
Figure 34	Relationship between water table level and precipitation (modified from Davis and de Wiest, 1966)	63
Figure 35	Relation between depth of water table and rate of evapotranspiration in different terrains (from Bouwer 1978)	65
Figure 36	The Masoni Ollastru river basin is located in a small river basin in the municipality of Capoterra, in the South of Sardinia.	68
Figure 37	Geological sketch map of Masoni Ollastru area	71
Figure 38	a) Map of Capoterra with the position of the geological section (b) that indicates the Geological model of the Capoterra plain as deduced from geophysical, geological and well data (Balìa, 2009)	72
Figure 39	Outcrop of leucomonzogranite of Villacidro Intrusive Unit intruded by basic dykes located four meters from the river bed.	72
Figure 40	Wall of leucomonzogranite of Villacidro Intrusive Unit located in the river source area in the west of the MORB.	74
Figure 41	Wall of monzogranite of Santa Barbara Intrusive Unit located in the river source area in the west of the MORB.	74
Figure 42	Southwest side of the MORB where the morphological differences between the Units of Villacidro and Santa Barbara can be seen. The Unit of Santa Barbara slopes are less steep and are more rounded; there are no large rocky crests like those of the Unit of Villacidro.	74
Figure 43	Geomorphological zones	75
Figure 44	Northeast side of the MORB, east of the old astronomic observatory, where a quartz dyke intrudes Units of Villacidro in direction NW-SE. The fractures density is high in the area surrounding the dyke.	76
Figure 45	Top called Punta Casteddu located in the north margin of the MORB in the middle of the mountainous zone side of the MORB. The granite walls of Unit of Villacidro in the top are very steep but the rest of the slope is more gently. The slope is covered by a slope debris and by the deposit of a complex mass movement (rock fall-rock avalanche occurred in 2008).	76
Figure 46	Panoramic picture of the geomorphological zones in the south margin of the MORB.	76
Figure 47	Scheme of the workflow to assess the permeability in the granitic basin.	78
Figure 48	Flowchart of discontinuities characterization	79
Figure 49	The field survey of fracture properties in Masoni Ollastru area	81
Figure 50	Location of stations	81
Figure 51	Digital photogrammetry workflow followed to obtain the Lineament map.	86
Figure 52	Classic Point Measurement tool in IMAGINE Photogrammetry Project Manager	87
Figure 53	Photogrammetry block with absolute orientation	88
Figure 54	DEM generated like a raster file (.img)	89
Figure 55	Location of accuracy point.	89
Figure 56	Orthophotos	90

Figure 57	Digital Photogrammetric Workstation or Softcopy Workstation, 3D vision: NVIDIA 3D Vision® 2 with a USB IR Emitter and a 3D LCD monitor ASUS.	90
Figure 58	Stereo Analyst for ArcGIS	90
Figure 59	Estimation the water budget for the basin.	92
Figure 60	Flowchart generate basin sub-basin perimeters	94
Figure 61	Map showing the meteorological stations around the Masoni Ollastru river basin.	96
Figure 62	Annual precipitation from 1951 to 2014 of nine stations surrounding the MORB.	99
Figure 63	Linear regression analysis of mean annual rainfall as a function of altitude in surrounding area of MORB basin.	101
Figure 64	Linear regression analysis of mean august rainfall as a function of altitude in surrounding area of MORB basin.	102
Figure 65	Linear regression analysis of mean annual temperature (TA) and mean August temperature (t) as a function of altitude in surrounding area of MORB.	103
Figure 66	CORINE land cover map in the MORB basin, the legend shows the 27 land cover classes reclassified into the classes of the land cover coefficient in the last column.	105
Figure 67	Map of the stations where the streamflow was measured.	109
Figure 68	Electromagnetic flowmeter (SEBA, model 801), sensor, wandng road and computer. Position and volume of water sensed by the flowsens.	110
Figure 69	Midsection method of calculation of streamflow in a cross section from punctual measurements.	111
Figure 70	General step of the flow measurement with the electromagnetic flowmeter in the field.	112
Figure 71	Pole diagram, great circle diagram and rose diagram of strike direction and dip direction for 332 fractures measured in the field.	113
Figure 72	Frequency distribution graphs of (a) strike and (b) dip angle for 332 fractures measured in the field.	114
Figure 73	Pole and rose diagram of sets of fractures defined and plotted by SG2PS (Sasvári & Baharev, 2014).	117
Figure 74	Pole diagram of 332 fractures measured in the field and mean poles for the sets separated by SG2PS software.	117
Figure 75	Stereonet equal-area projection of great circles and poles for joints of 11 station. On the pole diagram, it is plotted the contours with an interval of 1% with Terzaghi corrected intensity.	120
Figure 76	Map of lineaments	122
Figure 77	a. Rose diagram for the 945 lineaments collected from the stereo pairs. b. Histogram of the lineament length distribution.	122
Figure 78	Density of lineaments regarding (a) number of lineaments in the area of the map and (b) terms of length over area	123
Figure 79	Distribution of length for each set of lineaments.	124
Figure 80	Map of lineaments in a radius of 500 m around the geomechanical stations.	125
Figure 81	Rose diagram of sub-vertical fractures measured at the field and rose diagrams of lineaments surrounding the geomechanical stations.	128
Figure 82	Pole and rose diagrams (Schmidt-net, lower hemisphere) for fractures data, separated by the formation in which they were observed.	129
Figure 83	Maps of lineaments crossing each formation.	129
Figure 84	Graphics of density of lineaments in each formation and density of lineaments set in each unit. The density was evaluated as number of fractures in the area and like cumulative length in the area.	130
Figure 85	Map of density of lineaments	130
Figure 86	Map of density of intersection of lineaments	131
Figure 87	(a) Histogram for all values of aperture and (b) histogram for values of aperture bellow 20mm.	132
Figure 88	Relation of aperture of fractures and dip angle	133
Figure 89	Relation of fractures Aperture and Elevation. The stations in pink are located in Villacidro Intrusive Unit, and the stations in colour purple are located in Santa Barbara Intrusive Unit.	133
Figure 90	Relation of fractures Spacing and dip angle.	134
Figure 91	Relation of fractures Spacing and Elevation	134

Figure 92	Pole diagram, great circle diagram and rose diagram for the fractures with dip angle between 0° and 50°.	135
Figure 93	Relationship of subhorizontal fractures aperture and elevation	136
Figure 94	Relationship of subhorizontal fractures spacing and elevation.	137
Figure 95	Relationship between mean aperture and mean frequency of the subhorizontal fractures and geographical features like elevation, distance to the river and slope aspect.	138
Figure 96	Pole diagram, great circle diagram and rose diagram for the fractures with dip angle between 80° and 90°.	139
Figure 97	Relationship between mean aperture and mean frequency of the sub vertical fractures and geographical features like elevation, distance to the river, slope aspect and side of the valley.	140
Figure 98	Map showing the sub-basins of the RMO basin which pour point corresponds to a streamflow gauge. The perimeter of the RMO basin is surrounding all the sub-basins.	144
Figure 99	Mean annual precipitation map obtained using linear regression of precipitation and elevation from 1989 to 2011.	145
Figure 100	Mean august precipitation map obtained using linear regression of precipitation and elevation from 1989 to 2011.	146
Figure 101	Mean annual temperature map obtained using linear regression of temperature and elevation for the period of 1989 to 2011.	148
Figure 102	Mean August temperature (t) map obtained using linear regression of temperature and elevation for the period of 1989 to 2011.	148
Figure 103	Mean annual potential evapotranspiration map obtained from Turc (1954) equation with the modification of Santoro for Mediterranean arid areas. The map algebra used the maps of precipitation and temperature obtained through linear regression from 1989 to 2011.	150
Figure 104	Aridity index map obtained from De Martonne (1926) equation (Equation 25). The map algebra used the maps of precipitation and temperature obtained through linear regression from 1989 to 2011.	150
Figure 105	Mean annual effective precipitation. The map algebra used the maps of precipitation obtained through linear regression and potential evapotranspiration from Turc (1954) equation with the modification of Santoro (1970).	151
Figure 106	Slope coefficient map	152
Figure 107	Land cover coefficient map	152
Figure 108	Permeability coefficient map	153
Figure 109	Annual potential runoff coefficient map.	154
Figure 110	Mean annual potential runoff map	155
Figure 111	Mean annual potential effective Infiltration map	156
Figure 115	Graphic showing the discharge behaviour along the river in October and November of 2015.	157
Figure 116	Graphic showing the discharge and the precipitation along the river in on October of 2015	158
Figure 117	Graphic showing the discharge and the precipitation along the river in on November of 2015	158
Figure 124	Precipitation in the Capoterra station for the last three years. The current year has been drier, which is reflected in the stream flow of the Masoni Ollastru River.	159
Figure 125	Schematic transversal profile oriented N-S in the mountainous granitic area in MORB showing the hypothesis of the fracture distribution and the possible hydrogeological zonation in the granitic.	161

List of tables

Table 1	Structure of lateritic profile from top to base based on the work of Dewandel et al. (2006), Lachassagne et al. (2011) and Wyns et al. (2015a).	22
Table 2	Observable and measurable properties and terminology for single discontinuities from the British Geological Survey scheme for classifying discontinuities and filling (Gillespie et al. 2011)	29
Table 3	Classification of the spacing of fractures (Bieniawski, 1989).	37
Table 4	Fracture abundance measures, modified from Mauldon and Dershowitz (2000)	38
Table 5	Classification of fractures size based on Bieniawski 1984	41
Table 6	Types of fractures end and codes used in field and office (modified from United States Department of Agriculture 2012)	42
Table 7	Groundwater Conditions (Romana 1995)	50
Table 8	Categories for the number of joint sets (Wyllie & Mah 2004)	51
Table 9	Coefficients of physiographic indirect method to calculate potential runoff coefficient classified by aridity index (Spadoni et al. 2010a)	58
Table 10	Percentage of basins evaluated by Ghiglieri et al. (2014) classified by the Percentage deviation (PD) between the estimated C_k and the calculated C_s .	59
Table 11	Geographical elements affecting climatic factors.	61
Table 12	Methods to measure and to estimate the ET tested by Rana and Katerji (2000) classified on according to their scope and type of approach.	65
Table 13	Advantages and disadvantages of the methods to measure and to estimate the ET tested by Rana and Katerji (2000).	66
Table 14	Equations to estimate the evapotranspiration based on analytical and empirical approaches.	66
Table 15	Geological units outcropping in the area of the MORB.	72
Table 16	Parameters observed and instruments used to characterise the discontinuities in the field.	82
Table 17	Classes of discontinuities.	82
Table 18	Classification of the spacing of fractures (Bieniawski, 1989) Wyllie and Mah (2004).	83
Table 19	Classification of the separation of joints (Bieniawski 1989).	83
Table 20	Classification of fractures size based on Bieniawski 1984.	84
Table 21	Types of fractures end and codes used in field and office	84
Table 22	Corresponding range of JRC (joint roughness coefficient) values to roughness profiles (ISRM 1981).	84
Table 23	Categories and codes for fracture infilling modified from Bieniawski (1989).	85
Table 24	Classification for Weathering.	85
Table 25	Groundwater Condions by Bieniawski (1989).	85
Table 26	Flight lines and numbers of aerial photographs used for the photogrammetric project.	86
Table 27	Data and sources used to estimate parameter of the water budget.	93
Table 28	Meteorological stations around the MORB basin. The distance to the basin, distance to the sea, coordinates, height, period of data and data source number from table 26.	95
Table 29	Periods with precipitation data of each station.	96
Table 30	Periods with temperature data of each station.	97
Table 31	Average annual and average monthly precipitation for common periods with data in the stations around the MORB.	98
Table 32	Correlations evaluated using different periods and stations.	100
Table 33	Statistics for the annual rainfall data. The last three columns give the linear correlation coefficient between rainfall and elevation, and the mean absolute error (MAE) and mean square error (MSE) of prediction of rainfall by linear regression of elevation for each correlation.	101
Table 34	Statistics for the August rainfall data. The last three columns give the linear correlation coefficient between rainfall and elevation, and the mean absolute error (MAE) and mean square error (MSE) of prediction of rainfall by linear regression of elevation for each correlation.	102
Table 35	Average annual and average monthly temperature for 1989-2011 stations around the MORB.	103
Table 36	Statistics for the annual temperature data. The last three columns give the linear correlation coefficient between temperature and elevation, and the mean absolute error (MAE) and mean square error (MSE) of prediction of temperature by linear regression of elevation for each correlation.	103

Table 37	Statistics for the August temperature data. The last three columns give the linear correlation coefficient between temperature and elevation, and the mean absolute error (MAE) and mean square error (MSE) of prediction of temperature by linear regression of elevation for each correlation.	103
Table 38	Statistics for the August temperature data.	104
Table 39	Classes and values of the slope coefficient for an aridity index below 25.	104
Table 40	Classes and values of the land cover coefficient for an aridity index below 25.	105
Table 41	Classes and values of the permeability coefficient for an aridity index below 25.	106
Table 42	Geological formations in the MORB basin, classes classified into the classes of the permeability coefficient in the last two columns.	107
Table 43	Set of discontinuities measured in the field and their average parameters.	117
Table 44	Set of discontinuities in each station and their mean poles and planes; and range of dip direction and dip.	120
Table 45	Azimuth interval of the identified trends of the lineaments. The numbers in bold are the highest values, and the numbers underlined are the second highest values.	123
Table 46	Mode, median and mean length (m) for each set lineaments.	124
Table 47	Frequency of set of lineaments in a radius of 500m around each station. The frequencies in bold are the highest for each peripheral area, and the underlined values are the second more frequent. The set A is the most frequent for eight stations; followed in order by set B and set C.	125
Table 48	Correspondence of the sets of lineaments with the sets of fractures measured at geomechanical stations. The sets and frequency in bold are the more frequent in each station, and the underlined are the second more frequent, in italic are the third more frequent.	128
Table 49	Characteristics of the geomechanical stations and aperture and frequency of the sub-horizontal sets.	136
Table 50	Permeability calculated for geomechanical stations with the cubic law equation.	141
Table 51	Permeability of each geomechanical station and sets with higher frequency, aperture and contribution to the permeability.	143
Table 52	Perimeter and surface of the watersheds and sub-basins of the Masoni Ollastru basin.	144
Table 53	Statistics for the average annual and average August precipitation interpolated inside the RMO basin. The last two columns compare the mean values of precipitation.	145
Table 54	Statistics for the mean annual precipitation correlation. The last three columns give the linear correlation coefficient between rainfall and elevation, and the mean absolute error (MAE) and mean square error (MSE) of prediction of rainfall by linear regression of elevation for each correlation.	146
Table 55	Statistics for the August rainfall record and for the prediction of August rainfall by linear regression of elevation. The last three columns give the linear correlation coefficient between rainfall and elevation, the mean absolute error (MAE) and mean square error (MSE).	146
Table 56	Statistics for the average annual and average August temperature interpolated inside the RMO basin. The last two columns compare the mean values.	147
Table 57	Statistics for the average annual evapotranspiration and average aridity index interpolated inside the RMO basin. The last two columns compare the mean values obtained from linear regression and unique value.	149
Table 58	Statistic of PA (mm) and evapotranspiration maps of sub-basins	149
Table 59	Statistics for the average annual Effective Precipitation inside the RMO basin.	151
Table 60	Calculation of annual potential runoff coefficient C_k . Percent area of the basin that corresponds to each class of the partial coefficients (C_a , C_v and C_p) is multiplied by the values of the classes and added. The addition of the three partial coefficients is the runoff coefficient.	154
Table 61	Statistics for the mean annual potential runoff and mean annual potential effective infiltration maps in the RMO basin. The last four columns compare the mean values obtained from linear regression and unique value.	155
Table 62	Evaluation of potential runoff coefficient calculated with indirect physiographic method and runoff coefficient calculated with the measured runoff and precipitation in sub-basins.	157
Table 64	Streamflow measured in 12 stations in October and November of 2015 and characteristics of the area of the station.	157

List of abbreviations and symbols

HR	Hard Rocks
HRA	Hard Rocks Aquifers
DTH	Down-the-hole hammer
DFN	Discrete fracture network
RMR	Rock Mass Rating
BGS	British Geological Survey
CC	Correlation coefficient
MAS	Mean absolute error
MSE	Mean square error
q	Discharge
K	Permeability
\bar{K}	Tensor permeability:
\bar{G}	Intrinsic or geometric permeability
\bar{v}	Average velocity
g	Gravitational acceleration
ν	Kinetic viscosity
d	Aperture of the fracture
J	Gradient vector
\vec{J}_p	Projection of J on the plane of fracture
n	Normal to the plane
$n \otimes n$	Tensor product of n by itself
I	Identity matrix
f	Frequency of discontinuities
N	Number of discontinuities systems
\vec{L}	Scanline vector
\vec{V}_i	Normal unitary vectors
CI	Confidence interval
p_i	Plunge,
t_i	Trend of the i^{th} measure
R	Length of the vector
κ	Precision parameter
α_{95}	Radius of the 95% confidence Interval cone within which the mean vector of a larger hypothetical population would be.
\bar{x}	Mean discontinuity spacing
λ	Mean discontinuity frequency
Si	Planar discontinuities
ϑ	Angle formed between the rock face and the strike of the fractures
α	Complementary angle to θ , is the angle between the normal to the fractures and the rock face.
\vec{L}_x	Scan line in direction X
\vec{N}_i -axis	Mean pole
\vec{L}'_{xi}	Projection
n_i	Number of discontinuities
\vec{L}'_{xi}	\vec{N}_i -axis of the set i to obtain the projection
dm_x	Mean distance in the direction \vec{X}

f_x	Frequency number of discontinuities
E	Mechanical joint aperture
e	Hydraulic aperture
e	Conductivity aperture
JRC	Joint roughness coefficient ()
JCS	Joint compressive strength
σ'	Effective normal stress
IDW	Inverse distance weighting
P	Precipitation
P_A	Mean annual precipitation
P_{ef}	Effective precipitation
P_{Aef}	Mean annual Effective precipitation
T_A	Mean annual temperature
p	Precipitation of the hottest month
t	Temperature of the hottest month
ET	Evapotranspiration
AET	Actual evapotranspiration
PET	Potential evapotranspiration
PET_A	Mean annual potential evapotranspiration
Q_T	Total discharge
Q_G	Groundwater discharge
I_{ef}	Effective infiltration
Rs	Surface runoff
R_a	Average annual groundwater recharge
D_a	Average annual groundwater discharge
Q_{Sa}	Average annual surface runoff
Q_{Ga}	Average annual groundwater runoff
ET_{Ra}	Average annual evapotranspiration from recharge area
ET_{Pa}	Average annual evapotranspiration from discharge area
C_s	Runoff coefficient
CV	Coefficient of variation of annual runoff
AI	Aridity index
I_a	Aridity index De Martonne (1926)
C_k	Potential runoff coefficients:
C_a	Partial runoff coefficient: Slope angle coefficient
C_v	Partial runoff coefficient: Vegetation cover coefficient
C_p	Partial runoff coefficient: Permeability coefficient
R_{Ap}	Mean annual potential runoff
I_{Aef}	Mean annual potential effective infiltration

1 INTRODUCTION

1.1 *Hard rock in hydrogeological context*

The term Hard Rocks (HR) or fractured rocks in hydrogeology can refer to the hard basement or crystalline rocks (igneous and metamorphic) and consolidated sedimentary rocks (Sharp 2014), including karst and volcanic complexes. Michel and Fairbridge (1992) used the term hard rocks exclusively for basement rocks (plutonic and metamorphic rocks), excluding those susceptible to karstification (e.g. marble) (Lachassagne *et al.* 2011). The rocks named before have in common very low or negligible permeability due to intergranular or inter-crystal spaces (matrix permeability in HR is below 10^{-8} m/s) (Figure and Figure 1). However, groundwater in hard rock aquifers (HRA) is controlled by the discontinuities that act as conduits or barriers for fluids.

A discontinuity is a feature that breaks the continuity of the rock mass. There are different kinds of discontinuities of different origins, stratigraphic like unconformities, structural like fractures and geomorphological like cavities (Gillespie *et al.* 2011). They also vary in extension and size from microcracks to fault zones of hundreds of kilometres long and several meters wide (Wyllie & Mah 2004). The permeability in granitic rocks depends on the characteristics of the fracture network mainly on the orientation, the dimensions, the abundance and the number of sets. The structural heterogeneity makes the fractured rock mass anisotropic and heterogeneous.

The ambiguity to define HR in hydrogeology is because there are sedimentary and volcanic rocks that have not primary permeability but the secondary permeability is due to discontinuities other than fractures. Sedimentary terrigenous rocks that lost their primary porosity after diagenesis can be included as HR if their permeability is only due to fractures. Secondary permeability in volcanic rocks can be due to fractures, limits between flows and columnar joints. The karstic rocks (limestones and marbles) are a particular case because they also have dissolution forms (e.g. caverns); therefore they approached of their permeability is different to the HRA.

The meaning for hard rock adopted in this work is that of Michel and Fairbridge (1992). Therefore when referring to hard rock aquifers, the reference is implicit for plutonic and metamorphic rocks. The discontinuities in metamorphic rocks are foliation and fractures and in plutonic rocks fractures and damage zone. Plutonic and metamorphic rocks host fractured aquifers, although they differ in mineralogy and texture, they have similar hydrogeological properties (Wyns *et al.* 2015b). Approximately 30% of the continents are crystalline rocks that can be found in shields, massifs and cores of mountain ranges (Sharp 2014). The basement is continuous in depth from regional to continental scale; then there is a groundwater flow in that scale (Sharp 2014).

1.2 **Relevance of studying HRA**

The groundwater circulation in the hard rocks is an essential element in the field of water supply, hazardous waste repositories, energy, mineral resources, environment, and geotechnical and engineering–geological assessment.

Water supply and groundwater sustainable development

Water needs have been traditionally satisfied from easy to exploit, perennial and drinkable sources of surface water or groundwater. The porous sedimentary aquifers (unconsolidated sands and gravel, sedimentary rocks, porous or fractured volcanic rocks) have been the primary source of groundwater; they have a high permeability (Figure 1) are accessible, easy to drill, and Darcy's law well explains the flow. There are significant differences in structure and hydraulic parameters between the porous media and the fractured media (Figure 1 and Figure 2). For instance, sand aquifers have one flow regime controlled by the matrix, in contrast, hard rocks have two flow regimes, one from the matrix and one from the fractures (Nielsen 2007). HRA are different from the hydrogeological basins in the vertical variability of permeability, transmissivity, storability, flow; and chemical and physical properties of groundwater. HRA are highly vulnerable; they have low groundwater storage capacity, the recharge flux is variable, inter-annual recharge relation is better than that of the surface water and their alluvium deposits but much worse than in porous aquifers.

Porous, karstic and volcanic aquifers have better productivity than the HRA (Courtois *et al.*, 2010; Wyns *et al.* 2015b). The low productivity of HRA makes them suitable for small populations and are exploited where there is limited surface water sources and no conventional aquifers (Lachassagne *et al.* 2011).

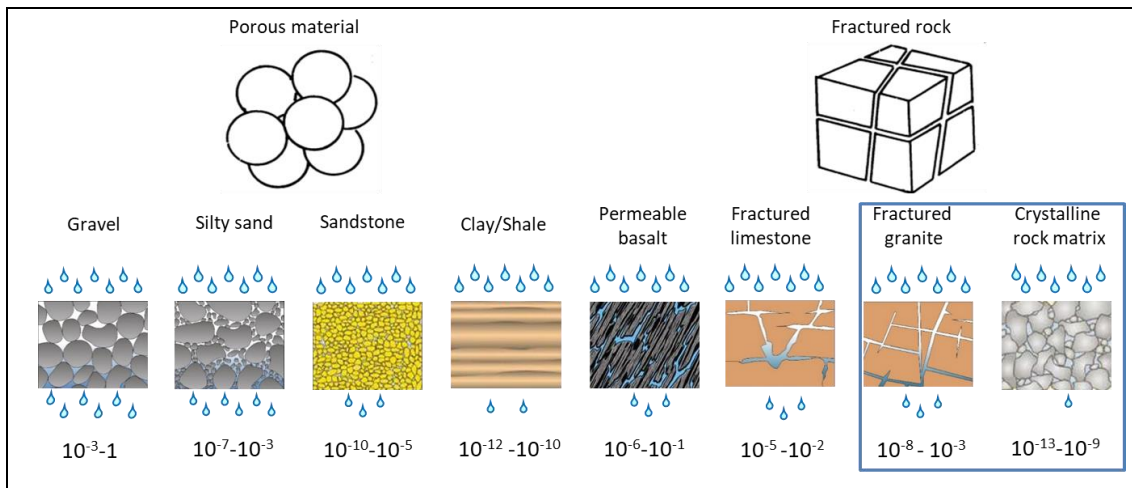


Figure Relation between texture and porosity.

Therefore, the research and exploitation of HRA are located mainly in arid and semiarid regions or where the sources of water have been limited or are becoming limited (Gilli *et al.* 2012; Sharp 2014). In Africa, South America, Australia and India communities exploit fractured aquifers. Also in the United States, some areas base their water supply on HRA (Shapiro 2002).

The increment on water demand for communities, industries and agriculture; the climate change; the overexploitation and pollution can lead to exhaustion of the hydric resources (Lachassagne *et al.* 2011). Such decreasing quality and quantity of hydric resources, requires improving the general knowledge on hydrogeology turning the attention towards the HRA (Shapiro 2002).

Groundwater sustainable development includes identifying the best technical and economic conditions to protect the recharge areas and hydraulic processes and to build wells. For instance, evaluate if is better to exploit local groundwater from HRA or

extended regional groundwater or surface water supply, according to economy and society (Sharp 2014).

Groundwater has been found in fractured crystalline rocks all around the world during the last decades. Deep drilling in Russia, USA and Germany found saline fluids in fractured crystalline basement (Bucher & Stober 2000). HRA's have high hydraulic gradients, and the piezometric surface is shallow and parallel to the topography (Lachassange et al., 2014). The HRA's flow out to streams, springs and catchment areas in hard rock in temperate areas maintain the streams during dry periods. All this confirming the hydrogeological potential of the HRA. The flow in the HRA is mainly through the upper areas of the weathering profile (e.g. saprolite in granitic rocks), deep infiltration is scarce; therefore, groundwater age and mineral content increase downwards in HRA.

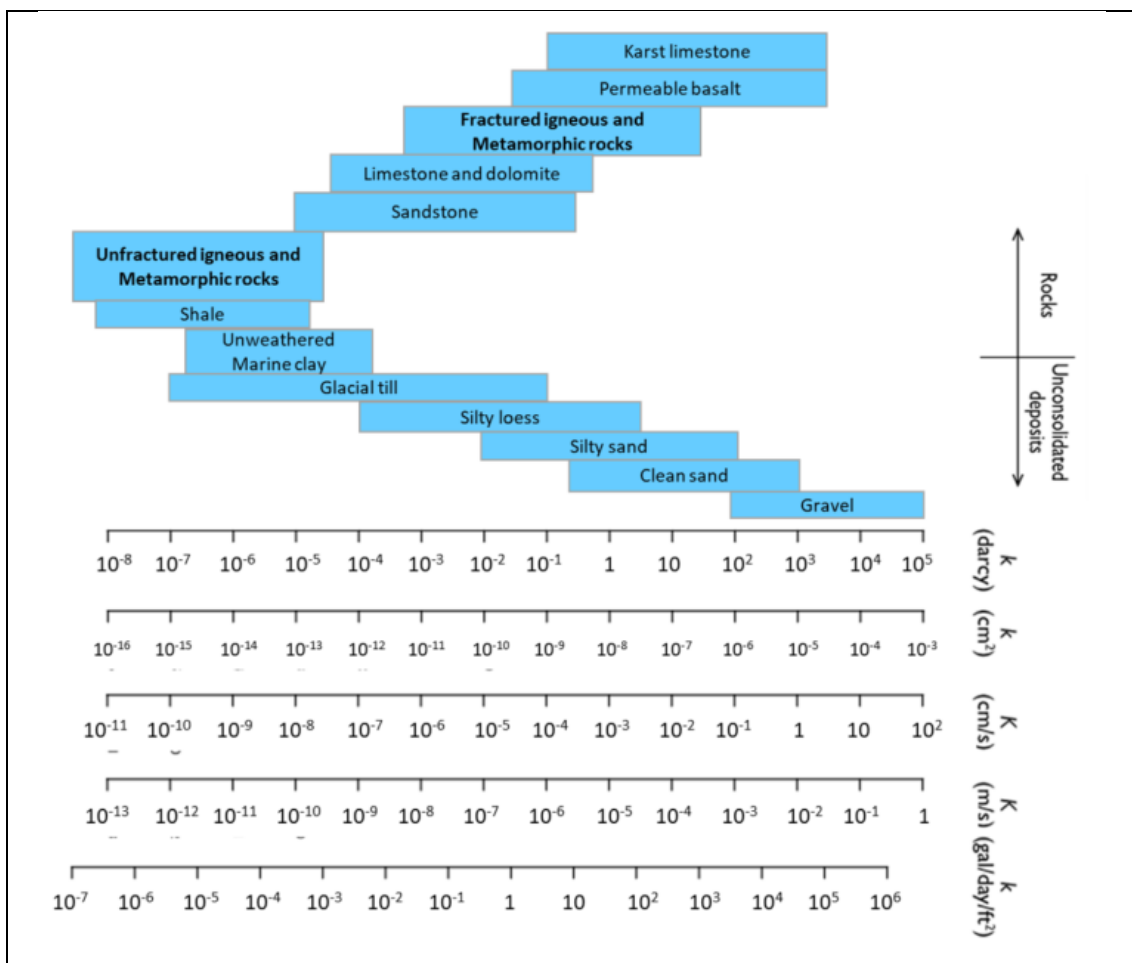


Figure 1 Range of value of permeability modified from Freeze and Cherry, (1979)

Hazardous waste repositories.

Extensive research on HR has been done to approach their impermeable properties (negligible water flow at the very slow rate) which make them ideal for nuclear waste disposal and toxic and dangerous waste storage (Shapiro 2002). Nuclear disposal should be done below the 300m ideally; then these studies were extended to hundreds or thousands of meters (Sharp 2014).

Environment.

Fractures in HRA can transport pollutants as colloids and pathogens, and can host bacterial activity. If the fractures are long and the water flow is fast, the contamination can be spread widely and fast, affecting not only human activities but also river and wetlands ecosystems.

Energy resources

An efficient geothermal reservoir to supply clean alternative power should have geothermal heat and enough groundwater to produce hydrothermal fluids. The ideal conditions for a geothermal reservoir are scarce, but deep fractured crystalline rocks with low permeability and enough heat are common and are known as Hot-dry rocks (HDR). The HDR project (1970 to 1995) in the USA and the European Geothermal HDR cooperation project (1987-currently) in Soult-sous-Forêts (France) studied models to extract thermal energy to produce electricity from low permeability basement rocks (Kelkar *et al.* 2016).

Geotechnical and engineering –geological assessment

The construction of infrastructure (e.g. tunnels, dams, roads, building foundations and mines) need to assess the geotechnical properties of the rock mass and the groundwater to prevent, monitor and correct engineering problems (Shapiro 2002).

Risk assessment and engineering problems in HR require the evaluation of fracture network geometry, individual fracture strength, intact rock strength (Guglielmi *et al.* 2005) and water flow. It is known that the most frequent triggering factor causing a mass movement is the water; the groundwater, itself, exerts diverse effects on the rock mass and thus in its stability (Hoek & Bray 1981).

It is essential to stand out that when a rock mass is fractured the stability is almost entirely dependent on the condition of the discontinuities (Pantelidis, 2009) and naturally in the water pore pressure. In fractured HR the water infiltration and circulation, the pore water pressure, and the groundwater outflows are affected by the discontinuities. Therefore the slopes of fractured rock have heterogeneous hydraulic properties. Thanks to the extensive observation of mass movements it can be said that the flow of groundwater and the mechanical deformation are coupled and should always be analysed together (Guglielmi *et al.* 2005)

The *hydromechanical coupling* in fractured crystalline rock slopes has been studied at laboratory and field scale but in both cases with several limitations achieving partial results. A rock sample analysed in the laboratory does not represent the complexity of the fracture media and field tests are only possible when the loading conditions can be controlled (Guglielmi *et al.* 2005; Bidgoli & Jing 2015). Bidgoli and Jing (2015) propose the numerical modelling using the distinct element method (DEM) (Cundall 1988) to evaluate the effect of the water pressure on the compressive strength and deformation of fractured crystalline rocks, performing experiments under mechanical and hydraulic loading.

1.3 Relevance of studying HRA in Sardinia

The aim of this work is developing a methodology to assess the permeability in a drainage area on crystalline rocks of a small river basin in meridional Sardinia. The Masoni Ollastru river basin (MORB) was chosen as a pilot area; it is located in the municipality of Capoterra, province of Cagliari. The area of the basin is 12.5 km², the elevation range is between 692 MASL in Monte Turrunari to sea level in the coast. The weather is typical Mediterranean with dry summers and highest precipitation in autumn and sometimes in spring. The vegetation consists of forests with species of high trunk and bushes to Mediterranean sclerophyllous vegetation (Barca et al., 2009). The drainage area and river channel are on crystalline Carboniferous-Permian fractured granites intruded by dykes. Quaternary alluvial and colluvial deposits cover sections of valleys and slopes. The floodplain and mouth are on quaternary alluvial and coastal deposits. The river runs from a mountainous area with sharp relief, steep slopes and dense vegetation in the West towards the coastal plain in the Gulf of Cagliari in the East.

The area of Capoterra is of special interest because it has experienced several cases of mass movements and floods triggered by intense rainfall and at the same time the south of Sardinia is classified as a semiarid region with water deficit. The most recent event related with mass movements and a flood had placed on October 22nd of 2008 preceded by the most intense rain ever recorded by the rain gauges in Sardinia (350 mm in three hours in the pluviometer of Capoterra). By other side, the island of Sardinia is characterised by a water deficit at most altitudes and drought periods like in 2003. The south of the island has elevated air temperatures, low seasonal differences and a high evapotranspiration (ET) deficit typical of semiarid climate. The south of Sardinia is classified as Mediterranean to subtropical climate influenced by mountains (MST1) and Mediterranean to subtropical climate partly semiarid (MST2).

In the majority of mountain areas in the Mediterranean, the scarcity of meteorological data is a frequent problem. Low order streams or small basins are usually ungauged and don't have piezometers, especially in remote, unpopulated areas if they are not readily accessible or don't represent an immediate interest. As a result, there are few continuous time periods or sites with all the parameters required to estimate a water balance. In hydrology these problems are standard, and the data can be estimated by spatial interpolation and through indirect physiographic methods.

Main Objective: This works aims at applying a methodology to characterise the fracture network in granitic rocks in a pilot area on the South of Sardinia to estimate the permeability and the water budget in an ungauged basin.

2 LITERATURE REVIEW

2.1 Permeability in hard rock aquifers

Although, the permeability in a HRA can be due to the inter-crystal spaces and to the discontinuities, the focus is rather on the permeability due to the discontinuities. The geometry of the fracture network makes the hydrogeological environment anisotropic, heterogeneous and discontinuous. Therefore, the hydraulic properties are difficult to understand and quantify. Sharp (2014) describes the fractured rock environment as “an intricate and hierarchic system, formed by inhomogeneities on local to regional scales”. Probe of this are the differences of five or more orders of magnitude found in hydraulic parameters from local to regional scale; and the fact that productive wells in HRA alternate impermeable intervals of sound rock with permeable fractures (Wyns *et al.* 2015a). Even inside a single fracture the permeability can change due to clogging, hydrothermal alteration and mineral precipitation.

The permeability of a fractured rock mass depends on several properties of the fracture network. Features like aperture, roughness, filling, joint clogging, turbulent flow, normal stress can change along a single fracture changing the geometry of the conduit, the permeability and the type of flow. The quantification of the properties of the fracture network is a challenge. Two main approaches can be used: the continuum and the discrete fracture network (DFN). The equivalent continuum approach can be used at basin scales when the density of the fracture is high, the orientation distribution is non-uniform, and the evaluated sample size is large in comparison to the fracture sizes. The DFN approach is basically used at small scales, mainly for engineering purposes. The continuum approach uses the three dimensional Darcy's law (or cubic law). The formula of the cubic law uses the cube of the aperture and the frequency of the fractures. The continuum approach simplifies the evaluation of the permeability, although further problems should be addressed in the analysis of flow through the fractured rock.

2.1.1 Darcy's law in three dimensions

An anisotropic medium formed by a fractured rock can be approached like an idealised model where the relationship of the anisotropy and the geometry of the conduits systems can be analysed (Snow, 1969). The idealised model assumes to have conduits of smooth parallel walls of the indefinite extent and constant orientations, apertures and spacing. The parallel plate flow equations for the average velocity (\bar{v}) and discharge (q) per unit width of a plate conduit were derived from the Navier-Stokes equations (Snow, 1969) under the following hypothesis (Király 1969)

- H1: water flows in plane and continuous fractures in an elementary volume
- H2: permeability is isotropic in the plane of the fissure
- H3: The terrain is saturated.

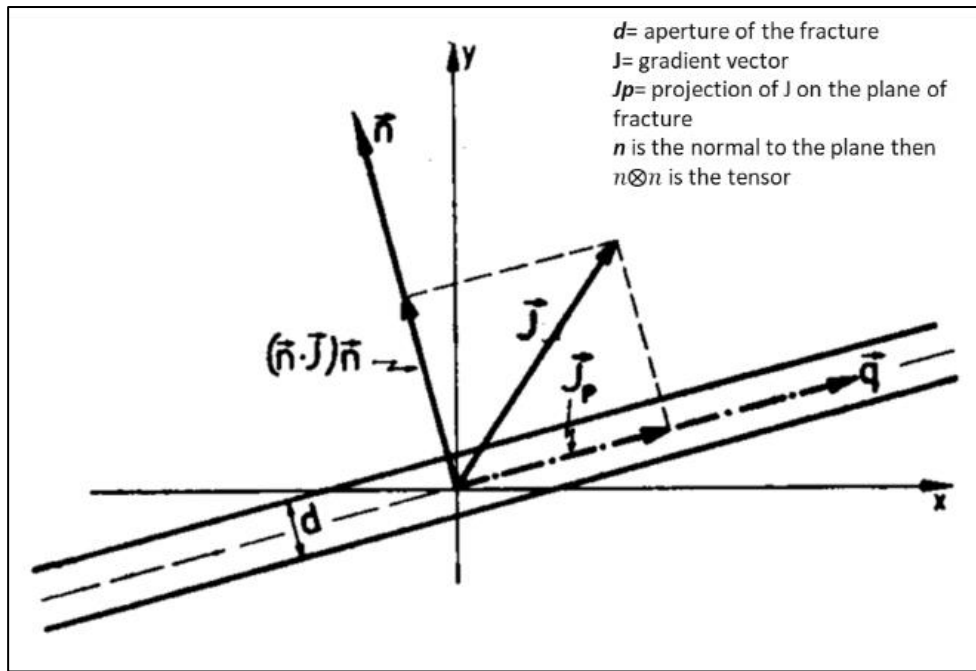


Figure 2 Two dimensional diagram for the computation of permeability tensor from fracture geometry (from (Kiraly 1971))

The permeability tensor K transform linearly the gradient vector J to the discharge vector q

$$q = KJ^{-1}$$

The discharge q for a discontinuity is:

Equation 1

$$\vec{q} = \frac{g}{12\nu} d^3 \cdot \vec{J}_p \quad (L^2 T^{-1})$$

g = gravitational acceleration

ν = kinetic viscosity

d = aperture of the fracture

\vec{J}_p = projection of J on the fracture plane

The gradient vector J projected on the plane of the fracture is:

$$\vec{J}_p = \vec{J} - (\vec{J} \cdot \vec{n})\vec{n} = I\vec{J} - (\vec{n} \otimes \vec{n}) \cdot \vec{J} = [I - \vec{n} \otimes \vec{n}] \cdot \vec{J} = \vec{A}\vec{J}$$

\vec{J} = gradient vector

I = Identity matrix

\vec{n} = is the normal to the plane

$n \otimes n$ is the tensor product of \vec{n} by itself

$$\vec{A} = [I - \vec{n} \otimes \vec{n}] = \begin{bmatrix} (1 - x_1^2) & (-x_1 x_2) & (-x_1 x_3) \\ (-x_2 x_1) & (1 - x_2^2) & (-x_2 x_3) \\ (-x_3 x_1) & (-x_3 x_2) & (1 - x_3^2) \end{bmatrix}$$

$$\vec{q} = \frac{g}{12\nu} d^3 \cdot \vec{A} \vec{J}$$

And K from the Darcy's law is:

Equation 2

$$\vec{K} = \frac{g}{12\nu} d^3 \cdot \vec{A}$$

Then the intrinsic or geometric permeability is:

Equation 3

$$\vec{G} = d^3 \vec{A}$$

The permeability for anisotropic terrain can be calculated taking into account the frequency f (number of discontinuities per meter in \vec{n} direction) to the equation 4 and 5.

Equation 4

$$\vec{K} = \frac{g}{12\nu} f d^3 \cdot \vec{A}$$

Equation 5

$$\vec{G} = f d^3 \vec{A}$$

If there are N discontinuities systems, the K tensor is given by:

Equation 6

$$\mathbf{K} = \sum_{i=1}^N \vec{K}_i = \frac{g}{12\nu} \sum_{i=1}^N f_i d_i^3 [\mathbf{I} - \mathbf{n}_i \otimes \mathbf{n}_i]$$

And

Equation 7

$$\vec{G} = \sum_{i=1}^N \vec{G}_i$$

2.1.2 HRA as a stratiform aquifer paleo-weathering profile

The exploitation and understanding of HRA have been limited because of the reasons explained above plus the difficulty of drilling hard rocks, except in the superficial unconsolidated weathered zone. In the 1950s, the invention of the down-the-hole hammer (DTH) allowed to drill deep wells to study the physical properties of weathered basement rocks. The boreholes revealed a zone of unweathered *fractured rock* that could reach tens of meters at the base of the weathering profile, underlying the unconsolidated weathered zone. Several authors studying that zone referred *subhorizontal jointing or sheet fractures in granites which spacing increased with depth* and could not be related with cooling of plutons (Jahns, 1943; Twidale, 2012; Ollier, 1988; Wright and Burgess, 1992; Chilton and Foster, 1995; Hill, Ollier and Joyce, 1995; Shaw, 1997; Taylor and Eggleton, 2001; Mabee *et al.*, 2002; Mandl, 2005; Lachassagne *et al.* 2011) However, this fractured zone was not thoroughly described or studied but for hydrogeologist interested in its permeability (Wyns *et al.* 2010). The subhorizontal joints or sheeting fractures probed to have an important hydrogeological role like reservoir and main conductors of flow (Mabee *et al.* 2002; Hsieh and Shapiro 1996; Day-Lewis *et al.* 2000; Paillet *et al.*, 1987; Paillet and Duncanson, 1994; Le Borgne *et al.*, 2006; 2006a, 2007; Boutt *et al.*, 2010).

The descriptions of the sheeting fractures and the fractured unweathered zone led to conclude that they referred to the same zone in granitic weathering profiles. Lachassagne *et al.* (2011) named this fractured zone in the deep part of the weathering profile "*fissured layer*".

The studies conducted after the discovering of the fissured layer in the 90's, showed that there are lateritic profiles independent of the latitudes and that the climate was not the determinative factor (Wyns *et al.* 2015b). Studies of lateritic profiles in France, South Korea, Burkina Faso, India, African and French Guiana concluded that the origin, location and depth of aquifers in plutonic rocks depend on the weathered profiles.

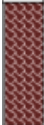
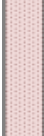


The conditions that produce a thick lateritic profile with a fractured layer of hydrogeological interest are (Wyns 2002; Wyns *et al.* 2003):

- rock exposed to surface outside of water bodies,
- regional uplift forming peneplains with the erosion rate lower than the weathering rate and
- millions to tens of millions years of weathering (Wyns 2002).

The climate can change in a shorter period than the required for a thick weathering profile, therefore it is not a determinative factor. Changes in the geodynamic trend lead to polyphase structures in the weathering profile (Dewandel *et al.*, 2006). Thick paleo weathering profiles in Europe were created during Carboniferous, infra Permian, infra Triassic, early Cretaceous, and early and middle Eocene (Wyns *et al.* 2003). The thickness of the saprolite in Europe is 20 m-30 m and for the fissured layer between 50 m-70 m; the total thickness of the weathering profiles is around 70 m to 100 m (Wyns *et al.* 2003) (Lachassagne *et al.* 2011).

Four layers have been identified in the weathering profiles of HR. Table 1 shows the vertical zones recognised in a weathering profile in HR and summarises their characteristics based on the work of Dewandel *et al.* (2006), Lachassagne *et al.* (2011), Lachassagne *et al.* (2014) and Wyns *et al.* (2015b) .

Table 1 Structure of lateritic profile from top to base based on the work of Dewandel et al. (2006), Lachassagne et al. (2011) and Wyns et al. (2015a).

LAYER	CHARACTERISTICS	Groundwater
 <p>Iron or bauxitic crust Thickness: 1-10 m</p>	It is product of recrystallisation of goethite grains by alteration of ferromagnetic primary minerals into massive hematite, or gibbsite/bohemite. Absent by erosion or rehydration or resilification or buried.	Small perched aquifers, and few springs.
 <p>Upper or weathered zone</p>	<p>A mix of clay minerals, hydroxides or oxides and residual minerals. It is separated into two parts from top to bottom: the and the isalterite.</p> <p>The Alloterite: lost the original structure of the rock, mainly clay.</p> <p>The Isalterite keeps the rock structure, but with pores where the dissolved minerals were. Half or two third of saprolite.</p> <p>Laminated Layer: base of isalterite with very dense horizontal fracturing (millimetric spacing, even cutting big crystals) in granular rocks.</p>	<p>The hydraulic conductivity is low (10^{-6} m/s) in saprolite dominate by clay minerals. Sandy-clayey saprolite from coarse granite and gneisses have higher water storage (5-30% bulk porosity). Often is the best source of groundwater" sharp, 2014</p>
 <p>Middle zone: Fissure layer Thickness: Double of saprolite</p>	High fracture density on fresh rock, Density and connectivity decrease downwards. The rock between fractures has low weathering. The isotropic granular rocks and metamorphic rocks with subhorizontal foliation have subhorizontal fractures.	This layer transmits or storage water depending on the thickness and saturation of the overlying saprolite. Permeability decrease with depth
 <p>Deep or massive zone: Fresh rock</p>	The basement has few deep tectonic fractures that can be interconnected forming a network or regional and continental scale for groundwater flow. Deep fractures can also be paths for thermal and mineral water.	The basement is considered impermeable at catchment scale (Maréchal et al., 2004)

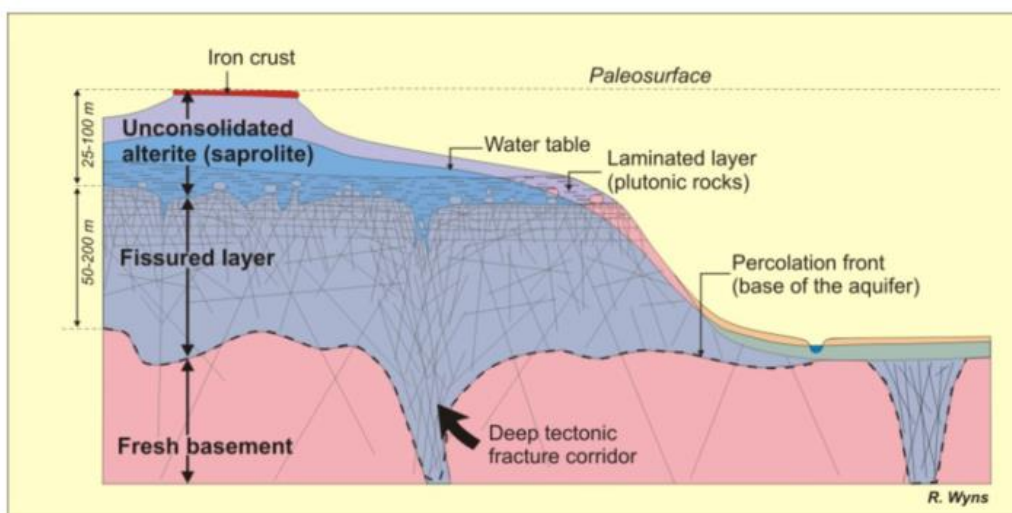


Figure 3 A conceptual model of a paleo-weathering profile in hard rocks showing the layers of the stratiform aquifer (Lachassagne et al. 2011). The figure shows a weathering profile of a granite compute by (from top to base): unconsolidated alterite (scapolite), fissured layer and fresh basement. The fissured layer has most of the aquifers (80%-90%).

The hydrogeological studies in HR have a different approach thanks to the identification of the hydraulic properties of the weathering profile in HR. The research can be focused on identifying the weathered zone and the fissured layer (zones with good hydraulic conditions) in thick paleo-weathering profiles of HR. However such identification needs a good understanding of the geological evolution of the basement and of the origin of the fractures.

The presence or absence of the fissured layer and its location in the weathering profile among other characteristics were insufficiently explained by the traditional proposed origins of fractures. The accepted origins of fractures responsible of the secondary permeability in superficial (0-100m) HRA were: vertical unloading by exhumation (offloading from erosion) or thermic contraction during emplacement of plutonic rocks and tectonics (Lachassagne *et al.* 2011). Plutonic rocks crystallised under high triaxial compression would experience vertical unloading by exhumation. It has been believed that the unloading causes dilation towards the surface and therefore sub-horizontal fractures (Holzhausen, 1989 and Farmin 1937). Wyns *et al.* (2015) confronted two plutonic bodies, a micaceous granite and a microgranite, that underwent the erosion of the same overlying paleosurface; but only the first had a fractured layer. Tension cracks would form after fast stress relieve, as it is the case of a sudden offloading in engineering works. Pollard and Aydin (1988), two specialists in rock mechanics, proposed that microcracks under high fluid pressure could evolve into joints. Nevertheless, the erosion processes causing offloading are prolonged, giving time to the crystals to reorganise themselves.

The tectonic origin of the fractures has been assumed by authors studying HRA, without proving the hypothesis; neither explaining the origin of the sheeting fractures. Tectonic permeable fractures are geographically and time-limited to active tectonic areas. Tectonic fractures have high dip angle, and are profound therefore would hardly be located at the permeable layers in HR and intersected by a well.

Hydrogeologists have worked with the previous assumptions, without an in-depth study or mechanic asses to evaluate the hypothesis. Lachassagne *et al.* (2011) and Wyns *et al.* (2015a) proposed that the origin of the fractures of hydrogeological relevance is due to mineral alteration during the long process of paleo-weathering.

The degree of alteration and swelling of minerals, like biotite, along the weathering profile in HR suggested that they could be responsible for the fissured layer. The weathered and fissured layers have products of biotite alteration such as chlorite and vermiculite (Figure 4 and Figure 5), with some swelling of the sheets, in the laminated layer all the biotite has been altered and has micro-fissures and the unweathered layer has sane biotite (Wyns *et al.* 2015a). The alteration of biotite into chlorite or vermiculite produces a potential increment in volume of the crystal about the 30% (Banfield and Eggleton, 1990), this happens at dozens of metres depth. The swelling is perpendicular to the cleavages of the mica flakes (Figure 5). The minerals that are swelled with the alteration of siliceous-aluminium rocks are: biotites, muscovite, and sericite.

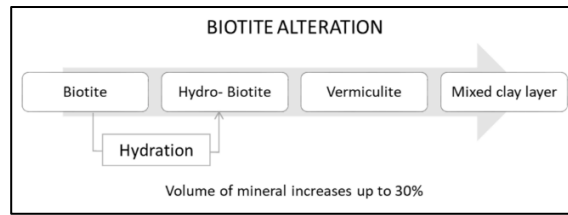


Figure 4 Biotite alteration

According to Wyns *et al.*, (2015a) the swelling of minerals like the biotite during weathering is responsible of subhorizontal fissuration in granites. In isotropic rocks where the minerals do not have a preferential orientation, like in granites, the crystals will not experience any swelling, but the horizontal and vertical stress will increase. In the vertical direction the lithostatic load will not allow any swelling (Wyns *et al.* 2015a) until it is compensated, then the vertical stress stop increasing and is replaced by dilation. If the stress deviator is higher than the elastic limit, the rock will crack, and the direction of the fissures is parallel to the principal stress, therefore subhorizontal (parallel to the paleo-topography). In the horizontal directions, the stress keeps increasing because of the medium in “infinite” in that direction. The maximum stresses are horizontal, and the minimum stress is vertical (Figure 5). Rocks with coarse crystals are more prone to have fissuration by mineral swelling than microgranular ones (Wyns *et al.* 2015a).

Quartz and rhyolite dykes can have fissures due to the stress of the altered surrounding rock. Dykes, veins, ancient fractures and geological contacts are prominent to develop a vertical fissure layer (Wyns *et al.* 2015a) locally deepening the weathering profile even hundreds of meters. The Length of dykes affected by alteration of the host rock can be over 200 m (Wyns *et al.* 2015a) The zones around this heterogeneity like dykes have relative good permeability and can be the only reservoir where the horizontal weathering profile has been eroded (Figure 3). The fissured layer is also present in the weathering profiles of basic and ultrabasic rocks where the pyroxenes and olivine would be the responsible of the fractures. The gabbro has the same process of horizontal fissuration than the granite.

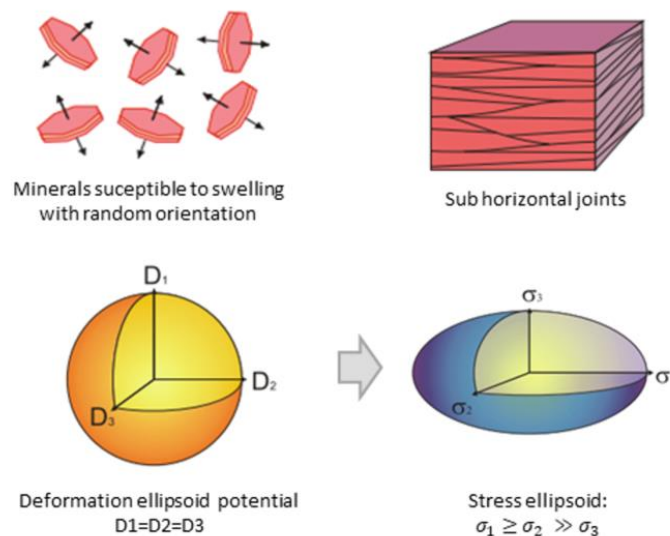


Figure 5 Deformation parameters, stress and fissuration in an isotropic rock like granite (Wyns *et al.* 2015a)

2.2 FACTORS AFFECTING THE PERMEABILITY IN HARD ROCK AQUIFERS.

The rock mass comprises intact rock limited by naturally occurring discontinuities. It is well known that the permeability in karstic and crystalline rocks depends mainly on the properties of the discontinuities. Nevertheless, the properties of the rock matrix and the geological evolution determines the type of discontinuities, the deformation and the weathering of a rock. Specifically, in HRA the discontinuities are fractures, the properties that influence the circulation of water in the fractures are the orientation, the size, the abundance, the quality and the stress variation. The properties of a fracture network can change from a place to another and are different depending on the directions. Therefore, the geometry of the fractures can make the hydrogeological environment anisotropic and heterogeneous and the permeability dependent on the directions and the place where it is measured.

The fracture network should be characterised accounting the spatial limitations (heterogeneity the scale and the orientation), the availability of data and the suitability of technics. The success of the characterisation relies on the quality of the description and measuring of the parameters. Unfortunately, the description of some parameters can introduce error due to subjectivity, inappropriate measuring method, and limitations of the scale and orientation of the feature.

2.2.1 Rock type

The geological classification of rocks is based mainly on their origin, composition, texture and structure. Classification of rock materials can also be based on engineering or hydrogeological properties. The geological nomenclature can give by itself information regarding hydrogeological behaviour. The lithology also conditions the degree of weathering and the morphology of the rock faces. The description of the lithology should be done especially in hydrogeological and geomechanical terms (rock classification, anisotropy, weathering, porosity, permeability, seepage). A complete description of the basic properties (colour, lustre, texture, structures and composition) will help to identify the geological unit and understand better its hydro-mechanical behaviour.

2.2.2 Discontinuities

A discontinuity is a feature that breaks the continuity of the rock mass. There are different kinds of discontinuities, stratigraphic like unconformities, structural like fractures and geomorphological like cavities (Gillespie & Styles 1999). They also vary in extension and size from microcracks to fault system of hundreds of kilometres long and several meters wide fault zone (Wyllie & Mah 2004) (Figure 6 and Figure 7).

The discontinuities act like conduits or barriers for fluids. The discontinuities affect the water infiltration, the pore water pressure, and the groundwater outflows. They are of particular importance in HRA, where they are almost entirely responsible for the water circulation. They also affect the weathering grade because the rock near the discontinuities planes is more exposed to the weathering agents. The properties of the discontinuities control the stability conditions and the deformations on a slope face. Slope failure rather occurs along

discontinuities because they are weakness zones or planes or their intersections than across intact rock. Discontinuities can be associated with mineralisation of economic interest.

The main features to identify in the discontinuities are their attitude (dip of azimuth and dip), the dimensions (visible trace length and aperture), the abundance (through the spacing) and the quality (roughness and weathering, the infilling and groundwater).

Types of discontinuities

Discontinuities are usually classified according to their origin because their genesis makes them share properties. The British Geological Survey (BGS) (Gillespie *et al.* 2011) proposed a standard terminology and classification of discontinuities with two principal categories: interface and break (Figure 7) is a scheme of the classification of discontinuities suggested by the BGS, which is explained in more detail below.

The term interface refers to boundaries between different materials, condition or state. There are primary and secondary interfaces. Primary interfaces are syngenetic with the material; they are associated with sedimentary and igneous genetic processes. Bedding planes are primary planar discontinuities in sedimentary rocks. Igneous rocks can have primary igneous layering due to the crystals accumulation (Lisle & Leyshon 2004). The secondary interfaces develop on the pre-existing material; and are associated with alteration, cementation, segregation and deformation (Gillespie *et al.* 2011). Secondary planar discontinuities product of deformation and metamorphic processes are known as foliation and can be slaty cleavage, schistosity and banding.

M. Gillespie, Barnes, and Milodowski (2011) second main category for discontinuities are breaks, referring to disruption of the physical integrity of the material. Breaks are produced by *chemical solution* or by *deformation*. Deformation breaks can be sharp with two surfaces opposing an insignificant distance or tabular (involve a band of deformed material). The deformation breaks are the product of rock failure along weak zones (lower strength and or stiffness) in any rock due to tectonic, burial compaction, unload, slope failure, cooling (among others) events.

The sharp discrete deformation breaks are known as fractures. Fractures are the result of brittle failure where the rock mass losses or reduces its cohesion by structural or non-structural causes (Gillespie *et al.* 1993). M. Gillespie, Barnes, and Milodowski (2011) classified fractures into *cracks*, *anti-crack* and *faults*. The term *crack* is equivalent to the term joint; they are fractures caused by small perpendicular opening displacement (aperture, d) of the opposing surfaces away from each other. They have negligible shear offset, little or no movement along their planes (Gillespie *et al.* 2011). They can be systematic or nonsystematic (arbitrary). Parallel joints make a *joint set*, and intersecting sets of joints make a *joint system* (Wyllie & Mah 2004). Fractures can deform by normal opening or closure, shear and dilation (Barton *et al.* 1985).

The probable genesis of joints are bulk extension (minor tectonic strain, the stress of tectonic events and isostatic rebound) or bulk contraction (cooling). Traditionally the origin of subhorizontal fractures in plutonic rocks has been assumed to be offloading from erosion or thermal contraction of plutonic rocks (Lachassagne *et al.* 2011). However, Lachassagne *et al.* (2011) proposed that sub horizontal fissuration at the base of the weathering profile in hard rocks be produced during long processes of weathering where minerals like biotite, pyroxenes and olivine alter incrementing their volume (see §2.1.2).

Anticracks are the result of closing displacement by pressure solution or chemical compaction common in crystalline carbonate rocks, can be dentate (e.g. stylolite) or smooth. Faults are fractures in which the opposing surfaces experienced relative movement or shearing displacement. Although the term fault indicates one fracture, usually they are a system of fractures associated with a damage zone. The fault plane can exhibit slickenside lineation due to the movement of the rock blocks.

Tabular deformation breaks, better known as *deformation bands*, are the result of brittle or ductile deformation or a mix. The deformation bands thickness is noticeable; syngenetic or post-genetic fractures can flank the band. Tabular deformation breaks were classified by M. Gillespie *et al* (2011) in five categories shown in Figure 7.

Discontinuities associated with specific processes or study fields have their widely used nomenclature. Such is the case of faults in mass movements specifically known as slip-surfaces. A useful term to study discontinuities is lineament. A lineament is a linear feature (straight or slightly curved) on the surface of the Earth recognisable at large scales on outcrops, topography, aerial photos and satellite images (Fossen 2016) that can correspond to geological features.

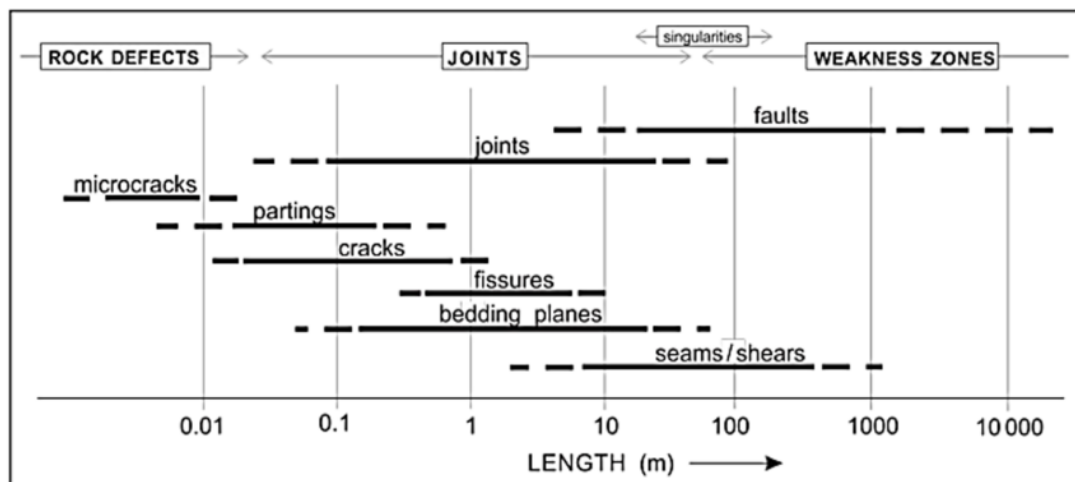


Figure 6 The difference in size between the main types of discontinuities (Palmström 2015).

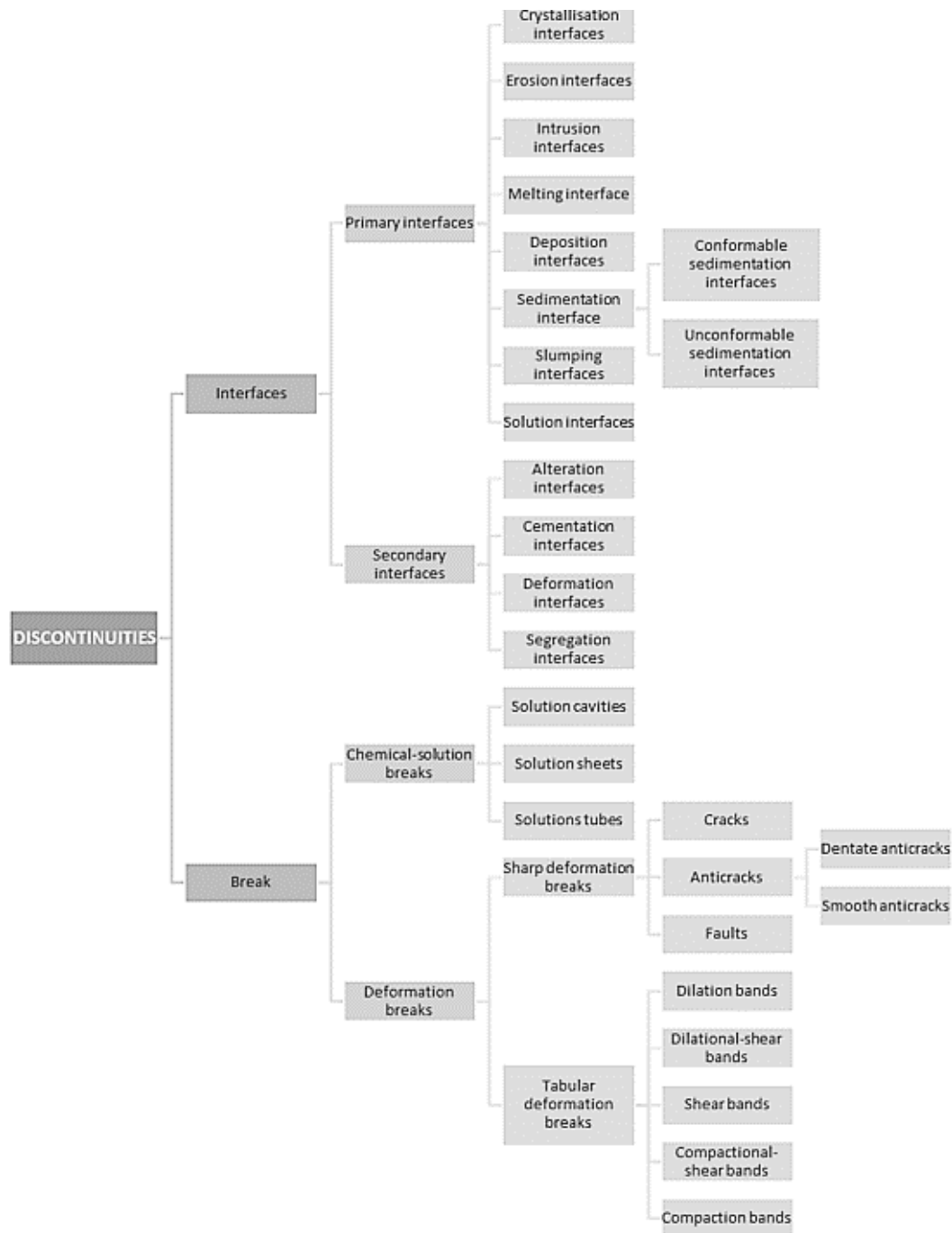


Figure 7 Diagram of classification of discontinuities proposed by the British Geological Survey (Gillespie *et al.* 2011).

Survey of discontinuities

Discontinuities are three-dimensional features however their properties are usually obtained from line sampling (1-D) and mapping (2-D). P. A. Gillespie *et al.* (1993)(Gillespie *et al.* 1993) in natural outcrops, cuts, drill cores, remote sensing images and geophysics profiles. Field surveys will depend on the accessibility, extension and representativity of the rock exposure. There are features of the discontinuities that variate spatially and very often exceed the sampling area. Therefore, the exposure of the discontinuities depends on the orientation and size of the outcrop, cut or drillcore. For example, few elements of a set of fractures parallel to the rock face or the direction of the drill core are intersected (see Figure 8). A map of

discontinuities obtained from remote sensing images represents the discontinuities that intersect the surface and their properties in that plane. While, information from cross sections (boreholes, geophysical profiles and rock faces) reflect the discontinuities and their properties in different planes taking into account depth. The rock mass assessment should be done bearing in account the three-dimensional rock volume or relating the 1D, 2D and 3D parameters (Marrett & Allmendinger, 1991; Walsh et al., 1991; Yielding et al., 1992). The size of the sampling area introduce problems because of the truncation of features, resolution limits and censoring. For example, if a set of fractures has longer spacing than the outcrop or drillcore. Other examples occur with the discontinuity extension (in surface and depth), the distribution pattern of fractures and the changes of the discontinuity properties in space (Lin *et al.* 2014). Geophysics, remote sensing, coring, emanometry (radon CO₂) calculations and multiscale approach, would complement the field surveys. The rock mass characterisation in 3D can be achieved by measuring along 2D cross sections in different sampling directions.

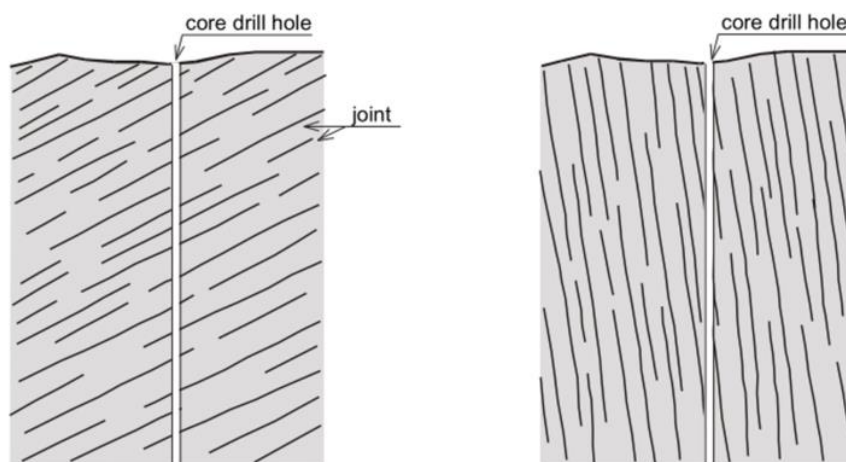


Figure 8 Influence of the angle of the drill core and the fracture sets (Palmström, Sharma and Saxena 2001).

Table 2 Observable and measurable properties and terminology for single discontinuities from the British Geological Survey scheme for classifying discontinuities and filling (Gillespie *et al.* 2011)

OBSERVABLE PROPERTIES			MEASURABLE PROPERTIES	
Terms to describe interfaces	Terms to describe breaks	Terms to describe interfaces and breaks	Type of property	Terms to describe dip angle
<i>Material on opposing sides *</i>	<i>Condition</i>	<i>Form</i>		
<ul style="list-style-type: none"> • crystal • gas • ice • liquid • magma • organic matter • rock • sediment • soil 	<ul style="list-style-type: none"> • closed • compound • dilatant • filled • healed • incipient • non-filled • open • sealed • simple 	<ul style="list-style-type: none"> • bifurcated • curved • equant • irregular • planar • ptygmatic • sigmoidal • sinuous • stepped • straight • sutured • tabular • tapered • tubular 	<ul style="list-style-type: none"> • aperture • attitude • dip • dip-slip • displacement • heave • length • oblique-slip • offset • persistence • strike • strike-slip • throw • width 	<ul style="list-style-type: none"> • bedding parallel • gently dipping • horizontal • moderately dipping • steeply dipping • vertical • a number from 1 to 90, e.g. 30° • a range, e.g. 30–40°
<i>Nature of transition</i>	<i>Sense of displacement on deformation breaks</i>			

<ul style="list-style-type: none"> • abrupt • alternating • diffuse • gradational 	<ul style="list-style-type: none"> • Closing displacement • opening displacement • shearing displacement 			
Relationship of opposing sides	Sense of displacement on faults			
<ul style="list-style-type: none"> • conformable • unconformable 	<ul style="list-style-type: none"> • dextral • dip-slip normal • oblique-slip • reverse • sinistral • strike-slip • thrust 			

P. A. Gillespie *et al.* (1993) described 1-D datasets from surveys along a line perpendicular (or forming a known high angle) to the strike of the fractures system, measuring the position and type of each discontinuity crossing the reference line. The 1-D survey can be done on rock faces, cuts, tunnels or drill cores. Piteau, (1970) describes this procedure like scanline technique, measuring and registering the most representative discontinuities systematically along a scanline \vec{L} , which orientation and length are known. The orientations, dimensions and quality of sub-parallel discontinuities intersecting the scanline are registered. It is advisable to record the data on a format designed especially for discontinuities properties. Hudson and Priest (1979, 1983) recommended to trace the scanlines (\vec{L}) orthogonal to examine the outcrop exhaustively and in three dimensions. 2-D fractures datasets are maps, for example, horizon map constructed from 2-D seismic profiles, cross-sections built from photomosaic of a rock face and box-counting analysis.

The present study focuses on fractures and the properties that affect the permeability (Figure 9). Below such properties are defined, together with some measurement techniques and their influence on the rocks mas behaviour.

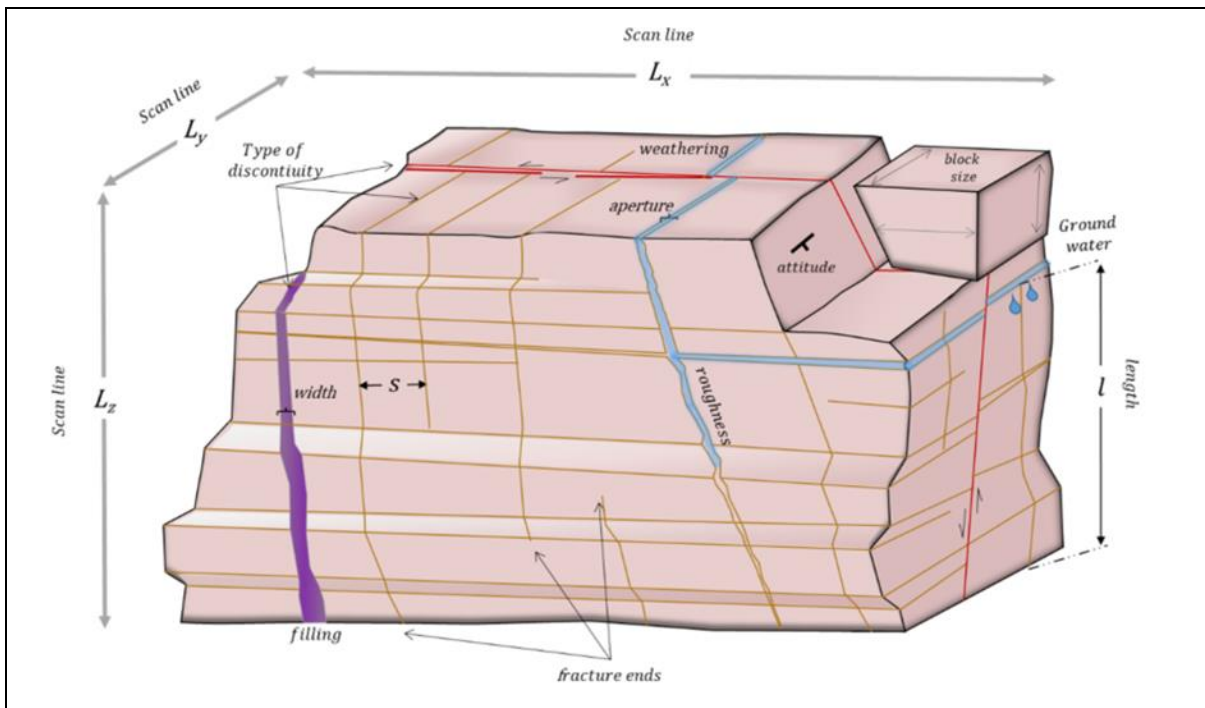


Figure 9 Block diagram showing the geomechanical properties of the fractures that are relevant in a hydrogeological characterisation.

2.2.3 Orientation or attitude

The strike and the dip direction characterise the attitude of a planar discontinuity (Figure 10). One angle measures the direction of a plane or a line with the north or with a reference system. The strike is the angle between the north and a horizontal line on the plane. The dip direction is the angle between the north and the direction of the maximum slope of the plane (the direction that a drop of water would follow). The second angle to define the attitude of the plane is the dip. The dip is the angle of maximum inclination of the plane from a horizontal reference.

Plotting fractures on Stereographic projection

The stereographic projection can represent three-dimensional, scattered geological data of planes and lines in two dimensions (Figure 10 and Figure 11). However, the stereographic projections can only represent angular relationships, but discontinuities analysis are more complicated because the measurements are taken from different locations and are associated with size among other parameters. The representation of the stereonet serves to determine the modal groups of directional data, although the finiteness of the circle makes it difficult.

Stereographic projection consists of circular grids that are the projection of a reference sphere hemisphere on its horizontal equatorial plane (orientated relative to the north) (Figure 12). The Schmidt net (also called equal area net or Lambert net) is used by the accuracy of data density; although it does not preserve the angular relationships allows to measure angles. The Schmidt net is an equatorial projection of the lower hemisphere which maintains the angular relationships, but the area in all the sphere is projected equally. The equal area projection permits to build contours around the concentration of poles; this cannot be done on the Wulff net. The upper and lower half of the sphere are north and south hemisphere respectively. The north-south lines are called great circles, the east-west lines are called small circles, and the perimeter is called primitive circle. There are two projections: the polar projection useful only to plot poles and the equatorial projection useful to plot planes and points (Figure 12).

Planes are represented crossing the reference sphere by the middle, the intersections of planes on the southern hemisphere of the Schmidt-net are arcs noun as great circles (Figure 13). The strike is represented like axial data (directions without sense). The intersection of a line crossing through the centre of the reference sphere and one hemisphere is a point (Figure 11). The arcs and points on the southern hemisphere surface are rotated to a horizontal surface as shown in Figure 13. Representation of great circles and poles can be done on the circular grids by hand, although fortunately there are several software that deal with stereographic projection.

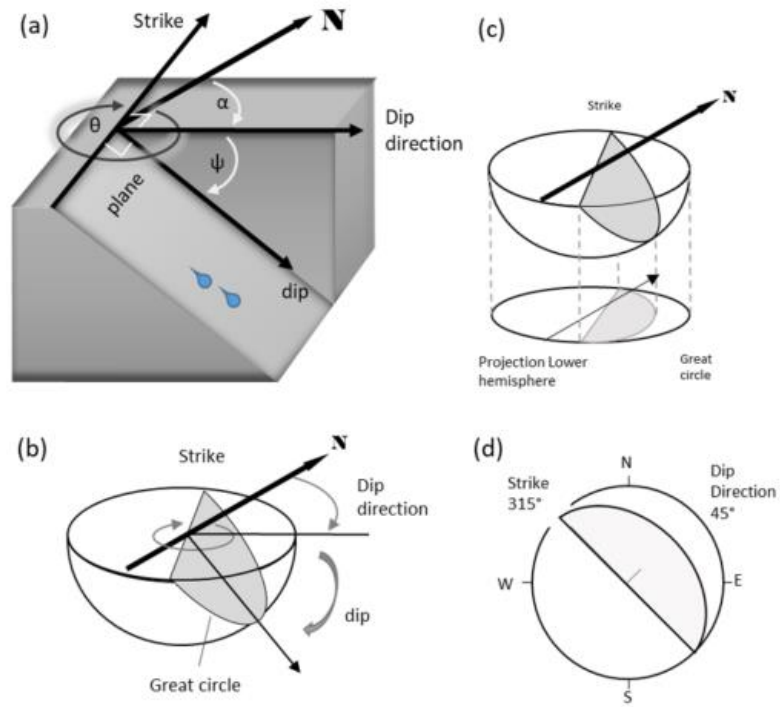


Figure 10 Plane orientation. (a) The terminology used to describe a measure the attitude of a plane. The horizontal angles are the strike (ϑ) and the dip direction (α), the vertical angle is the dip (ψ). (b) The intersection of the plane with the southern hemisphere of a sphere delineating a circle. The strike the dip direction and dip are also represented on the hemisphere. (c) Projection of the intersection of the plane and southern hemisphere on the circle. (d) Circle with the projection of a plane like a great circle, the strike and the dip direction are perpendicular. Modified from Wyllie and Mah (2004)

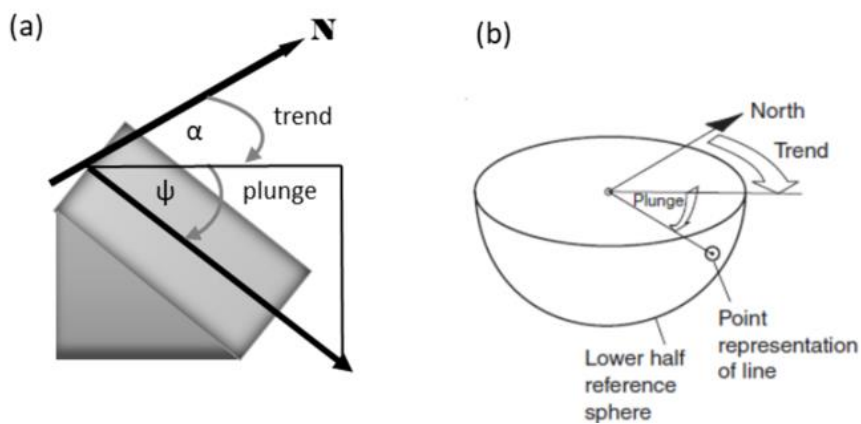


Figure 11 (a) Representation of the angles used to describe the attitude of a line. (b) Representation of a line a semi-sphere (lower hemisphere). The intersection with the surface of the semi-sphere is a point called pole. Modified from Wyllie and Mah (2004)

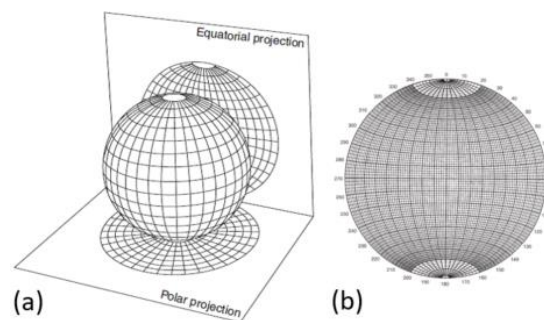


Figure 12 (a) Lambert equal area net or Schmidt net, polar and equatorial projections. (b) Equal-area equatorial net for plotting poles and great circles. Modified from Wyllie and Mah (2004)

There are different ways to plot the geological orientation data in a stereonet, below there is a description of the principle diagrams.

Pole diagram:

A radial line normal to a plane intersects the reference sphere and represents the plane as a point called pole (Figure 13). For a set of fractures V , there will be the corresponding planes with their normal unitary vectors \vec{V}_i pointing approximately to the same zone on the surface of the sphere (see Figure 14).

The determination of discontinuities sets requires plotting the poles to all the discontinuities. The pole concentrations correspond with preferential orientation of discontinuities planes. The analysis can be improved by assigning different symbols or colours to different types of discontinuities. The poles can be plotted on the equatorial or the polar projection; they would be precisely in the same position. A set of discontinuities with very high dip (sub-vertical) will have the poles very close to the perimeter and can be dipping in opposite directions

Contour pole density diagram:

The strike and dip among the elements of the sets of discontinuities are between a range. Then, the sets are recognisable as the concentration of poles but sometimes the data is scattered, and the sets are not immediately recognisable. Contours equivalent to the density of the concentration of poles help to determine the discontinuity sets and their mean orientation.

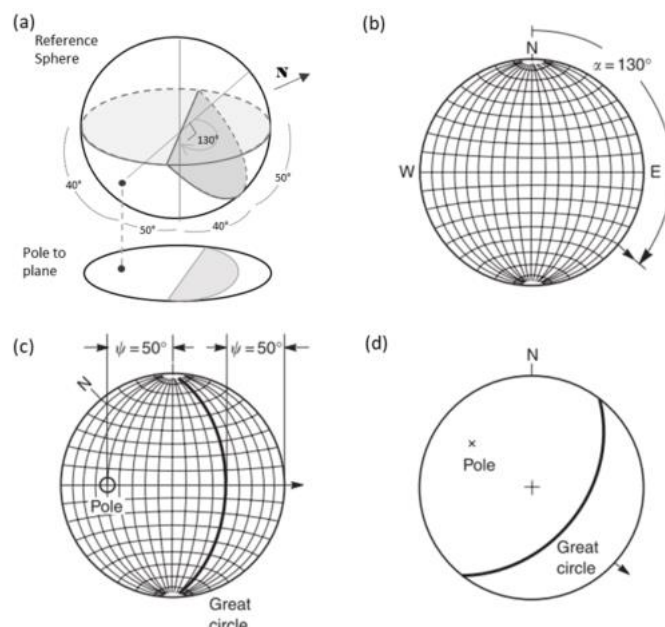


Figure 13 (a) Reference sphere with the representation of a plane striking 130° and dipping 50°. (b) Representation of measurement of the strike in an equal area net. (c) Representation of the measurement of the dip of a plane and the pole to the plane. (d) Great circle and pole to a plane with 130° strike and 50° dip. Modified from Wyllie and Mah (2004)

Contouring is done overlaying the pole diagram and a Kalsbeek net that consists of mutually overlapping hexagons, each with an area of 1/100 (1%) of the total area stereonet (Lisle & Leyshon 2004). The poles inside each polygon of the Kalsbeek net are count and the

percentage respect to the total number of poles calculated. The contours are drawn according to the percentages. (Wyllie & Mah 2004). The contour interval is usually 1%.

Stereographic software plots the contours although understanding the manual procedure gives a fair idea to interpret the contours.

Rose diagram:

The rose diagram represents the relative frequency of strike directions or dip direction. The circle is divided into equal arc intervals, and the data is grouped in those ranges. The relative frequency for each interval is represented by an equivalent radial distance like a point in the centre of the arc.

Great circle diagram

Useful in slope stability analysis because the failure modes can be assessed by plotting the mean planes of the sets of joint, faults and the rock face. The way two great circles intersects determine the shape of the blocks and the possible sliding direction.

The line of intersection of two planes in the stereo net is the point where the great circles cross each other.

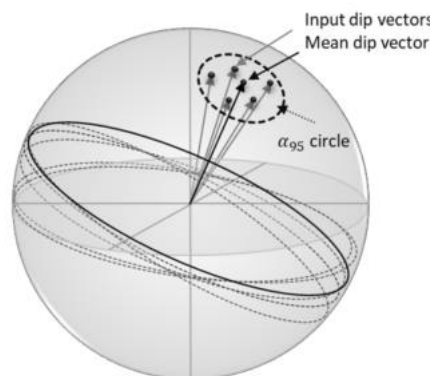


Figure 14 Representation of planes and their respective poles in a sphere.

Determination of preferred orientation of data with Fisher Statistics

Fisher (1953) developed a method to compute the average and a 95% confidence interval (CI) for data that can be represented like vectors. The sets of data should have unimodal or Fisher distribution, which is normal distribution of orientation, and vectors more or less parallel. The plane and linear data should be represented like trend azimuth and plunge angle. The direction cosines (l_i, m_i, n_i) are determined related to axes oriented north, east and down.

Equation 8

$$l_i = \cos(p_i) \cos(t_i); \quad m_i = \cos(p_i) \sin(t_i); \quad n_i = \sin(p_i)$$

Where p_i = plunge, t_i = trend of the i^{th} measure.

The components of the mean dip vector (\bar{l} , \bar{m} , \bar{n}) are calculated adding the direction cosine for each axial direction

Equation 9

$$\bar{l} = \sum_{i=1}^N l_i \quad ; \quad \bar{m} = \sum_{i=1}^N m_i \quad ; \quad \bar{n} = \sum_{i=1}^N n_i$$

Equation 10

R is the length of the vector (\bar{l} , \bar{m} , \bar{n}): $R = \sqrt{\bar{l}^2 + \bar{m}^2 + \bar{n}^2}$

The unit vector (\hat{l} , \hat{m} , \hat{n}) is given by the following equations,

Equation 11

$$\hat{l} = \frac{\bar{l}}{R}, \quad \hat{m} = \frac{\bar{m}}{R}, \quad \hat{n} = \frac{\bar{n}}{R}$$

The trend and plunge of the mean dip vector are obtained from the direction cosines.

Equation 12

Plunge of mean dip vector = $\left(\frac{180^\circ}{\pi}\right) \sin^{-1}(\hat{n})$

If $\hat{m} \geq 0$, trend of mean vector = $\left(\frac{180^\circ}{\pi}\right) \cos^{-1}\left(\frac{\hat{l}}{\cos(\sin^{-1}(\hat{n}))}\right)$

$\hat{m} < 0$, trend of mean vector = $360^\circ - \left(\frac{180^\circ}{\pi}\right) \cos^{-1}\left(\frac{\hat{l}}{\cos(\sin^{-1}(\hat{n}))}\right)$

The Precision Parameter κ has a range from 0 to ∞ , but it is acceptable when the value is ≥ 10

Equation 13

$$\kappa = \frac{(N - 1)}{(N - R)}$$

N: number of measurements.

α_{95} is the radius of the 95% confidence Interval cone within which the mean vector of a larger hypothetical population would be.

Equation 14

$$\alpha_{95} = \frac{180}{\pi} \arccos\left(1 - \left(\left(\frac{N - R}{R}\right) \left(\left(\frac{1}{P}\right)^{(1/N-1)} - 1\right)\right)\right)$$

P= 0.05 is the probability.

2.2.4 Discontinuities Spacing

The space x_i between adjacent plane discontinuities would depend on the direction and position (Priest & Hudson 1981). If the measuring of the spacing is done along a scanline of length X the mean discontinuity spacing \bar{x} and the mean discontinuity frequency λ can be estimated as follows (Priest & Hudson 1981):

Equation 15

$$\bar{x} = \sum_{i=1}^n x_i / n$$

n = number of values

The mean discontinuity frequency is reciprocal to the mean discontinuity spacing:

Equation 16

$$\lambda = 1/\bar{x} \quad \text{or} \quad \lambda = n/X$$

The spacing for planar discontinuities of random orientations along a scanline is biased by lack of precision.

The true spacing between two subparallel planar discontinuities (S) is the perpendicular distance between the planes. Hudson and Priest, (1979, 1983) advice to measure each set of fractures along a scan line perpendicular to the set. The outcrop face or drill cores are rarely perpendicular to the strike of the set of fractures to measure the *true spacing* directly with measuring tape. Instead, the *apparent spacing* (S_{ap}) is measured with a bias, and the true spacing should be calculated. One way to calculate the true spacing is using the angle (θ) formed between the rock face and the strike of the fractures, and the apparent spacing (see Figure 15) (Terzaghi 1965). The complementary angle to θ (α), is the angle between the normal to the fractures and the rock face. Also, using the angle cosines of α and the appropriate trigonometric function is possible to calculate the true spacing.

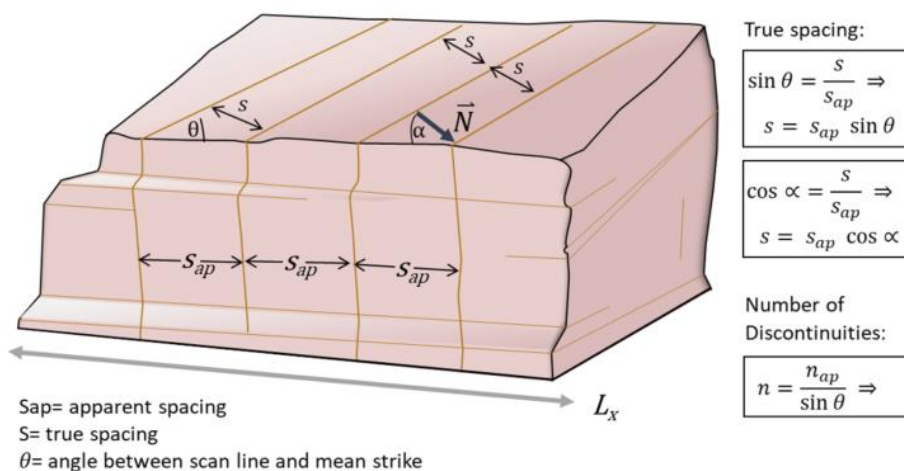


Figure 15 Calculation of true spacing for planar discontinuities using the angles θ or α and the apparent spacing.

The fractures in a set are subparallel in the best case, but usually, the orientation of the set is in a range that can be narrow or wide. Then to calculate the spacing (s_i) between two

consecutive fractures an angle θ_i should be estimated. A more simple and representative way is to determine the mean plane of the set of joints and only estimate one angle θ .

The spacing of a set of joints indicates its abundance. A set with low spacing therefore with higher frequency its prone to exert control on the flow direction (with the proper aperture and persistence). Rong *et al.* (2013) simulated fracture permeability tensor on three-dimensional fracture, in the simulations when the spacing of the fractures increase the principal values of permeability tensor decreased. Permeability of a set of fractures in HRA is inversely proportional to the spacing. Lin *et al.* (2014), Manda *et al.* (2013) and several authors calculate the number of fractures and the frequency from the spacing measured at field to use them in permeability of HRA studies. The approach of the HRA depends on the spacing of the discontinuities, shorter the spacing, higher the density of discontinuities (with orthogonal sets), then the medium can be treated as a continuum (equivalent to granular porous media) (Zhang *et al.* 1996).

The spacing controls the shape and size of blocks of intact rock and can even control the failure mode. The shorter spacing means more frequent fractures, if many sets have this feature, the block size would be smaller, and there will be a weak zone with little rock mass cohesion. A rock face with sets of joints with large spacing usually has better interlocking conditions. Therefore, the rock mass strength is related to the spacing together with the persistence. Classification of the spacing of fractures (Bieniawski, 1989) shows the widespread Bieniawski (1989) classification for spacing between discontinuities used in the RMR system.

Table 3 Classification of the spacing of fractures (Bieniawski, 1989).

Classification for Joints Spacing (Bieniawski)		
Description	Rock mass condition	Spacing between discontinuities (m)
Extremely close spacing		-
Very close spacing	Crushed/shattered	<0,06m
Close spacing	Fractured	0.06-0.2
Moderate spacing	Massive	0,2-0,6m
Wide spacing	Blocky/seamy	0.6-2m
Very wide spacing	Solid	>2m
Extremely wide spacing		-

The spacing distribution has different patterns depending on the lithology, the tectonics and the weathering. When the spacing is regular, there will be a normal distribution, typical of columnar jointed basal. Clustered discontinuities distribution has a high frequency of low spacing and low frequency of large spacing. Clusters are formed by spalling near the surface, or at the side of the joints because of stress or weathering. Randomly positioned discontinuities occur in homogeneous rocks.

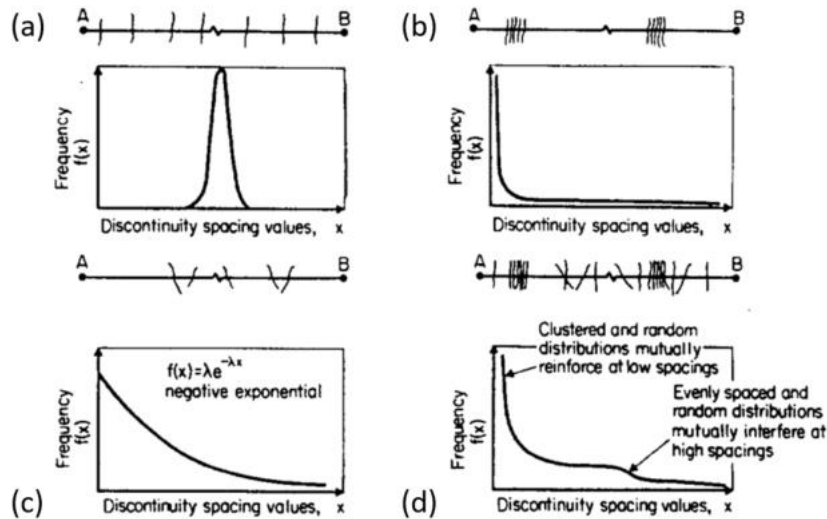


Figure 16 a) Fairly evenly spaced distribution. b) Clustered distribution. (c) Random distribution. (d) Combination of distributions. From (Priest & Hudson 1976)

2.2.5 The fracture abundance

The fracture abundance can be express regarding density, intensity or porosity; spacing persistence, dimensionless fracture density and degree of development.

Density, intensity and porosity are scale independent and can be measured in one dimension, two dimensions and three dimensions, this depends on the characteristics of the outcrops, the type of survey (Priest & Hudson 1976) and the objective. The abundance of fractures can be done for all the fractures intersecting a sampling region or for individual sets of subparallel fractures.

The density is calculated from the number of discontinuities by linear, areal or volume unit. The intensity is calculated as the number of fractures by unit length or measuring the length trace on a surface, or by calculating the area of the discontinuities in a volume of rock; for one, two and three dimensions respectively. The porosity is dimensionless then it relates the thickness of fracture on a unit length, the area of fracture on a surface and the volume of fractures in a volume of rock.

The discontinuities in the outcrop can be displayed in its totality or partially. Thus it is advisable to count the same visible feature like the endings or the middle point of the discontinuities, to avoid scale dependent and biased quantities.

Table 4 Fracture abundance measures, modified from Mauldon and Dershowitz (2000)

Fracture density	Fracture Intensity	Porosity
P_{10} number of fractures /length of scanline) $[L^{-1}]$ *	P_{10} number of fractures /length of scanline) $[L^{-1}]$ *	P_{11} thickness of fractures /length of scanline) $[-]$ *
P_{20} number of fractures /area of exposure) $[L^{-2}]$ *	P_{21} length of fracture traces /area of exposure) $[L^{-1}]$ *	P_{22} area of fracture traces /area of exposure) $[-]$ *
P_{30} number of fractures /volume of rock mass) $[L^{-3}]$	P_{32} area of fractures /volume of rock mass) $[L^{-1}]$	P_{33} volume of fractures /volume of rock mass) $[L^{-1}]$
*Depend on direction	*Depend on direction	*Depend on direction

The mean fracture spacing is the most used fracture intensity in rock mechanics as measured in a borehole (Mauldon & Dershowitz 2000).

Müller (1963) methodology to define the density of the planes and linear elements estimates the *mean spacing or mean distance* (named dm_x in Muller's work and s_i in this work). The procedure is described as follows:

- A scan line \vec{L}_x along the rock face is traced and its orientation and length measured.
- The orientations, and type of discontinuities that cross this scan line have to register.
- The data is represented on a Schmidt net to define the Unimodal sets of poles
- The mean pole (\vec{N}_i -axis) and the mean plane of each set i^{th} of discontinuities crossing this scan line are calculated.
- The scan line \vec{L}_x is projected like a vector on the \vec{N}_i -axis of the set i^{th} to obtain the projection \vec{L}'_{xi} .
- The mean intensity can be calculated for each set, by dividing the number of discontinuities n_i between \vec{L}'_{xi} (Equation 18); and the mean spacing (Equation 19) the opposite way (Figure 17 and Figure 18).

$$\frac{n_i}{L'_{xi}} = \text{Frequency} \quad \text{Equation 17} \quad \text{and}$$

$$\frac{L'_{xi}}{n_i} = \text{mean spacing} \quad \text{Equation 18} \quad \text{of the set in the direction } \vec{X}$$

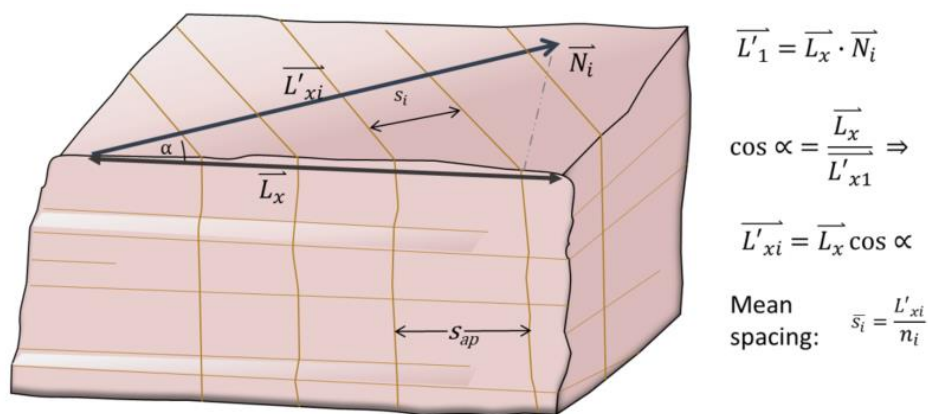
- If there is more than one measurement line the mean distance should be calculate on the total length.

$$s_{ix} = \text{mean distance in the direction } \vec{X}$$

$$s_{ix} = \frac{L'_1 + L'_2 + L'_3}{N} \quad (\text{meter}) \quad \text{Equation 19}$$

$$f_x = \text{frequency number of discontinuities}$$

$$f_x = \frac{N}{L'_1 + L'_2 + L'_3} \quad (1/\text{meter}) \quad \text{Equation 20}$$



\vec{N}_i = normal to mean plane of set i
 n_i = number of discontinuities in set i
 α : angle between scan line and normal to mean plane of set i

Figure 17 Calculation of mean distance or mean spacing for a set of planar discontinuities in the \vec{X} direction (normal to the mean fracture plane).

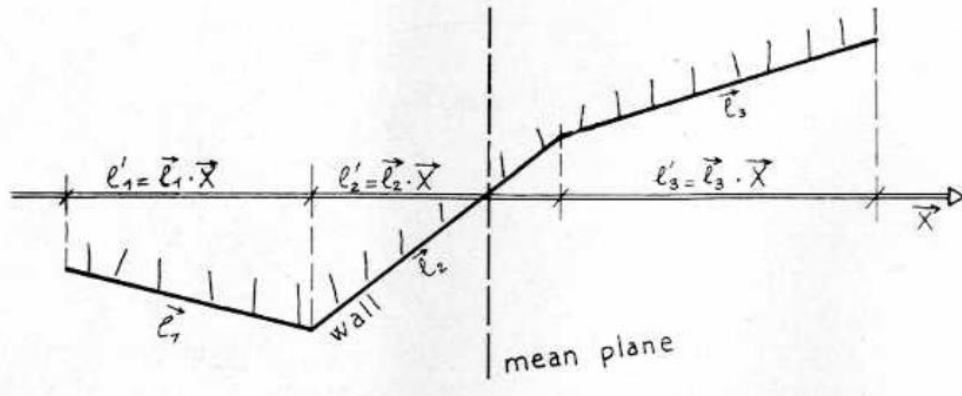


Figure 18 Computation of fracture spacing and frequency in the \vec{X} direction normal to the mean fractures plane by Müller (took from Király 1969).

Kyrally (1969) used the Müller (1963) method to calculate the mean intensity for each set of fractures, by dividing the number of discontinuities n on the length L'_1 , from the Figure 18. It is possible to work with more than one line of measurement, just projecting each fraction of line and then adding their projected values. The measure of density above is respect to the X-axis (the best axis). However, the X-axis is normal to the main plane of a set, but the planes of the set might be cutting the other axis. Therefore, there will be a mean spacing and therefore a mean density respect to them or a directional density for one joint system. These values can be calculated from the mean value of the spacing in X and the angles between the normal to the planes that intersect the other axis (Y or Z) and the X-axis. These mean intensities can be represented like a density tensor.

2.2.6 Persistence

Persistence of fractures refers to the length or area of the fractures. Although, it is a significant parameter is very difficult to measure it (Wyllie & Mah 2004). The fracture plane has a strike length and a dip length, knowing them can lead to estimate the size of the plane with probability theory (Wyllie & Mah 2004). However, the fracture plane can intersect the vertical or the horizontal walls of an outcrop, not necessarily in the way that it is representative, part of the plane can be hidden or displaced.

The fractures often exceed the extension of the outcrop and are difficult to impossible to track to estimate their length. At the field, this fact can be described, and the length indicated (e.g. >10m or >20m). However, there are ways to determine the average length. Pahl (1981) suggested a method to determine the average length of fractures for a set i in an outcrop using two perpendicular scan lines to define a rectangle, and count the fractures crossing the box and those contained inside. The calculations are shown in Figure 19

More persistent a fracture, higher possibilities to be connected and expose so it can influence the flow through larger areas serving as recharge, path or drainage. The hydrogeological relevance of a set of joints can be weighted by the persistence and the frequency. The flow in HRA requires that the persistence of the discontinuities be more significant than the spacing. Short length but short spacing can lead to interconnectivity and intricate or stepped flow path, without preferential flow direction. While single or few open long fractures could dominate the flow direction (Figure 20). Persistence in depth can be related to the depth of the fractures aquifer. Short not connected joints inside the rock mas may have high transient

water pressure, while long fractures linked to the surface acts like drainage (Wyllie & Mah 2004).

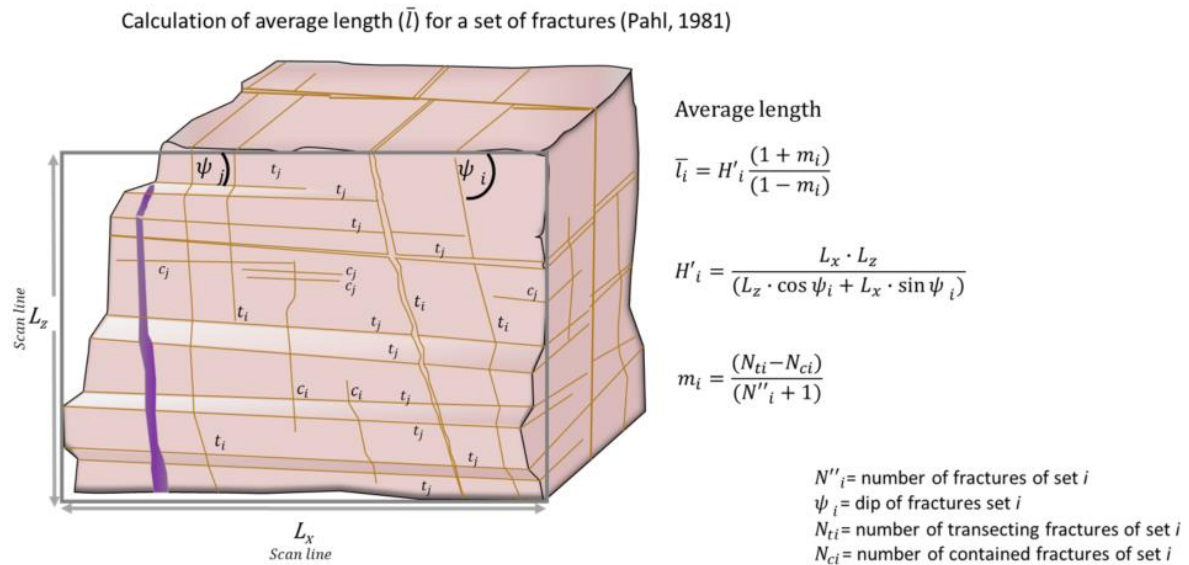


Figure 19 Determination of the average length for a set of fractures by Pahl (1981)

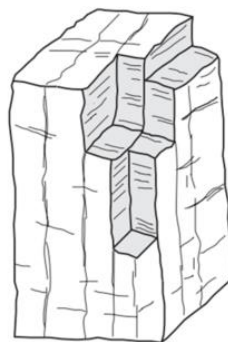


Figure 20 Example of a rock mass with long and continuous vertical joints and short not connected horizontal joints, leading to relatively high vertical permeability (Atkinson, 2000)

The length or area of the fractures is related to the block size, length of potential sliding surfaces. Long discontinuities and wide spacing lead form big blocks that in case of failure have significant volumes. Faults usually have greater persistence and lower friction angle than joints. Therefore persistence is one of the parameters used by Bieniawski (1989) RMR classification. The Classification of fractures size based on Bieniawski 1984 shows the categories to classify the trace length.

Table 5 Classification of fractures size based on Bieniawski 1984

Fracture persistence category		
Category	Trace length (m)	code
very low	<1	1
low	1-3	2
medium	3-10	3
high	10-20	4
very high	>20	5

2.2.7 Fracture endings

Fractures can finish against another fracture or in the rock matrix, though, fractures can exceed the size of the sampling area so the endings cannot be seen. At the sampling region a set of fractures with little persistence has their endings against rock mass or against more persistent fractures ends. The fracture that end in another fracture is usually newer. Short fractures that finish in rock matrix (dead-ends) are less connected and their contribution to the water flow is little (Bidgoli & Jing 2015). Fractures with dead ends would have less erosion of their filling and will influence less the formation of rock blocks. The flow direction change from one fracture that end against another fracture of different orientation.

The Table 6 shows the categories of fractures ends and the codes to describe them at field.

Table 6 Types of fractures end and codes used in field and office (modified from United States Department of Agriculture 2012)

Fracture end	
Description	code
Joint end extends beyond the exposure area	xb
Joint end terminates in solid rock inside exposure area	tr
Joint end terminates against another joint	tj

2.2.8 Aperture

The perpendicular distance between the surfaces of the rock at each side of a discontinuity filled with air or water (Wyllie & Mah 2004). Different from the width of filling of discontinuity, although if the filling has been partially removed it belongs to the category of the aperture. Aperture can be produced by:

- Shear displacement and dilation of rough surfaces,
- Tensile opening:
 - Tension at head of landslides,
 - Relaxation of steep valley walls after glacial retreat or erosion,
- Solution of discontinuities walls,
- Wash out of fillings.

The fractures originated through tensile opening and outwash can be very broad (metric). Instead, the fractures in the subsurface have a very tight aperture (around <0.5mm). The opening of a joint is not constant in space because the fracture walls are rough, neither in time because of deformation and crystallisation/solution on the discontinuity walls. The aperture exerts control on stability and the joint water pressure and flow (liquid and gas).

The permeability depends on the geometry of the void space among other parameters. In the cases of fissured rocks, the void space geometry is the space between the fractures surfaces that is controlled by the aperture, the frequency distribution, spatial correlation and contact area (Hakami 1995). The cubic law is a modification of Darcy's law applied to estimate the flow through fractures. The cubic law assumes laminar flow through an open space between smooth parallel plates. However, real fractures walls are rough, and the asperities of the

surfaces cause friction and tortuosity in the flow. Then a rough fracture with a wide aperture can conduct the same flow than a smooth fracture with a narrow aperture and (Dardashti & Ajalloeian 2015).

Depending on the scope of the study and the measuring the aperture can be mechanical or hydraulic (Figure 21):

- Mechanical joint aperture (E): is the average point to point distance measured geometrically between two rock joints surfaces, perpendicular to a selected plane, (Olsson & Barton 2001).
- Hydraulic aperture (e): equivalent space between flat parallel plates with laminar flow, deduced from flow tests applying the cubic law.

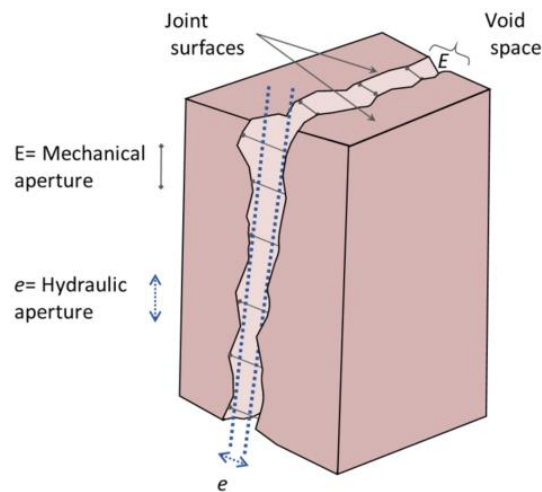


Figure 21 Block diagram showing the mechanical aperture and the hydraulic aperture.

Mechanical aperture can be measured in two-dimensional fracture section and be assumed for the three-dimensional feature. The aperture can be measured with a measure feeler gauge (Figure 22), a calliper or a measuring tape from the rock face, tunnels and drill cores and borehole camera in wells. The measuring of aperture requires to distinguish and neglect the effect of weathering and blasting (Barton *et al.* 1985).

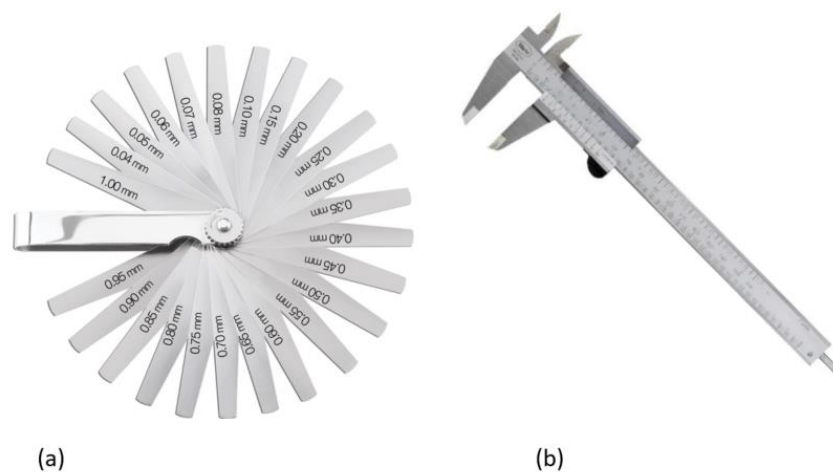


Figure 22 (a) The Measure feeler gauge has steel blades of different thickness to measure the gap between two parts. The 25 blades in carbon steel set taper from 1mm wide down to 0.04mm and 76mm long. (b) Calliper

The initial mechanical aperture can be estimated from the JRC (joint roughness coefficient) and JCS (joint wall compression strength) recorded by Barton *et al.* (1985).

Equation 21

$$E_0 \approx \frac{JRC}{5} \frac{0.2 \sigma_c}{JCS - 0.1}$$

σ_c = Unconfined compression strength (rock adjacent to fracture wall)

The hydraulic aperture can be estimated from boreholes pumping test of laboratory fluid flow experiments. Estimated from a well pumping test by placing a straddle packer to isolate discrete fractures. The cubic law gives the equivalent smooth wall aperture:

Equation 22

$$e = (12k)^{0.5}$$

k = hydraulic fracture conductivity (m/s)

The cubic law was proven valid for fractures with apertures from 0.004 to 0.25 mm, where the real mechanical aperture is almost the same than the conducting aperture (Witherspoon *et al.*, 1980). The aperture calculated from borehole pumping tests showed a lognormal distribution and a media value of 0.025 mm in a depth range of 7m-475 m in crystalline rocks in Barton (1988). A study at dam sites in the USA, 0-60 m depth, showed that the permeability was higher with aperture values between 0.05 mm and 0.15 mm (Barton *et al.* 1985).

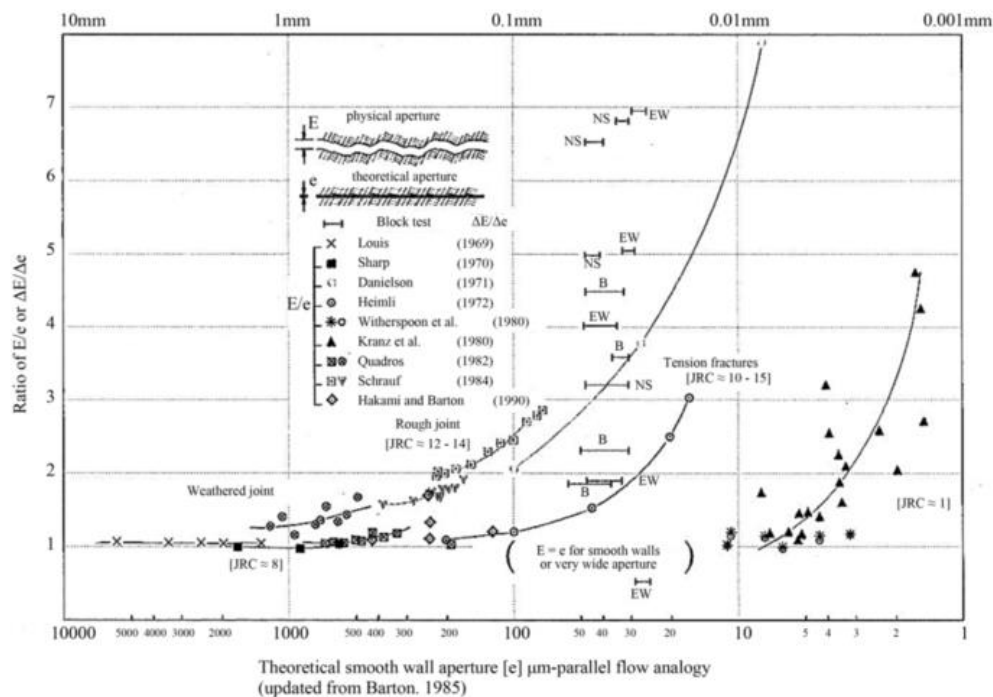


Figure 23 Comparison of real mechanical aperture with theoretical hydraulic apertures. The mismatch is caused by flow losses due to tortuosity and surface roughness. Took from Olsson and Barton (2001)

The cubic law can take into account the roughness and its effect on the flow applying a correction factor. Zimmerman and Bodvarsson (1996) studied how to replace the Navier–Stokes equations for the Hele-Shaw equations to estimate flow in fractures. The study looked for a way to relate the effective hydraulic aperture to the statistics of aperture distribution, finding that hydraulic aperture is less than the average aperture by a factor that depends on the ratio of the mean value of the opening to its standard deviation (Zimmerman & Bodvarsson 1996). Hakami (1995) showed that the ratio between mechanical mean aperture (E) and hydraulic aperture (e) was 1.1 - 1.7 for joints with a mean aperture of 0.1 – 0.5 mm.

The predicted relation between hydraulic aperture (e) and (E/e) for different values of JRC following an exponential behaviour.

Aperture can change due to deformation given by variations in stress or water pressure. The change on water pressure is given by the increment or decrease of water in the joints it consists on shear displacement and normal change of aperture. Shearing along rough fractures in granite causes roughness-induced dilation, modification of the aperture, the increment of the normal stress and locking the fractures (Barton 1982). Shearing cause lateral and normal displacement of the fracture surfaces changing the distribution and average aperture. The dynamic earthquake stress along the fractures unblocks the fluid and particles that will redistribute and restructure pore pressure (Wang and Manga, 2010). After an earthquake, there is an incrementing in the permeability proportional to the dynamic stress (Elkhoury *et al.* 2006). However, the permeability decrease to the original value due to refilling of the fractures by mineral precipitation and hydrothermal alteration, therefore the cause of the enhancement of aperture is inferred to be caused by mineral crushing or unblocking of soft mineral phases (Lachassagne *et al.* 2011).

High stresses may be affecting the rock mass. If there are high horizontal stresses acting almost perpendicular to a cut slope may cause blocks to move outward, and cause spalling of the surface of a cut slope.

The permeability can change in three orders of magnitude if the aperture changes (Barton *et al.* 1985). Conducting aperture changed from 0.06 to 0.03 mm in a block of fractured gneiss when the stress increased in 7MPa by insertion of flat jacks, Hardin *et al.* (1982). The increment in stress would lead to reducing aperture and permeability, as decreasing stress would increase the aperture and the permeability. Hydromechanical coupling relates the change in the mechanical aperture with the change in hydraulic aperture. Olsson and Barton (2001) proposed a model that takes into account two phases during a shear test on rough fractures. The first phase with initial JRC (JRC_0) previous to shear displacement with the original roughness. The second phase is posterior to the shear displacement and destruction of the asperities when the aperture has changed.

2.2.9 Roughness

This feature refers to the degree of asperity or irregularity of a rock surface, particularly of the planes of a fracture. The irregularities on the surface of the fractures are known as asperities. First order and second order asperities are depending on their size. The first correspond waviness or large-scale undulations. The second order corresponds to small-scale

irregularities or asperities such as ripples they have higher i values. Both orders can be measured on the field, but asperities can also be inferred from a direct shear test.

There are different ways to evaluate the surface roughness of rock samples. One way is measuring the inclination (i°) of the irregularities over the fracture plane. It is advisable to measure it over 2m length on the lower plane (over width the sliding may occur).

Another way is by visual comparison of a linear profile parallel to the sliding direction with reference profiles like those from the Joint Roughness Coefficient (JRC) developed by Barton and Choubey (1977) (Beer *et al.* 2002; Wyllie & Mah 2004). The JRC is probably the most used method that associates standard profiles combining irregularities and waviness to coefficients from zero for planar surfaces to 20 for rough, undulating surfaces (Figure 24). The relation between the roughness i and JRC is given by equation 18:

Equation 23

$$i = JRC \log_{10} \frac{JCS}{\sigma'}$$

JCS = Joint Compressive Strength on the fracture surface
 σ' = effective normal stress on the fracture surface

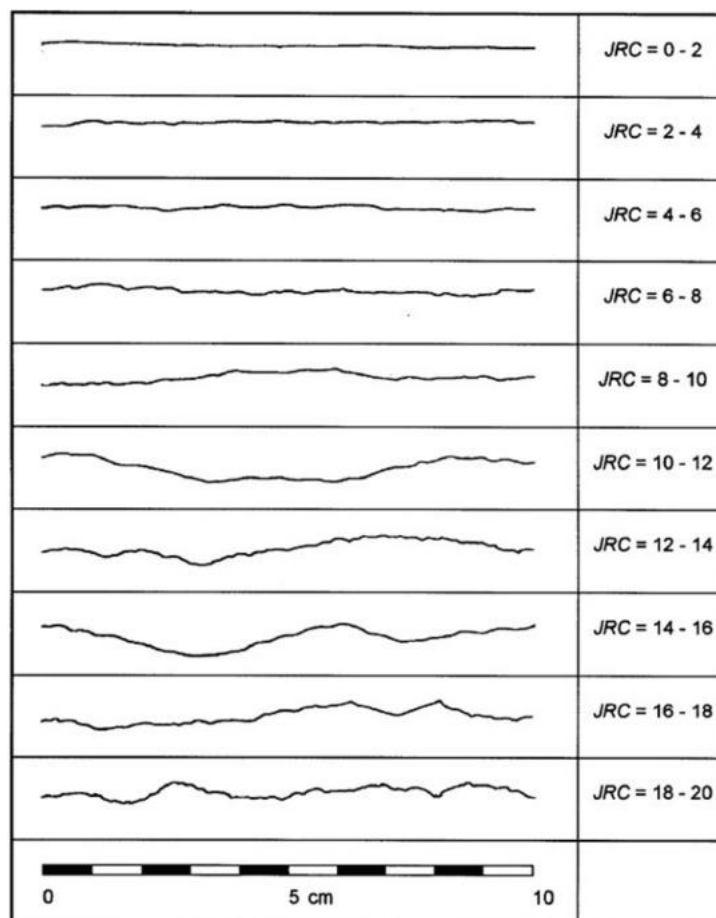


Figure 24 Roughness profiles and the corresponding range of JRC (joint roughness coefficient) values (ISRM, 1981).

The profile of the surface can be obtained using a Barton comb profilometer (carpenters' comb) (Figure 25). This instrument has very thin steel wires in a frame that allows them to slide to lay to the outline of the sample under test.

Visual comparing is subjective as proved by Beer, Stead, and Coggan (2002) asking around 124 people with different degrees of experience on JRC estimation to assign the JRC value to three profiles samples obtained randomly from a granitic block using a comb profilometer. The distribution of the JRC values assigned to the profiles was narrow for two samples and very broad for the third one (Figure 26). The experiment proved that better results are obtained from many observers, experienced observers and when the sample is similar to the reference profiles (Beer *et al.* 2002).

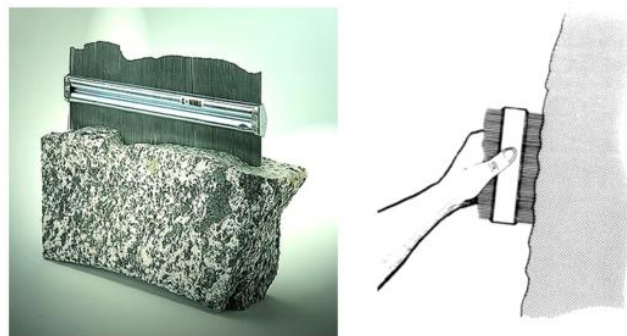


Figure 25 The practical measurement of joint surface smoothness (from Milne, Germain and Potvin, 1992)

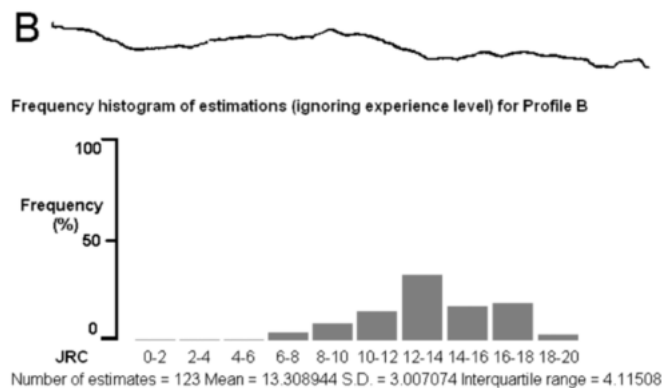


Figure 26 Profile used in the survey by Beer, Stead, and Coggan (2002) and the histogram of the distribution of the JRC values assigned by 123 people. Took from Beer, Stead, and Coggan (2002).

The calculation of flow using the cubic law assumes smooth fracture planes and constant aperture. Although, real fractures walls have irregularities and deformation that change the aperture and fluid flow (Dardashti & Ajalloeian 2015). Witherspoon *et al.* (1980) attributed a small reduction in flow rate (4-40%) due to of roughness.

This property is relevant in slope stability because the interlocking of rough un-displaced opposite surfaces adds stability. Shear strength and dilation can be estimated from roughness. However, the aperture, the filling and the displacement affect the relevance of the interlocking effect of roughness.

2.2.10 Weathering

Weathering processes can be divided into mechanical disintegration or chemical decomposition. Although, both types of processes can be acting at the same time. Mechanical disintegration by changes in humidity, freezing and thawing; creates discontinuities, break grains and open or increase the aperture of discontinuities already present. It is common in rocks with swelling clay mineral and micas.

Chemical decomposition is caused by oxidation, hydration, and carbonation. This weathering produces discolouration of the rock, decomposition or alteration of silicate mineral to clay mineral, and dissolution of carbonate and saline mineral.

Weathering is controlled by climate and humidity. Weathering is different depending not only on the material but also the geographic location because of the weather patterns.

There are rocks more and less resistant to weathering depending on their mineralogy and texture. Fine-grained rocks like claystone, shale, mudstones, slate and phyllite are very susceptible to weathering. Expansive clay minerals swell and shrink with moisture changes weakening the rock even in minutes. Rocks with medium to coarse grain like sandstones and granites are more resistant to weathering.

The rock mass is weathered where it is exposed to atmospheric factors or circulation of fluids. The discontinuities surfaces are usually more weathered than the intact rock because they expose the rock to the atmosphere and water. The intensity of the fracturation is related with the weathering because more fractures means more surface area expose to weathering. Discontinuities often develop a coating product of weathering that affects the shear strength, especially on planar and smooth surfaces. It is useful to describe the composition of the coating or take a sample (Wyllie & Mah 2004).

The product of weathering can get loose and be eroded from the slope surface, changing the morphology and exposing the fresh material to the atmosphere. Degradation of rock is related to slope stability. Weathering affects cohesion in discontinuities plains. Weathering can be responsible for the erosion of the toe of the slope or a reduction of the underlying layer leading to failure by toppling or rock fall.

The weathering influence the permeability in a fractured rock because advance alteration of the hard rock can generate zones with primary porosity. Weathering generates also fractures, but the alteration of minerals to clay or the moving of weathering product in empty fractures could decrease the conductivity.

There are classifications for the degree of weathering from geomechanics that can be use as well for hydrogeological purposes.

2.2.11 Filling

The filling is the material occupying the space between the fracture (breaks) planes. Such material can be filling the whole space or just partially. The filling has different compositions, textures and origins. The filling material can be syngenetic with the fracture or have been introduced later. The term filling refers mainly to solid materials; in part because gas, water or oil will not be easily observed in a sample.

Pieces from the wall's fracture become filling when they get loose and are displaced. The BGS categorized the filling according to with the components or with type (Figure 27).

The common filling components are: authigenic minerals (a mineral formed in its present location from fluid or magma), clasts, organic matter, recrystallized rock, and fluid (Gillespie *et al.* 2011).

Filling originated from magma should be named from the Igneous Rock Classification (for example basalt-filling). The types of filling are: 'Crusts', 'Veins', 'Sediments', 'Breccias', and 'Fault-rocks'. The Veins and crusts are both made of authigenic mineral fillings, the first filling space between the fracture walls, while the second is placed at the surfaces of the host fracture without uniting the sides. The crust can be single crystal or coatings on the fractures surfaces (Gillespie *et al.* 2011).

Fault rocks are classified in cataclasite and mylonites. The cataclasite are the product of rapid strain at relatively low temperature, slightly recovered or not recovered, they have incipient schistosity. The mylonite is the product of high strain rate and good recovery rate; they exhibit schistosity.

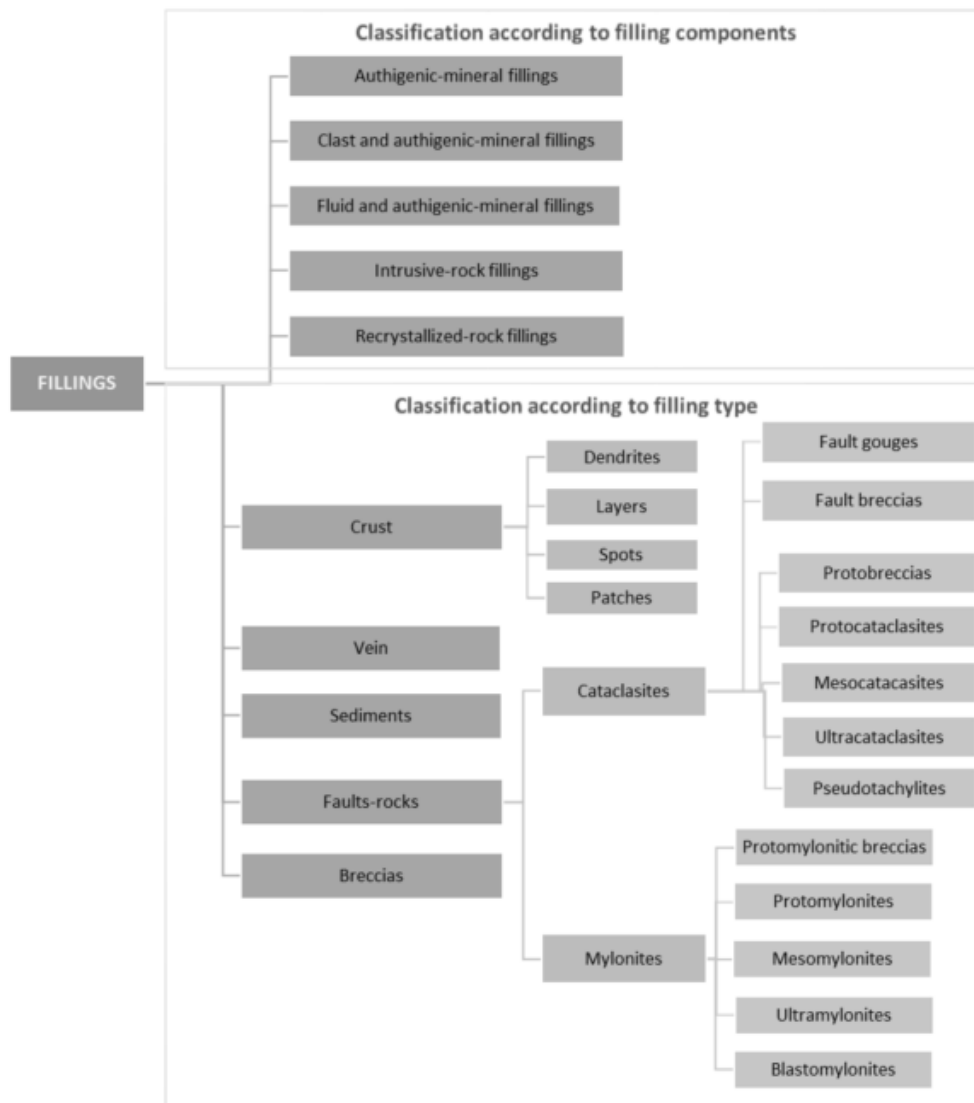


Figure 27 Classification of filling of discontinuities according to filling components and filling type by the BGS (Gillespie *et al.* 2011).

The filling affects the permeability of fractures because of its proportion and type of material. The degree of healing or development of crust in the fractures walls conditions the apertures and thus the permeability. The space for flow in a fracture can be controlled by the quantity and nature of particles moving in the fracture network. For example, the product of weathering in granite are loose crystals of sand size that can fill the fractures without blocking the flow. However if enough silt or clay accumulates in a fracture aperture, it could turn it into impermeable.

The strength of fractures depends on the thickness and the material of the filling. The thickness of the filling can be such that controls the shear strength. Shearing stress of fractures partially filled or clean is controlled by roughness (Romana 1993).

2.2.12 Groundwater

The quantity of water or its absence in individual breaks is direct information to identify sets of fractures conducting water and zones of drainage. The water observed in fractures is the product of seepage. The *seepage* is a slow movement (vertical and lateral) of water in a permeable medium, through porous or fractures, due to pressure differences under the action of gravity; from a zone with high head to an area with lower head.

The quantity of seepage depends on the season and location, but it is also a consequence of the characteristics of the discontinuities. The precipitation and temperature conditions the groundwater availability. During a dry season when the water table is low, even if the medium has very good permeability the fracture would be dry. The flow amount depends on the location because of the water table spatial variation and the local hydraulic gradients. Features like dykes, sealed- fractures, changes in lithology or fractures path can act as barrier for groundwater. The geometry of such elements can lead to irregular and perched water tables. The aperture and the filling of the fracture also condition how the groundwater would flow. Therefore the description of seepage or groundwater in fractures has to take into account the last rain, the climate and the filling. The description of groundwater in fractures has been classified according to with the presence or absence of filling like shown in Table 7

The water table, rainfall and temperature records; and surface drains and wells inventory are necessary data to assess the groundwater flow. Groundwater level, paths and water pressure indicate the degree of susceptibility to floods and mass movements and possible problems in construction.

Table 7 Groundwater Conditions (Romana 1995)

Groundwater Conditions (Romana 1995)				
Description	Unfilled joints		Filled joints	
	Joint	Flow	Filling	Flow
Comp. Dry	Dry	No	Dry	No
Damp	Stained	No	Damp	No
Wet	Damp	No	Wet	Some drips
Dripping	Wet	Occasional	Outwash	Dripping
Flowing	Wet	Continuous	Washed	Continuous

2.2.13 Number of sets

The relation of the mutual orientation, the spacing, the persistence and the number and types of discontinuities determine the shape and sizes of individual rock blocks and the geometry of the fracture network and potentially the flow path.

The number of sets affects the interconnectivity and how intricate the flow path can be. If there is one dominant set single it will dominate the flow direction, if there are three relevant sets the flow does not have a preferential direction (Figure 28 and Figure 29)

The number of sets can be recognized at field, observing the representative discontinuities belonging to sets over random discontinuities. However, the number of the sets is defined after the projection of the fractures in the stereonet to identify poles concentrations. A classification for the number of joint sets is given in Table 8

Table 8 Categories for the number of joint sets (Wyllie & Mah 2004)

Number of joint sets	
Category	
massive, occasional random joints	I
one joint set	II
one joint set plus random	III
two joint sets	IV
two joint sets plus random	V
three joint sets	VI
three joint sets plus random	VII
four or more joint sets	VIII
crushed rock, earth-like	IX

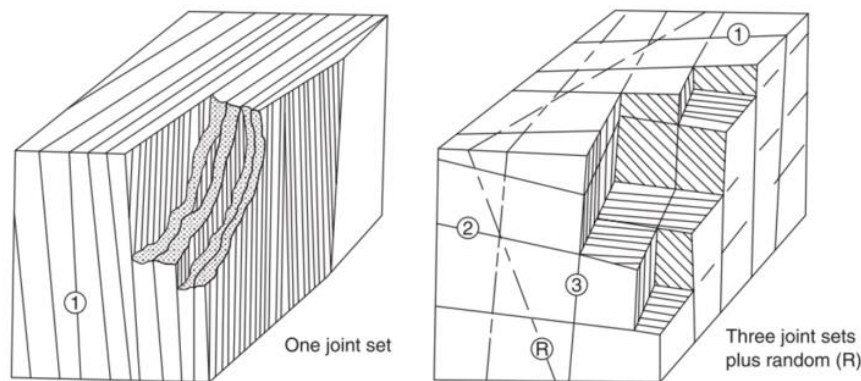


Figure 28 Effect of number of joints on the appearance of rock mass (ISRM, 1981).

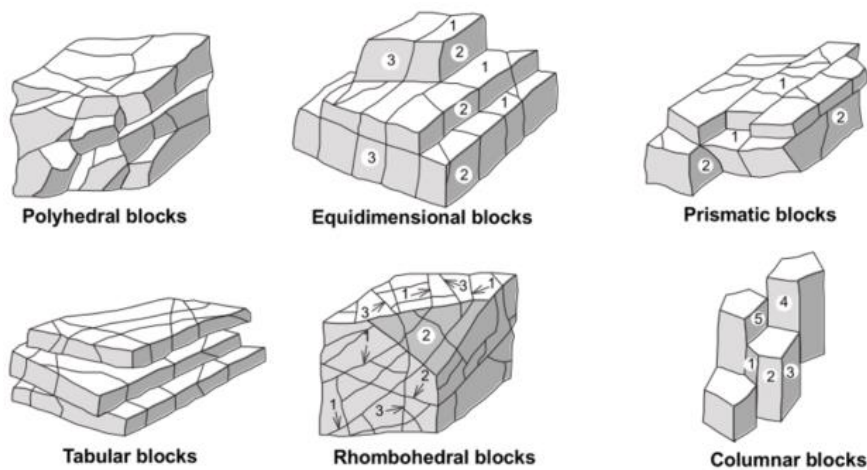


Figure 29 Examples of block shapes depending on the fractures pattern (Dearman, 1991) and main type of blocks (Palmström 1996).

2.3 WATER BUDGET

The estimation of a water budget in a watershed requires a long-term record of climate and hydrologic parameters and good knowledge of the physiographic properties and their relationships. However, many areas have a deficit of information, needing to interpolate or estimate the parameters from the available information.

The hydrologic cycle represents the dynamic of water among atmosphere, ocean and land. The hydrologic cycle is powered by sun radiation and geothermal fluxes. The water cycle can be assessed as water budget or radiation (energy) budget. Water from the atmosphere passes as precipitation (rainfall, or snow) to the land and oceans. The precipitation is the inflow of a hydrologic system. Part of the precipitation is intercepted by vegetation, but most of it reaches the soil to (1) be evapotranspiration; or (2) become part of runoff as overland flow, interflow and base flow or (3) infiltrate to become groundwater. The water from oceans and land flows back to the atmosphere through evaporation and evapotranspiration. Surface water and groundwater eventually discharge into large water bodies. Total discharge and evapotranspiration are the outflow processes of the hydrologic system (Figure 30).

Hydrological studies are usually confined to a hydro-morphological unit or area which supplies water, sediments and other fluvial materials to a river or a network of rivers. The spatial distribution and velocity of water among reservoirs in a given study area depend on the weather, topography, nearby water masses, anthropic intervention and the geo-hydrological characteristics of that area.

The collective behaviour of the catchment is called “catchment functioning” (Black, 1997). Holistically the behaviour of the catchment can be expressed in term of partitioning, transmission, storage and release of water, energy and matter (McDonnell et al., 2007; Wagener et al., 2007). Partitioning is the separation into different pathways due to interception, infiltration and surface runoff. Storage merely is the retention of water in a space during a period. Transmission is the flow of water through the catchment depending on the connectivity and moisture. The release of water from the catchment is the discharge and the evapotranspiration. (Blöschl 2013).

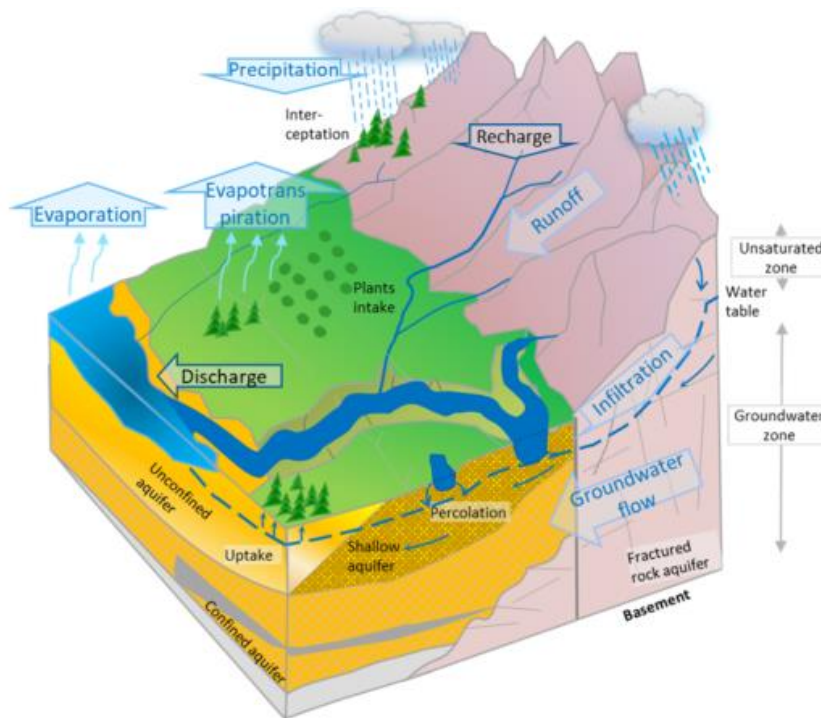


Figure 30 Schematic hydrologic cycle

There are two general phases in a catchment: the wetting and the drying. The wetting phase depends on frequency and intensity of precipitation, previous moisture and previous precipitations. The drying phase depends on how water is released, topography, geology, soil and ET. (Blöschl 2013).

Climatic factors like precipitation and evapotranspiration vary in space and time, mainly influencing discharge, water table and recharge dynamics. Time-dependent changes in inflow and outflow give transient effects to the groundwater system. The transient effects are more marked in the unsaturated zone. In fact, the hydrogeological system should always be analysed including unsaturated and saturated zones (Freeze & Cherry 1979).

The study of hydrogeological systems requires expertise in geology, hydrology, physics, chemistry and mathematics. Mathematics for groundwater flow is based on mathematics for heat flow, electricity and magnetism.

The features affecting the hydrologic cycle, the way they can be quantified and used to model hydrological and hydrogeological systems are described below.

2.3.1 ESTIMATION OF WATER BUDGET

The water budget is the application of mass conservation principle to water flow in a geographic location (watershed, aquifer, lake, etc.). The inflow into any storage should be equal to the outflow, ignoring short-term perturbations (Price 2013), although there is an error when each term is measured independent. The water budget is a coarse approximation, the hydrologic systems are far more complicated, and exact results are difficult to get (Freeze & Cherry 1979; Díaz *et al.* 2005; Gilli *et al.* 2012). The flow can take different paths, and the residence time in each reservoir is different, then the balance should be estimated for a period depending on the study and the data available. The error can be minimised choosing simplified components and the period with more trustful data.

The general form of the water budget at a watershed is:

$$\text{Inflow} = \text{outflow} - \text{change in storage} + \text{error}$$

In two simple terms, the total effective precipitation (P_{ef}) should be equal to the total discharge (Q_T). The total discharge in a basin includes runoff and groundwater outflows although the GW can move from one catchment to another or discharge directly to the sea. (Gilli *et al.* 2012).

$$P_{ef} = P - ET$$

$$P_{ef} = Q_T = Q_S + Q_G = I_{ef} + Rs$$

P = precipitation
 ET = evapotranspiration
 P_{ef} = effective precipitation
 Q_T = total discharge
 Q_S = surface discharge
 Q_G = groundwater discharge
 I_{ef} = effective infiltration
 Rs = surface runoff

The hydrologic budgets can be done in event scale to seasonal scale, but are usually estimated for one year. Given the annual variability of climatic factors and the consequent response of the catchment, the budgets are estimated over ten years with averaged parameters. During one year the difference between storage in the surface water reservoir, and groundwater reservoirs are minimised $P_a = Q_{Ta} + ET_a$.

$$P_a = Q_{Ta} + ET_a$$

Average of annual records $\Delta S_s = \Delta S_g = 0$
 P_a = average annual precipitation
 Q_{Ta} = average annual total discharge
 ET_A = average annual evapotranspiration

The annual runoff is the total volume of water discharged past a point of interest in a stream in one year divided by the contributing catchment area", the units are mm/yr (Blöschl 2013). Predict the annual runoff serves to understand the surface water balance of a landscape and also to deduce water availability, inter-annual variability and susceptibility to change. The variability of runoff can be evaluated also using the regime curve, the flow duration curve and the flood frequency curve ET, P and carry over of soil moisture and groundwater between years are responsible of the annual variability in runoff.

Although the water budget equations look simple and have few parameters; they have several limitations. The equations of the water budget use lumped-parameters approach and not a distributed-parameter approach that accounts heterogeneity. The use of annual averages ignore the interannual and seasonal changes. Therefore, the areal and the time variability is not accounted. Estimate the annual averages requires several years of records of, at least, precipitation, temperature and discharge (streamflow). The evapotranspiration is the most complicated parameter to obtain from methods of questionable accuracy.

2.3.2 Hydrologic modeling

Hydrologic modelling can be done in several ways, from basic point scale soil water balance accounting only vertical exchange to modern modelling of the watershed with inputs, outputs and geographic variation along a three dimension domain accounting horizontal flow (Figure 31).

Lumped models take the whole area of the catchment as uniform ignoring the spatial variability and processes depending on space. On the other hand, distributed model outputs vary spatially and can have different spatial configurations: Triangular Irregular Networks (TIN), Rectangular discretisation, planes and channel segments (sub-basins), discretisation in depth or separation in depth into saturated and unsaturated (Figure 32). Examples of models using discretisation are hillslope-scale hydrological processes during inter-storm and storm periods (Beven 2011), catchment-scale individualising processes for a grid-based numerical model.

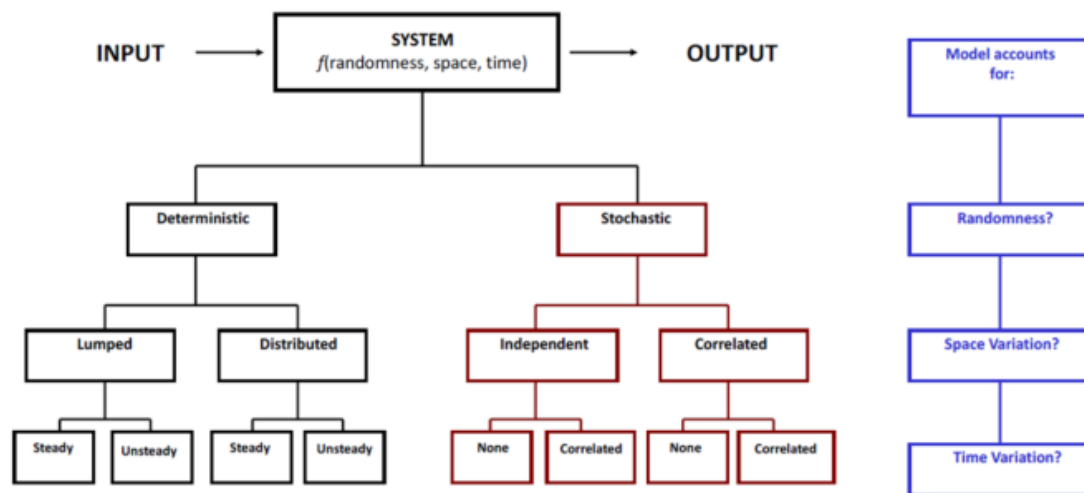


Figure 31 Types of hydrological models.

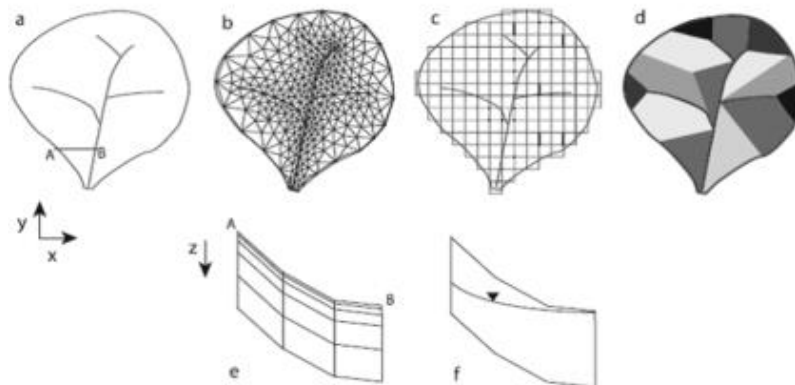


Figure 32 Spatial configurations (a) hypothetical catchment in the plan (XY) view, (b) Tin discretisation (c) rectangular grid discretisation, (d) planes and channel segment (e) Explicit discretisation of depth (Z) and (f) separation of depth into unsaturated and saturated.

Empirical or data-driven models relate through statistics, regressions and correlations the input and output information without the physical processes of the catchment. It is the traditional approach to hydrologic basins as a black box.

Conceptual or parametric models account for the physical, hydrological processes but use semi-empirical equations and parameters are derived from field and calibration.

Physically based models (or mechanistic models) are based on Newtonian mechanism, the causality of the component processes can be represented in an idealised mathematical deterministic way and in detail. These models use many parameters to describe the physical

properties of the catchment and measure state variables that are a function of time and space. They can be applied to model periods of several years to several decades. (Blöschl 2013; Devia *et al.* 2015).

Remote sensing, interpolation and GIS are tools that can provide separately some parameters of the catchment that helps to solve the water balance, but they cannot by themselves evaluate the runoff or the recharge.

The recharge or the effective infiltration are parameters hard to estimate, especially in areas without instrumental data. Through the assessment of the parameters of the water, balance is possible to get an approximation to the recharge. The evapotranspiration can be estimated through climatic elements while the runoff when is not directly measured has to be estimated understanding the hydrological connections among the complex spatial patterns of a catchment and the runoff variability.

2.3.3 Methods to predict runoff in ungauged streams

Hydrological studies in the ungauged basin can be challenging, the determination of runoff requires to choose an appropriate methodology (Grillone *et al.* 2014).

Several components of the watershed interact to produce an intricate temporal pattern of water fluxes that are the runoff response of the catchment (Blöschl 2013). The climate, vegetation (land cover), landform and soil co-evolve in time scale from years to millenniums in such way that generate fingerprints on the runoff response in the catchment. Notice the process that cause long term mean variability and their different effects in different catchments is important for understanding of the catchment systems. The landscape determines heterogeneity and organisation of the pathways for water. Summarizing, the landscape has spatial signatures that are related to the runoff temporal signatures. The signatures are the base to predict runoff in ungauged basins because they are manifesting the watershed functioning at different time scales (Blöschl 2013). The physiographic parameters and the controlling process are used to formulate similarity index to group similar catchments. The relationships observed in gauged basins can be extrapolated to ungauged basins with similar characteristics.

Similarity measures

Runoff similarities: similarity among catchments can be given regarding mean annual runoff or runoff coefficient. The runoff coefficient (C_s) is the ratio of the total depth of runoff to a total depth of rainfall during an event or the ratio of mean annual runoff to mean annual precipitation. The C_s depends on topography, land use and vegetal cover, soil type and moisture content (Mahmoud *et al.* 2014).

Climate similarity indices: The aridity index (AI) gives the first-order estimation of total annual runoff variability because it relates the water and the energy available. AI is the ratio between annual precipitation and potential evapotranspiration (PET) (UNEP, 1992), PET is calculated using the Penman (1948) formula. High AI corresponds to low runoff coefficient. The De Martonne (1926) proposed an aridity index (I_a) that uses temperature instead of PET, given the less available information regarding ET.

Equation 24

$$AI = P/PET$$

The Mediterranean climate requires the use of aridity index and the seasonality index to predict the annual runoff because the precipitation and potential evapotranspiration inter-annual variation in arid regions is significant and cannot be captured by conventional steady-state water balance models (Feng *et al.* 2012; Blöschl 2013).

Catchment similarity indices: Watersheds with same climatic conditions can have different runoff response due to the properties of the soil and the vegetation. For such cases, there are indices regarding the soil field capacity, texture, saturated permeability, slope and vegetation cover. The similarity indices serve to describe and group catchments of similar properties and behaviours and to extrapolate the runoff behaviour. This can be done by grouping or regionalisation, statistical prediction and process-based prediction.

2.3.3.1 Statistical methods of predicting annual runoff in ungauged basins:

Uses regional statistical techniques to infer information from other catchments to the catchment in the study. The statistics applied are those to estimate a random variable approaching the maximum amount of the spatial variance. The methods are

Regression methods: use of the analytical expression to transfer runoff signatures based on the relationship between climate and catchment.

Interannual variability: The Coefficient of variation of annual runoff CV (Kalinin 1971) has a relationship with the area of the catchment, smaller the area smaller the variability of the annual runoff. McMahon *et al.*, 1992 used a power-law relationship between the CV and the mean annual runoff, it indicated that arid zones have more variability.

Index methods: assumes homogeneity of the characteristics in a region except for locally varying scaling index.

The performance of all methods of predicting mean annual runoff in ungauged basins decreases with increasing aridity. Milly and Dunne (2002) compared the response of the annual catchment runoffs and their dependence with the annual precipitation of the previous year; they found that 80-90% of the variance in annual discharge in humid catchments could be explained by the precipitation while in arid areas only 40-80% could be explained by P. Budyko methods underestimate mean Q_a, and the regression models overestimate Q in arid catchments. Budyko models are better than regression models in arid areas.

Kennessey (1930) developed an empirical method to estimate the average annual runoff coefficient (C_k) and the water budget of a watershed from the main factors influencing the C_k such as climate characteristics, surface permeability, mean slope and vegetation cover (Ghiglieri *et al.* 2014; Grillone *et al.* 2014). The method has been adapted and improved by several authors especially in North Central Italy (Barazzuoli *et al.* 1989; Ghiglieri *et al.* 2014). The method includes calculating the De Martonne (1926) annual average aridity index (I_a) (Equation 25) from the climate component to later classify the physiographic components.

Equation 25

$$I_a = \frac{\left[\left(\frac{P_A}{T_A+10}\right) + (12\frac{p}{t})\right]}{2}$$

P_A= mean annual precipitation
T_A= mean annual temperature
p= precipitation of the hottest month
t= temperature of the hottest month

Kennessey (1930) proposed empirical numerical coefficients for the surface permeability, mean slope and vegetation cover, based on their values and of I_a Table 9. The coefficients are weighted according to the area that each class occupies resulting in the partial runoff coefficients: slope angle (C_a), vegetation cover (C_v), and permeability (C_p). The C_k of a watershed is calculated adding the three coefficients C_a , C_v and C_p ($C_k = C_a + C_p + C_v$) (Barazzuoli *et al.* 1989).

Equation 26

$$C_k = C_a + C_p + C_v$$

Equation 27

$$R_{Ap} = (P_A - ET_A)C_k$$

Equation 28

$$Ie_{Ap} = P_A - ET_A - R_{Ap}$$

The mean annual potential runoff can be calculated using Equation 27 and the mean annual potential effective infiltration Equation 28 (Farina & Gaspari 1990; Ghiglieri *et al.* 2014; Spadoni *et al.* 2010). Although C_k is valid on a yearly base, the monthly runoff figures, are significant in verifying the results obtained and the errors in the procedure (Mazza *et al.* 2014).

Table 9 Coefficients of physiographic indirect method to calculate potential runoff coefficient classified by aridity index (Spadoni *et al.* 2010a)

		Aridity index		
		$I_a < 25$	$25 < I_a < 40$	$40 > I_a$
Slope component C_a	>35%	0.22	0.26	0.3
	10-35%	0.12	0.16	0.2
	3.5-10%	0.01	0.03	0.05
	<3.5%	0	0.01	0.03
Permeability component C_p	Very low	0.21	0.26	0.3
	Low	0.16	0.21	0.25
	Moderate	0.12	0.16	0.2
	Good	0.06	0.08	0.1
	high	0.03	0.04	0.05
Vegetation component C_v	Bare rock	0.26	0.28	0.3
	Grass land	0.17	0.21	0.25
	Farm/shrubby Land	0.07	0.11	0.15
	Forest land	0.03	0.04	0.05

Ghiglieri *et al.* (2014) applied the method to obtain the C_k in 30 basins spread in Sardinia and validated the method with the instrumental data of 71 years (1922-1992). Although, there was high variability between the measured and estimated annual runoff coefficient in some basins due to high temporal variation of P and T . Among the basins studied by Ghiglieri *et al.* (2014), the basin of the River Leni (57.27 km²) is similar to the MORB because it has the recharge area in leucogranite of the Intrusive Unit of Villacidro. River Leni basin has a measured runoff coefficient (C_s) of 0.448 and an estimated potential runoff coefficient (C_k) of 0.392 and a percentage deviation of -12.5%. Other basins in granitic areas of Sardinia had a fair correspondence between C_s and C_k . The potential runoff and the water budget estimated

with this method are indicative of the magnitudes and spatial variations, but they do not reflect interannual variability.

Table 10 Percentage of basins evaluated by Ghiglieri et al. (2014) classified by the Percentage deviation (PD) between the estimated C_k and the calculated C_s .

Percentage deviation C_s and C_k	Range of PD in absolute value	Percentage of the 30 basins Evaluated in Sardinia inside the range of PD
0-10%	1.5-8.52%	20%
10-20%	11.63-19.55%	33.33%
20-30%	22.16-29.43%	23.33%
>30%	33.33-67.82%	23.33%

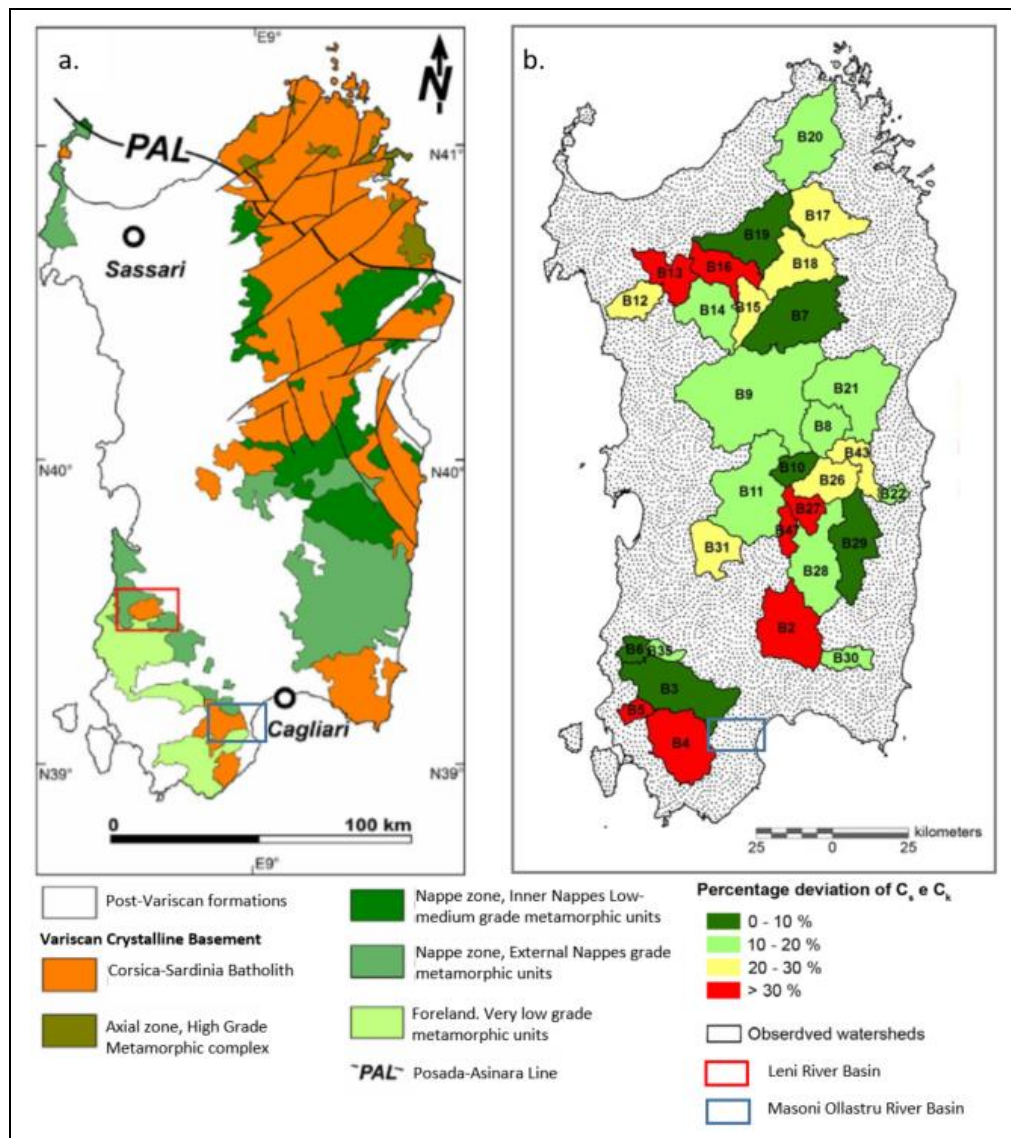


Figure 33 a) Geological sketch map of the Variscan basement of Sardinia. In orange the Corsica-Sardinia Batholith (modified from Cuccuru et al. 2015). The Leni River basin recharge area is over the Intrusive unit of Villacidro, the main unit that outcrops in the Masoni Ollastru river basin. b) Schematic representation of the percentage deviation (PD) of C_s and C_k in 30 watersheds (modified from Ghiglieri et al. 2014). The PD in Leni River basin is -12.5%, and for the other granitic areas of Sardinia the PD is between 1.5% and 30%.

Grillone et al. (2014) tested the Kennessey method in 61 Sicilian basins characterised by different climate conditions, surface permeability, mean slope and vegetation cover. The values of C_k were overestimated in relation to the measured C_s . Therefore, they calibrated the

Kennessey model to improve the relationship between the measured and potential runoff coefficients, but the improvement was not satisfactory. Grillone et al. (2014) looked for empirical relationships between C_s and geographical and meteorological parameters to improve the estimation of C_k . They found the best empirical relations between C_k and average annual rainfall and average annual temperature by a simple linear regression. They suggest that the estimation of the C_k could be improved collecting morpho-climatic and hydrologic characteristics of watersheds.

2.3.4 Interpolation meteorological and climatological parameters

Hydrologic models require spatialization of meteorological and climatological parameters like precipitation and *air temperature* to evaluate recharge and runoff processes in a watershed (Dobesch et al. 2007). Depending on the characteristics of the area and the scope of the study, a single point measurement can be enough. Nonetheless, more measurements and radar estimates may provide a more representative result (Sluiter 2009). Building a map of a meteorological/climatological element can be complicated because it requires a good understanding of the environmental, physical process related to it.

Meteorological or weather stations instruments record climatic variables and atmospheric observations. The rate or intensity of the precipitation refers to the depth of water that has fallen at a point during a particular interval of time (hours, days, months, years). The air temperature is measured with an air thermometer exposed to air currents, protected from the rain and at a height which won't get influenced by the soil temperature (Linslay et al. 1958).

The observations are usually constant, making the meteorological data very large and difficult to manage. Therefore, the data has to be treated statistically. However, the data gathering by the stations is not always stable neither in space nor time, because of displacement of stations or problems related to instruments. *The average data from a station that has been moved is not representative and introduce error* (Linslay et al. 1958).

Ideally, a network of meteorological stations should be distributed in such way that the collection of data would allow a reasonable spatial coverage and knowledge of rainfall, storm, temperature, wind (among others) patterns. In an area with similar climatic parameters, applying simple interpolations or average values to the whole area can be valid. Furthermore, climatic and meteorological factors present diversified spatial trends, being influenced by morphology. The climatic and meteorological data need to be interpolated to assign data to uncovered areas or to complete records with gaps. Continuous fields like temperature and no continuous field like precipitation events require different considerations to be correctly spatialized (Tveito 2007).

The improvement of numerical weather and hydrological modelling, the availability of high-resolution remote sensing and geospatial data and the development of GIS allows the interpolation to fine grids (Spadoni et al. 2010b). The majority of GIS incorporate interpolation methods and allow to relate numerous layers to derive estimates of parameters for any place at any time (Perdigao et al. 2007). Depending on the scope of the study, it is possible to generate yearly, monthly and daily maps. The results of interpolation improve when the methodological approach accounts for geographical data mainly topography (elevation, slope, aspect), land cover, hydrography and soil; land-sea gradients, circulation patterns; and

incomplete time series and numerical weather models (Sluiter 2009; Goovaerts 2000; Perdigao et al. 2007). The geographical environment shapes and influences spatial distribution of meteorological elements. Table 11 shows the correlations between climatic factors and geographical data that can be used as ancillary data in interpolation.

Table 11 Geographical elements affecting climatic factors.

Ancillary data Climatic factor	Land-sea gradient	Large water masses	Elevation	Land use	Latitude
Temperature	yes	yes	yes	yes	yes
Precipitation	yes	yes	yes	yes	yes
Wind speed	yes	yes	yes	yes	yes
Insolation	yes	yes	-	-	yes

Interpolation has to make sure assumptions like stationary, intrinsic hypothesis, isotropy and being unbiased. Stationery refers to “the condition that the probability distribution of the variable is constant in time and space, meaning that the same probability distribution function should be expected anywhere/anytime” Tveito et al., 2006

The period determines the type of interpolation. *Climate Normals* are three-decade averages of climatological variables including temperature and precipitation. When available data is not enough, a shorter interval can be used as a factor with low spatial variability. Climate reference maps use climate normals. Monthly and seasonal maps can be generated in case of anomalies or normalised values. Daily maps should be performed using absolute values (Sluiter 2009). Some examples of software for interpolation are Generic Mapping Tools (GMT), ESRI ArcGIS, R/GSTAT, and MISH/MASS.

The interpolation methods can be deterministic, probabilistic and a mix. The deterministic methods generate a continuous surface based on geometric characteristics of the station's network. The deterministic approaches are described below can be Nearest neighbour (NN) (Thiessen or Voronoi methods), Triangular Irregular Networks (TIN), Inverse Distance Weighting (IDW), Polynomial functions (splines), linear regression, Stochastic linear regression and Artificial Neural Networks.

The Probabilistic Methods are based on probabilistic theory, including the concepts of randomness and variance, requiring many elaborations. Examples are Optimum interpolation and Kriging. There are other methods specific for meteorology that combine deterministic and probabilistic methods like MISH and PRISM. MISH Meteorological Interpolation based on Surface Homogenized Data Basis (Szentimrey et al., 2007), it uses climate time series to estimate the spatial trend and the covariance statistically.

Tveito (2007) propose two main steps for interpolation (Sluiter 2009):

1. Normalization of in –situ data to obtain stationary spatial assumption. Usually, through linear regression model (or multiple linear regression for several predictors) to find the variable that influences the parameter.
2. Interpolation of normalised fields.
 - i. Choosing the right interpolation methods based on the timescale and the nature of variables.
 - ii. Correcting the use of interpolation method
 - iii. testing several methods
 - iv. validation

v. future research

The error of interpolation can be estimated in the following way:

- Data splitting: divides the data into estimation and validation data.
- Cross-validation: validation done several times, each time removing one station.
- Calculation of the Kriging variance. (Only for Kriging methods)

Tabios and Salas (1985) compared several methods of spatial interpolation for precipitation on 30 years of data from 29 stations in the north-central United States. They concluded their study that the Kriging and optimal interpolation techniques gave the lowest error, closed followed by the multiquadratic technique. The IDI and Thiessen polygon produced just fair results, and the polynomial interpolation had bad results (Tabios & Salas 1985). Goovarts (2000) used annual and monthly rainfall observations measured at 36 climatic stations in a 5000 km² in Portugal to develop three multivariate geostatistical algorithms for incorporating a DEM into the spatial prediction of rainfall: simple kriging with varying local means; kriging with an external drift; and collocated co-kriging. They compared the results of the three multivariate geostatistical algorithms using cross-validation with linear regression of rainfall against elevation and three univariate techniques: Thiessen polygon; inverse square distance; and ordinary kriging. The first three multivariate geostatistical algorithms outperformed the other interpolators. Ordinary kriging proved to be more accurate than linear regression when the correlation between rainfall and elevation is moderate (less than 0.75 in the case study). The inverse square distance and the Thiessen polygon had the more significant prediction errors. In conclusion, accurate prediction of rainfall should account elevation and spatial dependence.

The linear regression of the rainfall or temperature against elevation uses the linear correlation coefficient between the parameter and elevation. Linear regression models associate a predicted variable and one or more variables by physical reasons. The model is a global interpolator; its success can be estimated through cross-validation, calculating the mean absolute error (MAE) and mean square error (MSE) calculated for prediction of rainfall. The linear regression can be calculated in standard statistical programs.

Dyras and Ustrnul (2007) tested simple kriging, ordinary kriging, co-kriging, universal kriging and residual kriging; and deterministic methods like inverse distance weighting (IDW), splines and different trend surface analyses including regression approaches. They found that residual kriging was the best interpolation solution for a monthly and seasonal mean of air temperature and precipitation in Poland and smaller regions.

The residual kriging can be used to estimate temperature from its relation to topography. The relation between temperature and topography, land use and other physiographical features is deterministic. Multiple linear regressions can be used to establish the deterministic models. The remaining residual field can be interpolated with any spatial interpolation (kriging, splines or inverse distance methods). The use of kriging is preferred since it is based on a stochastic spatial structure function. The temperature can be interpolated for months, seasons and years (Tveito 2007).

2.3.5 CLIMATIC FEATURES

The climatic features that affect the components of a hydrological cycle are radiation, gravity force, temperature, pressure, humidity, wind and precipitation. Among the climatic factors

that establish the hydrological features of a region, are the amount and distribution of precipitation and the effects of temperature, and humidity on evaporation.

Meteorology plays an essential role in understanding hydrologic cycle dynamics, including the forecast of maximum precipitation. The atmospheric climate conditions of an area are statistically defined over an extended period. The climate can be classified according to the combination of climatic variables. In this sense, several classifications were defined and unanimously accepted throughout the scientific literature.

2.3.5.1 Precipitation

Precipitation is defined as moisture that precipitates from the clouds to ground either as rain, snow or ice (Linslay *et al.* 1958). The precipitation is the inlet of the hydrological cycle to the land and to a hydrogeological basin. Precipitation water, in general, becomes a part of the surface runoff, infiltration or surface retention. The intensity of precipitation conditions the water that may be infiltrated or may be a part of the runoff (Figure 34).

There are three types of precipitation: convective, frontal or cyclonic, and orographic rain. The latter one is produced in orographic clouds that are created by the mechanical lifting of air over hills and mountains. Usually, there is more than one type of precipitation acting simultaneously over an area (Linslay *et al.* 1958). Spreen (1947) conducted a study to evaluate the effect of elevation, height between station and nearer pick (rise), exposure and orientation. Founding that elevation was responsible for 30% of the variability, while all four parameters had 85% of the effect on the variability; this information was proven to be useful in rough terrain where data is sparse.

Precipitation is more frequent and higher on the windward side of mountains, but also in the crest of the mountain barrier. The amount of precipitation changes with proximity to the coast. It is higher near coastlines because of more water vapour from the sea, even if the orography can alter that situation (Linslay *et al.* 1958).

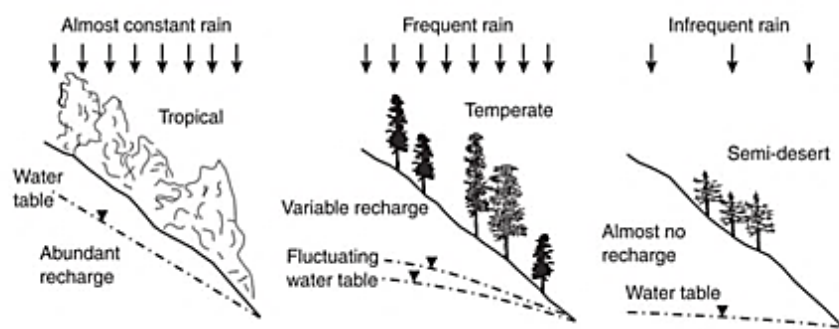


Figure 34 Relationship between water table level and precipitation (modified from Davis and de Wiest, 1966)

2.3.5.2 Air temperature

The radiant energy of the sun is the cause of heated air temperature. The temperature of the air is affected by the incidence of solar radiation, latitude, continentality, ocean currents, and prevailing winds the atmosphere. The variation during the year of the temperature in temperate zones is related to the seasonal change of solar elevation angle. This angle also is different depending on the latitude and changes during the year and during the day giving a sinusoidal trend to the temperature diary and annual cycles. The duration of the day, the clouds effect, and dense vegetation affects the insolation over the land then the temperature.

The slopes facing the north are colder than slopes facing the south due to the solar elevation angle.

The rate of change of temperature with height in the free atmosphere is called lapse rates or vertical temperature gradient (Linsley *et al.* 1958). Temperature decrease with elevation being lower at mountains, while is warmer in valleys or coasts. The lapse rate is positive when the temperature decreases with elevation, zero when the temperature is constant with elevation, and negative when the temperature increases with elevation (temperature inversion). The world's average lapse rate 0.6 to 0.7 °C per 100 metres (about 1.1 to 1.3 °F per 300 feet) in the lower atmosphere (troposphere). The cause of this gradient is that there is a less favourable radiation balance in the free air and because rising air undergoes a reduction of temperature associated with its expansion as the pressure of the overlying atmosphere declines. The normal lapse rate of no rising air is highly variable, being affected by radiation, convection, and condensation. The lapse rates are very variable near the land surface.

2.3.5.3 Evapotranspiration

The phase of the hydrologic cycle in which the liquid water in oceans and land ascends to the atmosphere as vapour, directly or through vegetation. The loss of water by evaporation and transpiration are treated as a single factor in hydrologic studies because in practice they are difficult to separate. Part of the precipitation in a watershed is evaporated from raindrops, and some are intercepted by vegetation and evaporated. Then water reaching the soil is less than that one recorded in rain gauges. Water is evaporated from the soil, and free water surface like streams and reservoirs (Linsley *et al.* 1958). Evaporation increases with rising surface temperature, decreasing relative humidity and increasing surface wind speed. Transpiration by plants also increases evaporation rates.”

Evaporation depends on meteorological factors (solar radiation, air temperature, vapour pressure, wind and atmospheric pressure) and characteristics of the evaporating surface. This process is powered mainly by solar radiation, and conducted by wind velocity that takes unsaturated air to the evaporation surface. The evaporation rate at a specific temperature is proportional to the wind speed and dependant on the vapour pressure of the air (Linsley *et al.* 1958). Evaporation from the soil depends on the characteristics of the soil and the depth of the water table (Figure 35). It is higher in soil saturated at surface level, while the soil loses its moisture the evaporation decreases and the soil temperature increases. Evaporation can be determined by water budget or energy budget approaches.

Transpiration is the loss of water from vegetation when the vapour pressure in the air is less than that in the leaf cells. It is the principal path that water inland takes to return to the atmosphere. The transpiration depends on the same meteorological factors than evaporation, and on the type, density and stage of development of plants. Solar radiation is responsible for the water movement within the plant, the transpiration and the growth. The transpiration is much more significant in the growing season (Linsley *et al.* 1958). The rate of available moisture in the soil conditions the transpiration; the available water, in turn, depends on the soil type. The type of vegetation and root range effect on transpiration in wet conditions is not clear, but in dry conditions, they are involved with water availability.

The global average of ET is the 57% (60% in Europe) of the average annual precipitation, while in arid or desert areas is 90 to 100% (Gilli *et al.* 2012; Sanchez-Toribio, 1992). Evaporation in arid and semi-arid regions can exceed the precipitation (Singhal & Gupta 2010). The ratio

between annual P and PET is less than 0.75 in limited water environments. Evaporation in rainy periods is low, then the moisture evaporated is limited to the quantity saturating the surface of the soil.

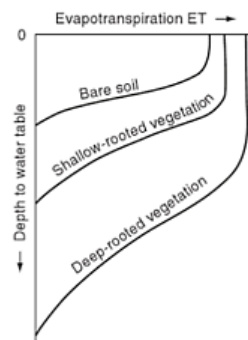


Figure 35 Relation between depth of water table and rate of evapotranspiration in different terrains (from Bouwer 1978)

The evaluation of ET usually focuses in agriculture zones with more or less homogeneous characteristic. Natural basins, in the other hand, have several types of vegetation at different stage and rooting, bares soil, variable slope and aspect making the water availability heterogeneous. The evapotranspiration in a natural basin is a decay function proportional to the moisture available

The Potential evapotranspiration (PET) (Thornthwaite, 1948) is the maximum theoretical evapotranspiration or the quantity of water that would be taken from land surface by ET if it would be enough water in the soil in the presence of vegetation with optimal development (Díaz *et al.* 2005; Gilli *et al.* 2012). It is calculated from meteorological data, depends on the evaporative capacity of the atmosphere.

The Actual evapotranspiration (AET) is the fraction of water taken from land moisture under the existing field conditions by evaporation and transpiration. Depends on the available water in the soil, the mechanic structure and the chemistry of the soil; and the type and phase of vegetation (Díaz *et al.* 2005; Gilli *et al.* 2012).

AET and PET are very close in discharge area (or swamps, waterlogged areas), but in recharge area, the AET is less than PET because of the low water table. In general, AET is 50-90% of PET. PET can be converted to AET in recharge area using soil moisture budget approach (Holmes & Robertson 1959)

There are many different ways to evaluate the ET, according to their approach they can be: hydrological, micrometeorological and plant physiological (Rana & Katerji 2000). There is not a universal correct evaluation of ET. Rana and Katerji (2000) did a review of ten methods to evaluate the ET in the Mediterranean climate but mainly for crops. The methods evaluated are in Table 12 and the conclusions of the comparing in

Table 13. The soil water balance is appropriate to estimate the ET in a watershed for months.

Table 12 Methods to measure and to estimate the ET tested by Rana and Katerji (2000) classified on according to their scope and type of approach.

ET measurement		
Hydrological	Micrometeorological	Plant physiological
<ul style="list-style-type: none"> ▪ Soil water balance ▪ Weighing lysimeters 	<ul style="list-style-type: none"> ▪ Energy balance and Bowen ratio ▪ Aerodynamic method ▪ Eddy covariance 	<ul style="list-style-type: none"> ▪ Sap flow method ▪ Chambers system
ET estimation		
Analytical approach	Empirical approach	

▪ Penman-Monteith model	▪ Methods based on crop coefficient approach	▪ Methods based on soil water balance modelling.
-------------------------	--	--

Table 13 Advantages and disadvantages of the methods to measure and to estimate the ET tested by Rana and Katerji (2000).

Measurement method	Advantages	Disadvantages
Soil water balance	Soil moisture simple to be evaluated with gravimetric method Not expensive if the gravimetric method is used	Large spatial variability Difficult to be applied when the drainage and capillary rising are important Difficult to measure soil moisture in cracked soils
Weighing lysimeter	Direct method	Fixed Difficult maintenance It could be not representative of the plot area Expensive
Energy balance/ Bowen ratio	Simple sensors to be installed Suitable also for tall crops It can be also used when the fetch is 20:1 Not very expensive if psychrometers are used	Difficult to have correct measurement of the wet temperature if psychrometers are used The sensors need to be inverted to reduce bias Difficult maintenance
Aerodynamic	Simple sensors to be installed It does not need humidity measurements Not very expensive	It needs to be corrected for the stability Not suitable for tall crops
Eddy covariance	Direct method with fast hygrometer	Delicate sensors Difficult software for data acquisition Hygrometer very delicate expensive
Sap flow	Suitable for small plots It takes into account the variability among plants	Difficult scaling-up The gauges need to be replaced every 1–2 weeks The soil evaporation is neglected
Chambers method	Suitable for small plots It can be used also for detecting emissions of different gases	It modifies the microclimate Difficult scaling-up

The ET can be measured directly with Evapotranspirometer, evaporimeter, lysimeters, experimental areas and soil humidity profiles. The empiric methods obtain the ET from meteorological data, but they need validation with direct measurements in the zone. Theoretical and direct measurement are delicate and expensive. The mean ET for a basin can be estimated through the water budget, knowing precipitation and streamflow mean values for extended period and evaluating subterranean flow. It is possible to perform the water budget for short periods (few days), but the error will be significant. The calculation of ET through the water balance from field plots (streamflow and precipitation) can be done, but the ideal conditions to make it successful are rare (Linslay *et al.* 1958). Empirical formulas that use parameters that control the evapotranspiration are related in Table 14.

Table 14 Equations to estimate the evapotranspiration based on analytical and empirical approaches.

ET estimation, analytical and empirical approach	
<p>Turc 1954</p> <p>Equation 29</p> $ET = \frac{P_A}{\sqrt{0.9 + \frac{P_A^2}{L^2}}}$	<p>P_A = mean annual precipitation mm/ year T_A = mean annual temperature °C $L = 300 + 25(T_A) + 0.05(T_A)^3$ Santoro (1970) proposed an adjusted L for Mediterranean climate. $L = 586 + 10(T_A) + 0.005(T_A)^3$</p>
<p>Thornthwaite</p> $PET = 16 \cdot Nm \left(\frac{10 \cdot T_m}{I} \right)^a$	<p>T_m = mean daily temperature of the month in C Nm = Correction factor of day length I = annual heat index mean daily global radiation of the month cal/cm² day</p>
<p>Hargreaves</p>	<p>R_a = solar radiation for the latitude T = mean air temperature T_{max} = maximum temperature T_{min} = minimum temperature</p>

<p>Equation 30</p> $ET_o = (0.0023Ra) + (T + 17.8) (T_{max} - T_{min})^{0.5}$	
<p>Penman-Monteith equation,</p> $\lambda ET = \frac{\Delta A + \frac{\rho c_p VPD}{r_a}}{\Delta + \gamma \left(1 + \frac{r_c}{r_a}\right)}$	<p>A= Available energy, Δ = slope of the saturation vapour pressure versus temperature function VPD= air vapour pressure deficit γ= psychrometric constant r_a= aerodynamic resistance r_c= bulk canopy resistance</p>
<p>Equation 31</p> $ET_{rad} = \frac{\Delta}{\Delta + \gamma^*} \frac{(R_n - G)}{\lambda}$ $ET_{aero} = \frac{86.4}{\lambda} \frac{1}{\Delta + \gamma^*} \frac{\rho c_p}{r_a} (ea - ed)$ $ET_{rad} + ET_{aero} = ET_o$ <p>ET_o = reference ET</p>	<p>Δ = slope of vapour curve γ^*= modified psychrometric constant R_n= net radiation G= soil heat flux λ= latent heat of vaporisation ρ= atmospheric density c_p =specifi heat of moist air ea= mean saturation vapour pressure ed= actual vapour pressure</p>

Turc (1954) obtained the empirical Equation 29 to calculate the annual real evapotranspiration after experimenting in more than 200 basins (Díaz *et al.* 2005; Brugioni *et al.* 2008; Spadoni *et al.* 2010a; Ghiglieri *et al.* 2014). Santoro (1970) analysed 192 basins in Sicily before proposing a different parameter “L” in the Turc (1954) equation valid for a temperature between 10°C and 18°C.

The International Commission for Irrigation (ICID), the Food and Agriculture Organization of the United Nations (FAO) and the American Society of Civil Engineers (ASCE) adopted the Penman-Monteith (P-M) method (Allen *et al.* 1998) as the standard method to evaluate the reference ET (ET_o) from climate data (López-Moreno *et al.* 2009). (Equation 31) is the most used method to estimate ET_o from climate data, which is highly demanding of data and which success relies on the availability and quality of the parameters in the equation, especially the canopy resistance (Rana & Katerji 2000). However, the climate data in many cases is restricted to precipitation and temperature. López-Moreno *et al.*, (2009) used the precipitation and temperature data to estimate the missing parameters for the equation Penman-Monteith in a mountainous area in the Mediterranean. They estimated the relative humidity and solar radiation from the maximum and minimum temperature data using different methods and kept the wind speed value as a constant. The result was satisfactory for the P-M with parameters estimated. The results were compared with those estimated using the empirical Hargreaves (HG) (Equation 30), which is considered a good alternative to P-M (López - Moreno, 2009).

Detto *et al.* (2006) evaluated the soil moisture and ET in an area with heterogeneous vegetation of grass, shrubs and trees (contrasting plant functional types, PFT) in Sardinia. They estimated ET accurately using micrometeorological measurements, ground-based thermal infrared thermometers, and high-resolution VIS/NIR remote sensing information. They also evaluated the soil water content and the ET for each vegetation type successfully. The typical wood vegetation (WV) species of Sardinia, representative of the broader Mediterranean water-limited region, confirm a high tolerance to prolonged dry periods, the trees were still transpiring at rates close to potential. Instead, the grass is less tolerant to water content fluctuations, transpires at lower rates than WV, and wilts as the dry summer season

commences. The change from grass to bare soil has a significant impact on increasing the sensitivity of the bulk ecosystem ET to soil moisture during the summer. Detto et al. (2006) concluded that footprint model to interpreted micrometeorological observations is crucial and the substantial impact of potential errors depending on the vegetation over ET and soil water balance in the water-limited ecosystem in the summer.

3 STUDY AREA

The Masoni Ollastru river basin was chosen like the pilot area to develop this work; it is located in the municipality of Capoterra in the province of Cagliari (Figure 36). Capoterra has three populated centres: Capoterra, Poggio dei Pini and La Maddalena. The main rivers in the area are San Girolamo, Masoni Ollastru

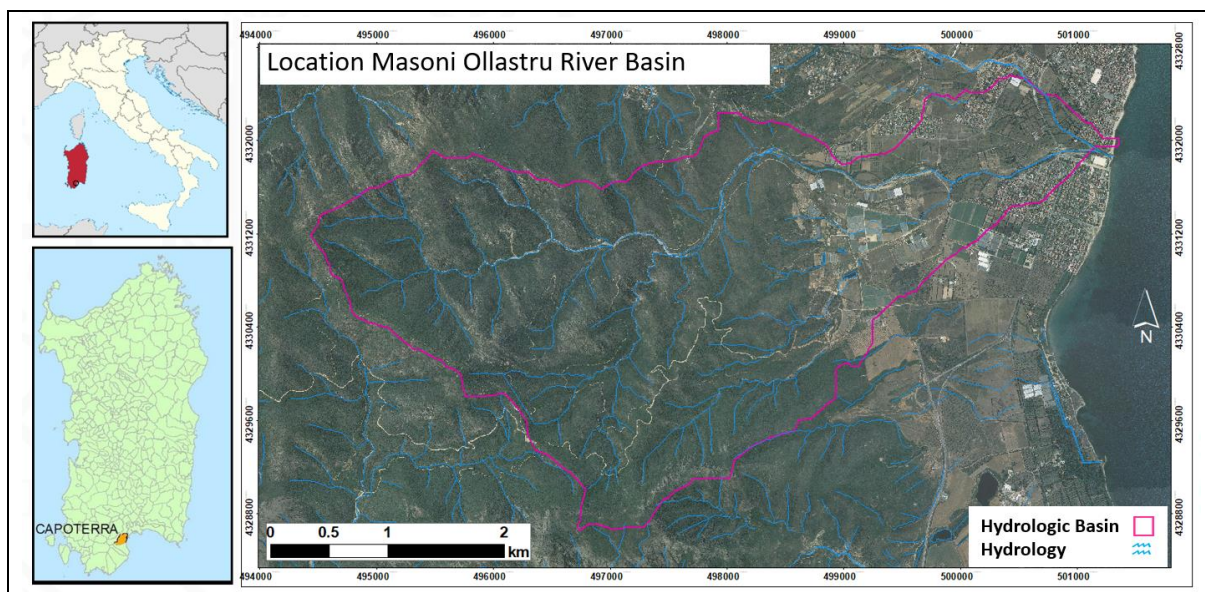


Figure 36 The Masoni Ollastru river basin is located in a small river basin in the municipality of Capoterra, in the South of Sardinia.

3.1 GEOGRAPHIC ASSESSMENT

The area of the basin is 12.5 km²; the elevation range is between 692 MASL in Monte Turrunari to sea level in the coast. The weather is the typical Mediterranean with dry summers and the highest precipitation in autumn and sometimes in spring. The vegetation consists in the forest with species of high trunk and bushes to Mediterranean sclerophyllous vegetation (Barca et al. 2009). The medium drainage area is only inhabited by a family of shepherds, then the only buildings are a house and farming facilities. Another construction is the old astronomic observatory of Cagliari (OAC) in Punta Sa Menta (Poggio di Pinni) built in 1978. The floodplain is lightly populated and is full of farms. The last segment of the river runs through the middle of the populated centre La Maddalena.

3.1.1 Meteo-climatic context

Italy is located in the temperate zone of the boreal hemisphere characterised by abundant precipitation, low pressure and marked seasons and it is inside the Mediterranean domain.

The Mediterranean climate has hot, dry summers and mild temperature and annual rainfall in winter (Rana & Katerji 2000). The dry months in the south of the Mediterranean are seven and in the north two to three months. The north has the rain season mainly in winter and the south in autumn. Mediterranean climate has precipitation seasonality (the difference between the amount of long-term rainfall fallen in the most and the least rainy months, proportioned to the total long-term annual rainfall) more than double than a continental climate. In Italy, the precipitation seasonality is 11%.

The Tyrrhenian Sea has a mitigating function of climatic extremes around him because is a reservoir of heat and humidity. The uneven relief produce temperature variation short distances, frequent rainfalls for adiabatic cooling and stau clouding (Costantini *et al.* 2013). The surface area covered by storms in the Mediterranean is often small, and concentrate near the epicentre of the storm. The runoff in the Mediterranean area is mainly from the mountains. Therefore these areas have particular attention to evaluate the streamflow susceptibility to changes (Lopez-Moreno *et al.*, 2009)

The average specific runoff in Italy is 554 mm/year, which is a much higher figure than the European average. Sardinia has torrential flows in most of its rives, the periods with maximum runoff are autumn and spring (Ghiglieri *et al.* 2014). 75% of the water in the Mediterranean area is used for agriculture, and 99% of that water used for irrigation is lost as evapotranspiration (Rana & Katerji 2000). Global change in the Mediterranean leads to increment in aridity and decrease in streamflow.

The mean annual precipitation in Italy is 932 mm, but along the country, the precipitation conditions are very different. The north of Italy has the maximum annual precipitation above 1900 mm, and the minimum values are at the Southeast of Cagliari around 400mm. Flat and hilly areas near mountains have the lowest rainfall intensities in Italy, among those areas is the southern Sardinia (Costantini *et al.* 2013).

The mean annual air temperature (MAT) of Italy is 12.6 °C (range minus zero to 20°C), 14° C in the central southern (Costantini *et al.* 2013). The mean annual potential evapotranspiration PET_A in the whole Italy is 1002 mm (from the Penman-Monteith method). The highest PET_A is above 1300mm in Apulia, Sicily and Sardinia. Mean annual precipitation in semi-arid regions is well below the annual potential evapotranspiration, and the actual evapotranspiration AET is considerably lower than the PET. The actual evapotranspiration is close to zero in the driest regions of the semi-arid zones, where maximal PET values and negligible rainfall is recorded. "As specific potential evapotranspiration conditions are absent, it is difficult to estimate E, because a series of other factors come into play, such as the pattern and magnitude of the precipitation, soil type and vegetation cover, etc."

The aridity index is below one for most of Italy. Southern Italy is classified as sub-humid or semiarid, as is the case for Sardinia and Sicily. The island of Sardinia is characterised by a water deficit at most altitudes. The mean annual precipitation in Sardinia is 764 mm (Delitala *et al.*, 2000), and the mean annual potential evapotranspiration is roughly 1,500 mm. There are episodes of drought, such as occurred in the summer of 2003. According to the climatic classification from the geo-referenced database for Europe, Sardinia has three climatic regions: Mediterranean sub-oceanic climates influence by mountains (M2); Mediterranean to subtropical climate influenced by mountains (MST1) and Mediterranean to subtropical climate partly semiarid (MST2). The last two are represented in the south of the island.

Elevated air temperatures, low seasonal differences and a high ET deficit, more significant in a semiarid climate.

The soils in Italy, are often rejuvenated by water erosion and are linked the climate geographically. Areas with unstable morphological position or deeply affected by men have slow pedogenesis of soil, and thin and weak developed soils, like Regosols and leptosols. If the soil preservation has been good, then the type of soils are Chernozems and Kastanozems. The soil moisture regime according to Soil Taxonomy (Soil Survey Staff 1999), can be represented by the soil aridity index (SAI), that is, the average number of days per year when the soil moisture control section is dry. Soils moisture of highest aridity is Xeric and dry xeric. Soil temperature regime classification (average soil temperature at 50cm) classifies most of Sardinia in the thermic regime.

3.2 GEOLOGICAL ASSESSMENT

The main geological feature of south-west Sardinia is the Campidano tectonic trough formed by a tensional event. The Campidano graben was originated at the late Cenozoic when the Corsican –Sardinian block separated from Spain and France. The crystalline basement has been affected by the Caledonian, Hercynian and Alpine orogenesis. The igneous-metamorphic basemen has experience rejuvenation due to the Alpine orogenesis. The relief underwent strong denudation, leaving weathered massifs with rounded and almost flat tops (Barrocu, 2007).

3.2.1 STRATIGRAPHY

The upper river basin has Carboniferous metamorphic rocks, Carboniferous-Permian plutonic rocks, and Quaternary fluvial, and colluvium deposits (Carmignani *et al.* 2001). The coastal plain and mouth are on quaternary alluvial and coastal deposits (Figure 37).

The metasedimentary rock of the Pala Manna Formation (early Carboniferous?) only covers a small fraction of the SE border of the basin. The late Carboniferous and Permian Plutonic Complex covers the upper and the medium part of the river basin and is represented by three units. The biotitic leucomonzogranite (Figure 39 Figure 40) of the Facies Punta de Peis de Pruna (Intrusive Unit of Villacidro), covers almost all the mountain and piedmont area. The Intrusive Unit of Santa Barbara, Facies S'Arcu Varzia, outcrops like a N-S wide band in the upper mountain part of the basin. The Facies S'Arriu de Sa Figu is also present inside the previous facies, like bodies of dark grey tonalite-granodiorite. The Late Carboniferous-Permian dyke complex intrudes the bigger plutonic bodies in the mountain and piedmont area of the basin like scattered elongated bodies with NW-SE to NNW-SSE directions. Two different compositions of dykes can be recognised: leucogranitic and hydrothermal dykes mainly of quartz; intermediate to basic dykes of andesitic or basaltic composition (Figure 39). The plutonic units in the basin cover approximately 8.3km². The Paleozoic basement, deepens very quickly towards the middle of the graben. The granitic rocks are considerably fractured at the transition to piedmont deposits, laminated on the top areas and significantly altered in depth (Barrocu 1971).

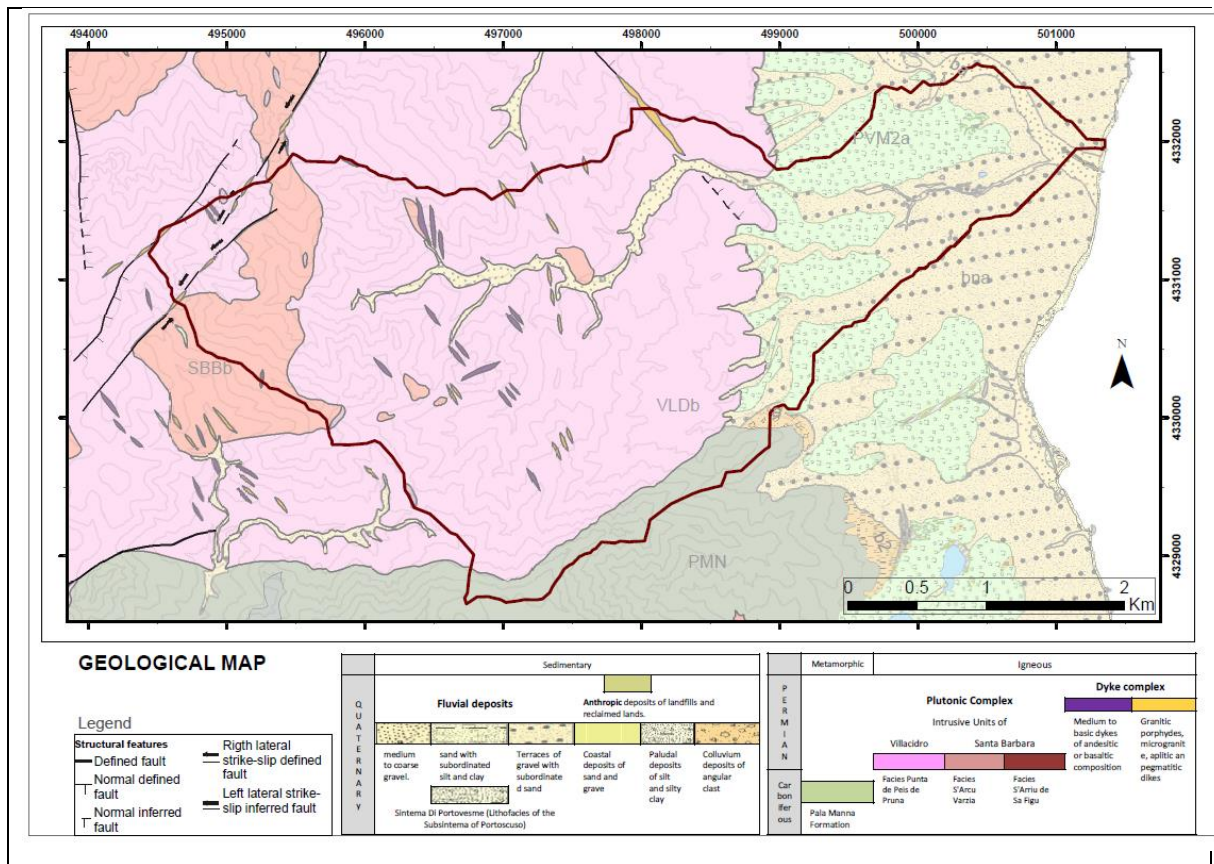
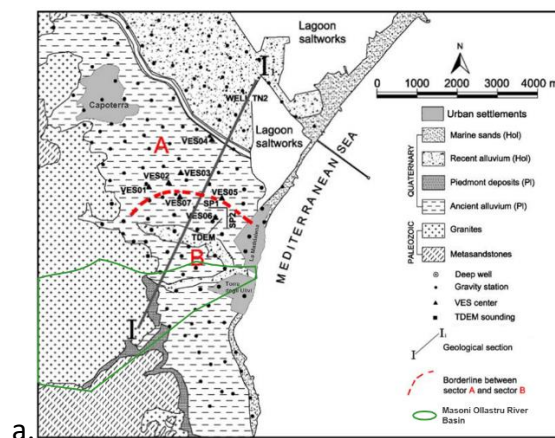
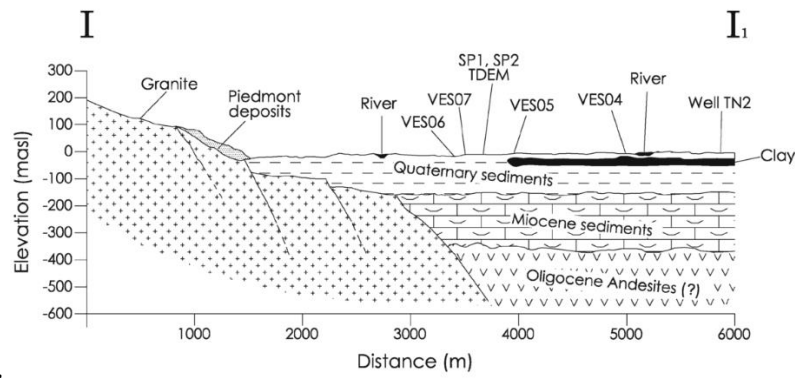


Figure 37 Geological sketch map of Mazoni Ollastru area

The contacts between the leucomonzogranite of the Facies Punta de Peis de Pruna (Intrusive Unit of Villacidro) and the micro-granodiorite of the Facies S'Arcu Varzia (Intrusive Unit of Santa Barbara) in the field are not sharp neither very evident through morphology. Like usually in the granitic plutonic complex the different lithology are closely related, and the textural and compositional variability of each type of granites make challenging to trace the contacts. However, the micro granodiorite was recognised by a slightly softer morphological expression, the slopes and the valleys are less steep and the vegetation covers good part of the N-S band (Figure 42). The leucomonzogranite has a very abrupt morphology, with rocky, narrow tops, deep valleys and less vegetation. Both units are intruded by the Dyke Complex (Figure 39).





b.

Figure 38 a) Map of Capoterra with the position of the geological section (b) that indicates the Geological model of the Capoterra plain as deduced from geophysical, geological and well data (Balia, 2009)



Figure 39 Outcrop of leucomonzogranite of Villacidro Intrusive Unit intruded by basic dykes located four meters from the river bed.

Table 15 Geological units outcropping in the area of the MORB.

Age	Geological Unit	
Lower Carboniferous?	Syntectonic deposit "culm" type	Pala Manna Formation. Alternation of metasandstone and metasiltstone with cross and plain-parallel lamination, local meta-conglomerate and elements of lydite and rare basic meta-volcanic chloritized rocks and meta- volcano-clastic
Upper Carboniferous and Permian	Plutonic complex of Sulcis-Arburese	Facies Punta de Peis de Pruna (Intrusive Unit of Villacidro). Biotitic leucomonzogranite equigranular to moderately inequigranular, isotropic texture of medium or medium to fine grain. Biotite crystals are not larger than 2 mm and only 7%.
		Facies S'Arcu Varzia (Intrusive Unit of Santa Barbara). Grey to pink biotitic-amphibolite micro-granodiorite with monzogranitic tendency, inequigranular and porphyritic of medium to coarse grain size.

		Facies S'Arriu de Sa Figu (Intrusive Unit of Santa Barbara). Dark grey microgranular tonalite-granodiorite, isotropic texture, sometimes markedly porphyritic. It outcrops like bodies of some meters to few hundreds of meters.
	Dyke complex	Intermediate to basic dykes of andesitic or basaltic composition, at times porphyritic, with phenocrysts of amphibole, generally very altered, in bottom mass from aphyric to microcrystalline. Leucogranitic and hydrothermal dykes mainly of quartz, often with mineralisation of barite and fluorite, sometimes too with sulphurs (Pb, Zn, Cu, Fe, etc). The texture is isotropic, sometimes porphyritic with alkaline K-feldspars phenocrysts, quartz, and rarely biotite and muscovite scattered in a bottom mass granophyric. They are mainly leucogranitic often profoundly related to the big late intrusion representing the late crystallisation hypabyssal phase.
Upper Pleistocene	Pleistocene continental deposits.	Lithofacies of the Subsintema of Portoscuso (Sintema Di Portovesme). Medium to coarse gravel with subordinate sand in alluvial terraces.
Holocene	Colluvium deposits	Mount side deposit. Detritus with angular clasts, sometimes partially cemented.
	Alluvial deposits	Alluvial deposit of medium to coarse gravel. Alluvial terrace deposit of Gravel with subordinated sand. Alluvial deposit of sand with subordinated silt and clay. Alluvial deposit of medium to coarse gravel.
	Shore sediments	Beach deposits of sand and gravel, sometimes with mollusc, etc. Lagoon deposits of silt and silty clay sometimes pebbly and peaty mud with fragments of molluscs.
	Anthropic deposit.	Landfills and reclaimed land.

The observed dykes are not very thick they have maximum 1m, although they are usually outcropping in sets. The thicker and outstanding dykes are quartzitic and are easily identified in remote sensing images. The thickest quartzitic dyke (Figure 44) is located to the east of the old astronomic observatory. Not mapped basic dykes were observed on the riverbed also outcropping in sets, but individually having an average thickness of 1 m. The areas where the dykes outcrop is more fractured. Near to the hydrothermal dykes, there are usually observed stockworks of hydrothermal veins.

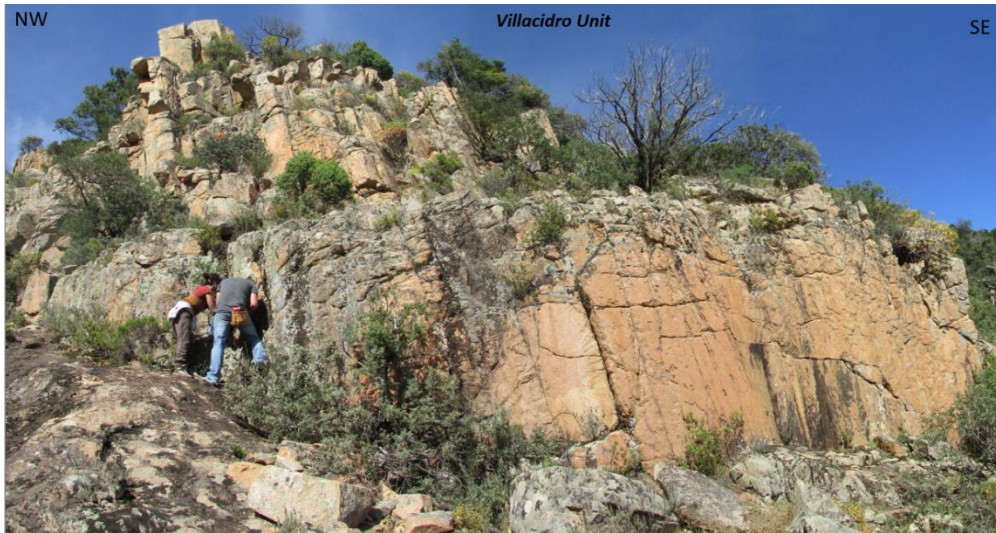


Figure 40 Wall of leucomonzogranite of Villacidro Intrusive Unit located in the river source area in the west of the MORB.



Figure 41 Wall of monzogranite of Santa Barbara Intrusive Unit located in the river source area in the west of the MORB.



Figure 42 Southwest side of the MORB where the morphological differences between the Units of Villacidro and Santa Barbara can be seen. The Unit of Santa Barbara slopes are less steep and are more rounded; there are no large rocky crests like those of the Unit of Villacidro.

3.2.2 GEOMORPHOLOGY

The Masoni Ollastru River runs from a mountain area in the West to the golf of Cagliari in the East. The area of the basin is 12.5 km²; the elevation range is between 692MASLin Monte Turrunari to sea level at the coast. Three geomorphological zones were recognised in the Capoterra area (Figure 43).

- Mountain area has an irregular profile, rarely above 1000 MASL.

The morphology corresponds to a structural Appalachian relief derived from Hercynian mountain system. The mountainous relief is abrupt, consists of steep slopes, narrow tops, dense net of drainage and deep valleys (Figure 42, Figure 45 and Figure 44). The granite present erosional shapes like spherical surfaces, granite sand, tors and tafoni. Processes of selective erosion are evident by the prominent outcropping of dykes and masses of porphyry and quartz (Carmignani et al., 2001, Barca et al., 2009) (Figure 44). The mass movements recognisable in the area of Capoterra are rocks fall, rock toppling, debris avalanche and debris flow (Figure 45).

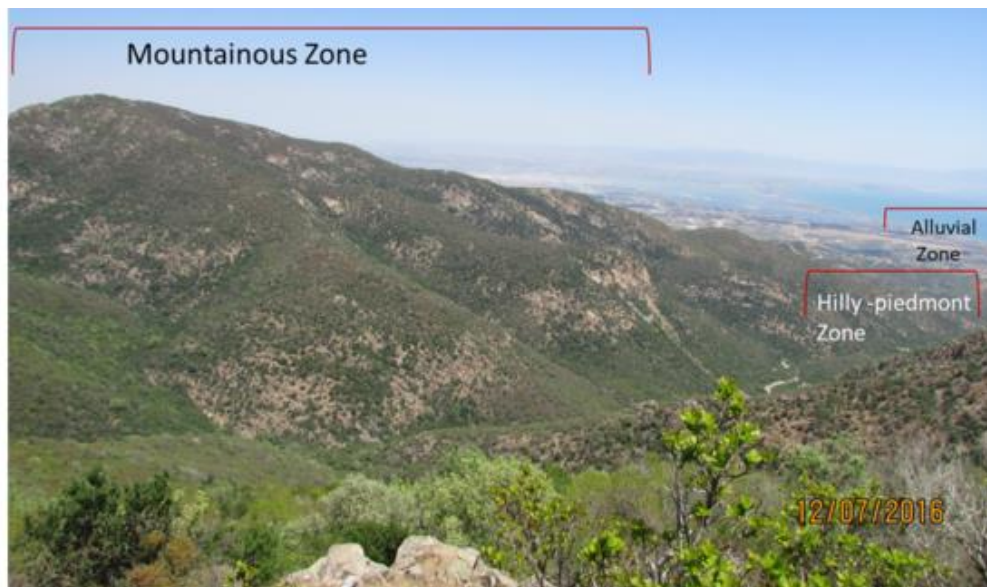


Figure 43 Geomorphological zones

The south margin has bare summits and steeper slopes and deeper tributaries valleys than the more vegetated south margin. The transversal profiles show staggered slopes, with larger stabs in the south margin. There are triangular facets in the valley sides, and few tributaries in the north seem to have hanging valleys, while some tributaries in the south margin are slightly displaced near the mainstream.

The valley of the mainstream is narrow to the west and becomes wider towards the east. The river in the mountain and hilly sector has segments with step-pool and riffle-pool morphology, the streambed is alluvial and also rocky. There are longitudinal and point bars mainly of the sandy conglomerate.



Figure 44 Northeast side of the MORB, east of the old astronomic observatory, where a quartz dyke intrudes Units of Villacidro in direction NW-SE. The fractures density is high in the area surrounding the dyke.

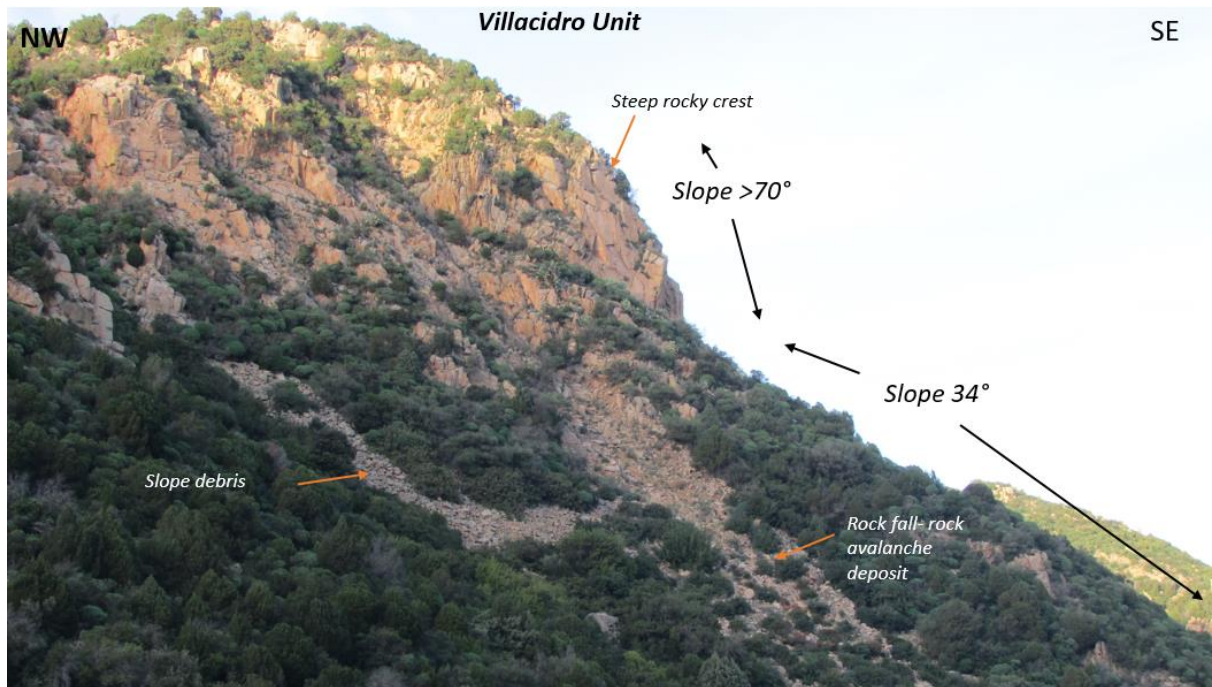


Figure 45 Top called Punta Casteddu located in the north margin of the MORB in the middle of the mountainous zone side of the MORB. The granite walls of Unit of Villacidro in the top are very steep but the rest of the slope is more gently. The slope is covered by a slope debris and by the deposit of a complex mass movement (rock fall-rock avalanche occurred in 2008).



Figure 46 Panoramic picture of the geomorphological zones in the south margin of the MORB.

- Hilly-piedmont Zone

The area where the mountains and flat area meet has alluvial cones which developed terraces, glacia and pediment. In the hilly area, the elevation is lower than in the mountainous zone, and the shapes are more rounded, the slope is gentle, and the drainage net is less dense than in the west.

- Alluvial Zone

The mainly flat area with long terraces of unit Sintema di Portovesme in contact with granitic hills. Towards the east, the terraces disappear and give place to the Holocene coastal plain. The river is sinuous until where it was canalised.

3.2.3 HYDROGEOLOGY

This has not been studied for hydrogeology purposes, however, in the bibliography of the area the authors define the hydrogeological unit in conceptual mode.

The granitic units are considered as one hydrogeological unit in Barca et al. (2009) and Lobina (2010). This consideration is based on the fact that the permeability in the granitic units depends on the fractures and is not related to the texture or composition of the magmatic rocks. These authors assume that the permeability is low in the crystal basement in accordance with conceptual values of permeability (Freeze and Cherry, 1979). They also suggest that it is possible that close to the faults and the dykes the permeability can be slightly higher due to the higher density of fractures. There are few wells in the basin of San Girolamo River over the leucomonzogranite showing an aquifer of 80m thick in the altered granite with some impermeable lenses.

Barrocu (2007) reported different permeability values in granite in Sardinia. He reported values of permeability of 10^{-8} m s^{-1} in a well in fractured granite in Pula (south-west of Sardinia) and values of permeability of 10^{-4} m s^{-1} in weathered granite and in microgranite dykes

The Capoterra plain has two aquifers (Balìa *et al.* 2009):

- A shallow aquifer hosted in Holocene alluvial deposits, characterized by little depth to water and variable thickness in the range 10–30 m, the hydraulic conductivity was found in the range 1.58×10^{-4} – $2.11 \times 10^{-4} \text{ m s}^{-1}$,
- A deeper multilayer aquifer about 100 m thick, partially or locally confined and hosted in alluvial deposit. The aquifers are separated by a clay layer or by several clay layers interbedded with gravels with a whole maximum thickness of 20–25 m. The hydraulic conductivity is in the range 6.79×10^{-7} – $1.92 \times 10^{-5} \text{ m s}^{-1}$.

The shallow and the deep aquifers have similar flow direction, hydraulic gradient and morphology of the piezometric surface. Both aquifers have a W–E gradient in accordance with the commonly accepted condition that most of the recharge is lateral through the fractured granites (Sciabica 1994).

The Pleistocene continental deposits (Lithofacies of the Subsintema of Portoscuso, Sintema Di Portovesme) reported permeability values of 1×10^{-6} – $1 \times 10^{-4} \text{ m s}^{-1}$. (RESMAR 2013).

4 MATERIALS AND METHODS

4.1 METHODOLOGICAL APPROACH

The methodology (Figure 47) that has been followed is adjusted to the particular physiographic and geological features, and to the data available regarding the Masoni Ollastru River basin. An overview of the remote sensing images, geological and geomorphological information served to plan the forthcoming work and realise the limitations. The challenges to determine the permeability in the MORB come from:

- The heterogeneity and anisotropy of fractured crystalline rocks make the permeability spatially variable.
- The lack of instrumental record of the hydrological parameters.
- The abrupt relief, steep slopes and dense vegetation in the catchment area.

The approach of the permeability of the granitic aquifer requires understanding the relations between the hydrogeological parameters and the discontinuities properties; and their spatial variability. Three main fronts were studied to evaluate the hydrogeological behaviour of the basin:

- A. Calculation of the permeability of the granitic aquifer from the fracture network parameters
- B. Analysis of spatial distribution of fracture properties along the river basin.
- C. Estimating the water budget for the basin.

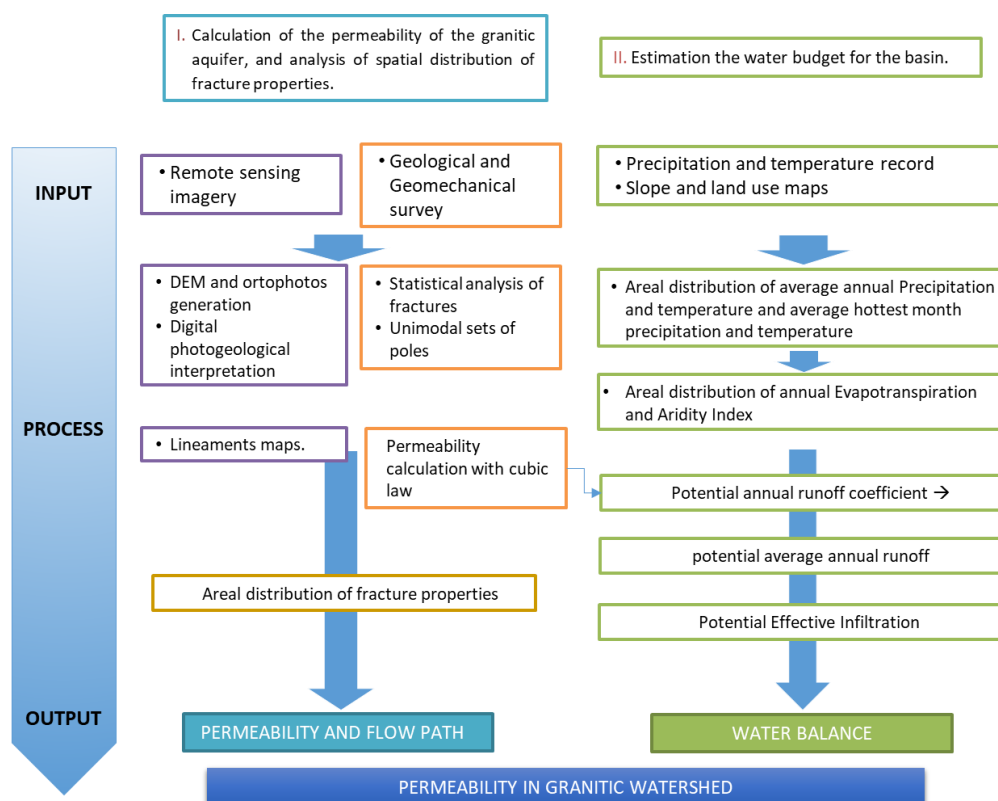


Figure 47 Scheme of the workflow to assess the permeability in the granitic basin.

The permeability of the granitic aquifer required a multiscale characterisation of the fracture network at outcrop and at remote sensing scale. The discontinuities features like fracture length and the distribution pattern are not measurable at the scale of the outcrop due to the limited access and size of the outcrops and to the cover effect of vegetation and relief. The fracture network has been characterised using field measurements and digital photogrammetry to generate a lineaments map (§4.2.2 and §5.1.1).

The permeability was calculated using the cubic law formula (§2.1.1 and §5.1.4) for individual stations and used as input to determine the potential runoff coefficient (§4.3.7 and §5.2.9). The flow direction was estimated from the main sets of joint and lineaments. To calculate k and to define the direction.

The Masoni Ollastru basin has an insufficient record of parameters, it is ungauged and the closest meteorological stations are two and five kilometres away. Therefore, the determination of the parameters of the water budget required the use of an indirect physiographic method to estimate the potential runoff coefficient (§2.3.3). The streamflow was measured in the mainstream on different cross-sections (§4.3.10 and §5.2.11) and meteorological data was collected to interpolate precipitation (§2.3.5.1, §4.3.2 and §5.2.2), temperature (§2.3.5.2, §5.2.3 and §4.3.3), evapotranspiration (§2.3.5.3), and aridity index (§4.3.4 and §5.2.4). Understanding the hydrologic characteristics is essential to predict the water availability.

4.2 Evaluation of permeability in fractured granitic rocks.

In the methodological approach explained that the calculation of the permeability in the fractured granite requires the characterisation of the fracture network through complementary methods (Figure 48):

- A. Discontinuities field survey.
- B. Digital photogrammetry to generate a lineament map.
- C. Identification of the sets of discontinuities and their distribution along the MORB.

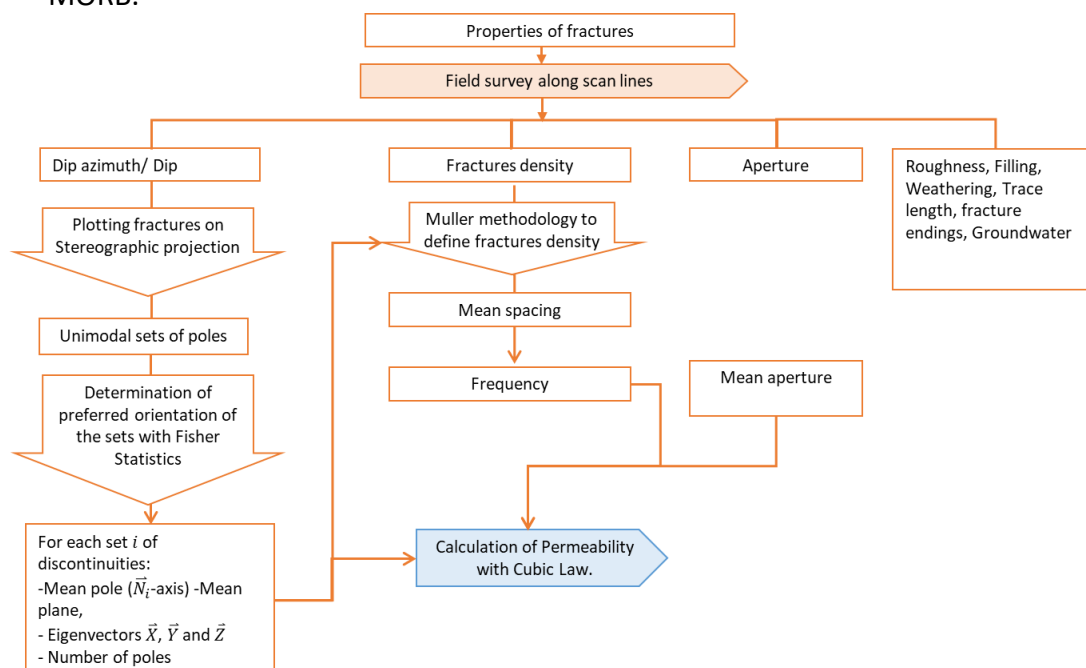


Figure 48 Flowchart of discontinuities characterization

The detailed methodology and instruments used for the geomechanical field surveys and the lineament map are explained below in § 4.2.1 and §4.2.2

The data obtained from field and remote sensing was tabulated and analysed to determine the main sets of fractures, the mean aperture and the frequency for each set and finally calculate the permeability with the cubic law equation.

The main steps followed with the data gathered from field and photogrammetry are summarized below.

1. Tabulated data in excel.
2. Plotting fractures on Stereographic projection. The orientation data of discontinuities planes was Represented the on a Schmidt net for each station to identify unimodal sets of poles. The software used was Stereonet 9.8 (Allmendinger *et al.* 2011; Cardozo & Allmendinger 2013).
3. Describing Orientation Data with Fisher Statistics. Calculate the average and 95% confidence interval (CI), the Fisher Median Vector and the corresponding mean plane for each set of joints. The sets of data should have unimodal or Fisher distribution, which is a normal distribution of orientation, and vectors more or less parallel.
4. Compute the eigenvalues, the eigenvectors \vec{X} , \vec{Y} and \vec{Z} , for each set of joints.
5. Calculate the densities and the mean distances of the plains in the direction of the mean pole. The scan line L is projected like a vector on the X-axis of each set to have the projection L'. The mean intensity can be calculated for each set, by dividing the number of discontinuities N on the length L'; and the mean spacing the opposite way.
6. Statistical analysis of the sets of discontinuities to define the variability, the maximum, and minimum values. Define mean values of aperture, trace length, roughness, filling, weathering and groundwater for each set of fractures.
7. Evaluate the relationship of the parameters of the fractures and lineaments with the location and geology (elevation, aspect, lithology, faults) in the basin.
8. Calculate the permeability using the cubic law for each set with the equation.

Equation 32

$$K = \frac{g}{12v} f d^3$$

9. Calculate the punctual permeability adding the permeability of each set, according with the equation:

Equation 33

$$K = \sum_{i=1}^N K_i = \frac{g}{12v} \sum_{i=1}^N f_i d_i^3$$

4.2.1 Assessment of rock mass properties

The field survey (Figure 49) aimed to review the lithological contacts and to evaluate if there were significant differences among the lithology that could affect the hydrogeological parameters.

The fractures field survey consisted in recording the orientation, the dimensions, the abundance and the quality of 332 discontinuities the fractures in eleven stations (nine natural rock outcrops and two artificial) spread along the river basin. The location of the stations (Figure 50) was affected by the accessibility, exposure, extension, representability and weathering. The dependence of the representability of the data on the exposure of the outcrops was overcome by choosing stations along the area in slopes with different trends and measuring scan lines \bar{L} in three semi orthogonal directions, two in horizontal directions and one in vertical direction, where the outcrop allowed it (Hudson & Priest 1979, 1983).



Figure 49 The field survey of fracture properties in Masoni Ollastru area

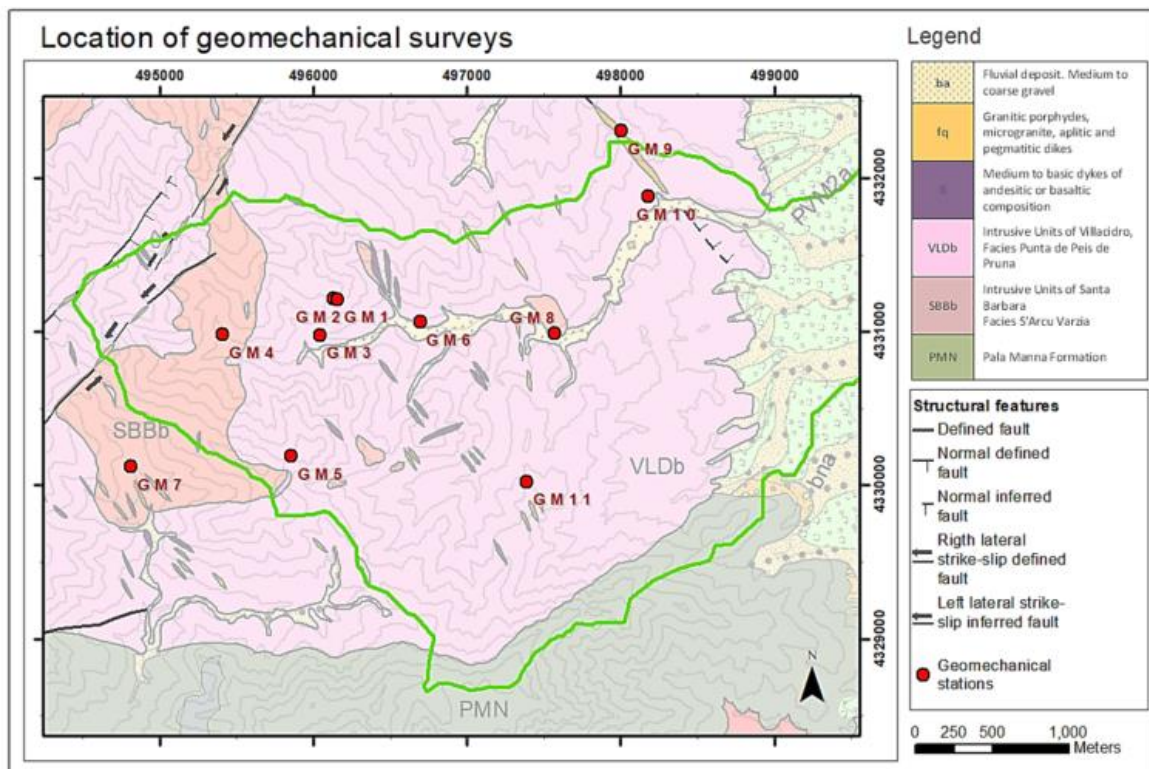


Figure 50 Location of stations

At each station, an initial overview of the whole outcrop defined the field sets of discontinuities and the scan lines. The assessing was done according to the scanline survey technique (Piteau 1970) measuring and registering systematically the sets of sub-parallel discontinuities intersecting each scan line. The features of each discontinuity were registered in a format designed specially. However, the number of sets were reviewed after the projection of the fractures in the stereonet. Table 16 summarises the features observed and the instruments used in the field survey.

Table 16 Parameters observed and instruments used to characterise the discontinuities in the field.

	Parameters	Instruments
1	Lithology	
2	Scan lines	Dip direction and dip
		Length
3	Type of discontinuity	
4	Orientation	Dip direction and dip
		Sense of dip
5	Spacing (m) between discontinuities	Measure tape
6	Dimensions	Aperture
7		Length
8		Ending
9	Condition of discontinuities	Roughness
10		Filling
11		Weathering
12	Groundwater in joints	--
13	UCS (MPa) unconfined compressive strength of intact rock material	Schmidt hammer
14	RQD (%) rock quality designation	Measure tape

1. The lithology texture and mineralogy were briefly described.
2. The scan lines orientation (strike and dip) and length were measured.

The next parameters were measured for each discontinuity.

3. The type of discontinuities found in the igneous complex and the metasedimentary rocks are referred in Table 17. The term joint was adopted for the persistent fractures while the term crack was applied for short irregular breaks.

Table 17 Classes of discontinuities.

Type of discontinuity	
Sharp deformation Breaks or fractures	Secondary planar discontinuities
Crack	Bedding planes
Joint	Foliation
Fissure	
Shear	
Fault	
Rupture (artificial cause)	

4. The orientation of the discontinuities in an outcrop was measured directly on the planes with the geological compass. The planes orientation was recorded as dip direction and dip. The Wilkie compass was used because of its design allows measuring the dip direction and the dip in one step without moving the compass from the plane, warranting the right measurement of dip.
5. Spacing. The apparent spacing was measured with a measuring tape in meters between sub-parallel joints in the direction of the scan line. However, the true spacing was calculated at the office from the apparent spacing and the cosine of the angle formed between the scan line and the mean pole of the set of fractures. The mean spacing was calculated for each set from the projection of the scan line on the normal to the mean plane and the number of joints. The values were classified according to Bieniawski (1989) (Table 18).

Table 18 Classification of the spacing of fractures (Bieniawski, 1989) Wyllie and Mah (2004).

Classification for Joints Spacing (Bieniawski, 1989)			Spacing between discontinuities (m) Wyllie and Mah (2004)
Description	Rock mass condition	Spacing between discontinuities (m)	
Extremely close spacing		-	<0,02m
Very close spacing	Crushed/shattered	<0,06m	0,02-0,06m
Close spacing	Fractured	0.06-0.2	0.06-0.2
Moderate spacing	Massive	0,2-0,6m	0,2-0,6m
Wide spacing	Blocky/seamy	0.6-2m	0.6-2m
Very wide spacing	Solid	>2m	2-6m
Extremely wide spacing		-	>6m

Table 19 Classification of the separation of joints (Bieniawski 1989).

Aperture category		
Category	Width range (mm)	code
Very open	>5	1
Open	1-5	2
Moderately open	0.1-1.0	3
closed	<0.1	4
	none	5

6. The aperture was measured with a calliper in millimetres. Often the aperture was variable, wider towards the surface and decreasing towards the rock mass; or variable due to the roughness. In those cases the interval of the aperture was recorded and averaged in office. The aperture was classified as shown in Table 19.
7. The Trace length was measured directly on the outcrop with a measuring tape in meters, and the plane on which was measured was recorded as well. The length was classified as shown in Table 20.

Table 20 Classification of fractures size based on Bieniawski 1984.

Joint persistence category		
Category	Trace length (m)	code
very low	<1	1
low	1-3	2
medium	3-10	3
high	10-20	4
very high	>20	5

8. The discontinuities endings or terminations were observed while measuring the length. The fractures ends were classified into three categories depending if the fractures ended outside the outcrop, against another fracture or in the rock matrix. A code from the United States Department of Agriculture (2012) was used to avoid writing the whole description. The type of end for each side of each joint was registered. For the combinations of ends, a numeric code was applied (Table 21).

Table 21 Types of fractures end and codes used in field and office

Fracture end			
Description	code	Ends combination	code
Joint end extends beyond the exposure area	xb	xb-xb	1
		xb-tr	2
Joint end terminates in solid rock inside exposure area	tr	xb-tj	3
		tr-tr	4
Joint end terminates against another joint	tj	tr-tj	5
		tj-tj	6

9. The roughness was measured with a Barton comb profilometer and compared with the roughness profiles proposed by Barton and Choubey (1977) (Table 22)

Table 22 Corresponding range of JRC (joint roughness coefficient) values to roughness profiles (ISRM 1981).

Barton and Choubey, 1977	
Typical roughness profiles for various JRC ranges	
Ranges	code
0-2	1
2-4	2
4-6	3
6-8	4
8-10	5
10-12	6
12-14	7
14-16	8
16-18	9
18-20	10

10. The filling was described according to its material and width; the classification followed the categories suggested by Bieniawski (1989) (Table 23).

Table 23 Categories and codes for fracture infilling modified from Bieniawski (1989).

Fracture filling	
Nature	code
None	0
Clean, open joint; no infilling present	1
Hard <5mm	2
hard >5mm	3
Soft <5mm	4
Soft >5mm	5

11. The weathering was described according to the classification suggested by Bieniawski (1989) (Table 24).

Table 24 Classification for Weathering.

Descriptor	Weathering condition of joint face rock material	code
Fresh	No sign of weathering.	1
Discoloured	Iron-stained or discoloured, but otherwise unweathered	2
Disintegrated	Physically disintegrated to a soil condition with original fabric still intact. The material is friable, and mineral grains are not decomposed.	3
Decomposed	Chemically altered to a soil condition with original fabric still intact. Some or all mineral grains are decomposed.	4

The Groundwater was described according to its material and width; the classification followed the categories suggested by Bieniawski (1989) (Table 25).

Table 25 Groundwater Conditions by Bieniawski (1989).

Groundwater Conditions Bieniawski 1989	
Description	Flow
Comp. Dry	No
Damp	No
Wet	No
Dripping	Occasional
Flowing	Continuous

4.2.2 Lineaments map

This process aimed to solve a photogrammetry project to obtain digital stereo pairs for the collection of stereo features. The photogrammetric process of orthorectification performed with IMAGINE Photogrammetry Project Manager allowed to generate a digital elevation model (DEM) of high resolution (5m) and orthophotos from old analogic aerial photographs. Subsequently, the digital stereo pairs and the orthophotos were interpreted using Stereo Analyst® for ArcGIS™ and 3D vision glasses (NVIDIA 3D Vision® 2 with a USB IR Emitter and a 3D LCD monitor). The final product was a map with over 900 lineaments digitalised. The orientation and the length were calculated for the lineaments. The digital photogrammetry workflow followed is represented in Figure 51

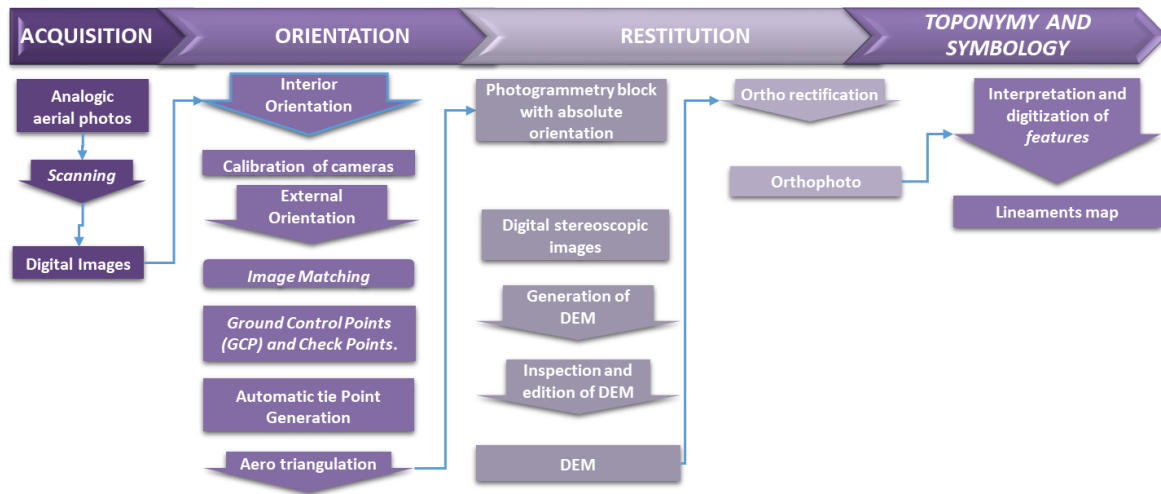


Figure 51 Digital photogrammetry workflow followed to obtain the Lineament map.

Acquisition: The selection of the aerial photos was based on the need for detailed information of joints and small fractures without sacrificing the overview of the structural features. The photogrammetric campaign performed by the Compagnia Generale Ripresearee (CGR SpA) in 1976 in Sardinia has the higher scale (1:10000) in the area. A total of 29 aerial photos from five strips were selected from that campaign. The aerial photos were acquired with three different photogrammetric cameras (Flight lines and numbers of aerial photographs used for the photogrammetric project. The analogic photos were borrowed from the Istituto di Geologia Ambientale e Geoingegneria del CNRA in Cagliari. The photos were scanned with a flatbed colour image scanner at a resolution of 600 dpi.

Table 26 Flight lines and numbers of aerial photographs used for the photogrammetric project.

Year	Flight	Number of photos	Camera	Focal length
1976	155	21-22-23-24-25-26-27	WILD RC5-8	152,45
1976	156	26-27-28	WILD RC 8a	151.79
1976	288	54-55-56-57-58-59	ZEISS RC RMK	153.07
1976	289	49-50-51		
1976	290	57-58-59-60-61		

The next steps in the photogrammetric workflow were performed with IMAGINE Photogrammetry Project Manager. The coordinate system used for the photogrammetric project was WGS84 UTM32N.

Orientation: The camera calibration certificates were provided by the CGR SpA to introduce the parameters for the interior orientation. Eight images did not have the fiducial marks then it was necessary to generate and measure alternative marks. The external orientation requires ground control points (GCP) that are points with accurate coordinates measured on the terrain. These points give an initial information of the relative position of the images and are basic for the absolute orientation to adjust the scale and level the stereoscopic model (Table 53). The GCP's were obtained from Sardegna Database Multiprecisione (DBMP) of Regione Sardegna. Most of the GCP's are on natural objects because the study area is scarcely populated and in 1976 had even fewer constructions. By this reason, the photogrammetric

block also included the more populated flat area where the GCP's were more accurate. A total of 232 points were measured in the images for the external orientation. Once that enough control and checkpoints were measured was possible to pass to the automatic tie point generation (ATP). The Tie Points are image points identified by the operator or by the ATP like corresponding points in the overlapping areas of the images, but they only have image coordinates. The appropriate strategy for automatic tie point generation was successful for 25 points in each photo.

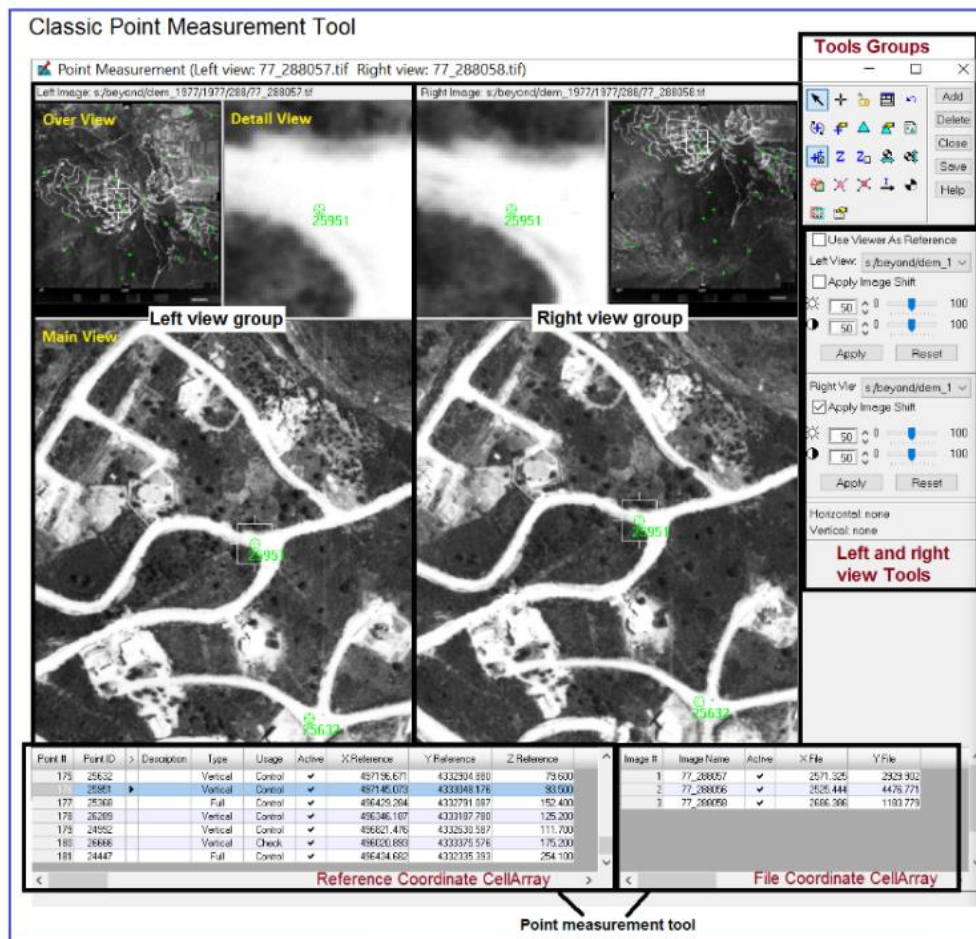


Figure 52 Classic Point Measurement tool in IMAGINE Photogrammetry Project Manager

Triangulation: The next step was the Aerial Triangulation that establishes the mathematical relationship among the sensor, the images and the ground. The accuracy of this process depends on the quantity of the matching points. IMAGINE uses the bundle project adjustment method to run the triangulation. A bundle is the processing of the information from the block of imagery on one simultaneous solution. Then through statistics the bundle project adjustment can identify, distribute and minimise the errors of the image measurements. The triangulation estimates exterior orientation parameters: the X, Y and Z and ω , ϕ and κ for each image. Ground coordinates are also calculated for the tie points, so they become control points. The Aerial Triangulation run successfully after adjusting some points (Table 54).

Generation of digital elevation model (DEM): The generation of a DEM is the fourth step in the main IMAGINE workflow for orthorectification, after setting the sensor frame, defining the interior and exterior orientation and performing the triangulation. It is done through a

process called Automatic Terrain Extraction (ATE) that determines the 3D coordinates of the objects of the overlapping areas of image pairs through a process of digital image matching (ERDAS 2013). The generation of the DEM required several attempts modifying the changing parameters to obtain a DEM with acceptable accuracy and few spikes and holes. Sardegna Geoportale has available digital terrain model for the whole Sardinia at a resolution of 10 m obtained from the contour lines of the topographic base (scale 1:10000). This DTM was used to set the Z search interval and to check the accuracy of the DEM. Areas of interest (AOI) were created to apply different strategies for mountainous, hilly, flat and excluded areas. The best results were obtained decreasing the size of the cc to 5 in the mountainous area. By the sharp relief ideally the smoothing should have been low to avoid missing topographic features. However the smoothing had to be moderate to avoid wide spread spikes and holes. The DEM extraction was applied to the image pairs with overlapping over 50%. The cell size of the DEM was set in 5m; the seed data were the GCP, the check and tie points. These points were also used to determine the accuracy of the produced DEM.

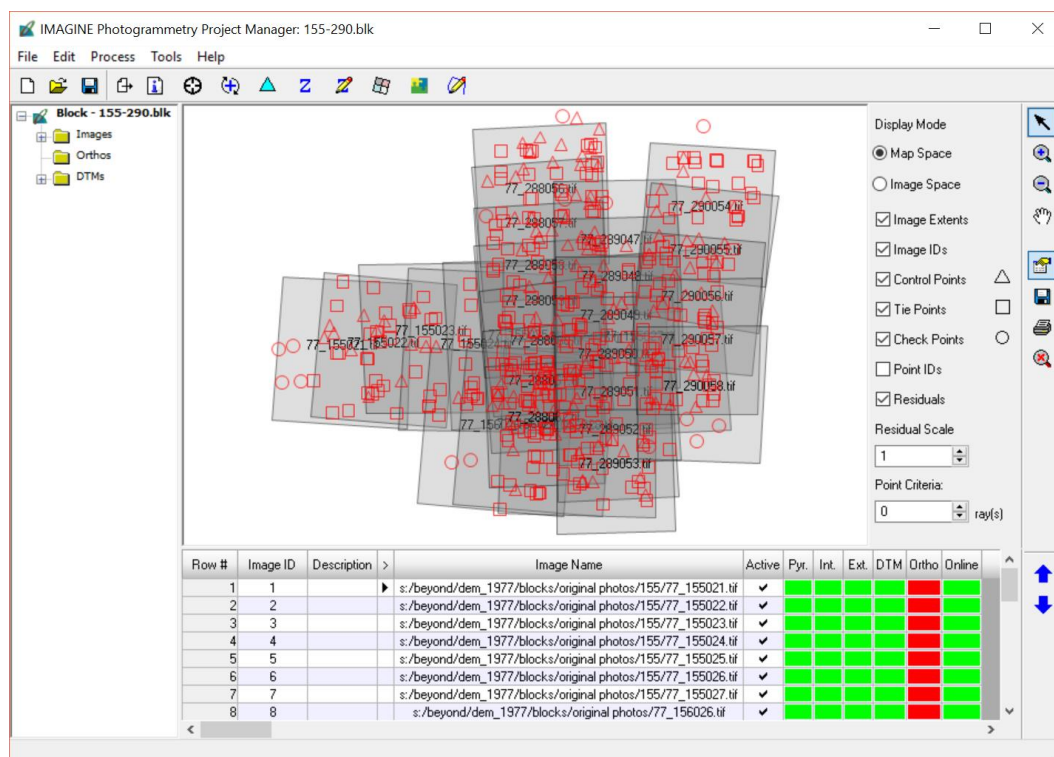


Figure 53 Photogrammetry block with absolute orientation

The abrupt relief, the high slope, the rocky tops and slopes usually cover with dense Mediterranean sclerophyllous vegetation introduced errors and gave rough textures to some slopes of the DEM (Figure 54). The holes and spikes were corrected in ERDAS creating AOI's around the problematic pixels and interpolating a new surface. 100 control points from Sardegna Database Multiprecisione were selected on stable features to check the accuracy of the DEM (Figure 55). The average error measured was 1.07m (maximum error is 9 m, and the minimum is -4). The areas with high errors were found in the borders of the DEM. Those borders were cut keeping the more certain inner area.

Orthorectification (Figure 56): The 14 aerial photos covering the mountainous area were orthorectified using as a base the DEM. At this point, the workflow for the photogrammetric project was completed in IMAGINE.

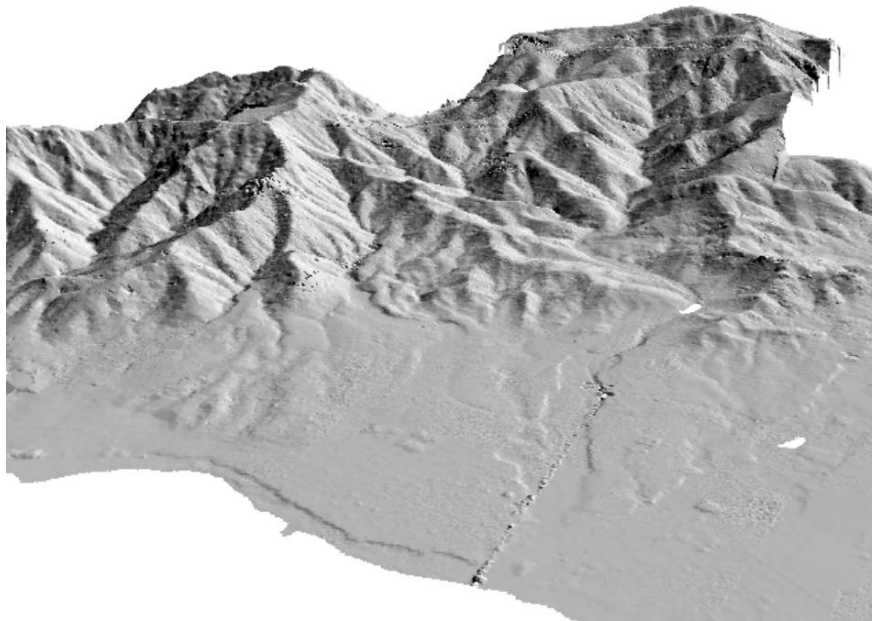


Figure 54 DEM generated like a raster file (.img)

Interpretation: The next step was to collect stereo features corresponding to lineaments from 9 stereo pairs. The software used was the Stereo Analyst for ArcGIS in ArcMap. The hardware used for 3D vision was the NVIDIA 3D Vision® 2 with a USB IR Emitter and a 3D LCD monitor ASUS. The USB IR emitter communicates the computer with the 3D Vision glasses to synchronize the alternating darken of the lenses with the refresh rate of the monitor (Figure 57). Thanks to this, different perspectives are perceived allowing the stereo vision, this technique is called alternate-frame sequencing (Boulos & Robinson 2009, NVIDIA 2012).

The lineaments were digitised like polylines using the feature collection tools of Stereo Analyst for ArcGIS. The orientations and length were calculated through a Python code and the Calculate Geometry tool of ArcMap, respectively. The orientations of the lineaments and the fractures measured in the field were represented in a Stereonet to identify the sets of discontinuities and the more relevant trends. The distribution of the measured parameters of the discontinuities were calculated through statistical analysis.

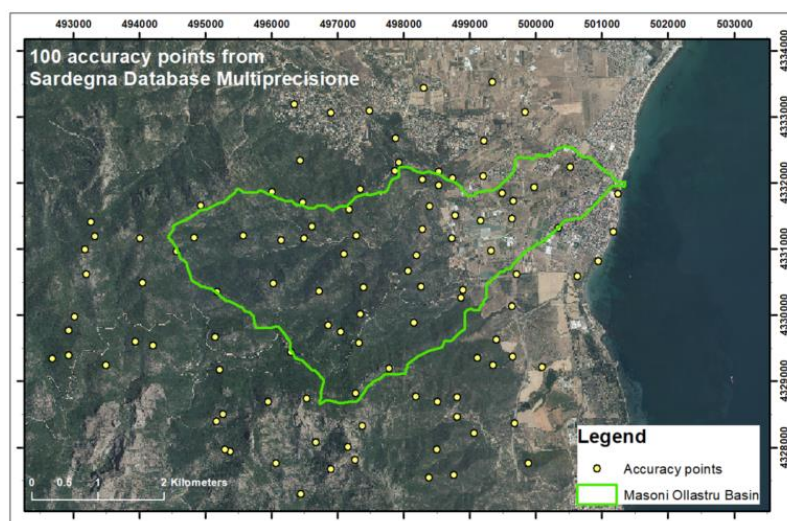


Figure 55 Location of accuracy point.

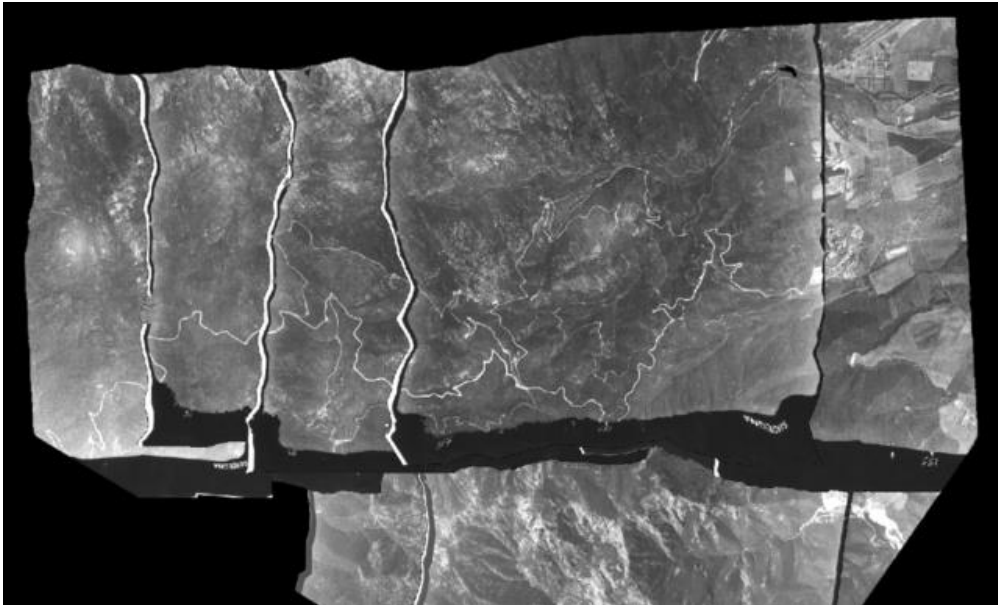


Figure 56 Orthophotos



Figure 57 Digital Photogrammetric Workstation or Softcopy Workstation, 3D vision: NVIDIA 3D Vision® 2 with a USB IR Emitter and a 3D LCD monitor ASUS.

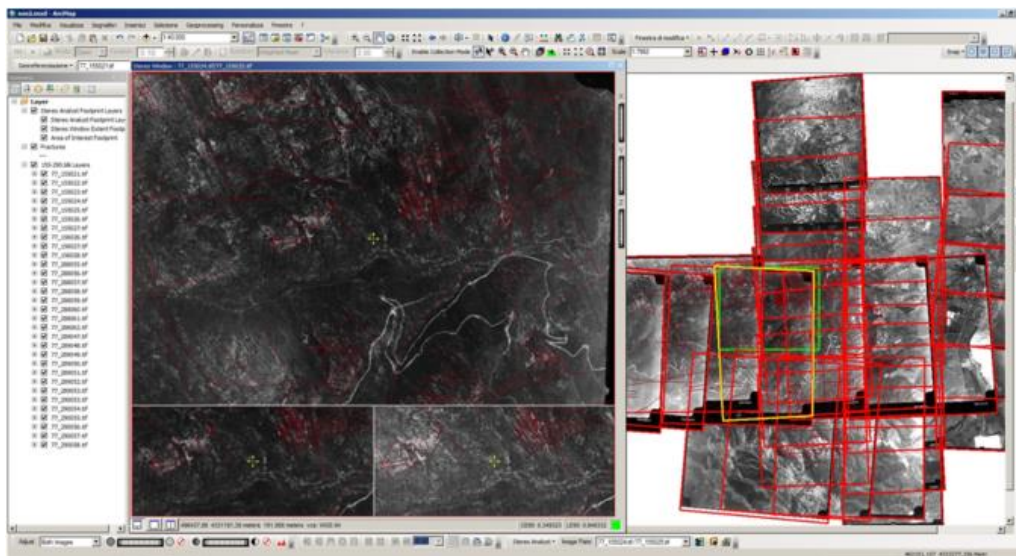


Figure 58 Stereo Analyst for ArcGIS

4.2.3 Calculation of hydraulic permeability with the three dimensional anisotropic Darcy's law

The idealised model of fractured media described with the three dimensional anisotropic Darcy's law also called cubic law was used to calculate the fracture permeability at each geomechanical station.

The median aperture and the frequency were used to calculate the permeability of each set of joints. The permeability at the station was calculated adding the hydraulic conductivities of the sets.

The apparent spacing measured in the field for sub-parallel joints sometimes was measured between fractures that were later classified in different sets with the Stereonet. Nevertheless, the identification number of the fractures between which the spacing was measured was written; making easy to calculate the apparent spacing between fractures of the same set at the office. The true spacing was calculated and the median spacing for each set. The frequency of number of fracture in a meter was calculated dividing 1m in the median spacing. The frequency was also calculated according to Pitau (1970) dividing the number of fractures in a set over the length of the projected scan line on the direction of the mean pole.

4.2.4 Spatial distribution of sets and parameters.

The distribution of the sets of fractures and lineaments was evaluated across the basin. The areal distribution of the sub-horizontal sets of joints and their aperture and spacing was evaluated to try to identify patterns of distribution. The spacing was evaluated to see if it was wider in the upper parts in accordance with the model of the fissured layer (§2.1.2) (Wyns *et al.* 2015a). The aperture was confronted with the elevation to observe if the upper zones had wider aperture due to less lithological load. The aperture was confronted also with the distance to the river to observe if the fractures are opening due to effect of water flow and weathering. The aperture could be higher in the upper areas due to wash out and erosion of the fractures walls, and the aperture in the lower area could be smaller due to deposition. However the erosive effect of the stream should be take into account in the stations over the river bed.

A map of density of lineaments was done to evaluate if there were concentrations of lineaments or a pattern in the distribution. A map of intersection of lineaments was also done to evaluate areas with better interconnection of fractures. The maps were done using the Density tools of the spatial analyst toolset of ArcGIS. The density tools calculated the density of input features (line or point) within the area of the map of lineaments around each output raster cell searching in a circular area of a set radius

4.3 Methodology to estimate the Water budget in the ungauged Masoni Ollastru Basin.

As it is often the case for small basins with a seasonal (intermittent) stream of little relevance the MORB does not have an instrumental record of its hydrological parameters; there are no wells neither stream gauges or meteorological stations inside the basin. The closest meteorological stations with the historical and current record are two and five kilometres

away from the perimeter of the MORB, and the closest gauged stream is Rio di Pula 14.27 km away.

Therefore the evaluation of the infiltration and runoff in the watershed have to be achieved through indirect methods, as explained in §2.3.3. The mean annual potential effective infiltration of the MORB was obtained from the water balance. The mean annual potential runoff was estimated calculating the average annual runoff coefficient (C_k) following a physiography-based indirect method.

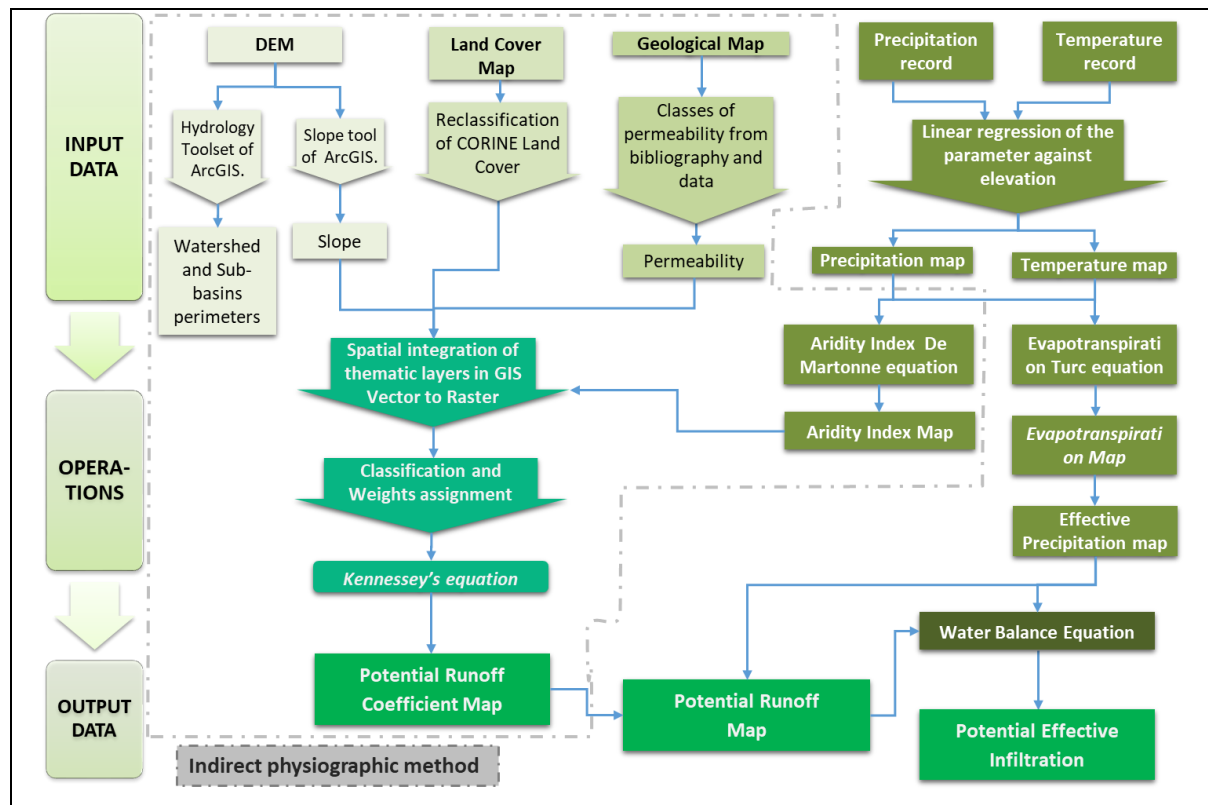


Figure 59 Estimation the water budget for the basin.

The C_k calculation requires mean slope, land cover parameters and permeability (Ghiglieri *et al.* 2014), that are classified into four or five classes that correspond to a numeric value. Those numeric values depend on the aridity index I_a of De Martonne (1926) (Equation 25). The classified parameters were weighted according to the area that each class occupied. The C_k of the watershed was calculated adding three components: slope angle coefficient (C_a), the land cover coefficient (C_v), and permeability coefficient (C_p). The base data and the sources used to estimate parameter of the water budget. The processing was done in a Geographical Information Systems (GIS) with thematic maps.

The hydrological balance was done following the methodology by Ghiglieri *et al.* (2014) and Spadoni *et al.* (2010). The hydro-meteorological parameters, mean annual precipitation (P_A) and annual evapotranspiration, for the water balance, had to be interpolated from meteorological data of stations around the basin. The potential annual ET was estimated using Turc (1954) equation modified by Santoro (1970) for Mediterranean arid areas (Equation 29 and §2.3.5.3). The computation of the PET_A and the I_a required knowing the P_A and T_A , and the average precipitation and temperature of the hottest month. The precipitation and temperature records were collected from the network of meteorological

stations in Sardinia, referenced in Table 27, and the data were interpolated to know their spatial distribution.

Table 27 Data and sources used to estimate parameter of the water budget.

	Data Source	Data	Product
1	Regione Sardegna	Precipitation and temperature historical record of “Servizio tutela e gestione delle risorse idriche, vigilanza sui servizi idrici e gestione della siccità”	Precipitation, Temperature, Evapotranspiration and Aridity Index
2	Istituto Superiore per la Protezione e la Ricerca Ambientale (ISPRA)	Precipitation and temperature record in pdf format of “Dati storici di pluviometria e termometria in tempo reale (PLUTER)”	
3	Centro di Documentazione dei Bacini Idrografici (CEDOC)	Precipitation and temperature current record	
4	Website Sardegna Geoportale	DTM of Sardegna at 10m resolution	Basin and sub-basins perimeters. Slope coefficient
5		Carta dell'Uso del Suolo in scala 1:25.000 – 2008, classified using the Corine Land Cover legend. CORINE (Coordination of information on the environment) Land Cover project, (EEA, 1997)	Land cover coefficient
6		Carta Geologica scala 1:25,000, (Geology map Scale 1:25,000)	Permeability Coefficient
7		Literature of the area and chapter 3 of this work	

The Masoni Ollastru River discharge was measured in several cross-sections along the stream using an electromagnetic flowmeter applying the midsection method. The discharge data was used to calculate actual runoff coefficients (C_s) for partial areas of the MORB (sub watersheds) delimited according to the streamflow gauge stations. The C_k was calculated for the sub-basins as well, and the values were compared.

First of all, the perimeter of the basin and sub-basins were delimited from the DTM of Sardegna (10m resolution) in ArcGIS.

4.3.1 Basin delimitation

The perimeter of the hydrologic basin and sub-basins of the River Masoni Ollastru were extracted from the DEM 10 m resolution from Sardegna Geoportale using the Hydrology Toolset in the tools Spatial Analyst Toolbox of ArcGIS. The workflow used is synthesized below (Figure 60).

- A. The sinks in the DEM were corrected using the tool “Fill”.
- B. The tool “Basin” automatically defines the drainage basins finding all sets of connected cells that belong to the same drainage basin and delimitating the ridge lines between basins. The product is a raster of drainage basins.
- C. The raster was converted to a polygon shapefile using Conversions tools Raster to Polygon.
- D. The targeted basin was selected and export as a new shapefile.

Although the Basin tool is very fast and efficient to delimitate watersheds the sub-basins were extracted through a longer process to obtain individual subbasins based on points of intersection (pour points) corresponding with stream flow control stations. The base once more was the DEM 10m resolution of Sardinia. The process to extract the sub-basins is explained in the next steps, each one associated with one tool of the Hydrology toolset.

- A. Possible irregularities (sinks or depressions) in the DEM are fixed with the tool “fill”.
- B. A flow direction raster is extracted from the repaired DEM. It represents the direction that water would follow out of each DEM cell.
- C. The Flow Direction Raster is the input to generate a Flow Accumulation raster that tabulates for each cell the number of cells that will flow to it. The obtained raster was cramped so the symbology was adjusted to identify better the significant accumulation that should correspond with streams.
- D. Created a point shapefile to draw pour points of interest according to the stream gauge stations over cells with high accumulation. From this step, the process is individual for each sub-basin.
- E. The Tool “Snap to Pour Point” relates the pour point shapefile and the Flow Accumulation to generate a raster of the pour point.
- F. Finally, the Watershed tool uses the snap pour point and the flow direction raster to identify the area contributing to the pour point.
- G. The watershed produced are raster files, they were converted to polygons. The area and perimeter were calculated, and polygons of individual areas or sub-basins were extracted with tool Overlay of Analysis tool.

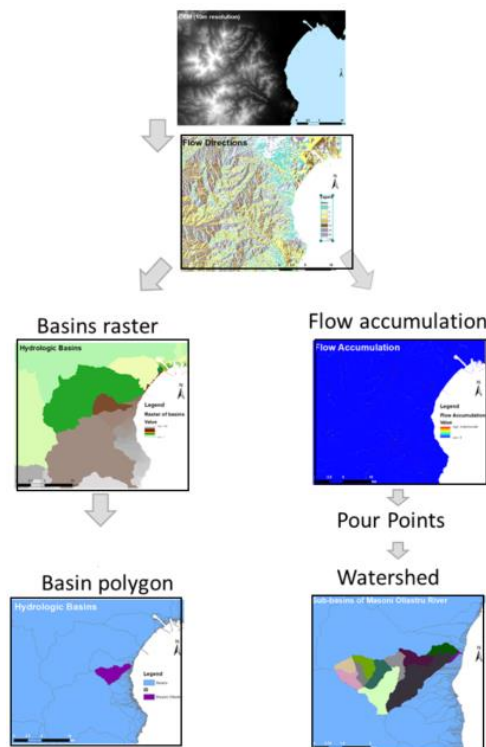


Figure 60 Flowchart generate basin sub-basin perimeters

4.3.2 Precipitation interpolation

The calculation of the water balance requires knowing the mean annual precipitation, mean annual temperature and the mean precipitation and temperature of the hottest month. Two approaches were applied to estimate mean precipitation and temperature in the basin. The most straightforward approach consisted of assigning to the un-sampled location the record of the closest gauge (Goovaerts 2000). Assuming that the precipitation and the temperature are the same in the whole basin from the mountains to the shore. The second approach used the meteorological data from the stations around the basin to interpolate the areal distribution through linear regression.

The main steps followed were:

1. Collection of data.
2. Define periods with the best data.
3. Calculate average annual P and T for each station for the periods defined before.
4. Determine the correlation coefficient and the linear regression equations between P_A and elevation.
5. Apply equation to DEM
6. Determine error with cross-correlation.

Data collection:

The closest weather stations were identified from the sources 1, 2 and 3 referred in the Table 27. 13 stations were selected around the MORB, approximately 2 to 17 km away from the basin perimeter and located in a range of elevation from 7 to 716 MASL (Figure 61 and Table 28). The period with data for most of the stations is 1922-2011 for precipitation and 1982-2011 for temperature.

Table 28 Meteorological stations around the MORB basin. The distance to the basin, distance to the sea, coordinates, height, period of data and data source number from table 26.

NAME	E	N	Elevation (MASL)	Distance to the sea (km)	Distance to the MORB (km)	Period with P data	Period with T data	Source
Capoterra 1	497463.5	4336169.9	54	5.60	5	1922-2011	1989-2011	2
Capoterra 2	497000.0	4334224.5	165	5	2	2014-2017	2014-2017	3
Santa Lucia di Capoterra	494603.3	4339003.9	62	9.00	7.5	2014-2017	2014-2017	3
Pula	500213.5	4317940.1	10	2.30	11	1922-2011	1988-2011	2
Is Cannoneries	487263.6	4320680.1	716	15.50	12.7	1925-2011	1973-2011	2
Cagliari	510200.0	4341850.0	101	1.30	13	1922-2011	--	2
Cagliari S.I	506824.9	4338855.1	7	0.00	9.5	1951-1981	1951-1971	2
Cagliari Elmas	505196.4	4343795.9	0	0.70	13.5	1951-2013 (Aug)	--	2
Cagliari Saline	512949.1	4340830.7	2	1.8	15.3	--	1900-1971	2
Pantaleo	4825136.2	4326810.1	240	18.50	12.2	1951-2011	--	2
Villa San Pietro	497960.1	4321580.7	53	4.80	8	2011-2015	2004-2015	2
Uta	497038.3	4343368.8	20	8.13	11.5	1951-1987, 1991	2012-2015	2

Campanasissa	480383.1	4340167.7	325	23.50	17	1951-1971	--	2
--------------	----------	-----------	-----	-------	----	-----------	----	---

The closest stations to the basin are both called Capoterra and are almost three kilometres away from each other and have an elevation difference of almost 100m. To distinguish then the older one with historical data was called Capoterra 1 while the newer was called Capoterra 2. The table 27 shows characteristics of the 13 weather stations, their distance to the basin, and distance to the sea, coordinates, elevation and period of data. Table 29 and Table 30 show the periods with data for precipitation and temperature, respectively. Only Capoterra, Pula, Is Cannoneris and Cagliari have long continuous records.



Figure 61 Map showing the meteorological stations around the Masoni Ollastru river basin.

Table 29 Periods with precipitation data of each station.

NAME	Period with Precipitation data		Interval years
Capoterra 1	1922-2011		89
Pula	1922-2011		89
Is Cannoneries	1925-2011		86
Cagliari	1922-2011		89
Cagliari Elmas	1951-2013 (Aug)		62
Cagliari S.I	1951-1981		30
Pantaleo	1951-2011		60
Uta	1951-1987		36
Campanasissa	1951-1971		20
Capoterra 2	2014-2017		3
Santa Lucia di Capoterra	2014-2017		3
Villa San Pietro	2011-2015		4

Table 30 Periods with temperature data of each station.

NAME	Periods of Temperature data			Interval years
Capoterra 1		1989-2011		22
Pula		1988-2011		23
Is Cannoneris		1973-2011		38
Cagliari S.I	1951-1971			20
Cagliari Saline	1900-1971			71
Uta			2012-2015	3
Capoterra 2			2014-2017	3
Santa Lucia di Capoterra			2014-2017	3
Villa San Pietro			2004-2015	11

The temperature data is scarcer than the precipitation data. Only nine of the thirteen stations were measuring temperature. Of those nine, only Capoterra 1, Pula and Is Cannoneris have a long-term coinciding record.

Calculate mean annual precipitation and temperature

The annual and monthly averages were calculated for each station for the periods of time in common with other stations. The P_A , the T_A and the monthly averages of P and T for the area of the MORB were calculated using two methods. The first and simplest way was assigning a unique value of the averaged parameter of the closest stations to the whole area of the basin. The selected station to assign the averaged valued to the whole basin was Capoterra 1. It was chosen because it is the closest station with historical data of both precipitation and temperature in a long-term interval (1989 to 2011). Although the chosen meteorological station is the closest one, it is located in a hilly area of Capoterra. Therefore it might not be representative of the precipitation in the mountains and the coast.

The second way was obtaining the areal distribution of the parameters trough linear regression interpolation, the sum of the values of each cell was divided by the number of grid points from the map. The linear regressions of the precipitation and temperature were done finding the group of stations with the best linear correlation coefficient (CC) between the parameter and elevation for a common period with data. The CC between two variables indicates how firmly they are inter-related. The value is between -1 and +1, closer the CC to +1 better the positive correlation. The CC was found using the CORREL function or the Analysis Toolpak add-in in Excel. The CC was calculated for different periods and different combinations of stations, leaving outside those stations that did not follow the trend. The error of the interpolation was estimated with cross-validation, running the correlation several times removing one station each time. The mean absolute error (MAE) and mean square error (MSE) were also calculated.

The linear regression of mean precipitation versus elevation is based on the increment of precipitation with increment in elevation. The linear regression of *mean temperatures versus altitude* was done based on the fall of temperature with increasing elevation in the free atmosphere or vertical temperature gradient (Linslay *et al.* 1958).

Initially, the CC for the precipitation regression was found for several combinations of stations and for different periods according to the availability of data, to test the suitability of the interpolation method and its limits in the area surrounding the MORB basin.

Table 31 shows the annual averages and monthly averages precipitation for individual stations in different periods.

Table 31 Average annual and average monthly precipitation for common periods with data in the stations around the MORB.

Stations	Elevation MASL	Mean annual and monthly precipitation (mm)												
		Annual	Jan	Feb	Mar	Apr	May	Jun	Jul	Aug	Sep	Oct	Nov	Dec
1951-2011 (Correlation 1, 2 and 3)														
Capoterra 1	54	530.1	57.3	60.9	53.3	50.1	29.1	10.8	2.8	7.5	37.8	72.6	76.9	71.0
Pula	10	480.1	55.6	59.5	51.0	43.4	27.9	9.6	3.8	7.5	39.2	52.2	65.9	70.9
Is Cannoneris	716	1038.2	142.8	131.5	115.7	102.4	55.7	18.3	4.9	15.6	59.8	124.9	136.1	154.8
Cagliari Elmas	0	408.2	43.4	46.6	39.7	39.9	25.0	10.0	2.9	7.3	33.0	53.3	59.4	53.9
Pantaleo	240	829.4	106.6	102.1	83.1	66.9	44.0	19.4	6.9	14.4	50.3	101.3	117.2	121.5
1951-1987 (Correlation 4 and 5)														
Capoterra 1	54	520.4	55.6	72.6	59.6	38.6	29.1	11.4	1.9	7.5	33.4	72.3	70.7	67.7
Pula	10	496.4	54.3	73.9	63.1	35.6	30.7	8.8	2.4	5.6	37.8	56.4	68.0	66.5
Is Cannoneris	716	1068.0	153.6	153.3	137.7	88.4	56.9	15.5	4.9	13.7	57.8	137.8	135.4	155.1
Cagliari Elmas	0	427.0	45.1	54.7	46.5	32.6	27.0	9.5	2.6	8.0	32.0	59.9	54.1	56.4
Pantaleo	240	879.2	114.5	119.7	99.4	60.2	43.0	18.3	6.7	10.3	46.4	115.4	123.2	125.5
Uta	20	508.4	54.5	65.3	56.1	40.2	30.7	13.2	3.9	8.6	35.0	72.7	92.6	66.1
1951-1971 (Correlation 6 and 7)														
Capoterra 1	54	534.4	53.9	67.7	56.3	34.7	26.3	12.3	1.5	5.9	38.6	85.6	75.6	76.0
Pula	10	505.6	55.9	59.5	62.2	40.4	32.1	10.0	1.5	5.4	36.8	67.4	69.8	73.0
Is Cannoneris	716	1092.4	166.2	142.2	131.3	86.6	50.6	14.3	5.1	14.6	61.6	165.7	138.6	179.1
Cagliari Elmas	0	421.3	45.1	45.8	41.1	28.8	24.2	9.0	1.7	7.5	32.2	63.8	58.6	63.5
Pantaleo	240	900.9	121.0	112.2	95.7	53.2	36.3	15.6	6.7	9.1	46.3	127.5	138.0	146.1
Uta	20	499.1	51.6	56.9	49.0	36.4	26.4	12.7	3.2	6.2	31.3	72.0	99.6	78.8
Campanasissa	329	843.0	112.5	98.6	83.8	49.8	37.4	10.1	11.9	11.8	40.7	107.1	134.0	152.6
Cagliari (S.I.)	0	444.3	48.1	46.9	42.1	29.7	24.6	10.2	1.0	8.0	39.9	63.7	64.9	65.2
1989-2011 (Correlation 8)														
Capoterra 1	54	551.2	56.6	43.4	43.4	68.7	29.7	10.1	4.1	7.9	45.1	75.3	89.4	77.4
Pula	10	455.0	57.8	38.0	32.4	55.2	23.7	10.9	5.9	10.4	41.4	45.8	62.4	77.8
Is Cannoneris	716	992.1	126.6	98.8	83.6	123.6	53.8	22.4	5.0	18.5	62.7	105.6	137.2	154.4

The behaviour of the annual precipitation was compared for the stations with historical record to identify if they followed a similar trend in time (Figure 62).



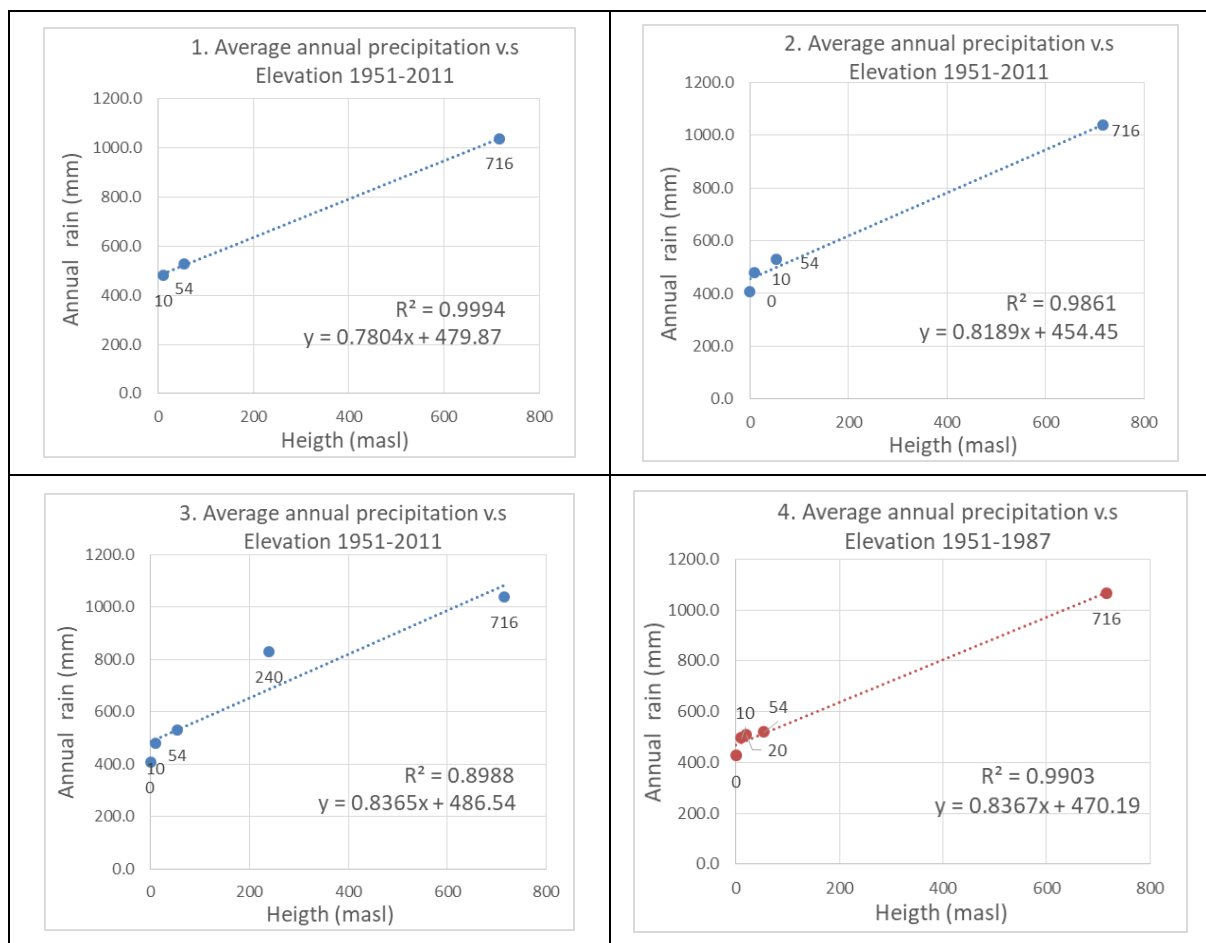
Figure 62 Annual precipitation from 1951 to 2014 of nine stations surrounding the MORB.

In general, the trend of the precipitation is similar for all the stations, and there is a marked increment of annual precipitation with elevation. Since no noticeable difference was observed the correlations was done taking all the stations into account (Table 32).

Table 32 Correlations evaluated using different periods and stations.

Correlation	Period	Size interval (years)	Stations	Number of Stations	Correlation Coefficient
1	1951-2011	60	Capoterra1, Pula, Is Canoneris	3	1.000
2			Capoterra1, Pula, Is Canoneris, Cag Elmas	4	0.993
3			Capoterra1, Pula, Is Canoneris, Cag Elmas, Pantaleo	5	0.899
4	1951-1987	36	Capoterra1, Pula, Is Canoneris, Cag Elmas, Uta	5	0.995
5			Capoterra1, Pula, Is Canoneris, Cag Elmas, Uta, Campanasissa	6	0.887
6	1951-1971	20	Capoterra1, Pula, Is Canoneris Cag Elmas, Uta, Campanasissa, Pantaleo	7	0.941
7			Capoterra1, Pula, Is Canoneris, Cag Elmas, Uta, Campanasissa	6	0.986
8	1989-2011	22	Capoterra1, Pula, Is Canoneris	3	0.994
9	1989-2011	22	Capoterra1, Pula, Is Canoneris, Cag Elmas	4	0.980

The correlations using very disperse stations (correlations 3 and 5) have lower CC; while the best-obtained correlation was obtained using the stations Capoterra, Pula and Is Cannoneris for the period 1951-2011. However, the nine correlations are very close to 1, showing a clear relation between precipitation and elevation in the south of Sardinia (Figure 63).



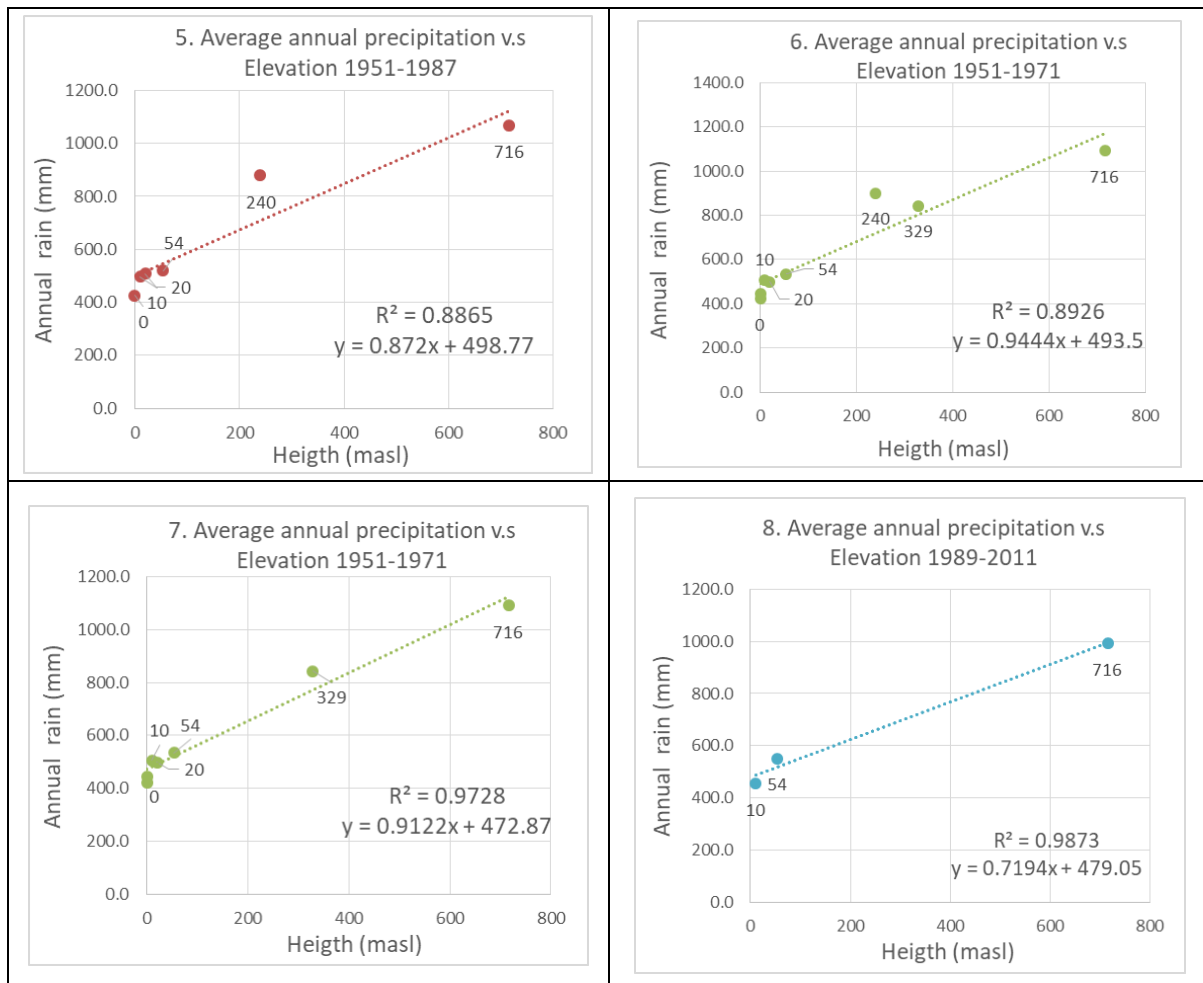


Figure 63 Linear regression analysis of mean annual rainfall as a function of altitude in surrounding area of MORB basin.

Table 33 Statistics for the annual rainfall data. The last three columns give the linear correlation coefficient between rainfall and elevation, and the mean absolute error (MAE) and mean square error (MSE) of prediction of rainfall by linear regression of elevation for each correlation.

Correlation	Period (years)	Precipitation (mm)				Correlation Coefficient	MAS	MSE
		Mean	Standard Deviation	Min	Max			
1	1951-2011	683	302	480	1038	1.000	<u>20</u>	644
2		614	287	408	1038	0.993	34	644
4	1951-1987	604	261	427	1068	0.995	31	1675
6	1951-1971	685	257	421	1092	0.941	59	7687
7		649	261	421	1092	0.986	37	2628
8	1989-2011	666	286	455	992	0.994	32	1045

Maps for six correlation of P_A were done applying the regression equations to the Sardena DEM (10m resolution) in ArcGIS using the Raster Calculator tool. The graphics of the P_A v.s elevation, the CC, MAS and MSE values showed that the station Pantaleo does not follow the behaviour of the other stations. The best CC and the lowest MAS were obtained using the stations Capoterra, Pula and Is Cannoneris for the period 1951-2011. However, the temperature data for those three stations are available only from 1989 to 2011. Therefore

the P_A Map with the correlation eight done with Capoterra, Pula and Is Cannoneris stations for 1989-2011 was chosen to calculate the water budget the PET_A .

Calculate the average precipitation (p) of the hottest month

August was identified as the hottest month from the monthly averages temperatures in Table 35. The stations and the period used for the interpolation of the average precipitation of August were those of the correlation 8. Table 34 shows the CC, the MAS and the MSE for the map of August average precipitation done with linear regression.

Table 34 Statistics for the August rainfall data. The last three columns give the linear correlation coefficient between rainfall and elevation, and the mean absolute error (MAE) and mean square error (MSE) of prediction of rainfall by linear regression of elevation for each correlation.

Average August Precipitation (p) 1989-2011										
Station	Elevation MASL	Precipitation (mm)						Coefficient Correlation	MAS	MSE
		Average	Max	Min	Standard deviation	Value estimated	error			
Capoterra 1	54	8	51	0	14.2	9.5	-1.60	0.96	1.28	1.79
Pula	10	10	6	0	1.8	8.9	1.51			
Is Cannoneris	716	19	44	0	16.0	17.8	0.72			
Average	260	12	34	0	10.7	12.1	0.21			

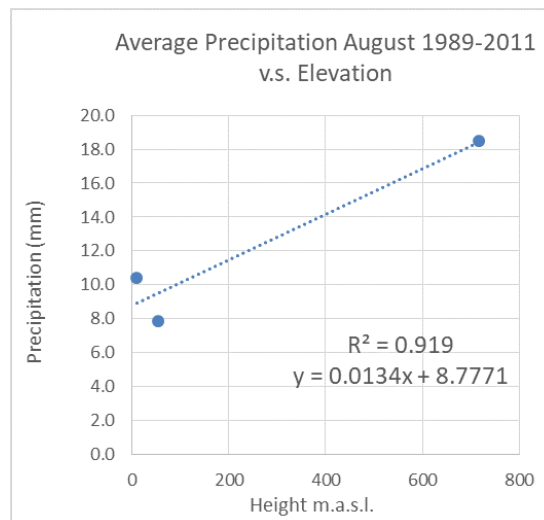


Figure 64 Linear regression analysis of mean august rainfall as a function of altitude in surrounding area of MORB basin.

4.3.3 Temperature interpolation

The stations used for the linear regression of temperature versus elevation were Capoterra 1, Pula and Is Cannoneris. Those are stations with the most prolonged common periods with data, and geographically representative of the MORB basin. Figure 65 shows the relation between the temperature and the elevation and the regression equations. Table 36 and Table 37 show the CC and the error of the maps of T_A and average August temperature (mean temperature of the hottest month t).

Table 35 Average annual and average monthly temperature for 1989-2011 stations around the MORB.

Average annual and monthly Temperature (°C) 1989-2011														
Station	Elevation MASL	Annual	Jan	Feb	Mar	Apr	May	Jun	Jul	Aug	Sep	Oct	Nov	Dec
Capoterra 1	54	18.4	10.5	11.0	13.4	15.5	19.9	24.3	27.4	27.8	23.8	19.9	15.2	11.7
Pula	10	17.2	9.9	10.4	12.4	14.4	18.2	22.4	25.6	25.9	22.7	19.0	14.7	11.1
Is Cannoneris	716	14.1	6.7	6.7	8.9	10.4	15.7	20.3	23.8	23.9	19.0	15.6	10.9	7.6
Average	260.00	16.6	9.0	9.4	11.6	13.6	17.9	22.3	25.6	25.9	21.8	18.2	13.6	10.1

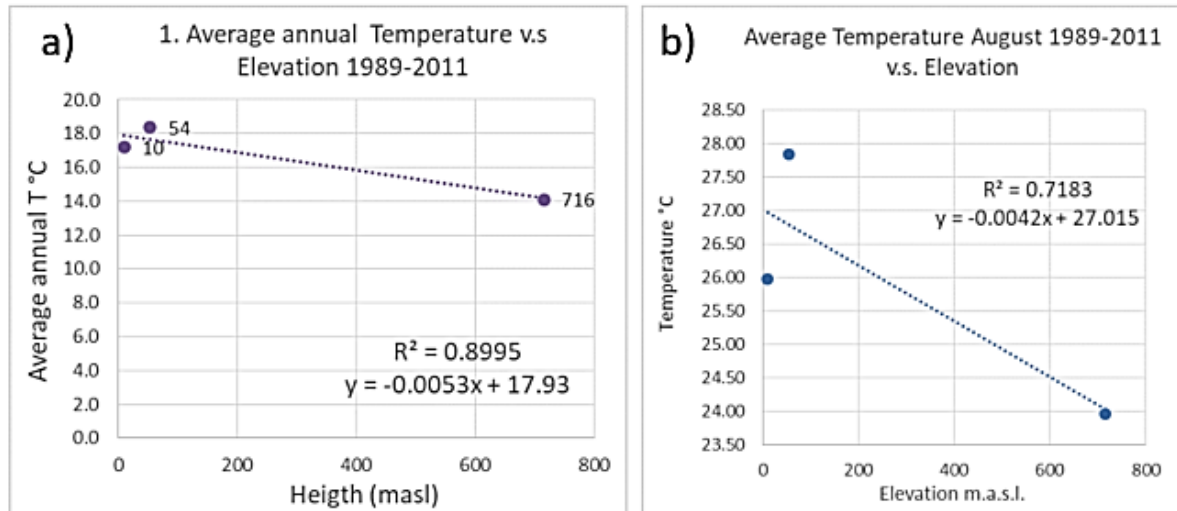


Figure 65 Linear regression analysis of mean annual temperature (T_A) and mean August temperature (t) as a function of altitude in surrounding area of MORB.

Table 36 Statistics for the annual temperature data. The last three columns give the linear correlation coefficient between temperature and elevation, and the mean absolute error (MAE) and mean square error (MSE) of prediction of temperature by linear regression of elevation for each correlation.

Average Annual Temperature T_A 1989-2011										
Station	Elevation (MASL)	Temperature (°C)						Correlation Coefficient	MAS	MSE
		T_A	Max	Min	Standard deviation	Value estimated	error			
Capoterra	54	18.36	22.68	17.33	1.04	17.65	0.71	-0.948	0.544	0.339
Pula	10	17.21	19.72	11.16	1.53	17.87	-0.66			
Is Cannoneris	716	14.12	15.69	12.61	1.02	14.37	-0.25			

Table 37 Statistics for the August temperature data. The last three columns give the linear correlation coefficient between temperature and elevation, and the mean absolute error (MAE) and mean square error (MSE) of prediction of temperature by linear regression of elevation for each correlation.

Average Temperature August (t) 1989-2011										
Station	Elevation MASL	Temperature (°C)						Correlation Coefficient	MAS	MSE
		Aug	Max	Min	Standard deviation	Value estimated	error			
Capoterra 1	54	27.6	34.0	25.3	1.8	26.8	1.05	-0.85	0.76	0.71
Pula	10	26.0	27.4	23.6	1.0	27.0	-0.98			
Is Cannoneris	716	24.0	28.3	20.5	2.1	24.2	-0.23			
Average	260.00	25.9	29.9	23.1	1.6	26.0	-0.05			

4.3.4 Estimation of Evapotranspiration and Aridity index

The PET_A was calculated using the Turc (1954) equation and the modification of the parameter L proposed by Santoro (1970) for the Mediterranean arid areas. The PET_A obtained with the modification of Santoro (1970) is higher especially towards the west. The PET_A used to obtain the rest of parameters of the water budget was the one adjusted for Sicily and valid for temperatures between 10°C and 18°C, given the similarities and proximity of both islands. Therefore the values of P_{Aef} , R_{Ap} and I_{Aef} would be lower than those obtained with the simple Turc (1954) equation. The aridity index applied in the physiographic method to calculate the C_k is the one proposed by De Martonne (1926) (Equation 25). The PET_A and the I_a were calculated using the average values of precipitation and temperature from 1989 to 2011 for Capoterra 1, Pula and Is Cannoneris.

The PET_A and the I_a spatial distribution were estimated using the maps obtained from linear regression interpolation and applying the formulas with the tool Raster Calculator in ArcGIS. Table 38 shows the values obtained using the averaged values of P and T and the values obtained from the maps.

Table 38 Statistics for the August temperature data.

1989-2011		Average Temperature (°C)		Average Precipitation(mm)		From Interpolation		
Station	Elevation (MASL)	Annual	August	Annual	August	I_a	PET_A (mm)	
							Turc	Santoro
Capoterra 1	54	18.4	27.9	551.2	7.9	11.47	438.92	443.29
Pula	10	17.2	26.0	455.0	10.4	10.72	423.04	426.23
Is Cannoneris	716	14.1	24.0	992.1	18.5	24.13	552.71	592.20
Average	260	16.6	25.9	666.1	12.3	15.44	471.56	487.24

The aridity index I_a in the MORB basin is minor than 25. Therefore the partial coefficients to calculate the runoff coefficient are in Table 9.

4.3.5 Slope Coefficient map

The Slope map was obtained from the Sardegna DEM (10m resolution) using the tool "Slope" from the toolbar "Spatial analysis tools" in ArcGIS. The slope tool gives the option to calculate the slope as a percentage of slope or degree of slope. The classes of the slope coefficient C_a are in percentage of slope. Therefore the raster of the slope was obtained in those units. The slope raster was reclassified to the four categories of the slope coefficient (Table 39) using the tool "Reclassify" in the Spatial Analyst toolbar and transformed into a polygon shapefile. The values of the slope coefficient C_a were assigned in the attribute table and the areas calculated for each class. The slope shapefile was converted into a raster with the C_a values.

Table 39 Classes and values of the slope coefficient for an aridity index below 25.

Slope (C_a)	Slope classes	$I_a < 25$
	>35%	0.22
	10% < S < 35%	0.12
	3.5% < S < 10%	0.01
<3.5%	0	

4.3.6 Land cover Coefficient map

The land cover coefficient map in raster format was extracted from the vectorial file of Land Cover Map of CORINE. The land cover map of Corine classified the terrain of the MORB basin into 27 classes (Bossard, *et al.* 2000). Those 27 classes were reclassified into four classes (Table 40 and Figure 66) the values of the land cover (C_v) were assigned, and the area of each class was calculated using the tools of the Attribute Table. The file was converted to raster using the tool “feature raster” and to obtain the C_v coefficient map.

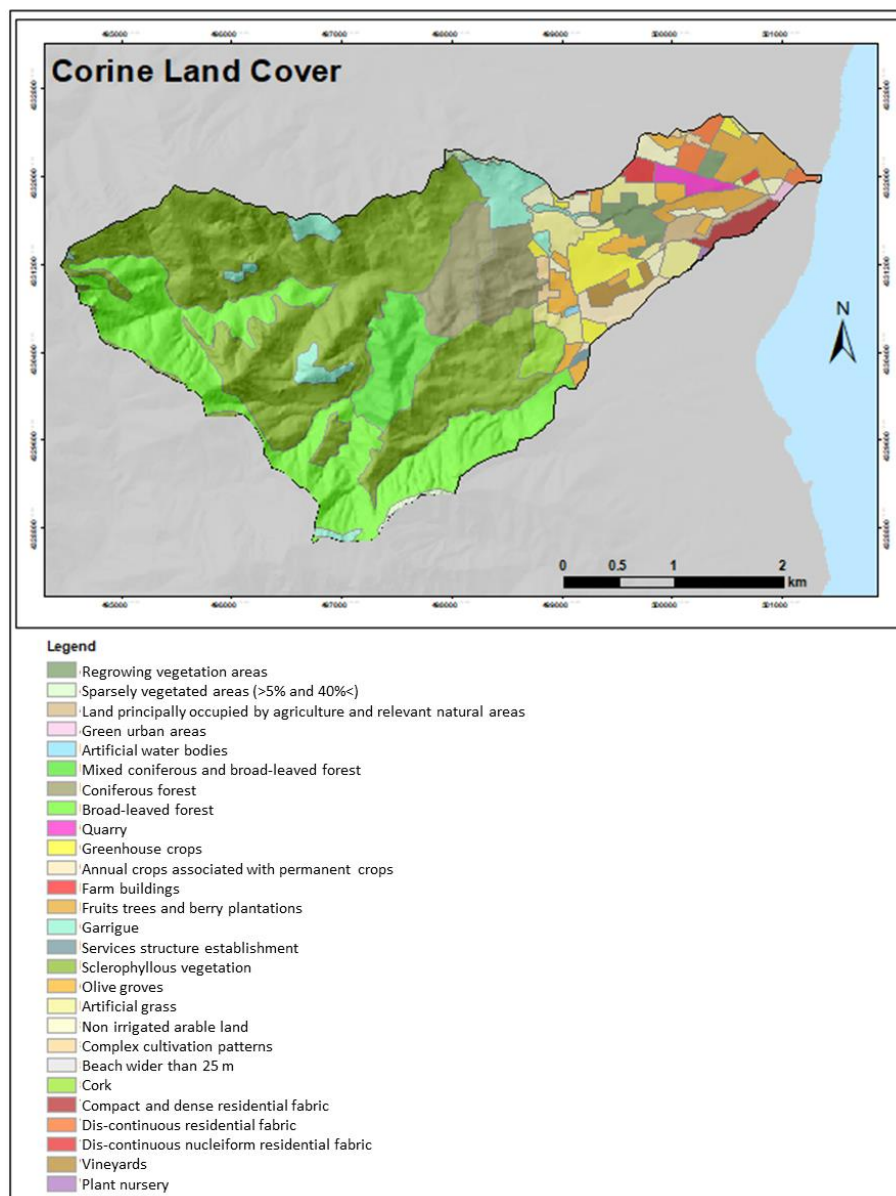


Figure 66 CORINE land cover map in the MORB basin, the legend shows the 27 land cover classes reclassified into the classes of the land cover coefficient in the last column.

Table 40 Classes and values of the land cover coefficient for an aridity index below 25.

Land cover (C_v)	Land cover classes	la < 25
		No vegetation
	Grazing land	0.17
	Cultivation/shrubby	0.07
	Woods/forests	0.03

4.3.7 Permeability Coefficient map

The geological map of Sardinia in vectorial format was used to apply permeability classes to the lithology and generate the permeability coefficient (C_p) Map. The geological formations of the MORB basin were classified according to conceptual and calculated permeability values into the five classes of the permeability coefficient (C_p) (Table 41). The shapefile of the geological units was edited adding a field to the attribute table to assign the C_p value using “Field Calculator” tool. Afterwards, the file was converted from polygon shapefile to raster using the tool “feature to raster” and the field of the C_p to assign the cell values to the raster.

The Capoterra plain has two aquifers (Balía *et al.* 2009) (§3.2.3): A shallow aquifer (10 m-30 m thick) hosted in Holocene alluvial deposits with hydraulic conductivity in the range 1.58×10^{-4} – 2.11×10^{-4} $m s^{-1}$; and a deeper multilayer aquifer (about 100 m thick), partially or locally confined and hosted in alluvial deposit. The hydraulic conductivity is in the range 6.79×10^{-7} – 1.92×10^{-5} $m s^{-1}$.

The class C_p assigned to the Holocene alluvial deposits was “Good” taking into account the permeability of the shallow aquifer of the Capoterra (Balía *et al.* 2009) (Table 42).

The Pleistocene continental deposits (Lithofacies of the Subsistema of Portoscuso) reported permeability values of 1×10^{-6} – 1×10^{-4} $m s^{-1}$. (RESMAR, 2013). Therefore the class of the C_p assigned was “moderate”.

The conceptual values of permeability for fractured igneous and metamorphic rocks is in the range of $10^{-8} < K < 10^{-4}$ $m s^{-1}$ (Freeze and Cherry, 1979), while unfractured igneous and metamorphic rocks have permeability ranging between $10^{-13} < K < 10^{-9}$ $m s^{-1}$. Permeability values in granite in Sardinia have been found in the order of 10^{-8} $m s^{-1}$ in a well in fractured granite in Pula (south-west of Sardinia) and in the order of 10^{-4} $m s^{-1}$ in weathered granite and in microgranite dykes (Barrocu 2007). In this work, the values of hydraulic conductivity in surface were estimated between $10^{-8} < K < 10^{-2}$ $m s^{-1}$ (mean value of 3.5×10^{-3} $m s^{-1}$). Taking into account that the enhanced permeability can be due to a broader aperture in surface weathered granite than in a well and the scope of the permeability coefficient map is to obtain the potential runoff coefficient; the class of C_p assigned to the igneous complex was “Good” (Table 42).

The class of permeability coefficient assigned to the metasedimentary rocks of the Pala Manna Formation is “low”, in accordance with the conceptual permeability of metamorphic rocks.

Table 41 Classes and values of the permeability coefficient for an aridity index below 25.

Permeability Coefficient (C_p)	Permeability classes	K ($m s^{-1}$)	C_p for $I_a < 25$
		Very low	$< 10^{-9}$
	Low	$10^{-9} < K < 10^{-7}$	0.16
	Medium	$10^{-7} < K < 10^{-5}$	0.12
	Good	$10^{-4} < K < 10^{-2}$	0.06
	High	$10^{-2} <$	0.03

Table 42 Geological formations in the MORB basin, classes classified into the classes of the permeability coefficient in the last two columns.

Geological Formation		Age	Permeability class	C _p
Pala Manna Formation. Alternation of metasandstone and metasilstone with cross and plain-parallel lamination.	Syntectonic deposit "culm" type	Lower Carboniferous	low	0.16
Facies Punta de Peis de Pruna (Intrusive Unit of Villacidro). Biotitic leucomonzogranite of medium or medium-fine grain, equigranular to moderately inequigranular, isotropic texture.	Plutonic complex del Sulcis-Arburese	Upper Carboniferous and Permian	low	0.06
Facies S'Arcu Varzia (Intrusive Unit of Santa Barbara). inequigranular and porphyritic grey to pink biotitic-amphibolite micro-granodiorite with monzo granite tendency of medium to coarse grain size.			low	
Facies S'Arriu de Sa Figu (Intrusive Unit of Santa Barbara). Dark grey tonalite-granodiorite, with isotropic micro-granular texture is sometimes markedly porphyritic by phenocrystals.			low	
intermediate to basic dykes of andesitic or basaltic composition	Dyke complex		low	0.06
leucogranitic and hydrothermal dykes mainly of quartz			low	
Lithofacies of the Subsistema of Portoscuso (Sintema Di Portovesme). Alluvial medium to coarse gravel in terraces, with subordinate sand.	Pleistocene continental deposits.	Upper Pleistocene	Medium	0.12
Mount side deposit. Detritus with angular clast, sometimes possibly partially cemented.	Colluvium deposits	Holocene	Good	0.06
Alluvial deposit. Medium to coarse gravel.	Alluvial deposits		Good	0.06
Beach deposits. Sand and gravel, sometimes with mollusc, etc.	Shore sediments		Good	
Anthropic deposit. Landfills and reclaimed land. Holocene	Holocene continental deposits.		Good	0.06

4.3.8 The parametric runoff coefficient (C_k) calculation.

The values of each class of partial coefficients were multiplied by the percentage of surface belonging to the class. Once the classes are weighted with the area, the products were added and divided into 100 to obtain C_a, C_v and C_p. Finally, the sum of the three coefficients is the C_k.

$$C_k = C_a + C_p + C_v$$

The maps of the C_k was done using the "Raster Calculator" adding the three rasters of each coefficient. The average, the minimum and the maximum values of the C_k rasters were taken from the Raster Properties tool, Raster toolset in Data Management toolbox. The C_k was calculated for sub-basins delimited according to the streamflow gauge stations.

The annual runoff coefficient (C_s) should be known in order to evaluate the validity of the physiographic method to calculate the potential annual runoff coefficient. The C_s is the fraction of the average annual precipitation that flows like surface runoff (R_A/P_A). The

estimation of C_s was done for the watersheds delimited in accordance with the flow measurements (4.3.10). However, the measurements were limited to the humid period, because the river remains dry between approximately from May to October. The precipitation data of the period corresponding to the measurement of the streamflow (March 2015-March 2016) was provided only of the meteorological station Capoterra 2.

In an attempt to evaluate the C_s having into account the spatial variation, the areal distribution of precipitation for the period 2015-2016 was evaluated. Given that the precipitation data was punctual it was required to spatialize it to know the mean precipitation of the watersheds. The spatialization of the annual precipitation as function of altitude with linear regression done for different periods and for different stations, showed a good correlation coefficient (§4.3.2). The trend of the different linear regressions have a similar trend (Figure 63), therefore, those relationship between precipitation and elevation are valid for other periods.

The 8th correlation for a period of 22 years (1989-2011) (Figure 63) was taken as the reference of the relationship of precipitation and elevation.

Hence, the equation for the precipitation in the period 2015-2016 was obtained using the equation of the 8th and the punctual data of Capoterra 2 (annual precipitation 489 mm and elevation 165 MASL) for the period 2015-2016

$$y = 0.7194x + 371.199$$

Where y is the precipitation (mm) and x is the elevation (MASL).

The map of the spatial distributed annual precipitation of 2015-2016 was done and the mean values for the watershed were obtained from the statistics of the raster.

The runoff was calculated from the streamflow measurements. However, the streamflow measurements were not continuous and that there is a dry period when the stream flow is zero, the values of the instantaneous streamflow were averaged for the humid period (October-April) and the average streamflow for the dry season was zero. The cumulated runoff was obtained multiplying the average instantaneous discharge for the seconds in a year and divided in the surface of the watershed.

4.3.9 Water balance to MORB basin

The parameters needed to execute a water balance to estimate the efficient infiltration are: precipitation, evapotranspiration and runoff (Equation 28). The P_A the PET_A and their distribution in the basin were calculated from meteorological data as explained above. The mean annual potential runoff (R_{Ap}), in the other hand, was calculated from the P_{Aef} multiplied by the parametric runoff coefficient C_k (Equation 27). The actual runoff coefficient is the relation between the average runoff and the average precipitation ($C_s = \bar{R}/\bar{P}$).

Equation 34

$$R_{Ap} = (P_A - ET_A)C_k$$

$$R_{Ap} = (P_{Aef})C_k$$

Equation 35

$$Ie_{Ap} = P_A - ET_A - R_{Ap}$$

$$Ie_{Ap} = P_{Aef} - R_{Ap}$$

4.3.10 Streamflow measurement

The discharge was measured in several cross-sections mainly in the mainstream in different days when the weather and the stream conditions were favourable. These measurements were done using an electromagnetic flow meter (SEBA, Model 801) applying the midsection method (Rantz *et al.* 1982). Since March of 2015, the discharge was measured in 11 cross-sections along the river to have a regular record of a hydrological year (Figure 67). The flow measure was limited by the low precipitation therefore low streamflow, the instrument depth measuring limit of 4 cm, and the torrential regime of the stream. The river has been dry or with very low flow even during the rainy seasons.

The electromagnetic flowmeter measuring is based on the Faraday principle. A conductive fluid that crosses a magnetic field produces an electromagnetic field proportional to the fluid velocity. The flow sensor is cylindrical; it has two electromagnetic coils that generate a magnetic field and two electrodes on opposing sides that detect the voltage generated by the fluid all of this protected by isolating materials (Figure 68). The water sensed around the sensor is a spherical volume of about 120mm diameter. The sensor is supported by a wading road positioned on the stream bed (Figure 68 and Figure 70). The wading measurements usually are more accurate than those took from a cable or a bridge. The sensor takes two measurements per second and calculates the average. The minimum period of a measurement is 30 seconds. The computer of the equipment calculates the average flow velocity and the standard deviation. The measurements with the electromagnetic flowmeter are punctual. Therefore several velocities should be measured in the cross-section of the stream.

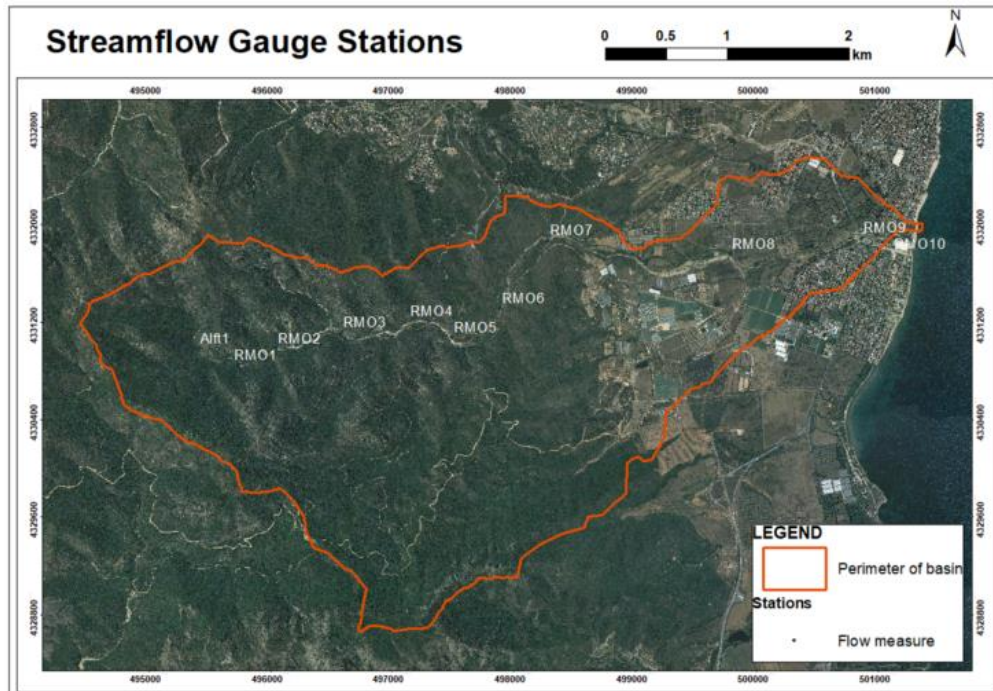


Figure 67 Map of the stations where the streamflow was measured.

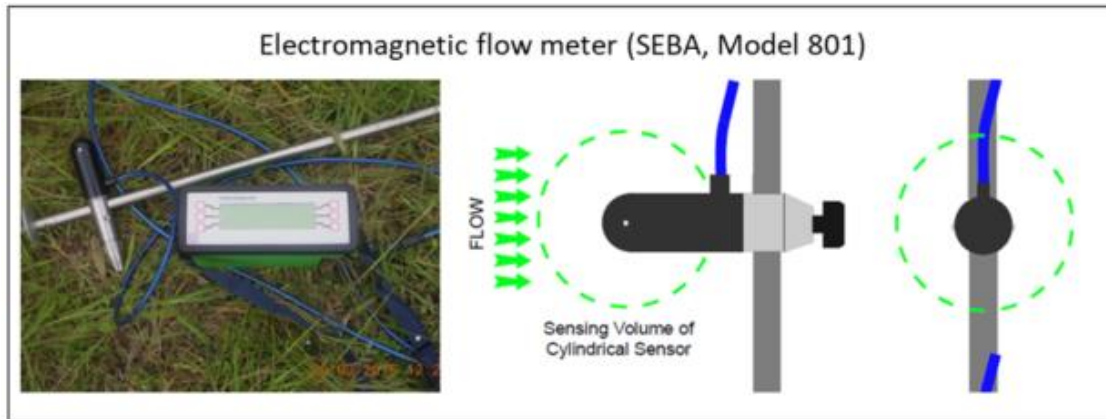


Figure 68 Electromagnetic flowmeter (SEBA, model 801), sensor, wading rod and computer. Position and volume of water sensed by the flowsens.

The calculation of streamflow at a cross section was done using the mid-section method (Figure 69). It consists on divided the stream cross sections in minor areas in which the measured punctual velocity is assumed to be uniform. The flow is calculated for each cell multiplying the area and the velocity and finally the partial flows are added. A field form to record the stream bed and the flow parameters were designed, and an excel sheet to calculate the streamflow in office .

The flow-measurement equipment required includes (1) flowmeter, (2) top-setting wading rod, and (3) Tape measure or tagline, (4) and a field form to record the width, depth, velocity and standard deviation (Figure 70).

1. The steps followed in field and office to measure the streamflow are summarised below:
2. Select a cross section across the total width of the stream. The flow should be uniform and free of eddies, dead water near banks, and excessive turbulence.
3. Measure the width (W) of the stream by stringing a measuring tape from bank to bank at right angles to the direction of flow.
4. Determine the spacing or width (w_i) of the verticals. Space the verticals so that no subsection has more than 10 % of the total discharge. Each vertical is measured at a partial width W_i of the stream.
5. If the stream width is less than 1,5 m or 5 ft, use vertical spacing widths of 0,15 m (15 cm) or 0.5 ft.
6. If the stream width is greater than 1,5 m or 5 ft, the minimum number of verticals is 10 to 25. The preferred number of verticals is 20 to 30.
7. Measure the depth at each vertical or where the streambed seems to change form draw the profile of the streambed.
8. Reconsider the width of the cells if necessary and determine the mid-point of the cross section's cells.
9. For uniform cross sections, if the total width W m has n cross sections, then each cross section width is equal to $W/n = w$. The mid-point of each cross section is equal to $w/2$. The first mid-point is equal to $w/2$, and each consecutive measure point in the width of the stream can be calculated adding $w/2$ to the previous mid-point. Otherwise, for irregular cross sections of width w_i the midpoint of the first interval is $w_1/2$ and the next ones are $W_i + w_{i+1}/2$, it is convenient to draw the verticals and the mid-points in the profile.

10. Determine the correct depth position of the sensor at each mid-point. The total depth can be measured with the depth gauge rod or a rigid meter. The sensor should be set at 20%, 60% and 80% of the total depth.
11. If the depth is less than 0,8 m or 2.5 ft, → one measurement at 60% of the depth is required at each measurement section.
12. If the depth is greater than 0,8 m or 2.5 ft → two measurements should be taken at 20% and 80% of the total depth.
13. Measure the velocity. The wading rod should be kept vertical, and the flow sensor kept perpendicular to the tape rather than perpendicular to the flow while measuring velocity with an electronic flowmeter.
14. Calculate the flow using the midsection method. Compute the discharge in each increment by multiplying the averaged velocity or single velocity in streams less than 0,8 m (2.5 ft.) deep in each increment by the increment width and averaged depth. The edge of the stream have a depth and velocity of zero, and near them there is zero or negative flow. The discharges of each increment have to be added, except those with the negative flow, to compute the total stream discharge (Figure 69).

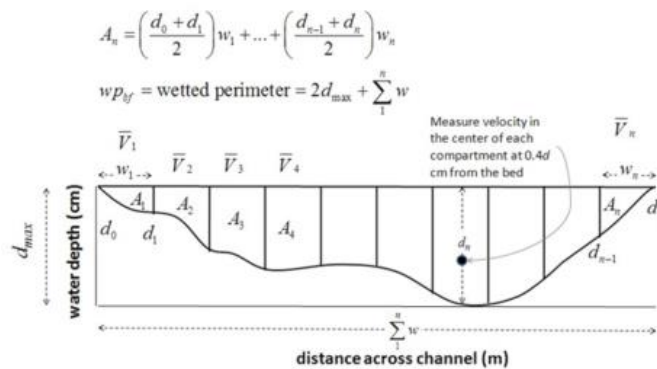


Figure 69 Midsection method of calculation of streamflow in a cross section from punctual measurements.

Measuring Stream Flow



Measure width of the stream ,
Determine the spacing or width of the
verticals



Measure the depth at each vertical,
and determine the mid point and
depth of sensor



Measure the velocity holding the wading rod vertical, and the flow sensor kept
perpendicular to the tape



Figure 70 General step of the flow measurement with the electromagnetic flowmeter in the field.

5 RESULT

5.1 PERMEABILITY IN GRANITIC WATERSHED

During the field survey, 332 fractures were measured in 11 stations along the basin, and 945 lineaments were digitized from the stereo pairs.

Sets of fractures

Figure 71 shows the pole, great circles and rose diagrams (for a strike and dip direction) in Stereonet for all the fractures measured in the field. The pole diagram shows two main groups of fractures. One group is of subhorizontal fractures without a preferred dip direction and the second tendency are sub-vertical fractures with variable dip direction.

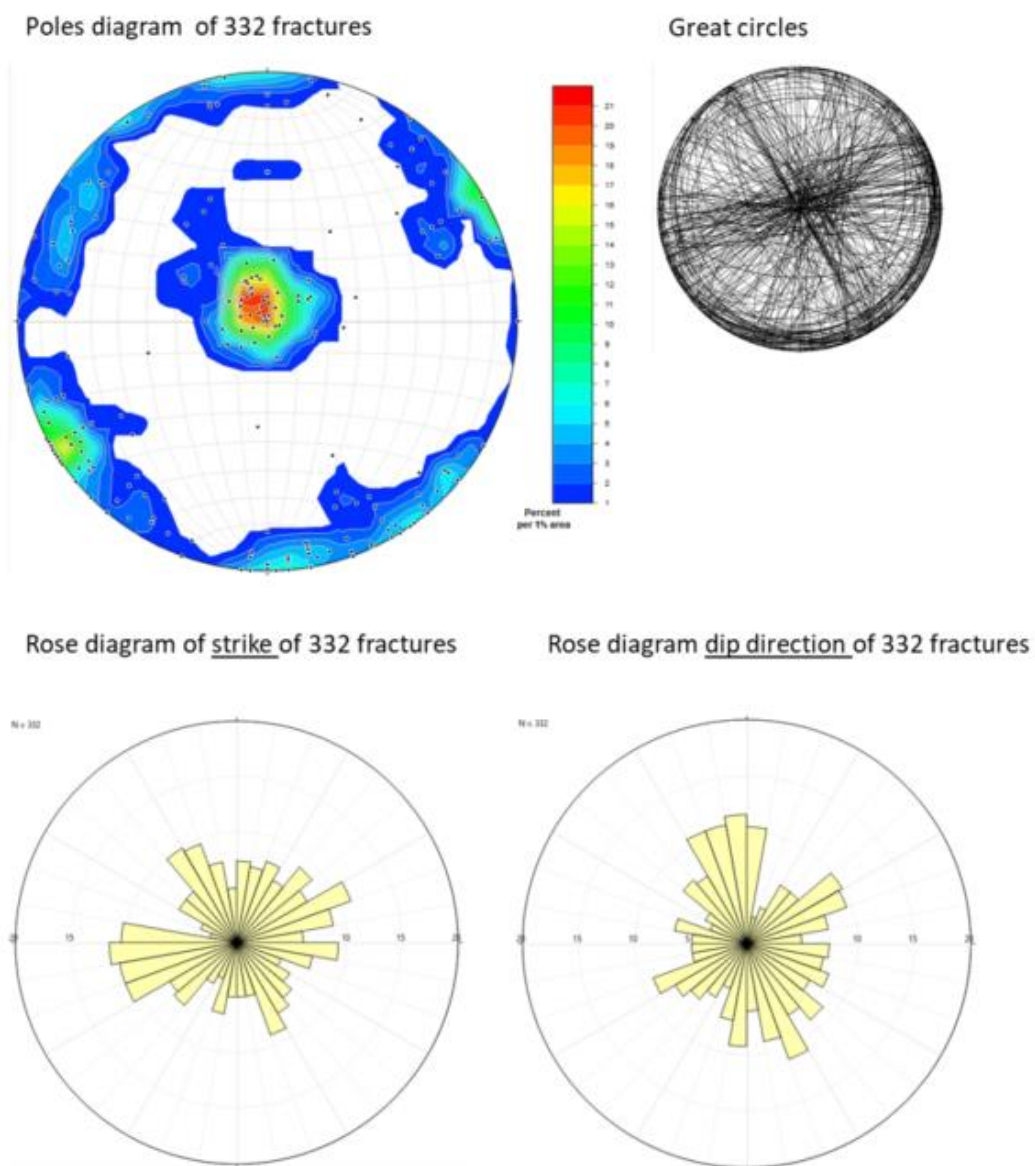


Figure 71 Pole diagram, great circle diagram and rose diagram of strike direction and dip direction for 332 fractures measured in the field.

Figure 72 *a* and *b* show the frequency distribution of the strike direction and dip angle for 332 fractures measured in the field. The distribution of the strike direction is polymodal. The interval between 240° to 270° (17%), the interval between 315° to 330° (8%), and the interval between 45° and 90° (18%) are the most common strike directions. The frequency distribution of the dip angle shows that 60% of the fractures have high dip angles (70°-90°) and 20% have low dip angle (0°-20°). There are not many oblique fractures.

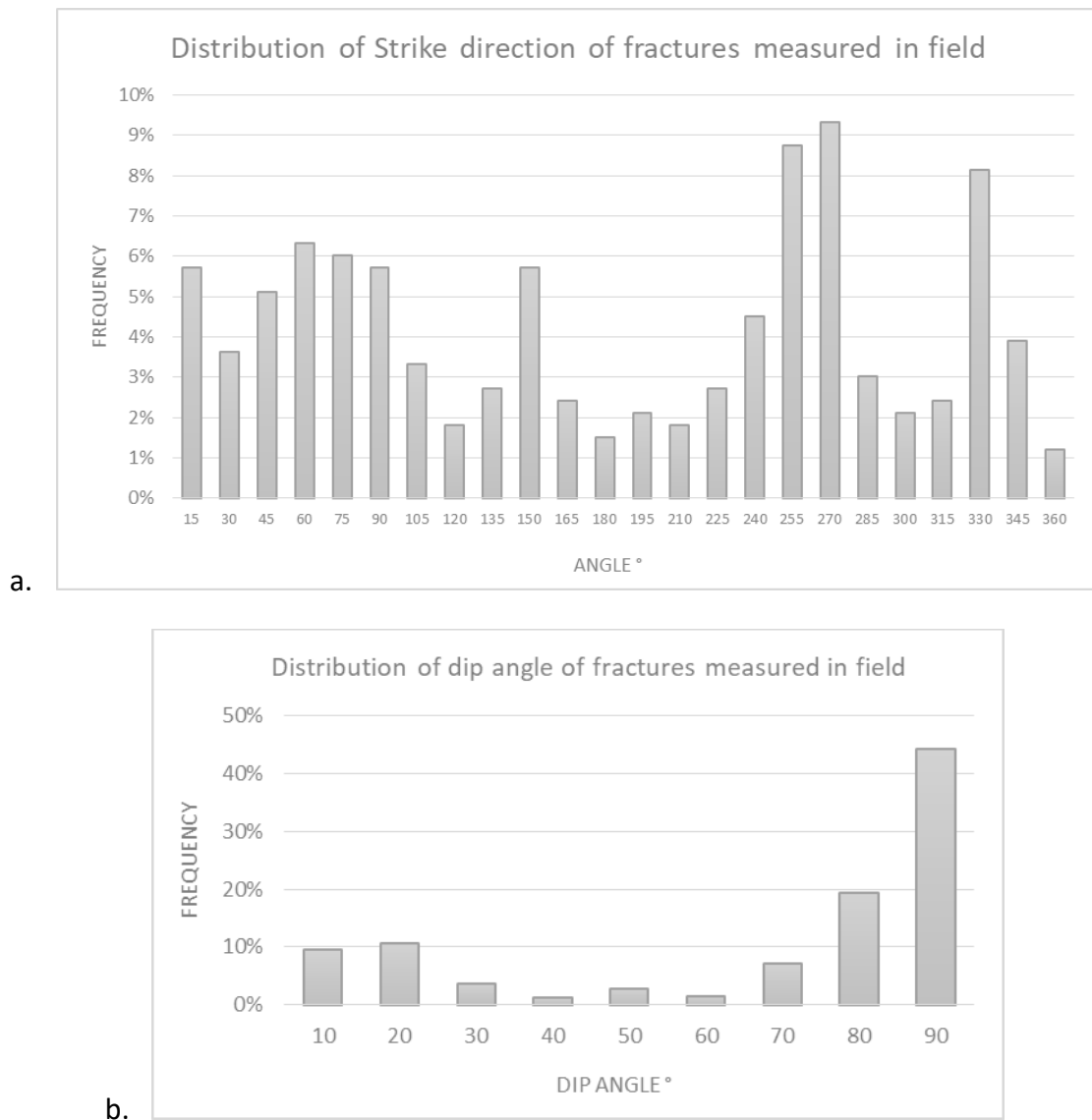
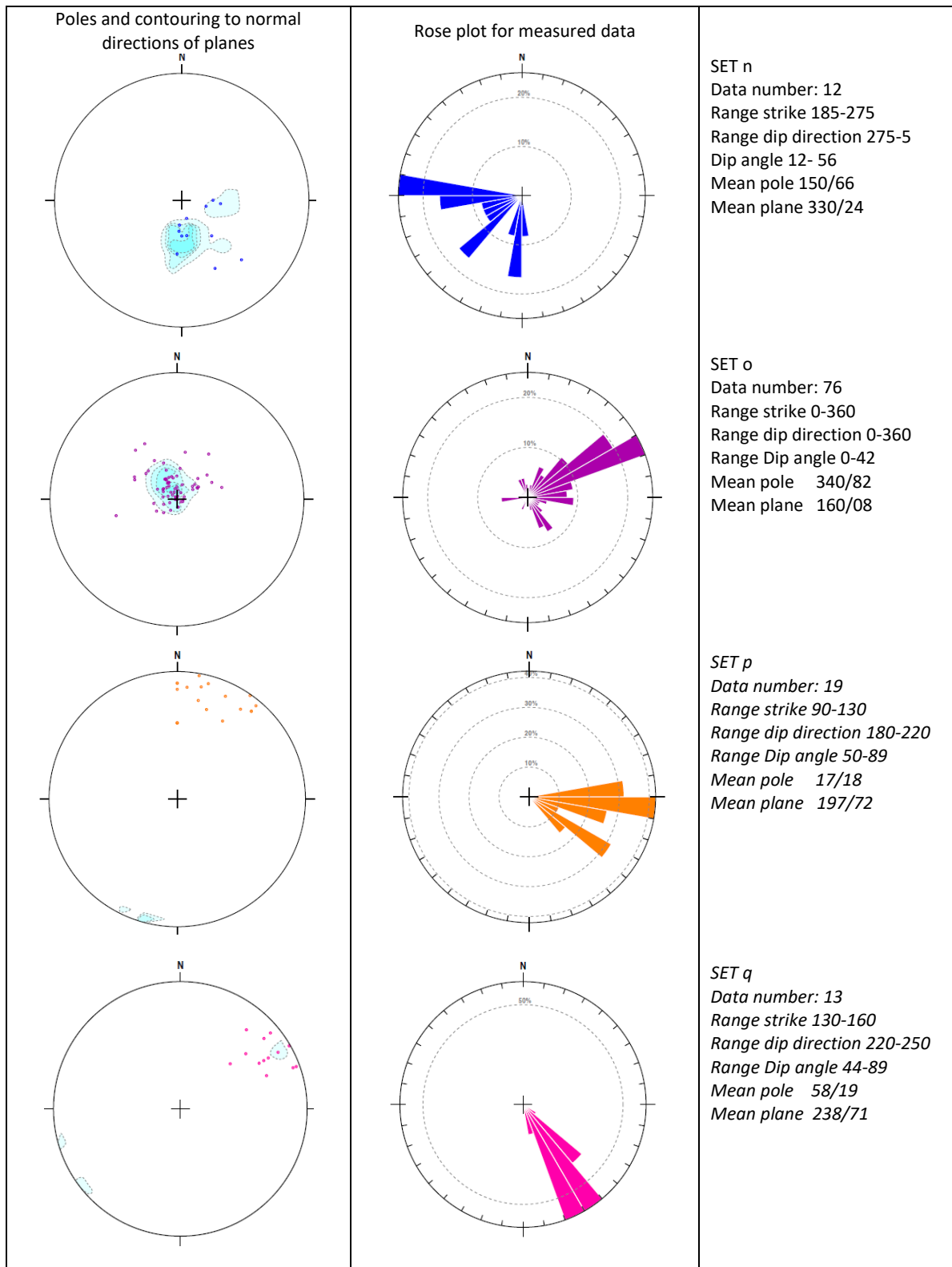
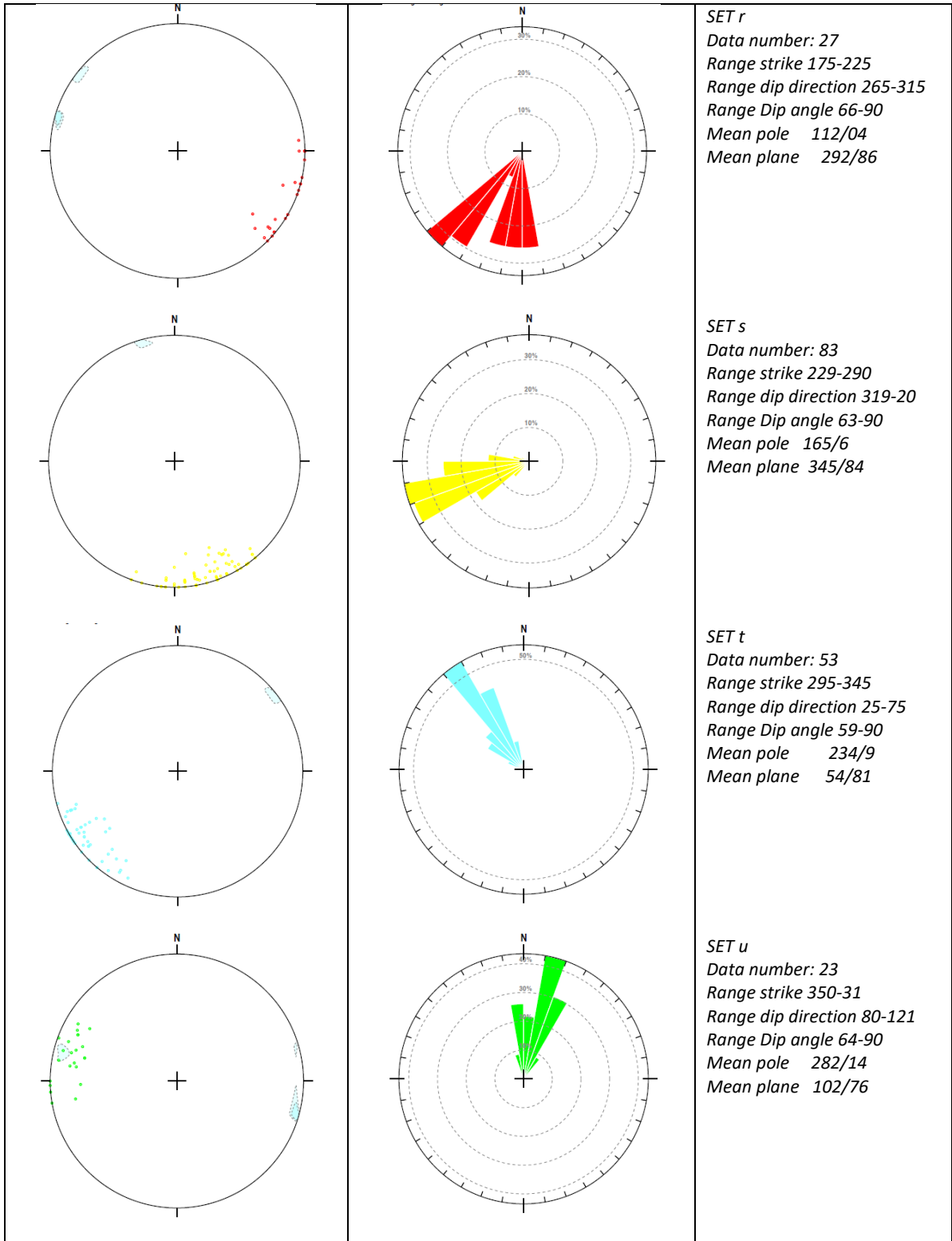


Figure 72 Frequency distribution graphs of (a) strike and (b) dip angle for 332 fractures measured in the field.

Figure 73 shows the pole diagram and rose diagram for nine identified sets of fractures. The identification of sets of fractures has been carried out by SG2PS software. The number of fractures; the range of the strike, dip direction and dip; and the mean pole and mean plane are recorded in the last column of Figure 73. Figure 74 shows the poles to all the fractures and the mean poles and the Fisher statistics (§2.2.3) for the sets. The table in Figure 74 shows the trend and plunge, the confidence intervals (α_{95} is a_{95} and α_{95} is a_{99}), the precision parameter κ and the length of the mean vector associated to the mean pole. The α_{95} is small for sets o, s and t (2, 6 and 7 in the table) and high n, p and q (1, 3 and 4 in the table). κ is higher than ten for all the sets.





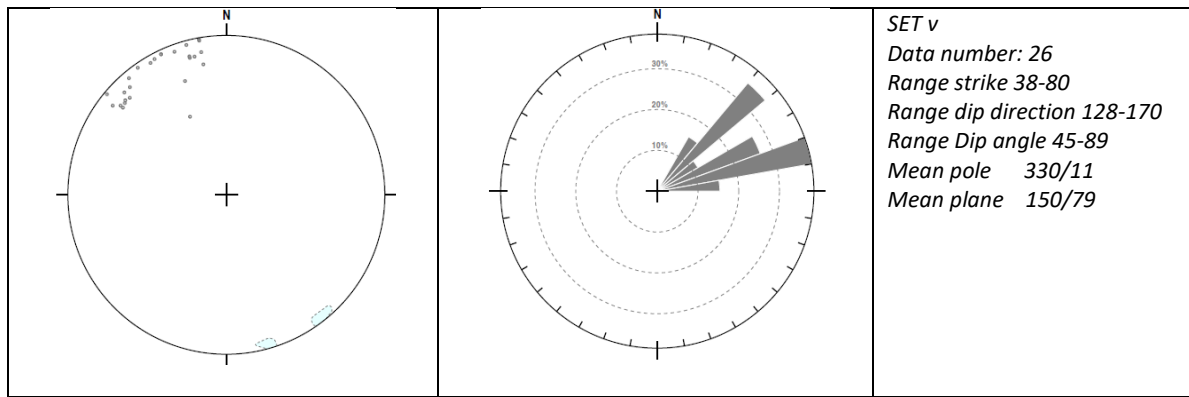


Figure 73 Pole and rose diagram of sets of fractures defined and plotted by SG2PS (Sasvári & Baharev, 2014).

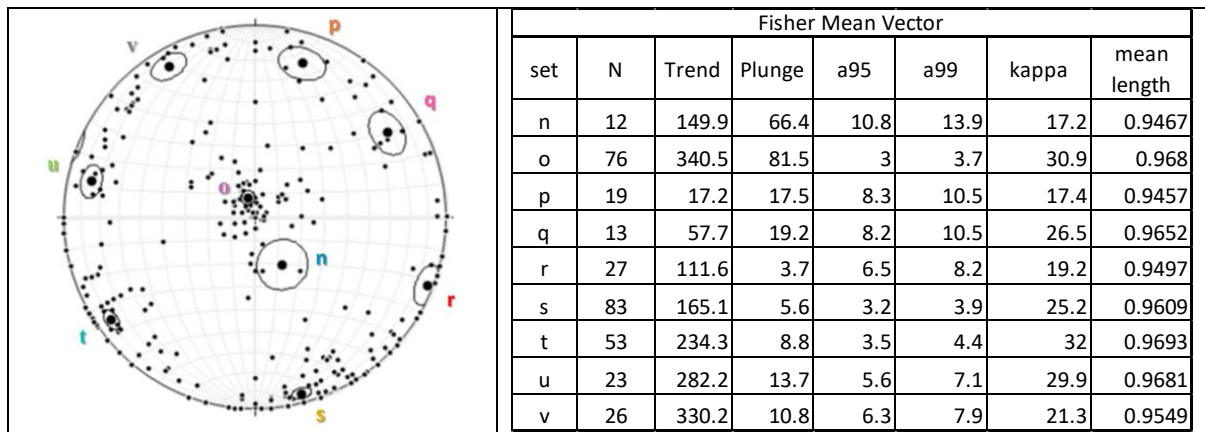


Figure 74 Pole diagram of 332 fractures measured in the field and mean poles for the sets separated by SG2PS software.

The range of the strike, dip direction and dip; the attitude of the mean plane; the number of observations and the frequency of the sets of fractures are represented in Table 43.

Two sets (*n* and *o*) have dip angle between 0° and 56°, the other seven (*p*, *q*, *r*, *s*, *t*, *u* and *v*) sets have dip angles between 44° and 90°. Three main sets of joints were recognized in the field data corresponding to two sub-vertical sets, *s* (strike and dip 255°/84°) and *t* (strike and dip 324°/81°), and one sub horizontal set *o* (strike and dip 70°/8°) (Figure 73 and Table 43).

Table 43 Set of discontinuities measured in the field and their average parameters.

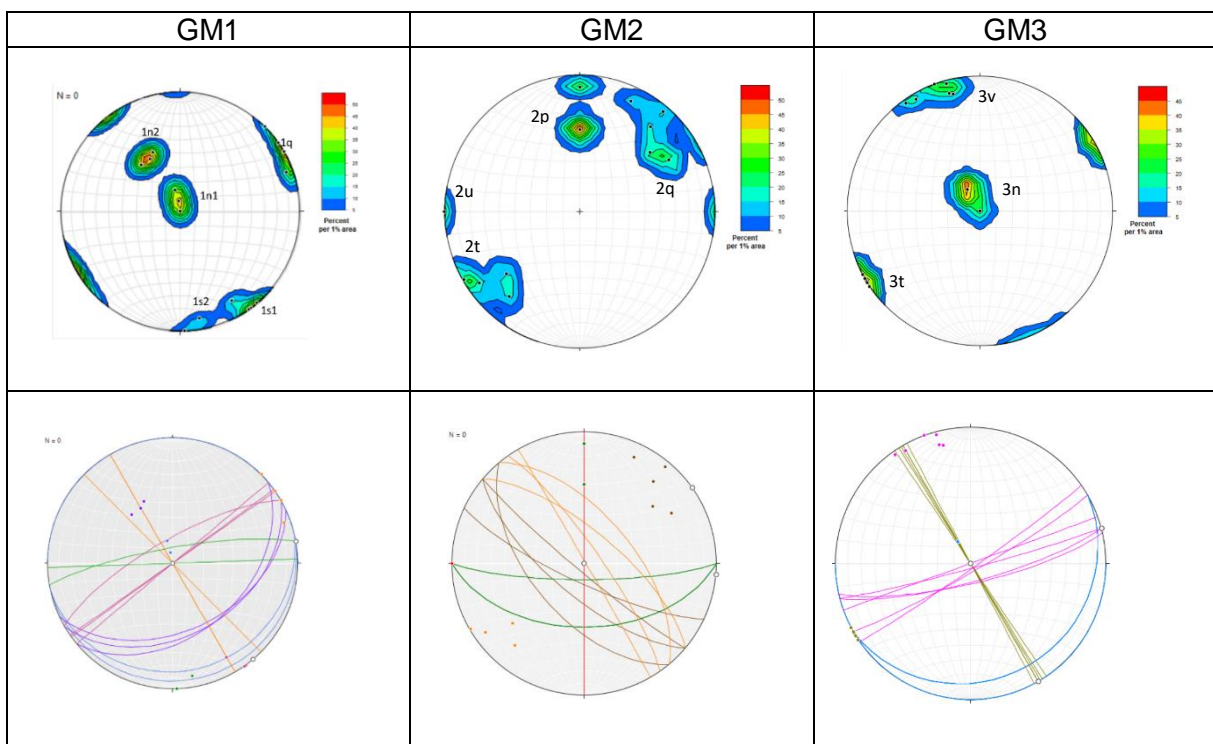
Set		n	o	p	q	r	s	t	u	v
		Dip <56°			Dip 44°-90°					
RANGE	strike °	185-275	0-360	90-130	130-160	175-225	229-290	295-345	350-31	38-80
	Dip direction °	5-275	0-360	180-220	220-250	265-315	319-20	25-75	80-121	128-170
	Dip °	12-56	0-42	50-89	44-89	66-90	63-90	59-90	64-90	45-89
Mean plane	Strike °	240	70	107	148	202	255	324	12	60
	Dip direction °	330	160	197	238	292	345	54	102	150
	Dip °	24	8	72	71	86	84	81	76	79
Number of discontinuities		12	76	19	13	27	83	53	23	26
% of total number		4	23	6	4	8	25	16	7	8

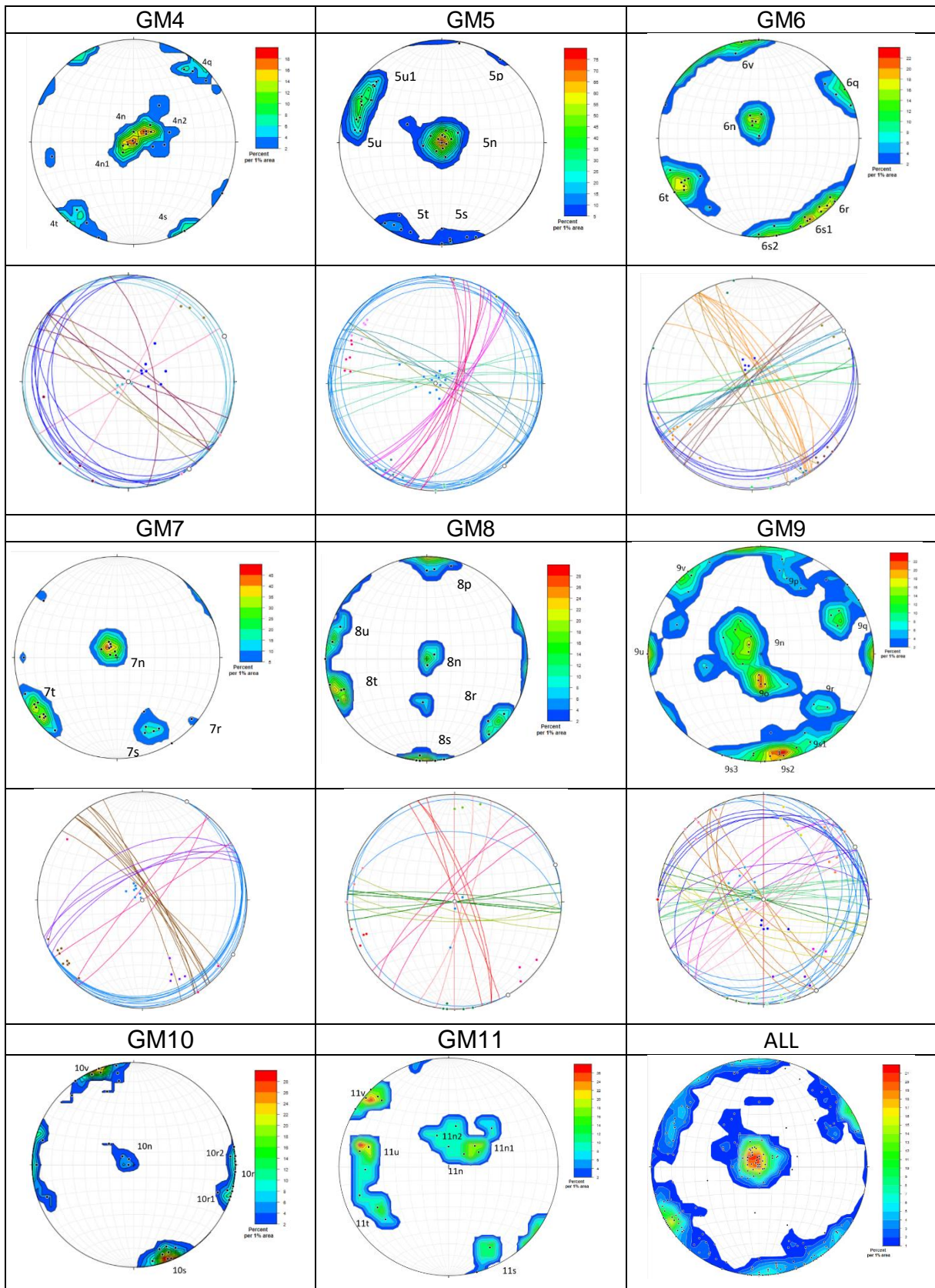
Figure 75 shows the pole and great circle diagrams on the equal-area projection for fractures of 11 geomechanical stations. The sets of fractures identified are evidenced on the pole diagrams with their names and are distinguished by colours in the great circle diagrams. The sets at each station were named with the number of the station and the letter of the main set individualised for the whole data (Table 43). Identifying unimodal tendencies at each outcrop often showed two concentrations of poles inside a single set of fractures defined for the whole data. The distinction of sets at each outcrop, then, was more detailed.

The stereonet diagrams show that all the stations, but station GM2, have one or two sub horizontal sets of fractures. The sub-vertical sets are always present (two sets in GM3 to eight sets in GM9). Sets with an oblique dip angle are rare, station GM1, GM8 and GM9 have one. The sub-vertical sets do not show an apparent uniform tendency among stations. However, most of the stations (GM1, GM3, GM4, GM6, GM7, GM9 and GM11) have one set trending NW-SE and one set trending NE-SW, almost orthogonal between them. Stations GM1, GM2, GM5, GM6, GM8 and GM9, have one set representing E-W trending. Stations GM2, GM5, GM8, GM9, GM10 and GM11 have one set trending N-S.

Stations GM1 and GM2 are separated 23 m and only have in common one sub-vertical set trending NW-SE. Station GM9 is located 50 m to the west of a fault zone, trending NW-SE, and is the station with higher fracture density and number of sets.

The mean poles and mean planes for each set of fractures are shown in Table 44. The information reported in table is: the number (n) and name of the sets, the sample size (N), the attitude of the mean pole (trend and plunge) and of the mean plane (strike, dip direction and dip); the range of strike, dip direction and dip for each set of fractures at each station. The colours correspond to the colour of the circles, the sets with low dip angle are always in blue.





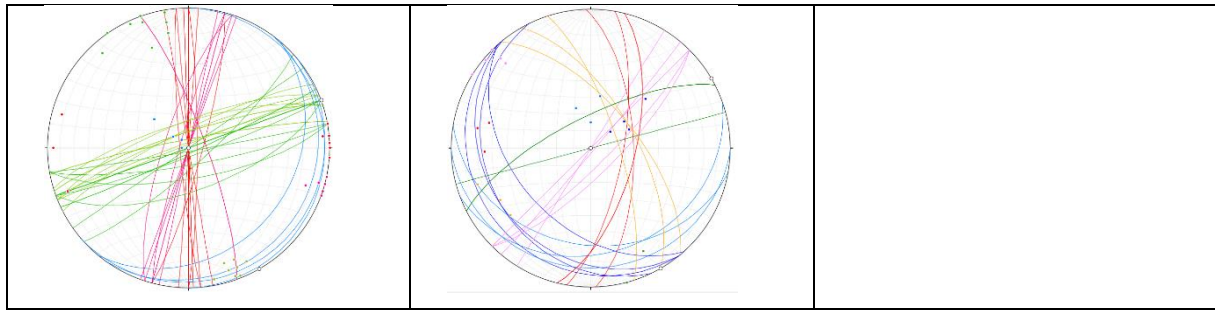


Figure 75 Stereonet equal-area projection of great circles and poles for joints of 11 station. On the pole diagram, it is plotted the contours with an interval of 1% with Terzaghi corrected intensity.

Table 44 Set of discontinuities in each station and their mean poles and planes; and range of dip direction and dip.

n	Set	N	Trend	Plunge	Strike °	Dip direction°	Dip°	Range strike °	Range dip direction °	Range dip °
GM1										
1	1q	5	58	1.2	148	238	89	135-160	225-250	84-90
2	1s1	4	145	3.7	235	325	86	230-240	320-330	75-90
3	1n	3	348	82.7	78	168	7	77-90	167-180	0-15
4	1n2	3	329	47.2	59	149	43	50-65	140-155	42-45
5	1s2	2	174	5	264	354	85	260-268	350-358	80-90
		17								
GM2										
1	2q	5	42.5	19.4	132.5	222.5	70.6	115-150	205-240	57-85
2	2p	5	0	28.1	90	180	61.9	90	180	50-80
3	2t	4	231.5	15.4	321.5	51.5	74.6	310-330	40-60	60-80
4	2u	1	270	0	0	90	90	0	90	90
		15								
GM3										
1	3n	7	330	79.3	60	150	10.7	60-90	150-180	0-15
2	3v	6	338.6	5.7	68.6	158.6	84.3	55-77	145-167	78-90
3	3t	6	239.2	0	329.2	59.2	90	326-332	56-62	90
		19								
GM4										
1	4n2	8	64.1	70.7	154.1	244.1	19.3	125-194	215-284	12-36
2	4n1	7	254.4	87	344.4	74.4	3	50-90-210-340	45-7-140-300	1-12
3	4q	6	220.9	8.1	310.9	40.9	81.9	290-350	20-80	70-90
4	4s	3	140.1	0	230.1	320.1	90	210-240	300-330	90
5	4t	3	41.7	11.4	131.7	221.7	78.6	125-140	215-230	75-82
		27								
GM5										
1	5n	16	316.8	87.9	46.8	136.8	2.1	28-357	30-360	0-15
2	5v	7	287.9	16.3	17.9	107.9	73.7	08-27	98-117	69-77
3	5s	6	172.5	5.9	262.5	352.5	84.1	250-270	340-360	73-86
4	5u	5	306.8	15.3	36.8	126.8	74.7	30-43	120-133	69-79
5	5t	5	207.8	9.2	297.8	27.8	80.8	289-305	25-35	71-86
6	5p	2	22.5	1.5	112.5	202.5	88.5	100-125	190-215	88-89
		41								
GM6										
1	6t	9	236.9	13.9	326.9	56.9	76.1	305-340	35-70	59-90
2	6n	6	348	76.5	78	168	13.5	65-105	155-195	2-20
3	6r	6	134	4.5	224	314	85.5	220-230	310-320	81-89
4	6s1	5	151.6	4	241.6	331.6	86	238-245	328-335	81-89
5	6s2	4	172.5	3.5	262.5	352.5	86.5	260-270	350-360	79-90
6	6q	4	60.1	7.8	150.1	240.1	82.2	140-160	230-250	75-89
7	6v	2	329	5.2	59	149	84.8	75-80	165-170	78-89
		36								
GM7										
1	7t	11	234.5	8.4	324.5	54.5	81.6	310-330	40-68	78-86
2	7n	10	323.8	80.6	53.8	143.8	9.4	20-70	110-160	2-4
3	7s	5	155.2	25.8	245.2	335.2	64.2	240-250	330-340	50-70
4	7r	3	149.7	15.2	239.7	329.7	74.8	38-238	128-238	80-90
		29								
GM8										
1	8s	9	180.6	0.7	271	0.6	89.3	260-276	355-04	84-90

2	8t	4	250	7.5	340	70	82.5	335-345	65-75	76-89
3	8p	3	6.7	11.7	96.7	186.7	78.3	90-105	180-195	75-83
4	8u	3	279.9	5.4	9.9	99.9	84.6	0-20	90-110	80-90
5	8r	3	133.3	8.7	223	313.3	81.3	215-230	305-320	75-86
6	8n	3	173.9	77.9	263	353.3	12.1	151-275	005-355	5-35
		25								
GM9										
1	9s2	12	172.8	5.5	262.8	352.8	84.5	250-274	358-04	82-90
2	9n	9	291.2	71.1	21.2	111.2	18.9	10-360	60-152	9-41
3	9q	6	56.2	15	146.2	236.2	75	130-159	220-249	61-90
4	9v	5	319.2	4.8	49.2	139.2	85.2	42-62	132-150	75-90
5	9o	5	169.7	68.6	259.7	349.7	21.4	230-275	320-05	16-30
6	9p	4	17.7	22.7	107.7	197.7	67.3	102-120	192-210	60-70
7	9u	3	270	0	0	90	90	0	90	90
8	9s1	3	158.6	17.9	248.6	338.6	72.1	242-263	332-353	63-82
9	9s3	3	194.3	0	284.3	14.3	90	278-290	8-20	90-90
10	9r	2	132.4	29	222.4	312.4	61	220-225	310-315	56-60
		52								
GM10										
1	10v	16	338.9	4.8	68.9	158.9	85.2	48-80	138-170	65-90
2	10s	10	161.2	8.2	251.2	341.2	81.8	243-259	333-349	75-87
3	10r1	9	118.3	7	208.3	298.3	83	192-200-340	70-282-290	76-90
4	10r2	8	81.9	4.4	171.9	261.9	85.6	170-184-0-15	90-105-260-274	82-90
5	10n	4	307.1	78.5	37.1	127.1	11.5	0-50	90-140	4-26
		47								
GM11										
1	11v	5	311.4	5.4	41.4	131	84.6	32-243	122-333	75-90
2	11u	4	279	24.1	9	99	65.9	358-14	88-104	64-71
3	11n1	4	52.7	62.9	142.7	232.7	27.1	138-154	228-244	15-44
4	11n2	3	357.3	66.9	87.3	177.3	23.1	70-100	160-190	15-31
5	11t	3	240.9	22.9	330.9	60.9	67.1	320-342	50-72	64-74
6	11s	3	157.1	12.1	247.1	337.1	77.9	243-255	333-345	72-90
		22								

5.1.1 Sets of Lineaments

The digital photogrammetry allowed to digitise 945 lineaments (Figure 76) in the granitic and metamorphic rocks in the mountainous area of MORB and a neighbouring area to the west and south-east.

Figure 77b shows the lineament's length histogram. Three main trends were recognised in the lineaments corresponding to sets A (azimuth interval 315°-340°), B (azimuth interval 45°-75°) and C (azimuth interval 75°-90°, 270°-290°) (Figure 77a and Table 45). The lengths measured were between 5 m and 2270 m and had a lognormal distribution.

Table 45 shows the lineaments classified in six sets with the information regarding their strike interval, number of observations, cumulative length and frequency respect to the total number of lineaments. The density calculated dividing the number of lineament of each set over the area of the map and the density dividing the cumulative length of each set over the area of the map are also recorded in Table 45. The last row shows the sets of sub-vertical fractures (from Table 43) that have a similar strike.

Figure 78 shows the density of lineaments in terms of a number of lineaments in the area of the map and terms of length over the area. Set A has the highest frequency in terms of number of lineaments (28%) followed by set B (23%) and Set C (19%). However, the frequency in term of length for sets A and B (27%) and lower for set C (21%). Set A has the highest density in terms of number of lineaments in the area of the map (11.5 n/km²) followed by set B (9.7 n/km²) and Set C (7.9 n/km²). However, the density in terms of length over the area is the same for sets A and B (3.16 km/km²) and lower for set C (2.48 km/km²).

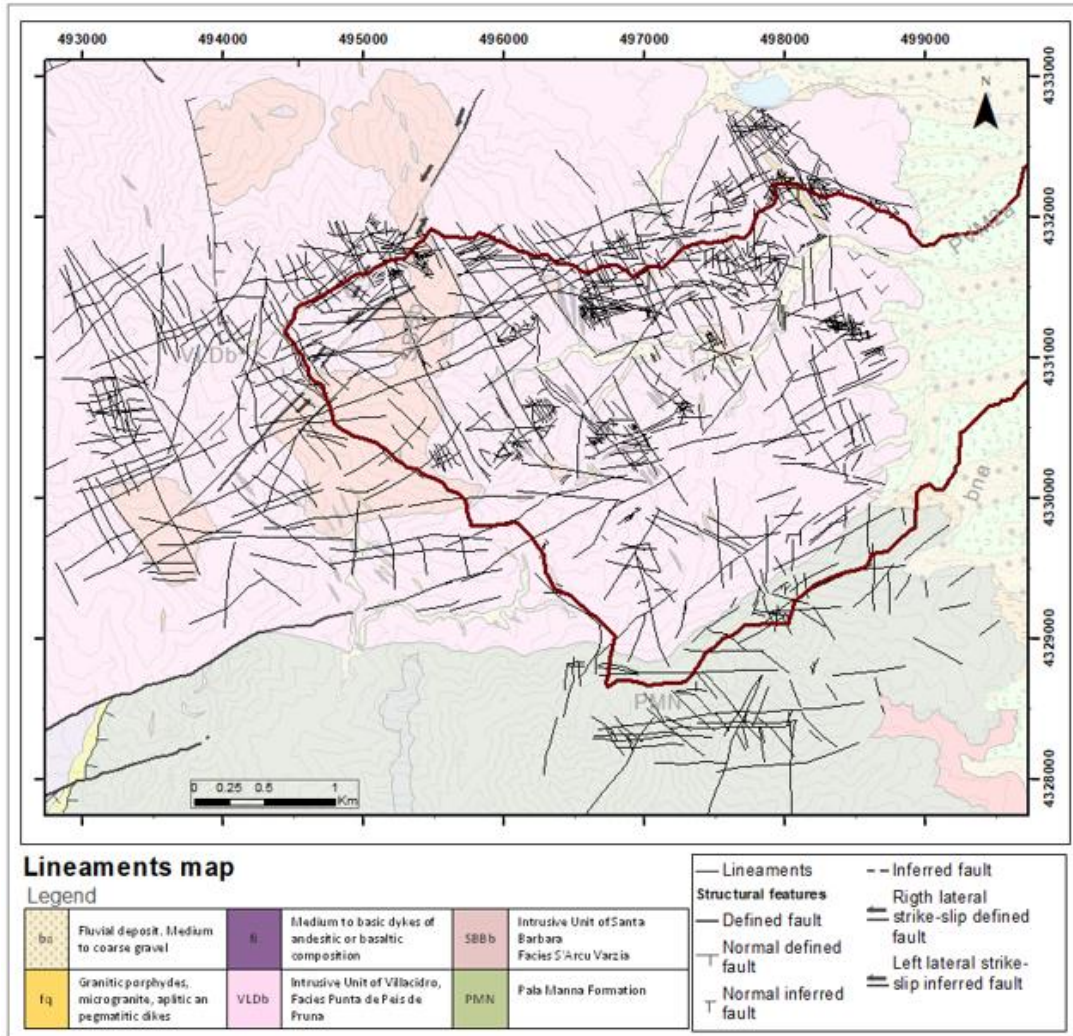


Figure 76 Map of lineaments

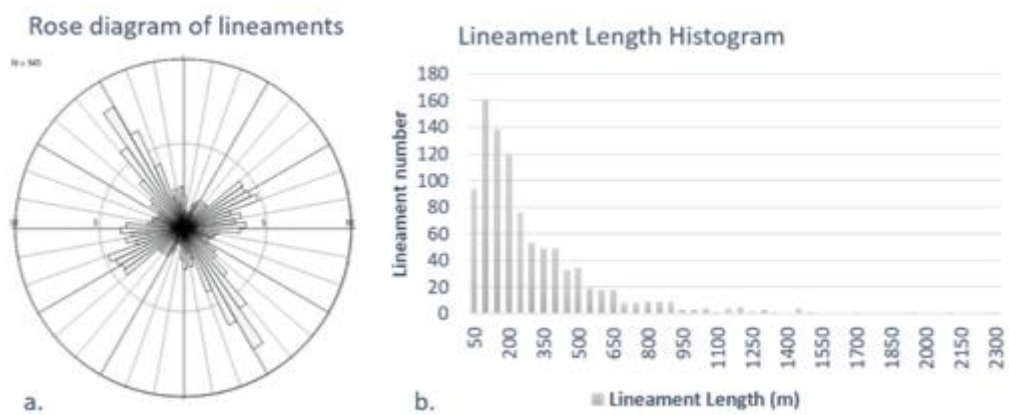


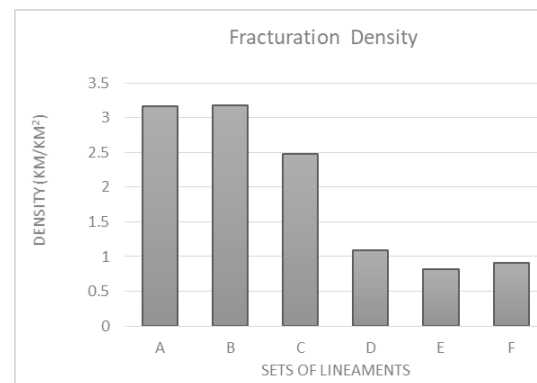
Figure 77 a. Rose diagram for the 945 lineaments collected from the stereo pairs. b. Histogram of the lineament length distribution.

Table 45 Azimuth interval of the identified trends of the lineaments. The numbers in bold are the highest values, and the numbers underlined are the second highest values.

Set	A	B	C	D	E	F
Strike interval °	315°-340°	45°-75°	75°-110	340°-10°	290°-315°	15°-45°
Width of Interval	25°	30°	35°	30°	25°	30°
Number of lineaments	261	220	181	105	91	87
% of total <u>number</u>	28	<u>23</u>	19	11	10	9
Density (number/area km ²)	11.5	<u>9.7</u>	8.0	4.634959	4.016965	3.840395
Cumulative length (m)	71715	72002	56087	24581	18568	20534
% of total <u>length</u>	27	27	<u>21</u>	9	7	8
Cumulative (length km /area km ²)	3.2	3.2	<u>2.5</u>	1.1	0.8	0.9
Correspondence with fracture sets from field	q and t	s and v	p, s and v	r and u	p and t	u and v



a.



b.

Figure 78 Density of lineaments regarding (a) number of lineaments in the area of the map and (b) terms of length over area

The lineaments length distribution analysed by sets and the mode, median and mean values are shown in Figure 79 and Table 46. Lineaments of sets B and C have the highest mean length values (312 m and 320 m respectively). The mode for all sets is between 50 and 200m. The sets with higher mode values are C (150-200m) and D (100-200m), and the lowest mode belongs to set E (0-50m) The lineaments length analysed by sets showed lognormal distribution (A, B, C, E); set D has a bimodal distribution and set E has a negative exponential distribution. The sets with a broader distribution are A, B and C. These sets have approximately the 85% of the lineaments below 600m. While sets D, E and F have the 85% of the lineaments below 450m.

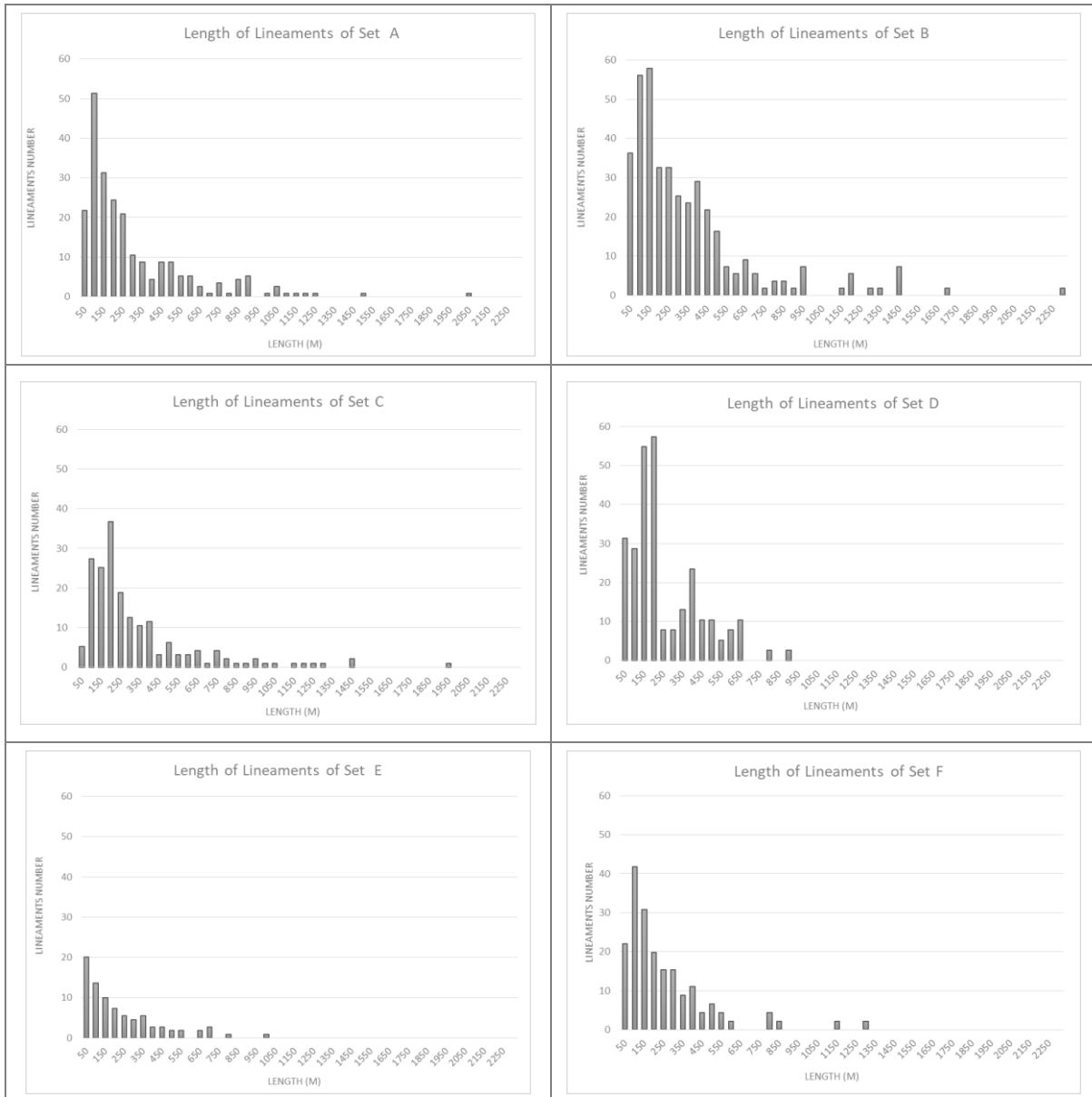


Figure 79 Distribution of length for each set of lineaments.

Table 46 Mode, median and mean length (m) for each set lineaments.

Set	Set A	Set B	Set C	Set D	Set E	Set F
Strike interval °	315°-340°	45°-75°	75°-110	340°-10°	290°-315°	15°-45°
Mode interval (m)	50-100	50-150	150-200	100-200	0-50	50-100
Median (m)	205	291	<u>276</u>	187	215	216
Mean (m)	267	<u>312</u>	320	246	224	250

Figure 80 shows the lineaments in a peripheral area of 500 m of radius around each geomechanical station. Table 47 shows the number of lineaments of each set and the frequency respect to the total number inside the circles of Figure 80 for each buffer around the geomechanical stations.

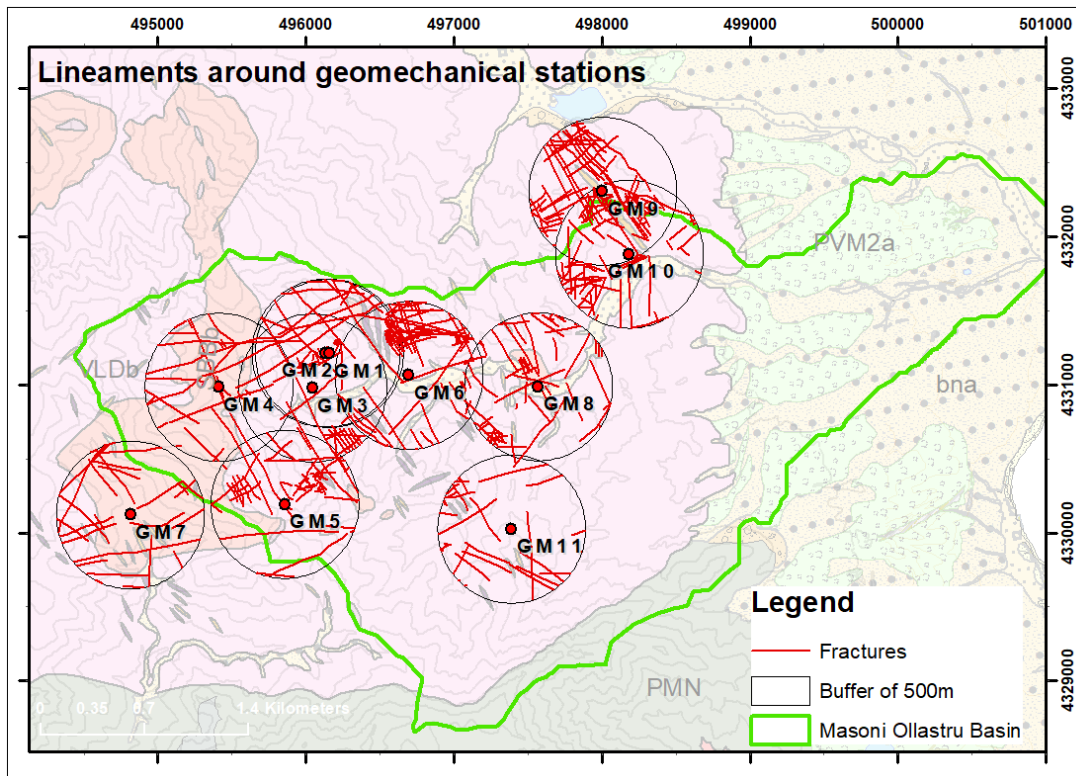


Figure 80 Map of lineaments in a radius of 500 m around the geomechanical stations.

Table 47 Frequency of set of lineaments in a radius of 500m around each station. The frequencies in bold are the highest for each peripheral area, and the underlined values are the second more frequent. The set A is the most frequent for eight stations; followed in order by set B and set C.

Set lin	A	B	C	D	E	F	Total	A	B	C	D	E	F
Azimuth interval °	315°-340°	45°-75°	75°-90°, 270°-290°	340°-10°	290°-315°	15°-45°		315°-340°	45°-75°	75°-90°, 270°-290°	340°-10°	290°-315°	15°-45°
station	Number of lineaments around station							% of total number					
GM1	139	43	74	16	46	16	334	42	13	<u>22</u>	5	14	5
GM2	139	43	74	16	46	16	334	42	13	<u>22</u>	5	14	5
GM3	109	103	30	13	55	12	320	34	<u>32</u>	9	4	17	4
GM4	38	72	17	1	10	2	140	<u>27</u>	51	12	1	7	1
GM5	34	17	12	4	15	5	87	39	<u>20</u>	14	5	17	6
GM6	122	48	44	15	40	17	286	43	<u>17</u>	15	5	14	6
GM7	4	8	9	2	4	1	28	14	<u>29</u>	32	7	14	4
GM8	42	18	7	7	5	10	92	46	<u>20</u>	8	8	5	11
GM9	12	20	17	12	12	11	84	14	24	<u>20</u>	14	14	13
GM10	28	19	22	20	17	14	120	23	16	<u>18</u>	17	14	12
GM11	6	8	8	2	7	3	34	18	24	<u>24</u>	6	21	9
TOTAL	673	399	314	108	257	107		36	<u>21</u>	17	6	14	6

Figure 81 shows rose diagrams for the sub-vertical sets of fractures at the geomechanical stations and the lineaments surrounding the stations. The correspondence of the sets of fractures with the sub-vertical sets of lineaments is expressed in Table 48 and Figure 81.

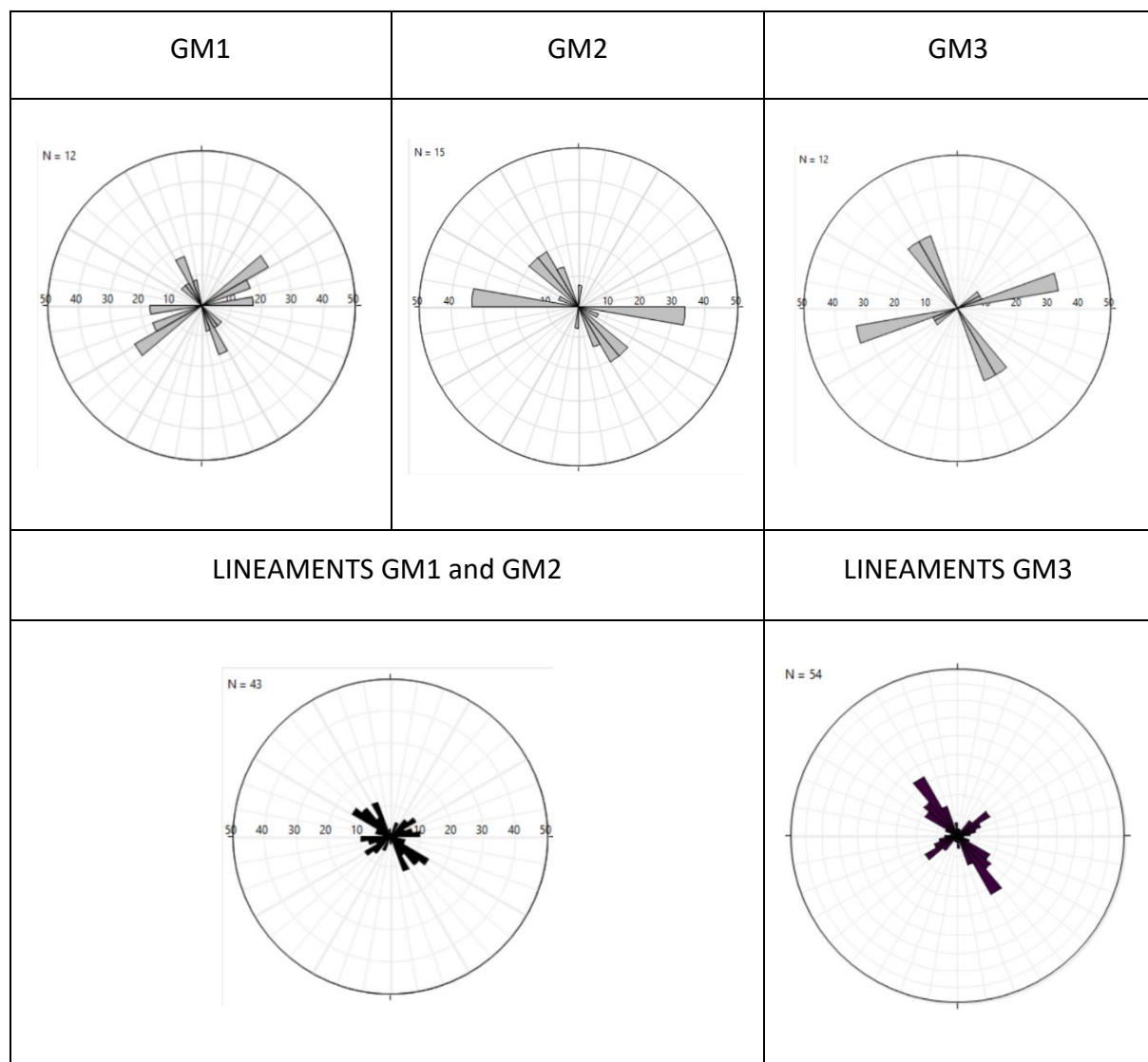
Most of the more common sets of fractures at each station correspond to the main sets of lineaments A, B and C.

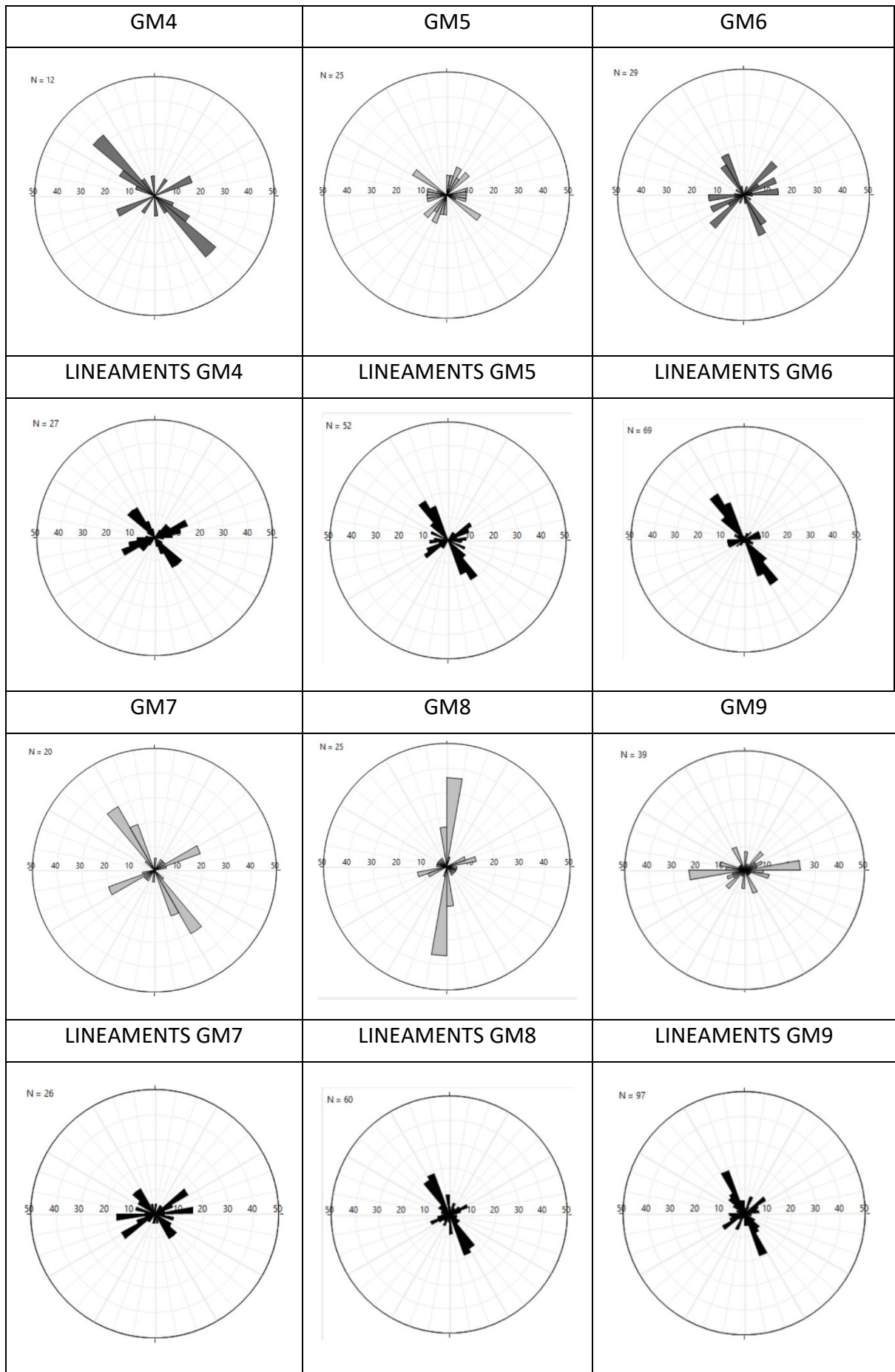
Set A (trend NW-SE) is the most frequent in number of the geomechanical stations followed by set B (trend NE-SW) and set C (trend E-W). Set E is the fourth more frequent in the areas around the geomechanical stations, although in the whole area its abundance is very similar to sets D and F.

The fractures set q and t correspond to the lineament set B (trending NW-SE). The fractures sets s, and v corresponds to the lineament set B (trending NE-SW). The sets s and p and C have the same E-W trending.

The fracture sets with low dip angle were not compared with the lineament sets because it is not sure that their plane was digitised in the lineament map and the value of the strike has a vast range.

Table 48 shows the sets of fractures with a strike inside or very close to the interval of the set of lineament placed in the column of the lineaments sets. The column with the symbol % gives the values of frequency of each lineament set over the area surrounding the station, and the last row (total) shows the sets of fractures extracted for the whole area and the frequency of the lineaments sets for all the circles together.





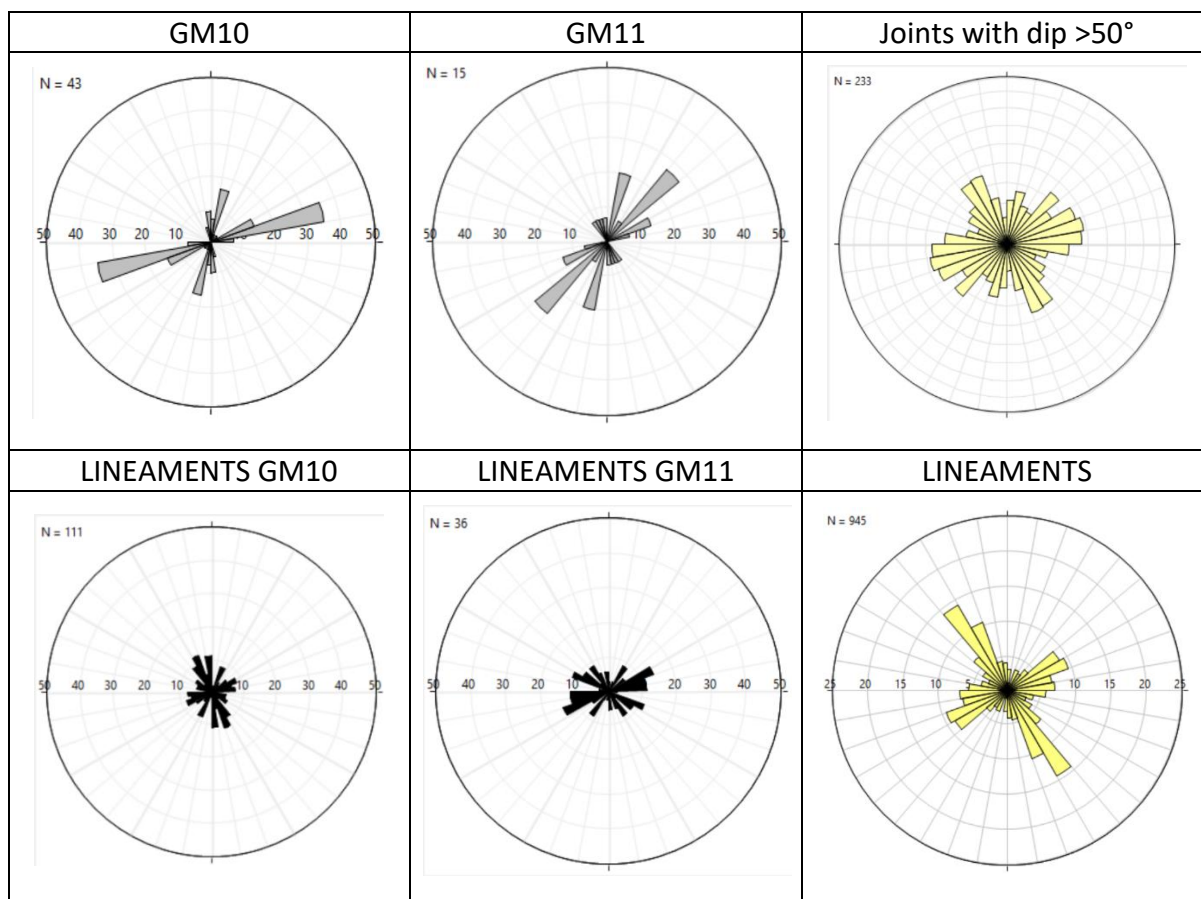


Figure 81 Rose diagram of sub-vertical fractures measured at the field and rose diagrams of lineaments surrounding the geomechanical stations.

Table 48 Correspondence of the sets of lineaments with the sets of fractures measured at geomechanical stations. The sets and frequency in bold are the more frequent in each station, and the underlined are the second more frequent, in italic are the third more frequent.

Set lineaments	A		B		C		D		E		F	
Azimuth interval °	315°-340° 135°-160°		45°-75° 225°-255°		75°-90°, 270°-290° 255-270, 90-110		340°-10° 160°-190°		290°-315° 110°-135°		15°-45° 195°-225°	
	Fracture sets	% lin	Fracture sets	% lin	Fracture sets	% lin	Fracture sets	% lin	Fracture sets	% lin	Fracture sets	% lin
GM1	1q 148/89	42	<i>1s1</i> 235/86 <i>1n2</i> 59/43	13	1s2 264/85	<u>22</u>		5		14		5
GM2	<u>2q</u> 133/71 <i>2t</i> 322/75	42		13	2p 90/62	<u>22</u>		5		14		5
GM3	<u>3t</u> 329/90	34	3v 69/84	<u>32</u>		9		4		17		4
GM4	<u>4q</u> 311/82 <i>4t</i> 132/79	<u>27</u>	4s 230/90	51		12		1		7		1
GM5	5t 298/81-	39	<i>5u</i> 37/75	<u>20</u>	<u>5s</u> 263/84	14		5	<i>5p</i> 112/88	17	5v 18/73	6
GM6	6t 327/76 6q 150/82	43	6r 224/86 6v 59/85	<u>17</u>	6s2 263/87	15		5		14	<u>6s1</u> 24/86	6
GM7	7t 325/82	14	<u>7s</u> 245/65 <i>7r</i> 240/75	<u>29</u>		32		7		14		4
GM8	<u>8t</u> 340/83	46	8r 223/81	<u>20</u>	8s 271/89 <i>8p</i> 97/78	8	8u 10/85	8		5	8r 223/81	11
GM9	<u>9q</u> 146/75	14	<i>9v</i> 50/85 9s1 248/72	24	9s2 263/85 9p 108/67 9s3 284/90	<u>20</u>	9u 0/90	14		14	9r 224/61	13
GM10		23	10v 69/85 <u>10s</u> 251/82	16		<u>18</u>	10r 172/86	17		14	<u>10r1</u> 208/83	12
GM11	11t 331/67	18	<i>11s</i> 247/78	<u>24</u>		<u>24</u>		6		21	<u>11u</u> 9/66 <i>11v</i> 41/85	9
TOTAL	q, t	36	s, v	<u>21</u>	s, p	<u>17</u>	r, u	6	p, t	14	u, v	6

5.1.2 Spatial distribution of fractures and lineaments.

Figure 82 shows the fractures measured in field grouped by lithology and their pole and rose diagram, number of observations and strike intervals where the frequency is higher.

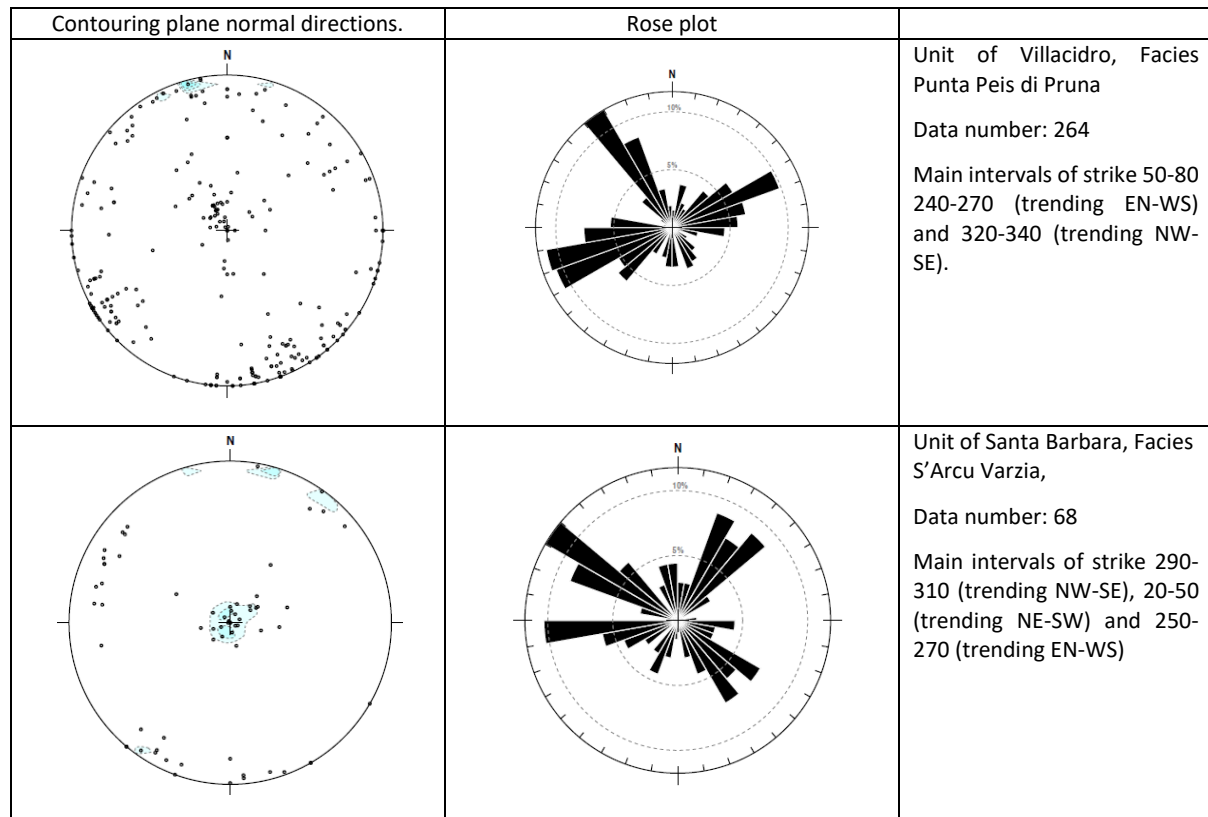


Figure 82 Pole and rose diagrams (Schmidt-net, lower hemisphere) for fractures data, separated by the formation in which they were observed.

The density and distribution of the lineaments by each lithology are shown in Figure 83 and Figure 84.

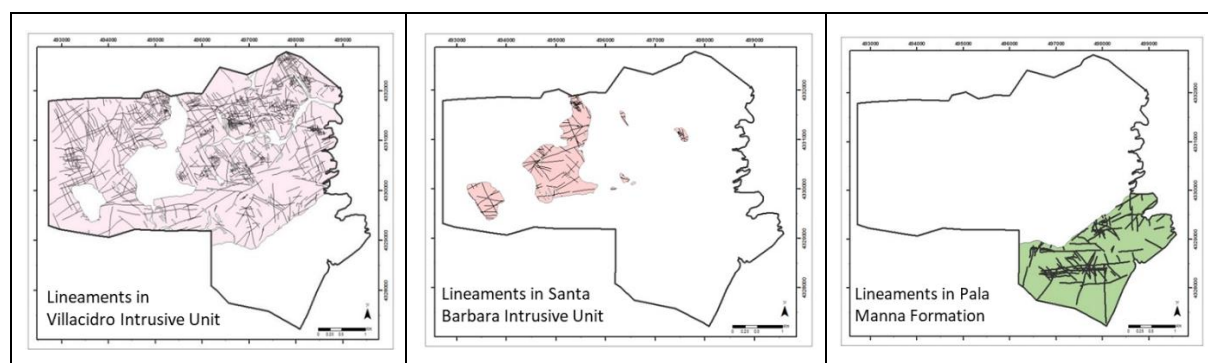


Figure 83 Maps of lineaments crossing each formation.

Figure 84 shows the density in term of number of fractures over an area of the geological unit and density regarding cumulative length over the area of the geological units. The granitic geological units show a very similar density of fractures, although both exhibits to be more fractured than the metasedimentary Formation Pala Manna. The sets more prevalent in the granitic rocks are sets A, B and C; while sets C and D affect more Pala Manna Formation.

Figure 85 and Figure 86 illustrate the density distribution of the lineaments and their intersections (§4.2.4). The map of the density of lineaments and density of lineaments intersection shows higher density in the granitic formations. The density in both maps is higher in the north of the basin and elevated areas. There is also a higher concentration of lineaments near some dykes and faults.

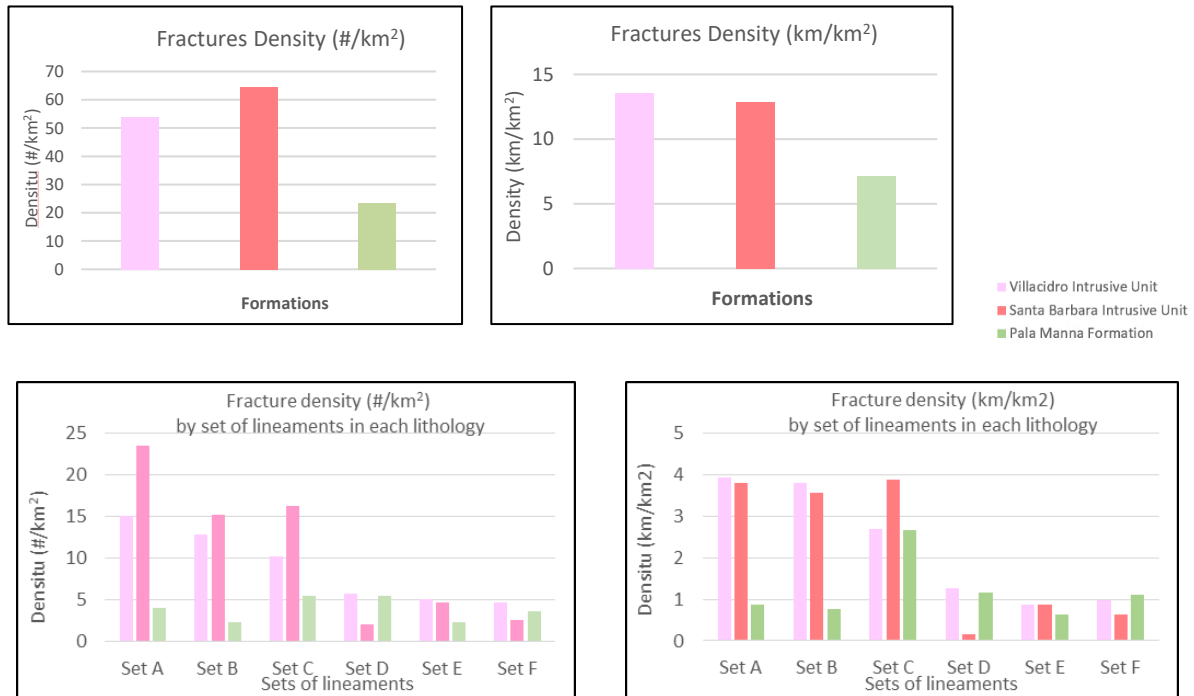


Figure 84 Graphics of density of lineaments in each formation and density of lineaments set in each unit. The density was evaluated as number of fractures in the area and like cumulative length in the area.

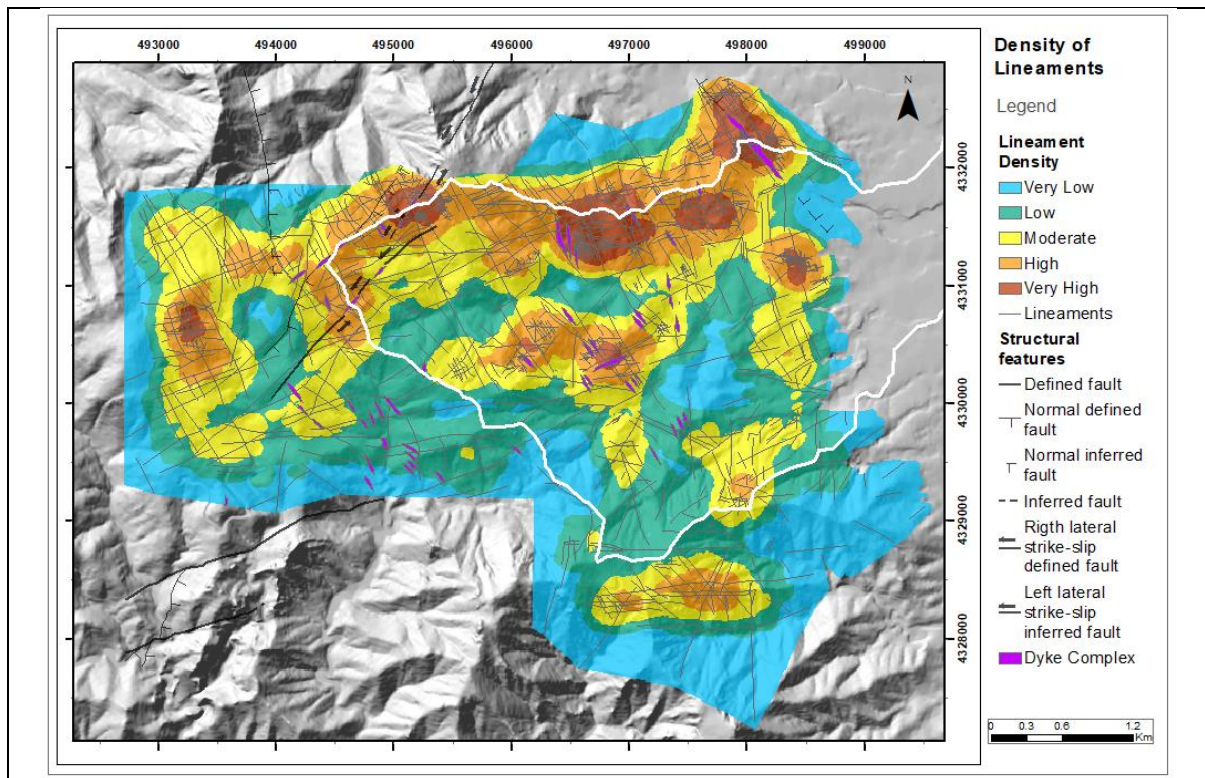


Figure 85 Map of density of lineaments

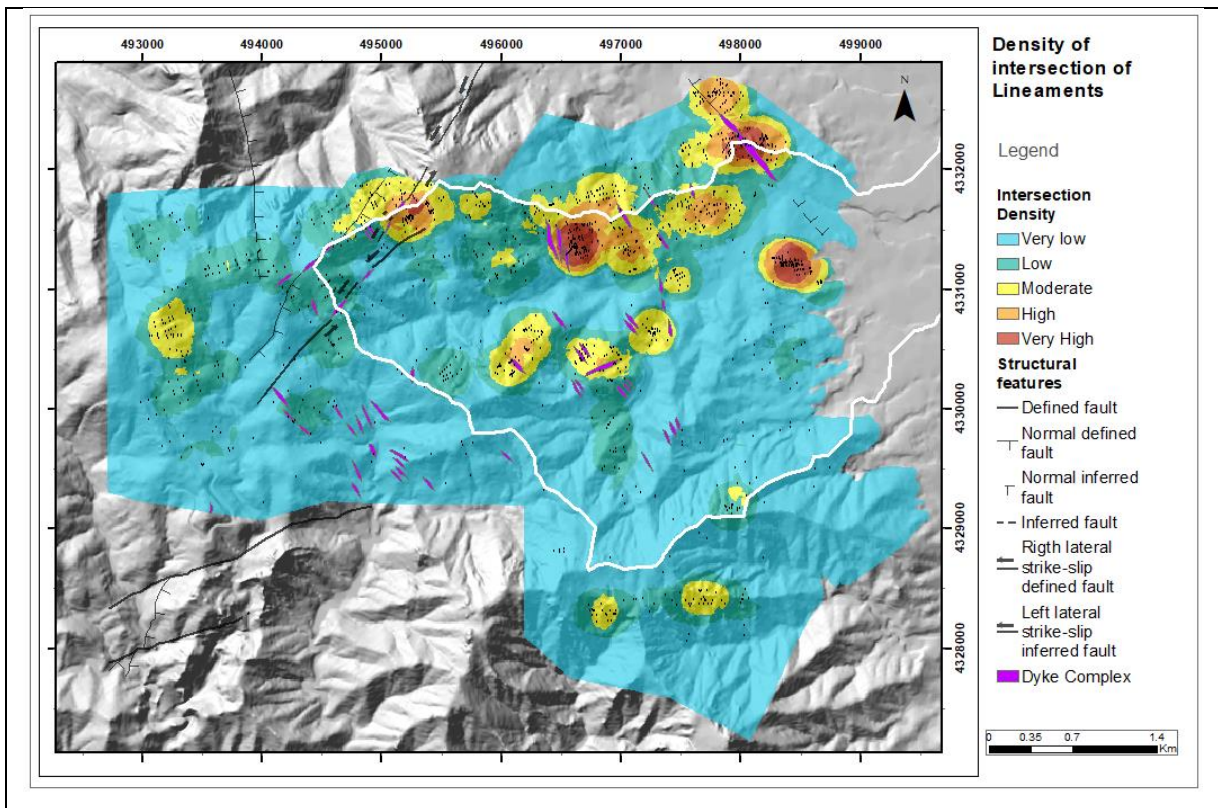


Figure 86 Map of density of intersection of lineaments

5.1.3 Distribution of fracture properties

Aperture

Figure 87 represents the frequency distribution of the aperture for all the fractures measured in the field. The fractures that are closed is the 40%, and those with an aperture between 0.2 and four millimetres are other 40%. There are few fractures with an aperture wider than 30 mm. The histogram for aperture below 20mm shows a scattered distribution, but the values of the aperture are concentrated below 1mm.

Figure 88 and Figure 89 are graphs of aperture against dip angle and elevation. The aperture of the fractures with dip below 70° are mainly 10 mm. While the aperture of the fractures dipping over 70° are mainly below 20 mm but can reach higher values (up to 80 mm).

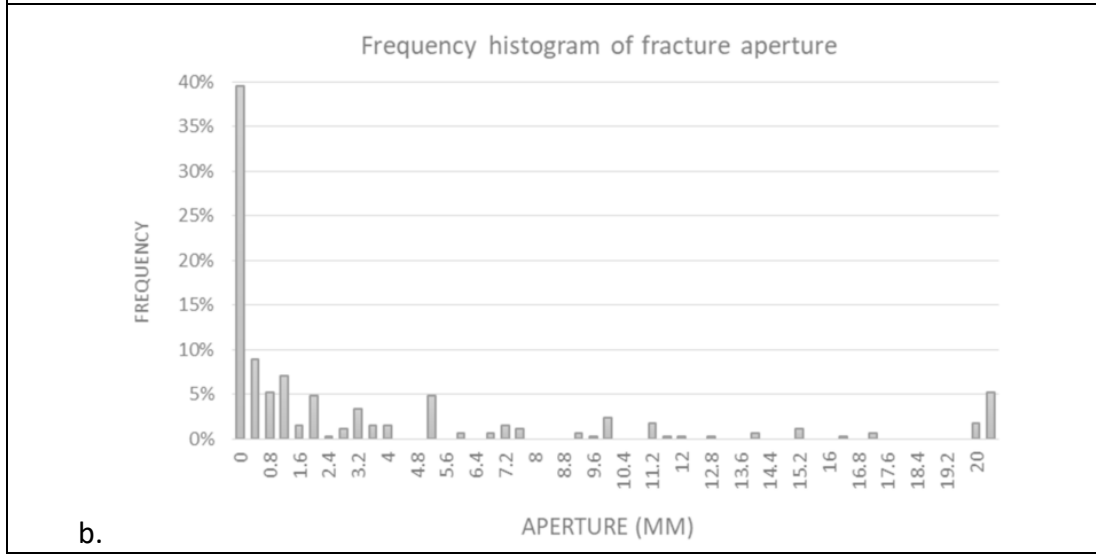
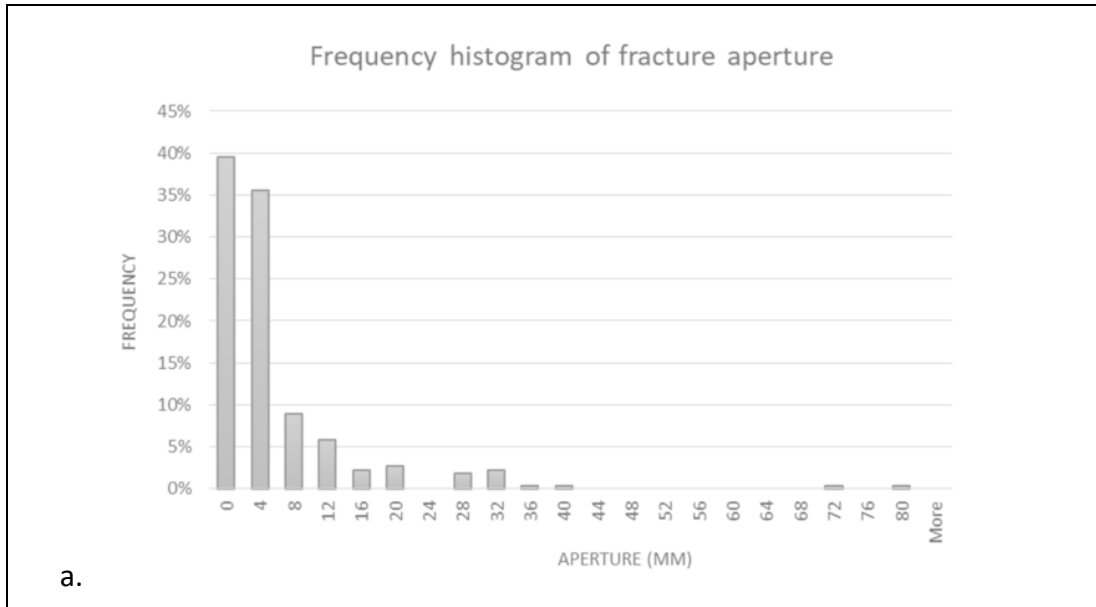


Figure 87 (a) Histogram for all values of aperture and (b) histogram for values of aperture bellow 20mm.

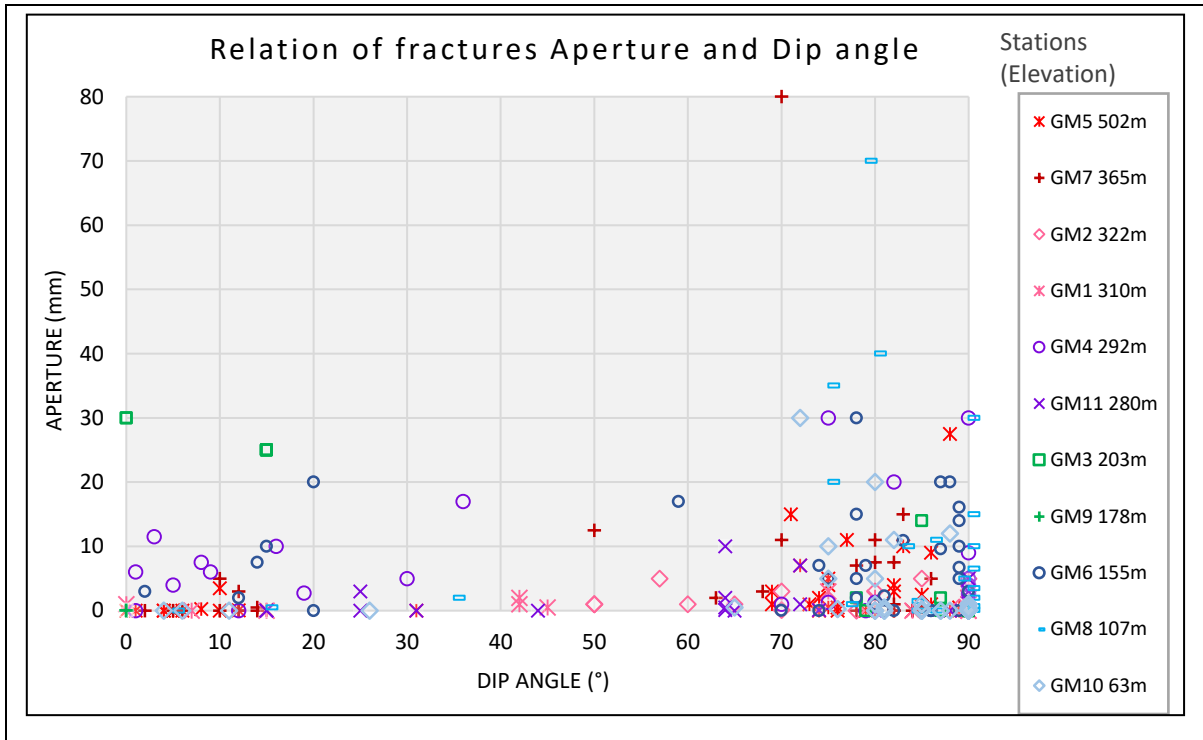


Figure 88 Relation of aperture of fractures and dip angle

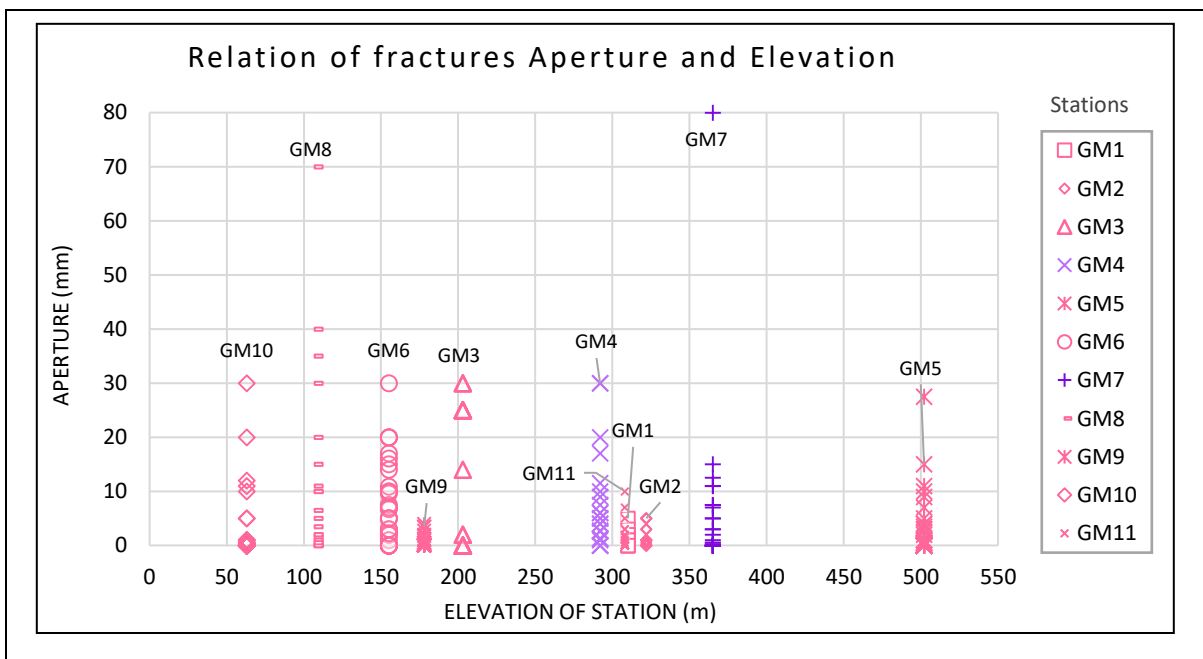


Figure 89 Relation of fractures Aperture and Elevation. The stations in pink are located in Villacidro Intrusive Unit, and the stations in colour purple are located in Santa Barbara Intrusive Unit.

Spacing

Figure 90 and Figure 91 represents the spacing for all the fractures measured in the field against dip angle and elevation, respectively. The spacing of all the fractures is mainly between 0.1 and 1 m. The spacing between fractures dipping below 40 is mainly around 0.3 m and for the fractures dipping over 60 is more concentrated around 0.15 m.

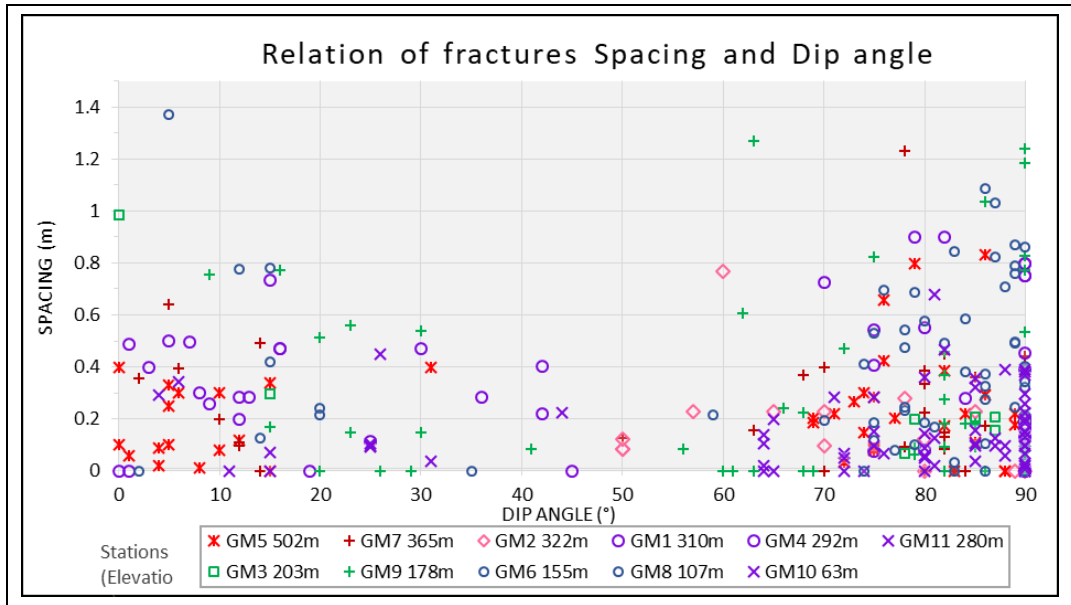


Figure 90 Relation of fractures Spacing and dip angle.

Below there are graphics relating fracture parameters and geographical position of the stations with the aim of identifying patterns in the distribution. The relationship of spacing of the sub-horizontal fractures and the elevation was examined to determine if the model of the stratiform aquifer (§2.1.2 and §4.2.4) is valid in this area. The distribution of the aperture was examined to determine if there was an observable effect of the lithostatic pressure and of the weathering (§4.2.4). The spatial distribution of the spacing of sub-vertical fractures was evaluated to see if the valleys had structural control. The spacing does not have an apparent tendency with elevation. The stations located between 107 MASL and 178 MASL have a more extensive range of spacing, although the sets of joints might condition this.

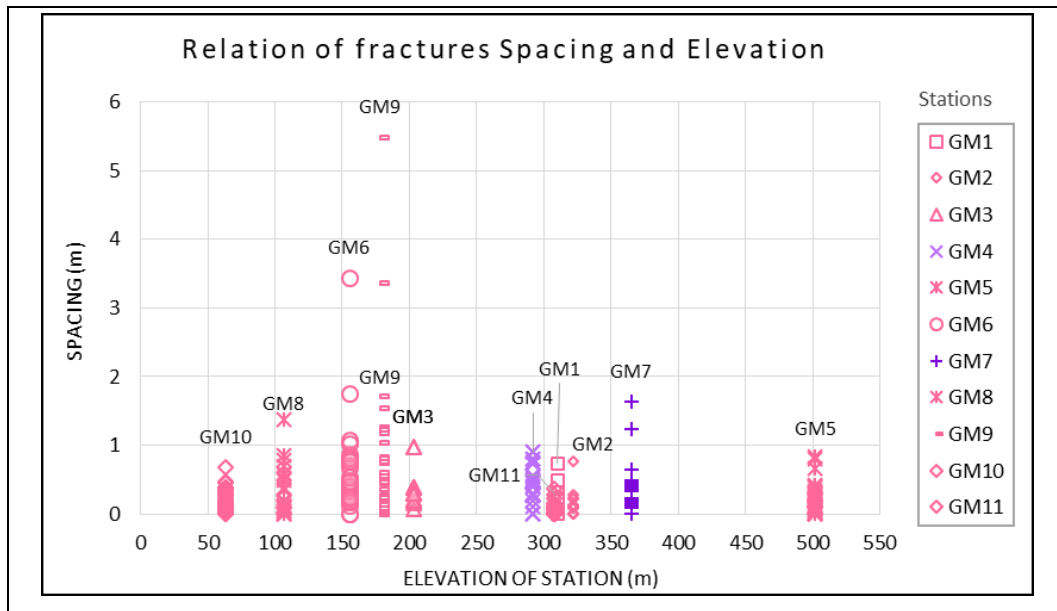


Figure 91 Relation of fractures Spacing and Elevation

Figure 92 shows the pole diagram, the great circle diagram and the rose diagram (for strike and dip direction) of the fractures measured in the field with dip angle below 50°.

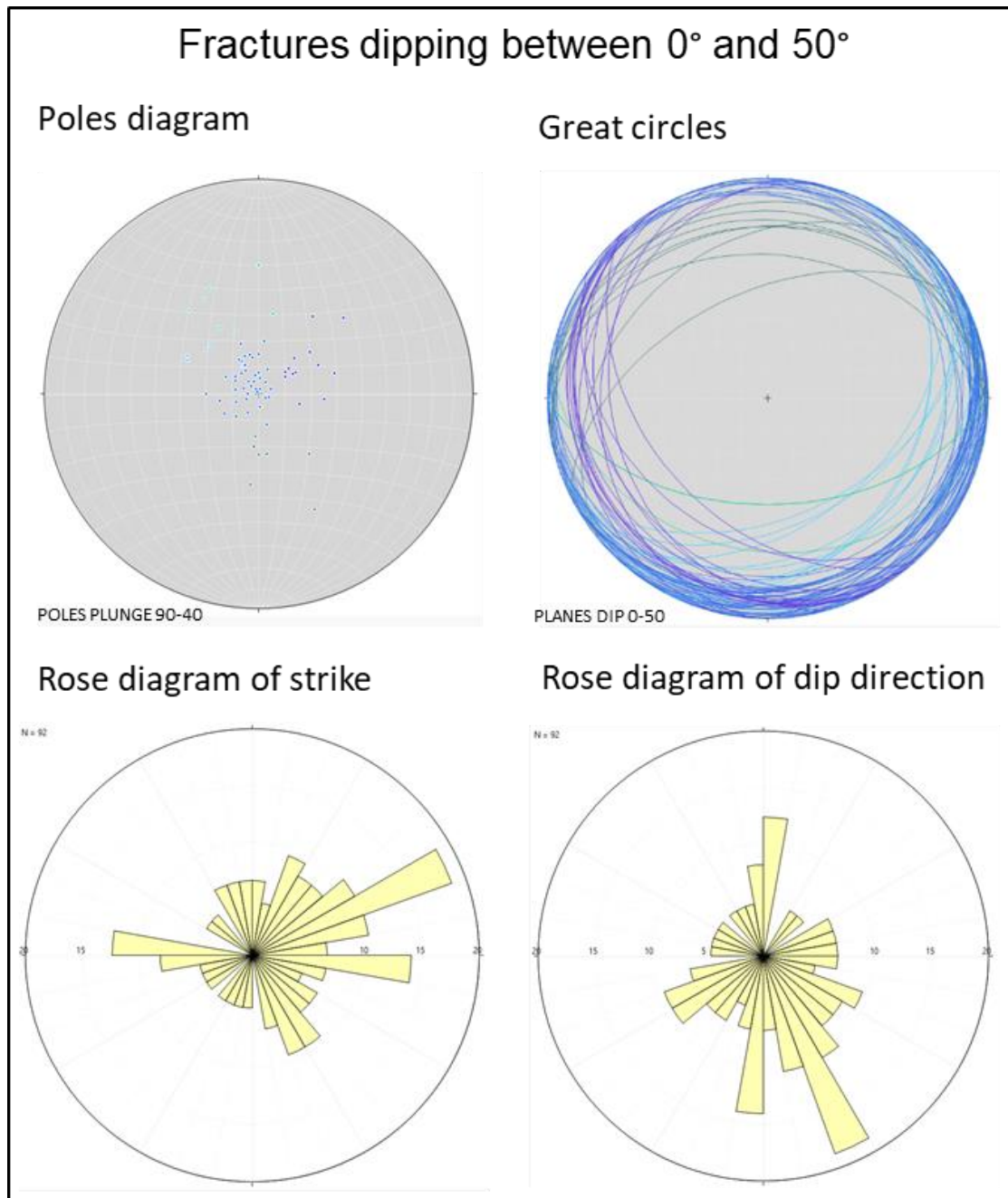


Figure 92 Pole diagram, great circle diagram and rose diagram for the fractures with dip angle between 0° and 50°.

The dip directions of the fractures with low dip angle are very variable, although there is a preferential direction towards SE

Characteristics of the geomechanical stations and aperture and frequency of the sub-horizontal sets. Ten of 11 geomechanical stations have a subhorizontal set, of those, in five stations the sub-horizontal set is closed. The mean aperture for all the subhorizontal fractures is 0.125 mm. The mean spacing is 0.431 m, and the mean frequency is 2.2 m⁻¹.

Table 49 Characteristics of the geomechanical stations and aperture and frequency of the sub-horizontal sets.

Features of the station				SUB HORIZONTAL SET				
Sta_ tion	Height (MASL)	Slope Direction	Forma_ tion	Lithology	Range dip °	Mean aperture (mm)	Mean spacing L'/N (m)	Frequency N/L' (m ⁻¹)
GM1	310	NW	VLDb	Leucomonzogranite	0-15	0	0.827	1.210
GM2	322	NE	VLDb	Leucomonzogranite	-	0		0.000
GM3	203	S	VLDb	Leucomonzogranite	0-15	15	0.281	3.562
GM4	292	SW	SBBb	Monzogranite	1-36	6	0.457	2.191
GM5	502	NW	VLDb	Leucomonzogranite	0-15	0	0.181	5.530
GM6	155	SW	VLDb	Leucomonzogranite +basic dykes	2-20	7.5	0.405	2.468
GM7	365	E	SBBb	Monzogranite + Quartz veins	2-4	0.25	0.197	5.068
GM8	107	S	VLDb	Leucomonzogranite	5-35	0.5	0.815	1.227
GM9	178	E	VLDb	Leucomonzogranite + quartz dykes	9-41	0	0.315	3.171
GM10	63	SE	VLDb	Leucomonzogranite	4-26	0	0.980	1.020
GM11	308	NW	VLDb	Leucomonzogranite	15-44	0	1.614	0.636
media						0.125	0.431	2.191

Figure 93 and Figure 94 show the relationship between the aperture and spacing of the subhorizontal fractures and the elevation. Figure 95 contains graphics comparing the mean values of aperture and spacing of the sub-horizontal set of each station with the elevation, slope aspect, valley side and distance to the river of the station.

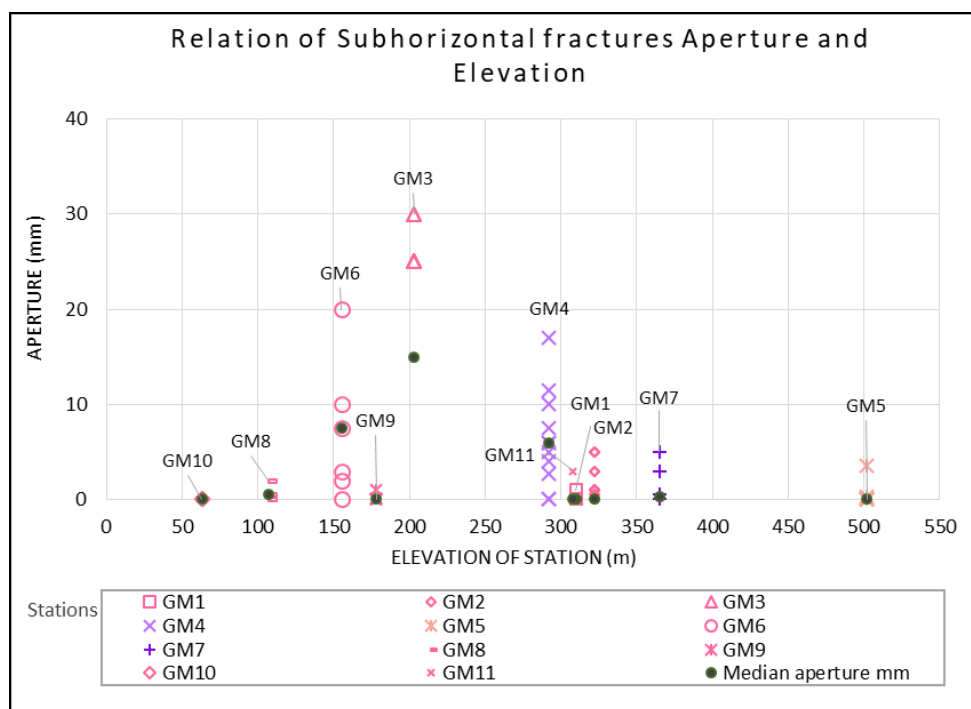


Figure 93 Relationship of subhorizontal fractures aperture and elevation

The mean aperture increases with an elevation between the stations GM10 (63 MASL) and GM3 (203 MASL) and decreases between GM3 and GM5 (502 MASL). The fractures in station GM9 are not representative because they are filled with quartz veins. The mean spacing of subhorizontal fractures decreases with elevation. The frequency of sub-horizontal sets shows a tendency to increase with elevation. There are five stations located near the river bed where the subhorizontal fractures aperture is wider than for the stations 200 to 1000 meters away from the river. The frequency near the river is variable, but it is maximum for stations GM7 and GM5 located between 600 and 800 meters away from the river. The aperture of the fractures in the stations facing the north, east and west is lower than the aperture for three stations facing southeast, south and southwest. Although, station GM1 is facing south and has a low aperture. The frequency is higher for the sets facing E, SE, SW and W.

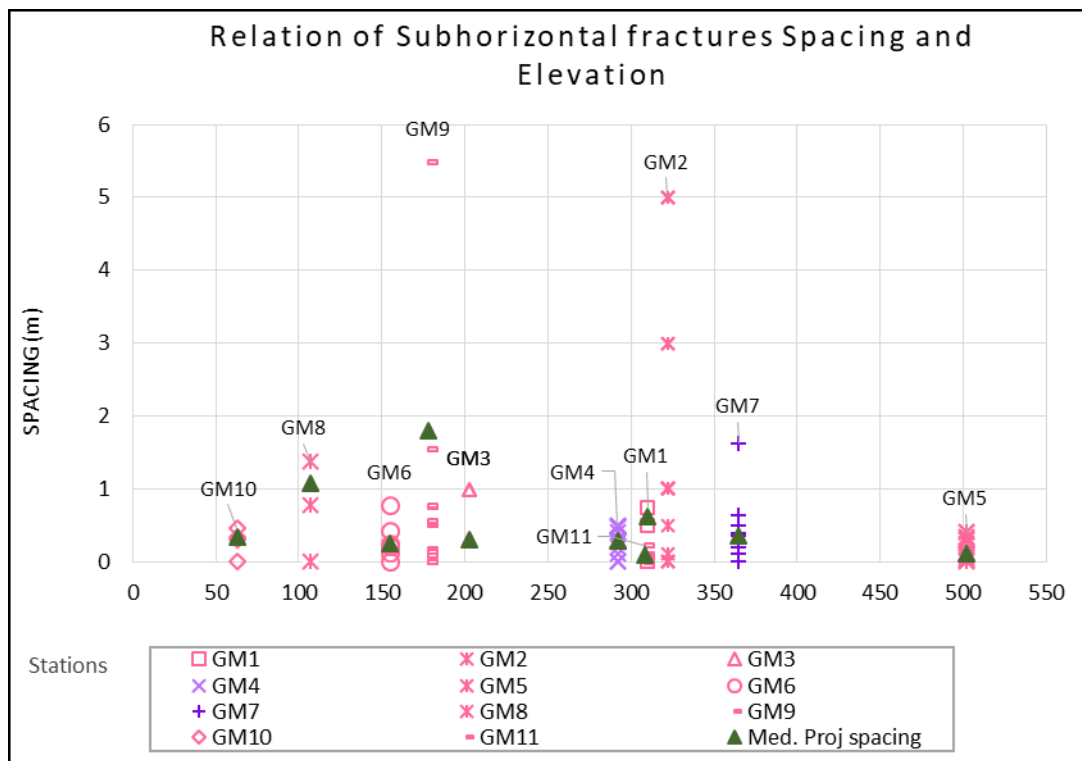


Figure 94 Relationship of subhorizontal fractures spacing and elevation .

Figure 96 shows the pole diagram, the great circle diagram and the rose diagram (for strike and dip direction) of the fractures measured in the field with dip angle between 80° and 90°.

The rose diagram of dip direction shows that there are two directions more frequent, one toward the NWN and other towards NE.

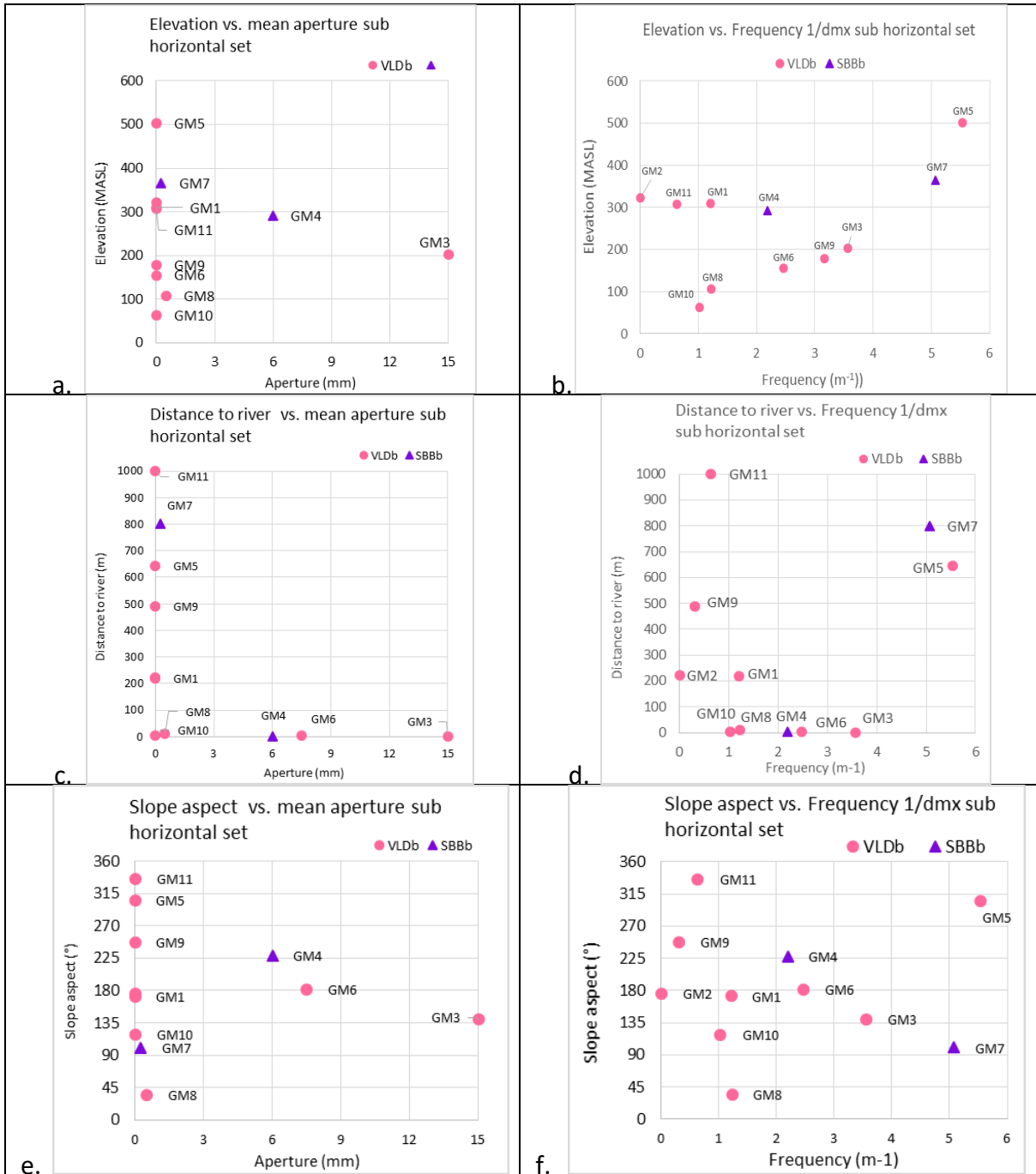


Figure 95 Relationship between mean aperture and mean frequency of the subhorizontal fractures and geographical features like elevation, distance to the river and slope aspect.

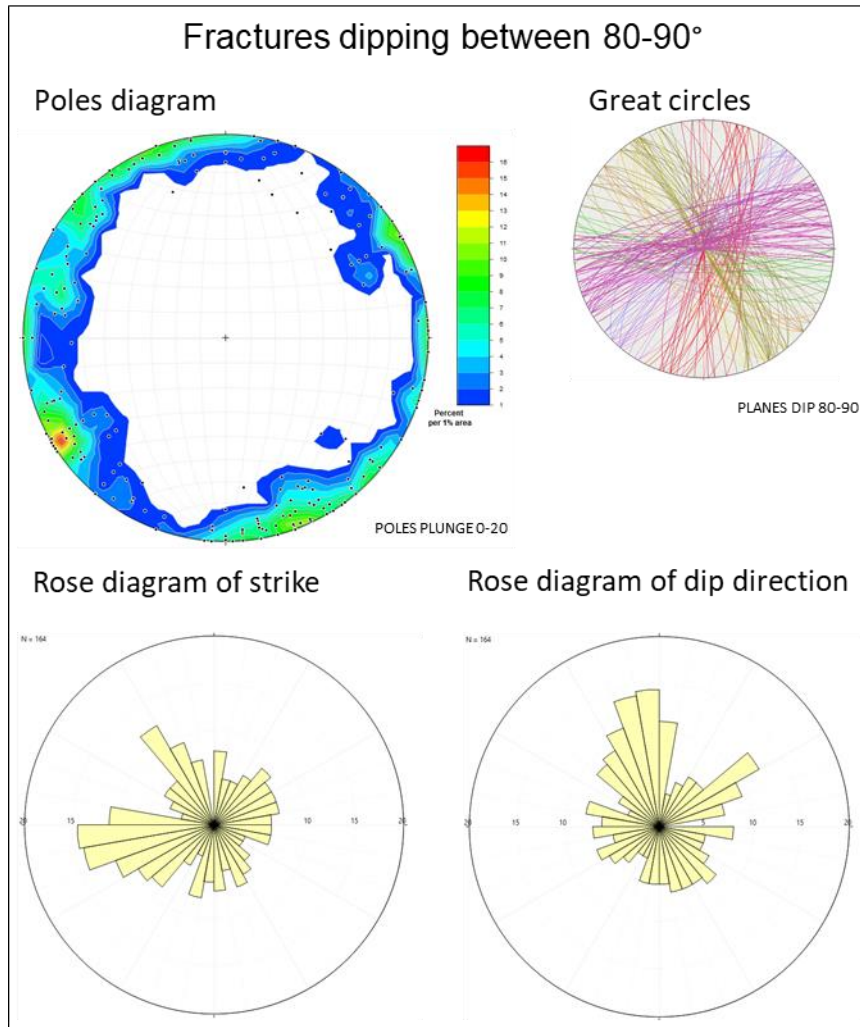


Figure 96 Pole diagram, great circle diagram and rose diagram for the fractures with dip angle between 80° and 90°.

Sub-vertical sets

Figure 97 contains graphics comparing the mean values of aperture and spacing of the sub-vertical sets of each station with the elevation, slope aspect, valley side and distance to the river of the station.

The aperture does not seem to have a relationship with the elevation, the distance to the river or the slope aspect. The highest values of the aperture are found closer to the river. The highest aperture values are in the Stations GM8 (slope aspect towards NE) and GM4 (slope aspect towards SW).

There is a slight trend in the frequency of sub-vertical sets to decrease with elevation and moving away from the river. It was found that the frequency of the sub-vertical sets is higher in the slopes facing S, SE and E; and in the north and centre of the basin.

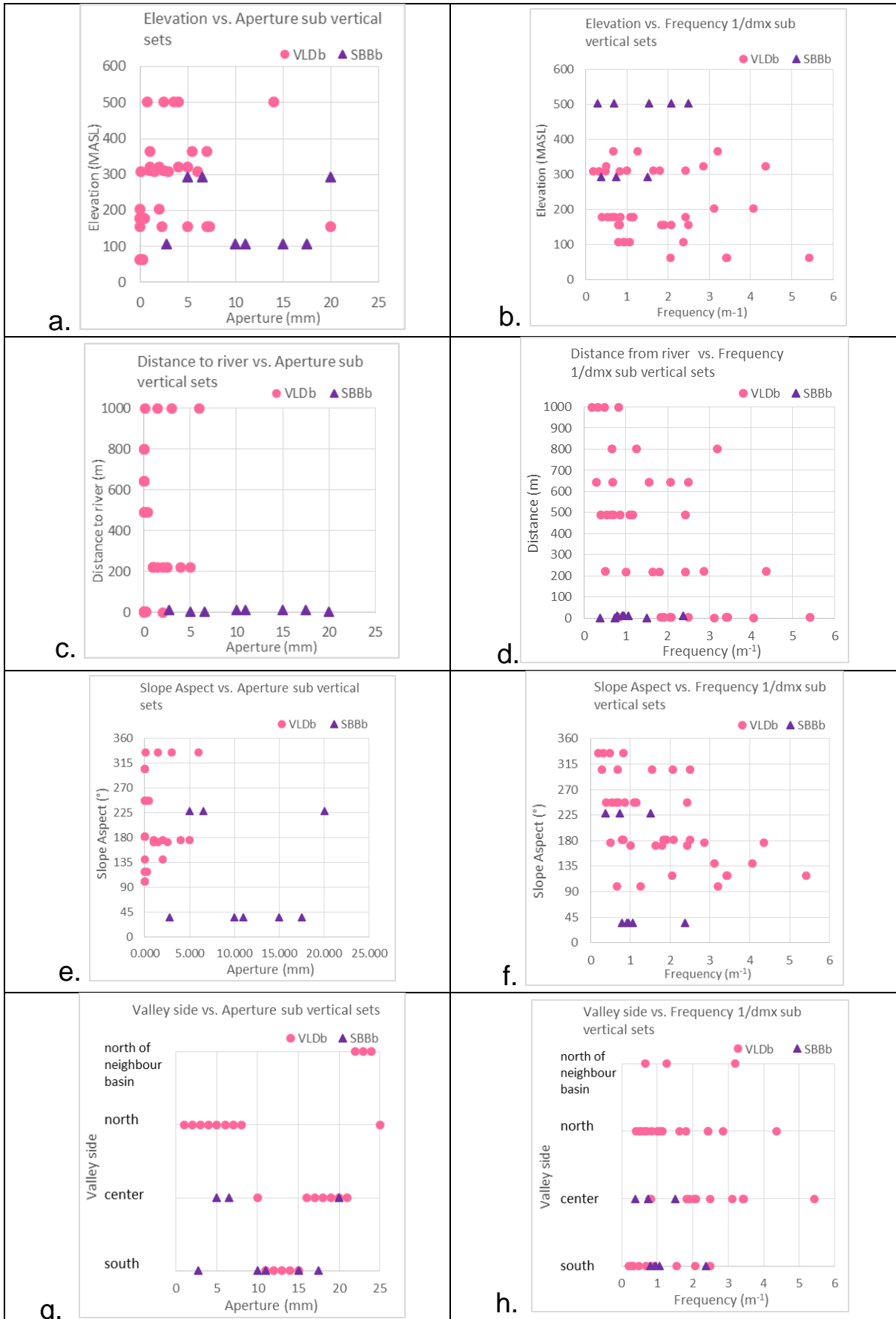


Figure 97 Relationship between mean aperture and mean frequency of the sub vertical fractures and geographical features like elevation, distance to the river, slope aspect and side of the valley.

5.1.4 Permeability.

Table 50 shows the data used to calculate the permeability with the cubic law (2.1.1) for each set of fractures and each station. The information of each set of fractures is the name of the set, number of fractures N, and attitude of the mean plane. The mean aperture is in the fifth column. The mean spacing (sixth column) from the projected spacing and the frequencies calculated for spacing are in the seventh column. The eighth column shows the values of permeability calculated using the cubic law.

Table 50 Permeability calculated for geomechanical stations with the cubic law equation.

1	2	3	4	5	6	7	8
SET	N	Dip direction°	Dip°	Mean aperture (m)	Mean spacing L'/number (m)	Freq n/L' (m ⁻¹)	Permeability (m/s)
GM1							
1q	5	238	88.8	0.0010	0.3709	2.6963	2.64E-06
1s1	4	324.7	86.3	0.0025	0.6196	1.6140	2.47E-05
1n1	3	168	7.3	0.0000	0.8266	1.2098	0.00E+00
1n2	3	148.5	42.8	0.0010	0.6114	1.6355	1.60E-06
1s2	2	354	85	0.0015	1.4918	0.6703	2.22E-06
total							3.12E-05
GM2							
2q	5	222.5	70.6	0.004	0.2294	4.3586	2.73E-04
2p	5	180	61.9	0.001	0.0506	19.7616	1.94E-05
2t	4	51.5	74.6	0.002	0.3498	2.8585	2.24E-05
2u	1	90	90	0.005	1.9924	0.5019	6.15E-05
total							3.77E-04
GM3							
3n	7	150	10.7	0.015	0.2807	3.5619	1.18E-02
3v	6	158.6	84.3	0.002	0.2460	4.0655	3.19E-05
3t	6	59.2	90	0	0.3207	3.1178	0.00E+00
total							1.18E-02
GM4							
4n2	8	244.1	19.3	0.01	0.37752	2.64886	2.60E-03
4n1	7	74.4	3	0.006	0.45652	2.1905	4.64E-04
4q	6	40.9	81.9	0.005	1.35612	0.7374	9.03E-05
4s	3	320.1	90	0.0065	0.66423	1.5055	4.05E-04
4t	3	221.7	78.6	0.02	2.70095	0.37024	2.90E-03
total							6.46E-03
GM5							
5n	16	136.8	2.1	0	0.181	5.530	0.00E+00
5v	7	107.9	73.7	0.004	0.401	2.495	1.57E-04
5s	6	352.5	84.1	0.0025	0.482	2.074	3.18E-05
5u	5	126.8	74.7	0.00075	0.648	1.543	6.38E-07
5t	5	27.8	80.8	0.0035	1.463	0.684	2.87E-05
5p	2	202.5	88.5	0.014	3.548	0.282	7.58E-04
total	41						9.76E-04
GM6							
6t	9	56.9	76.1	0.0070	0.5455	1.8331	6.16E-04
6n	6	168	13.5	0.0075	0.4052	2.4682	1.02E-03
6r	6	314	85.5	0.0000	0.4014	2.4911	0.00E+00
6s1	5	331.6	86	0.0023	0.4800	2.0834	2.48E-05
6s2	4	352.5	86.5	0.0050	0.5245	1.9065	2.34E-04
6q	4	240.1	82.2	0.0073	1.2645	0.7908	3.02E-04
6v	2	149	84.8	0.0200	1.2060	0.8292	6.50E-03
total	36						8.70E-03

GM7							
7t	11	54.5	81.6	0.001	0.3130	3.1949	3.13E-06
7n	10	143.8	9.4	0.00025	0.1973	5.0681	7.76E-08
7s	5	335.2	64.2	0.007	0.7950	1.2579	4.23E-04
7r	3	329.7	74.8	0.0055	1.5096	0.6624	1.08E-04
total	29						5.34E-04
GM8							
8s	9	0.6	89.3	0.00275	0.4207	2.3768	4.84E-05
8t	4	70	82.5	0.011	0.9419	1.0617	1.38E-03
8p	3	186.7	78.3	0.01	1.0464	0.9557	9.37E-04
8u	3	99.9	84.6	0.015	1.0936	0.9144	3.02E-03
8r	3	313.3	81.3	0.0175	1.2622	0.7923	4.16E-03
8n	3	353.3	12.1	0.0005	0.8148	1.2273	1.50E-07
total	25						9.56E-03
GM9							
9s2	12	352.8	84.5	0.00045	0.4130	2.4214	2.16E-07
9n	9	111.2	18.9	0	0.3154	3.1710	0.00E+00
9q	6	236.2	75	0.0003	0.8673	1.1530	3.05E-08
9v	5	139.2	85.2	0.0002	1.1746	0.8513	6.67E-09
9o	5	349.7	21.4	0.00005	0.5586	1.7901	2.19E-10
9p	4	197.7	67.3	0.000025	0.9207	1.0861	1.66E-11
9u	3	90	90	0.00015	1.5588	0.6415	2.12E-09
9s1	3	338.6	72.1	0	1.8818	0.5314	0.00E+00
9s2	3	14.3	90	0.0001	1.4314	0.6986	6.85E-10
9r	2	312.4	61	0.0001	2.5017	0.3997	3.92E-10
total							2.57E-07
GM10							
10v	16	158.9	85.2	0.00025	0.1846	5.4173	8.30E-08
10s	10	341.2	81.8	0.00025	0.2913	3.4324	5.26E-08
10r1	9	298.3	83	0	0.2933	3.4091	0.00E+00
10r2	8	261.9	85.6	0	0.4878	2.0502	0.00E+00
10n	4	127.1	11.5	0	0.9799	1.0205	0.00E+00
total							1.36E-07
GM11							
11v	5	131	84.6	0.0015	5.2881	0.1891	6.25E-07
11u	4	99	65.9	0.006	2.0951	0.4773	1.01E-04
11n1	4	232.7	27.1	0	1.8705	0.5346	0.00E+00
11n2	3	177.3	23.1	0	1.3580	0.7364	0.00E+00
11t	3	60.9	67.1	0.0001	1.2071	0.8285	8.12E-10
11s	3	337.1	77.9	0.003	3.0918	0.3234	8.56E-06
	22						1.10E-04

Relates the permeability values with the number of sets (n), the lithology, and the subhorizontal fractures; and shows the set of fractures that contributed more to the permeability. The fracture sets that contribute more to the permeability at each station are always sub-vertical sets with the wider aperture, in none case the wider is also, the more frequent set. The sets with wider aperture do not have a favorite trend.

Table 51 Permeability of each geomechanical station and sets with higher frequency, aperture and contribution to the permeability.

Station	n	Formation Lithology	Elevation MASL	Sub-horizontal set	More Frequent set	Trending more frequent set	Set with wider aperture	trending of the set with the wider aperture	Set with higher k	Permeability m/s
GM1	5	Leucomonzogranite	310	1n1 closed	1s1	SW-NE	1s1	NE-SW	1s1	3.12E-05
GM2	4	Leucomonzogranite	322	no	2p	E-W	2q and 2u	NW-SE	2q	3.77E-04
GM3	3	Leucomonzogranite	203	3n	3v	ENE-WSW	3n	ENE-WSW	3n	1.18E-02
GM4	5	Monzogranite	292	4n1, 4n2	4n1, 4n2	NW-SE	4t	NW-SE	4t	6.46E-03
GM5	6	Leucomonzogranite+ basic dykes	502	5n, closed	5n, 5v	NNE-SSW	5p	WNW-ESE	5p	9.76E-04
GM6	7	Leucomonzogranite+ basic dykes	155	6n	6n, 6t	ENE-WSW	6v	ENE-WSW	6v	8.70E-03
GM7	4	Monzogranite + Quartz veins	365	7n	7t, 7n	NW-SE	7s	ENE-WSW	7s	5.34E-04
GM8	6	Leucomonzogranite	107	8n	8p, 8t	E-W	8r	NE-SW	8r	9.56E-03
GM9	10	Leucomonzogranite + quartz dykes	178	9o, 9n	9s2, 9o	E-W	9s2	E-W	9s2	5.48E-08
GM10	5	Leucomonzogranite	63	10n closed	10s, 10r1	ENE-WSW	10s	ENE-WSW	10s	1.36E-07
GM11	6	Leucomonzogranite	308	11n1, 11n2 closed	11v	NE-SW	11u	N-S	11u	1.10E-04
								AVERAGE		3.50E-03

5.2 Water budget in the ungauged Masoni Ollastru Basin.

5.2.1 Basin delimitation

The basin of the River Masoni Ollastru, extracted from the DTM 10m resolution, has an area of 12.57 km². The ten sub-basins extracted using the workflow for a watershed with pour points in the streamflow gauge stations are called watersheds to distinguish them from the sub-basins that do not overlap each other. The flowmeter station RMO4 was not used to extract sub basing because it is very close to the station RMO5 and there are no tributaries or relevant areas pouring to the segment between the basin RMO4 and RMO5. Table 52 shows the area and perimeter of the watersheds and sub-basins

Table 52 Perimeter and surface of the watersheds and sub-basins of the Masoni Ollastru basin.

Watersheds	Perimeter (m)	Surface (m ²)	Sub-basins	Perimeter (m)	Surface (m ²)
WsAlf1	3409	618380	SbAlf1	3409	618380
WsRMO1	5417	1442903	SbRMO1	4721	824366
WsRMO2	5677	1936755	SbRMO2	3551	494147
WsRMO3	6528	2744492	SbRMO3	4328	80771
WsRMO5	8240	3798433	SbRMO5	5159	105397
WsRMO6	11671	6171543	SbRMO6	8723	237226
WsRMO7	12980	7018166	SbRMO7	5218	847554
WsRMO8	15996	8019872	SbRMO8	5427	100145
WsRMO9	17292	11725531	SbRMO9	11783	3704546
WsRMO10	18384	12455960	SbRMO10	4457	714446
RMO	19046	12566187			

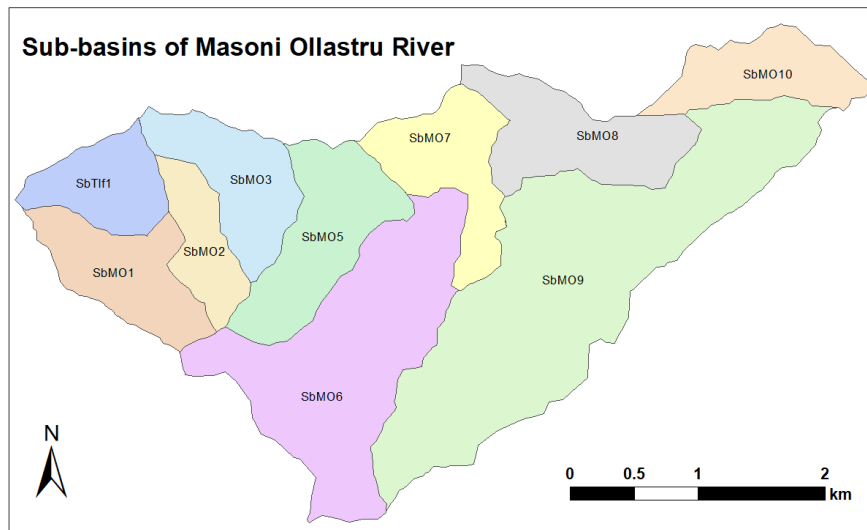


Figure 98 Map showing the sub-basins of the RMO basin which pour point corresponds to a streamflow gauge. The perimeter of the RMO basin is surrounding all the sub-basins.

5.2.2 Precipitation interpolation

The map of mean annual precipitation in the Masoni Ollastru basin exhibits a range of 495 mm of precipitation. Due to the type of interpolation, the areal precipitation distribution

follows the pattern of the topography. The lowest value of P_A (479.23 mm) and the lowest average august precipitation (8.78 mm) is in the lowest area of the basin. The maximum values of P_A and mean August precipitation (974.53 and 18.01 mm, respectively) are found in the highest area of the basin in the mountains in the west.

The mean value of P_A from the linear regression interpolation map for the whole basin is 630.8 mm; while the value assigned from the closest station was 551.2 mm. The difference between the mean values is 79 mm, and the difference of the unique value with the minimum value of the regression is 72 mm. However, the difference between the unique value and the maximum value of the regression in the mountains is 423 mm. In August the difference of the mean, minimum and maximum values of the regression and the unique values are 3.7 mm, 2.82 mm and 6.41 mm, respectively.

Table 53 Statistics for the average annual and average August precipitation interpolated inside the RMO basin. The last two columns compare the mean values of precipitation.

Precipitation data from linear regression interpolation						Unique value Capoterra 1	Difference mean of interpolation and unique value (mm)
Parameter	Min	Max	SD	Number of pixels	Mean		
Mean annual Precipitation P_A (mm)	479.23	974.53	113.66	271264	630.8	551.2	79
Mean August Precipitation p (mm)	8.78	18.01	2.12	271264	11.6	7.9	3.7

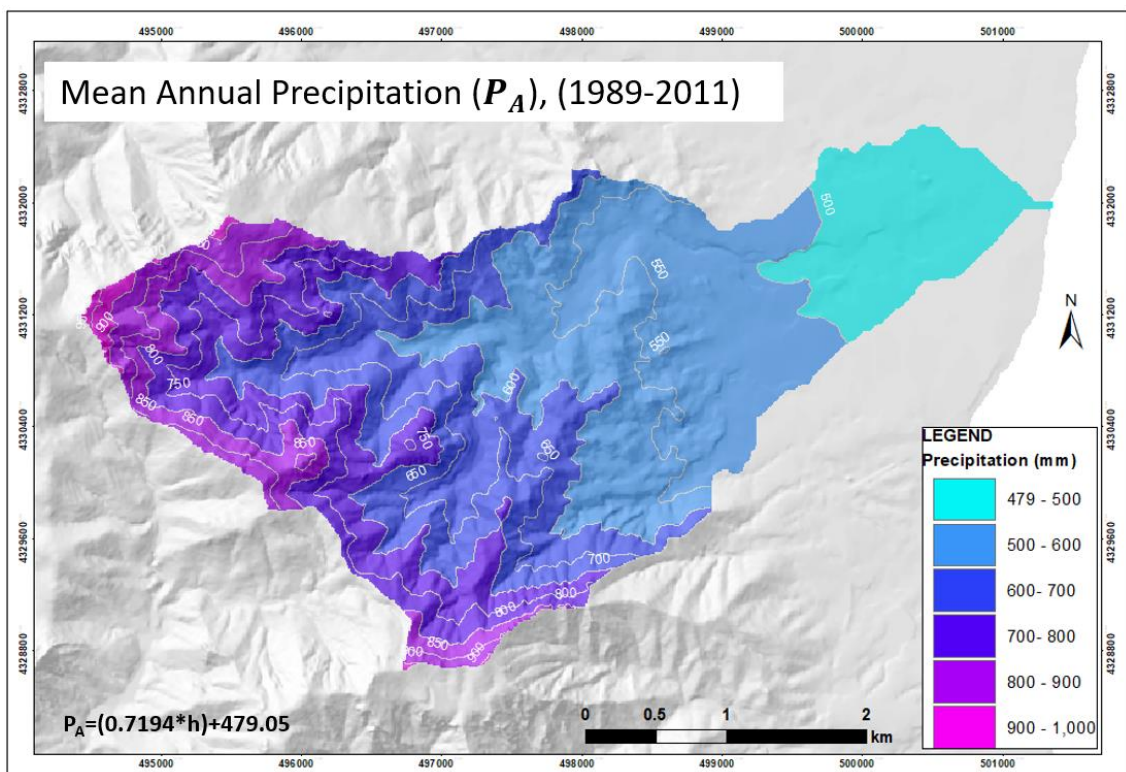


Figure 99 Mean annual precipitation map obtained using linear regression of precipitation and elevation from 1989 to 2011.

Table 54 Statistics for the mean annual precipitation correlation. The last three columns give the linear correlation coefficient between rainfall and elevation, and the mean absolute error (MAE) and mean square error (MSE) of prediction of rainfall by linear regression of elevation for each correlation.

Mean Annual Precipitation (P_A) 1989-2011										
Stations	Elevation MASL	Precipitation (mm)						Coefficient Correlation	MAS	MSE
		Average	Max	Min	Standard deviation	Value estimated	Error			
Capoterra 1	54	551.2	886.0	335.0	165.4	516.86	34.331	0.994	32.3	1045.7
Pula	10	455.0	692.0	325.4	114.9	486.96	-31.930			
Is Cannoneris	716	992.1	1748.2	638.0	260.6	961.44	30.643			
Average	260.00	666.100	1108.733	432.800	180.300	655.087	32.301			

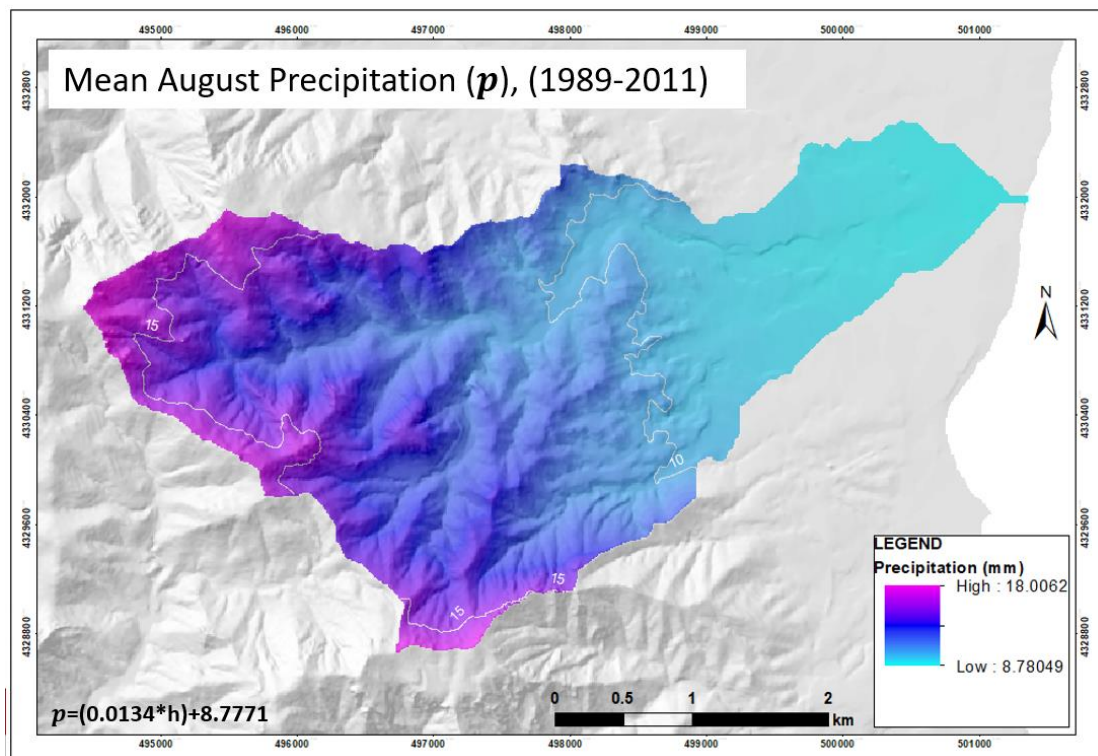


Figure 100 Mean august precipitation map obtained using linear regression of precipitation and elevation from 1989 to 2011.

Table 55 Statistics for the August rainfall record and for the prediction of August rainfall by linear regression of elevation. The last three columns give the linear correlation coefficient between rainfall and elevation, the mean absolute error (MAE) and mean square error (MSE).

Mean August Precipitation (p) 1989-2012										
Station	Elevation MASL	Precipitation (mm)						Coefficient Correlation	MAS	MSE
		Average	Max	Min	Standard deviation	Value estimated	error			
Capoterra 1	54	7.9	51	0	14.28	9.481	-1.60	0.96	1.28	1.79
Pula	10	10.4	6	0	1.82	8.93	1.51			
Is Cannoneris	716	18.5	44	0	15.95	17.76	0.72			
Average	260.00	12.26	33.67	0.00	10.68	12.06	0.21			

5.2.3 Temperature interpolation

The map of average annual temperature in the Masoni Ollastru basin exhibits a range of 3.65 °C. Due to the type of interpolation, the areal temperature distribution follows the pattern of the topography. The minimum T_A (14.28°C) and the lowest average august temperature (24.12°C) is in the flat lowest area of the basin in the east. The maximum values of T_A and average August temperature (17.93°C and 27.01°C respectively) are found in the lowest area of the basin in the mountains in the west.

The mean value of T_A from the linear regression interpolation map for the whole basin is 16.81°C; while the value assigned from the closest station was 18.4 °C. The difference of the mean values is 1.59 °C. The difference of the unique value with the minimum and maximum values of the regression is 4.12°C and 0.47°C. In august, the difference of the mean, minimum and maximum values of the regression and the unique values are 1.77°C, 3.78 °C and 0.89 °C, respectively.

Table 56 Statistics for the average annual and average August temperature interpolated inside the RMO basin. The last two columns compare the mean values.

Parameter	Temperature from linear regression interpolation				Unique value	Difference mean of interpolation and unique value
	Min	Max	SD	Mean	Capoterra 1	
Mean annual Temperature T_A (°C)	14.28	17.93	0.84	16.81	18.4	1.59
Mean august Temperature t (°C)	24.12	27.01	0.66	26.13	27.9	1.77

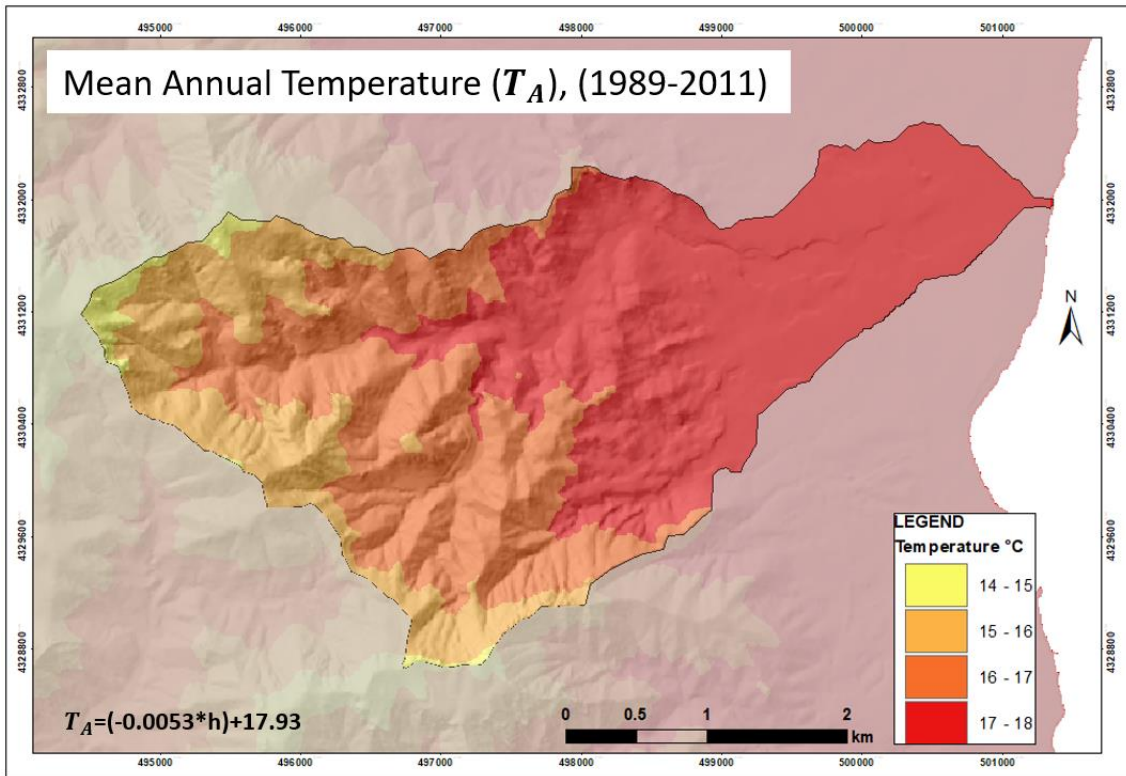


Figure 101 Mean annual temperature map obtained using linear regression of temperature and elevation for the period of 1989 to 2011.

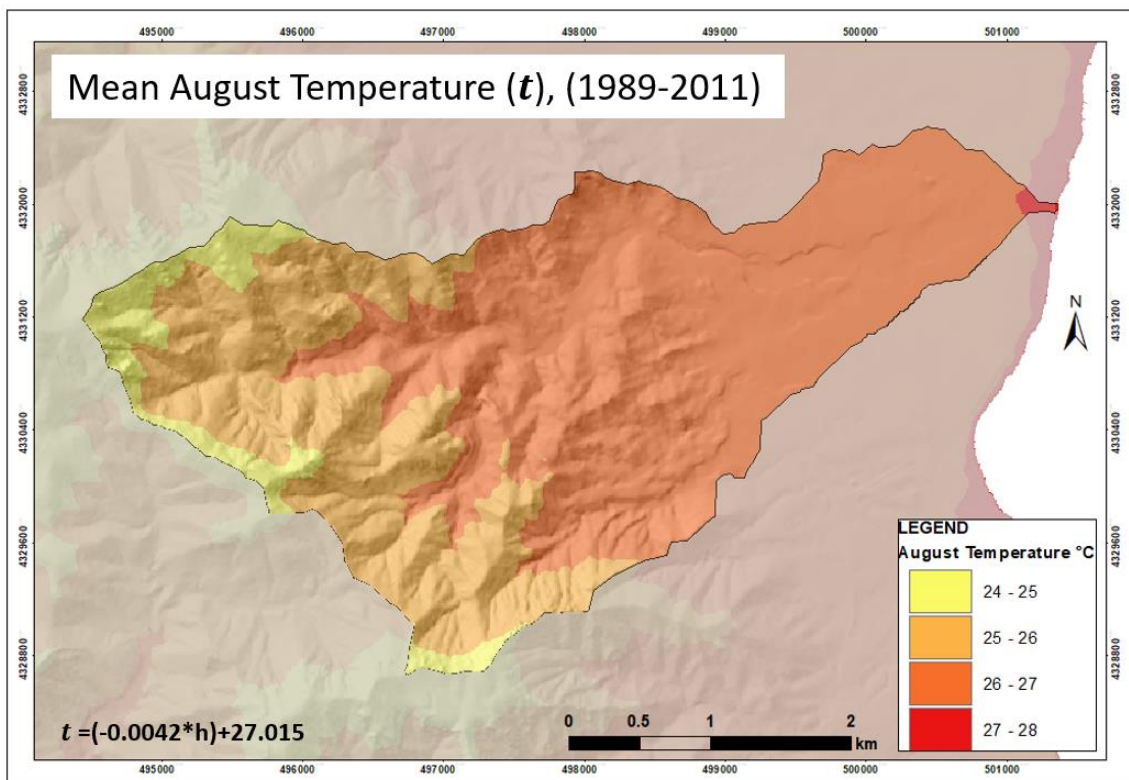


Figure 102 Mean August temperature (t) map obtained using linear regression of temperature and elevation for the period of 1989 to 2011.

5.2.4 Estimation of Evapotranspiration and Aridity index

The evapotranspiration calculated using the equation of Turc (1954) and that one modified for Mediterranean arid areas give very similar results, therefore the next procedures to calculate the mean annual potential runoff and the mean annual potential effective infiltration (Equation 27 and Equation 28) use only the Turc –Santoro equation (Equation 29). Table 57 contains the statistics of the Evapotranspiration and aridity index (Equation 25) areal distribution and the comparison with the values obtained using unique values from a fix weather station.

The aridity index values range (10.5-24.6) is lower than 25. Therefore the values of the first column to calculate the runoff coefficient using the parametric method (Table 9) were used to calculate the runoff coefficient for the whole basin.

Table 57 Statistics for the average annual evapotranspiration and average aridity index interpolated inside the RMO basin. The last two columns compare the mean values obtained from linear regression and unique value.

From precipitation and temperature interpolated with linear regression					Unique value	Difference unique value and values of regression		
Parameter	Min	Max	SD	Mean	Capoterra 1	Mean	Min	Max
Mean annual potential Evapotranspiration (mm) (Turc-Santoro)	421.6	594.4	45.89	492.23	470.2	23.03	48.61	-124.2
Mean annual potential Evapotranspiration (mm) (Turc)	418.7	553.5	38.52	480.89	510.5	29.61	91.83	-42.97
Aridity Index (I_a)	10.5	24.6	3.10	14.52	11.4	3.12	0.87	-13.15

Table 58 Statistic of P_A (mm) and evapotranspiration maps of sub-basins

	Statistic of P_A (mm) map of sub-basins				Statistic of Annual Evapotranspiration (mm) map of sub-basins				Area m ²
	Mean	Min	Max	SD	Mean	Min	Max	SD	
Ws_Alf1	686.97	974.53	818.02	63.57	560.26	520.94	594.40	16.44	618380
Ws_RMO1	658.90	974.53	802.12	63.36	555.99	510.24	594.40	17.24	824366
Ws_RMO2	622.93	974.53	783.51	69.16	550.47	495.37	594.40	19.87	494147
Ws_RMO3	594.15	974.53	767.45	77.40	545.23	482.51	594.40	23.51	80771
Ws_RMO5	558.06	974.53	737.11	87.44	534.98	465.06	594.40	28.50	105397
Ws_RMO6	543.42	974.53	715.63	88.63	527.64	457.56	594.40	30.09	237226
Ws_RMO7	525.81	974.53	698.71	95.41	521.06	448.20	594.40	33.70	847554
Ws_RMO8	493.29	974.53	677.05	106.44	511.88	429.90	594.40	40.07	100145
Ws_RMO9	482.75	974.53	640.93	110.90	496.88	423.69	594.40	43.97	3704546
Ws_RMO10	481.20	974.53	632.06	113.32	492.83	422.77	594.40	45.65	714446

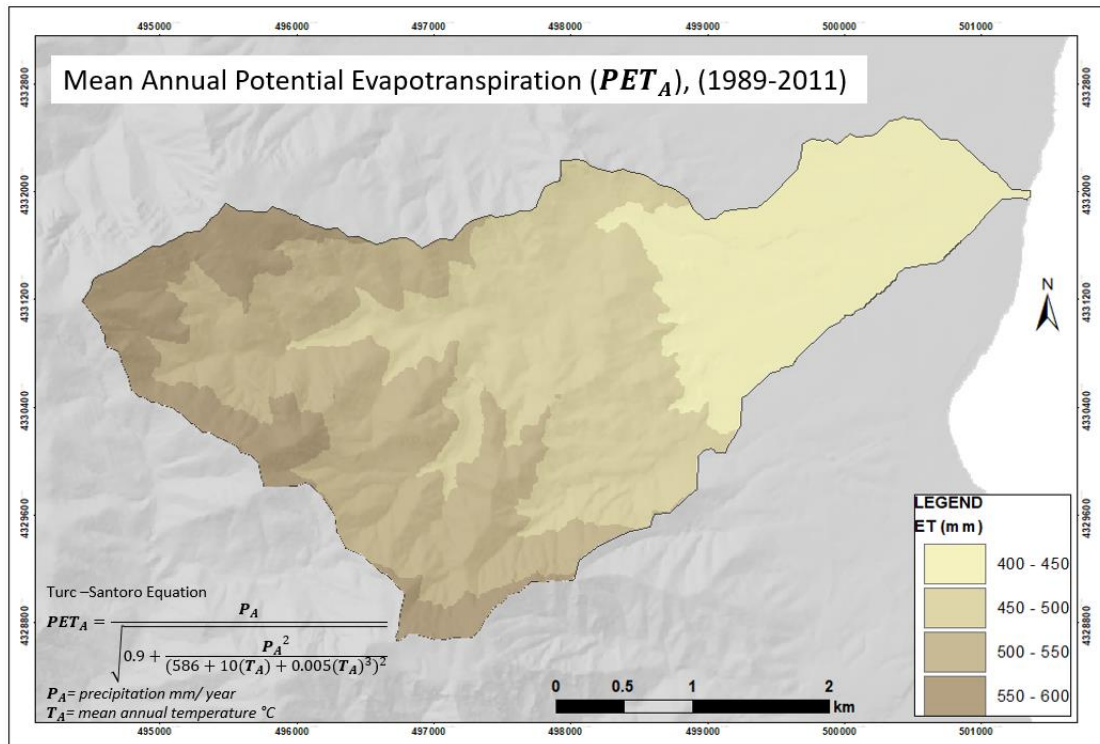


Figure 103 Mean annual potential evapotranspiration map obtained from Turc (1954) equation with the modification of Santoro for Mediterranean arid areas. The map algebra used the maps of precipitation and temperature obtained through linear regression from 1989 to 2011.

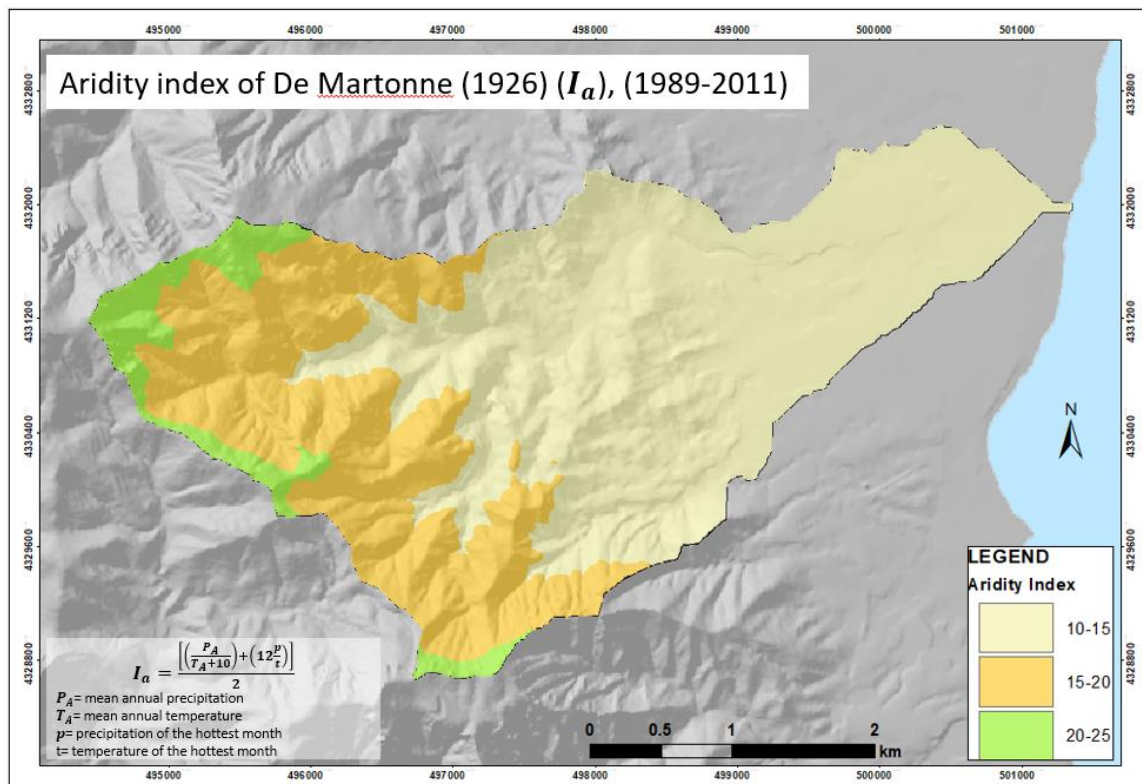


Figure 104 Aridity index map obtained from De Martonne (1926) equation (Equation 25). The map algebra used the maps of precipitation and temperature obtained through linear regression from 1989 to 2011.

5.2.5 Mean Annual Effective Precipitation (P_{Aef})

The map of P_{Aef} was obtained subtracting the PET_A map (5.2.4) to the P_A map (5.2.2). The map of mean annual effective precipitation in the Masoni Ollastru basin exhibits a range of approximately 320 mm of effective precipitation (Table 59). Due to the type of interpolation, the areal precipitation distribution follows the pattern of the topography. The lowest value of P_{Aef} (57.64 mm) is in the lowest area of the basin. The maximum values of P_{Aef} (380.13 mm) are found in the highest area of the basin in the mountains in the west. The mean value of P_{Aef} for the whole basin is 138.54 mm.

Table 59 Statistics for the average annual Effective Precipitation inside the RMO basin.

Average annual Effective Precipitation ($P_{Aef} = P_A - PET_A$)				
Parameter	Min	Max	SD	Mean
Average annual Effective Precipitation (mm)	57.64	380.13	68.47	138.54

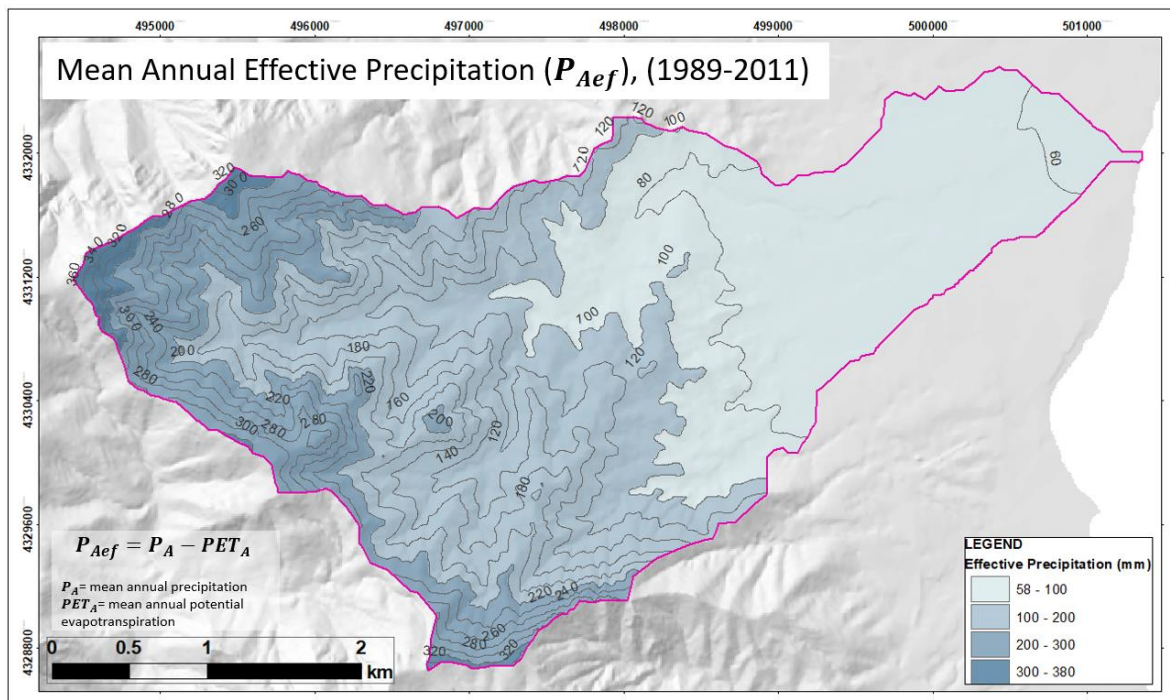


Figure 105 Mean annual effective precipitation. The map algebra used the maps of precipitation obtained through linear regression and potential evapotranspiration from Turc (1954) equation with the modification of Santoro (1970).

5.2.6 Slope coefficient map

The slope coefficient map shows that most of the mountainous area has a slope over 35%, the area meeting the alluvial plain and the floodplain in the mountainous area has a lower slope (10-35%). The coastal plain and small parts of the valley in the middle course of the stream have a low slope (>10%). The area closest to the mouth is the flattest with a slope lower than 3.5%.

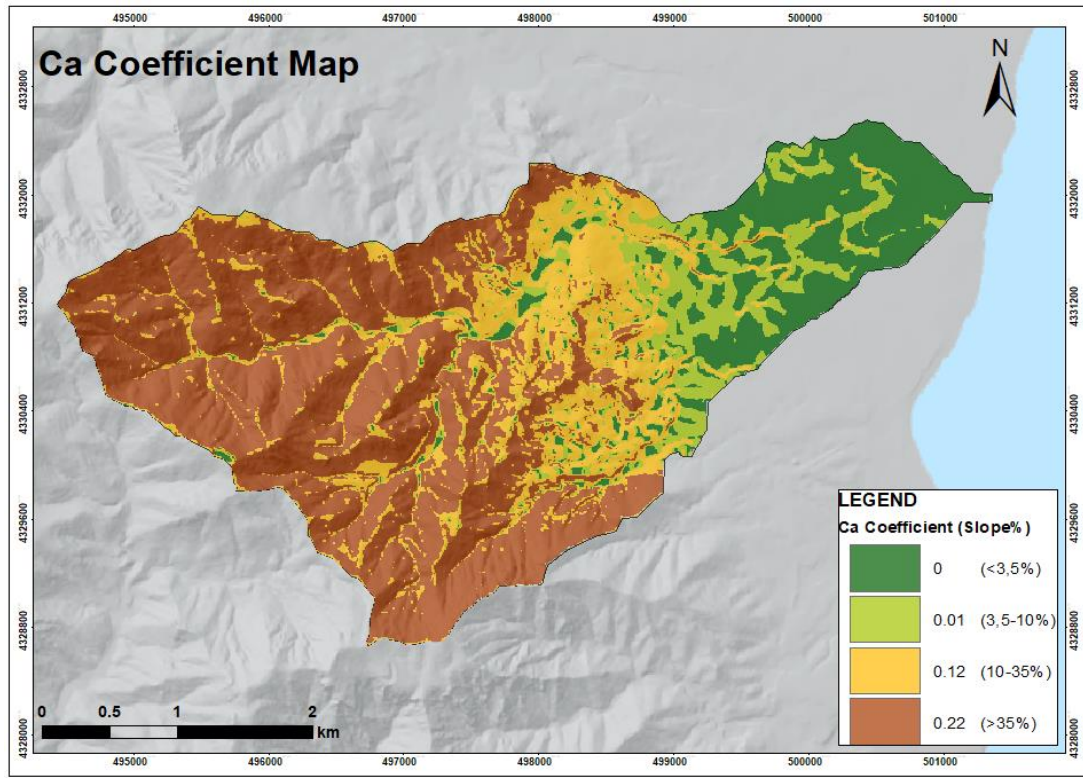


Figure 106 Slope coefficient map

5.2.7 Land use or vegetation map

The land cover coefficient map exhibits a large area covered by woods; this area corresponds to the upper and middle course of the RMO. On the other hand, the lower course of the river in the coastal plain has cultivation, grazing land and areas without vegetation. The widespread land use in the lower course is the cultivation.

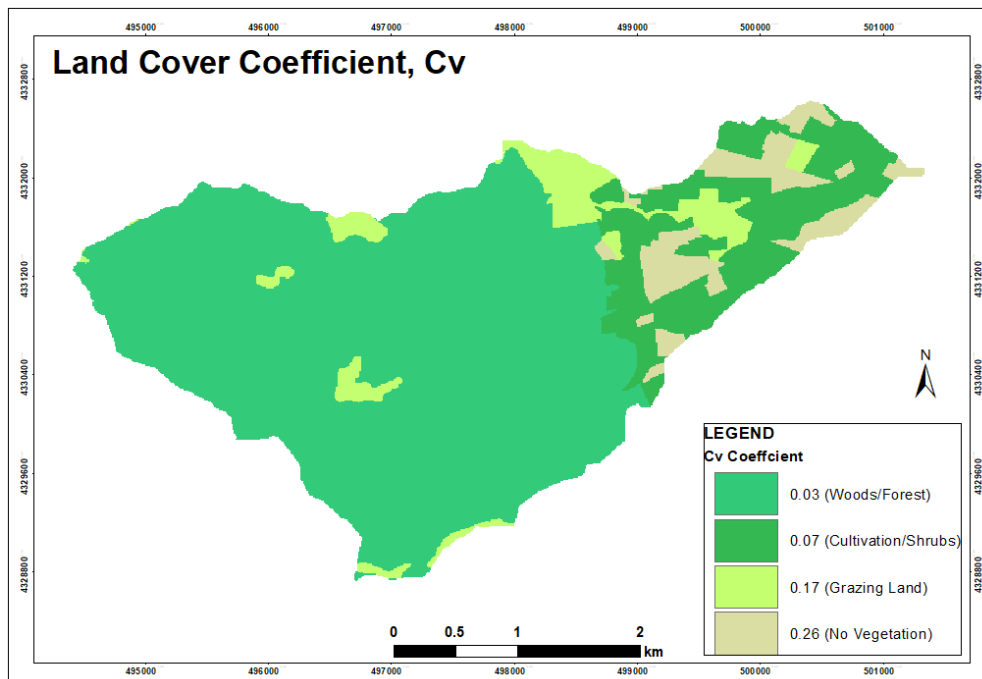


Figure 107 Land cover coefficient map

5.2.8 Permeability Coefficient map

The permeability coefficient map was obtained assigning permeability classes from previous studies in the area for the Holocene and Pleistocene units, from conceptual values for the metamorphic unit, and from calculated values for the plutonic rocks (see §3.2.3 and §4.3.7). The south east margin of the mountainous zone has low permeability due to the metamorphic rock outcropping in that area. The plutonic and dykes complex have good permeability according to the values obtained from the calculation with the cubic law (see §5.1.4). Pleistocene deposits of terraces below the hills where the current streams have not eroded them have a medium permeability. The Holocene deposits in the coastal plain and valleys have good permeability.

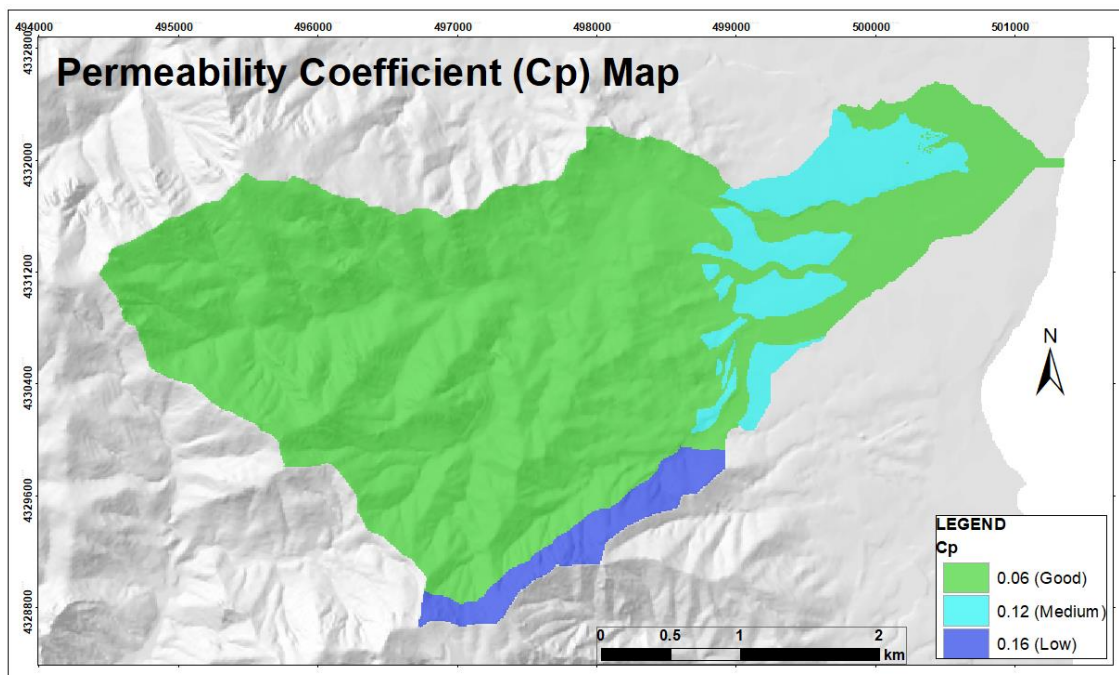


Figure 108 Permeability coefficient map

5.2.9 Runoff coefficient calculation

The surface of the basin belonging to each class of the partial coefficients is related in Table 60. The annual potential runoff coefficient (C_k) in the RMO basin is 0.2730.

The map of the annual potential runoff coefficient gave a mean value of 0.272. The mountainous granitic area has higher values of C_k , mainly between 0.3 and 0.4 in the upper valley and 0.2 to 0.3 in the middle valley. The coastal plain and the valleys have lower values of C_k . The coastal plain C_k values are mainly between 0.1 and 0.2, but the areas without vegetation have 0.3 and 0.4.

Table 60 Calculation of annual potential runoff coefficient C_k . Percent area of the basin that corresponds to each class of the partial coefficients (C_a , C_v and C_p) is multiplied by the values of the classes and added. The addition of the three partial coefficients is the runoff coefficient.

		la < 25	Area km ²	% Area	Partial coefficient * %area
Slope (Ca)	>35%	0.22	6.7134	53.4240	0.1175
	10% < S < 35%	0.12	2.7110	21.5738	0.0259
	3.5% < S < 10%	0.01	1.2465	9.9192	0.0010
	<3.5%	0	1.8953	15.0828	0
	Ca				
Land cover (Cv)	No vegetation	0.26	0.7204	5.7329	0.0149
	Grazing land	0.17	0.8475	6.7442	0.0115
	Cultivation/shrubby	0.07	1.8235	14.5114	0.0102
	Woods/forests	0.03	9.1179	72.5586	0.0218
	Cv				
Permeability (Cp)	Very low	0.21		0.0000	0.0000
	Low	0.16	0.5441	4.3296	0.0069
	Medium	0.12	1.2480	9.9311	0.0119
	Good	0.06	10.7737	85.7359	0.0514
	High	0.03	0	0	0.0000
	Cp				
Potential Runoff coefficient	Total Area		12.5662		
	$C_k = C_a + C_p + C_v$				0.2730

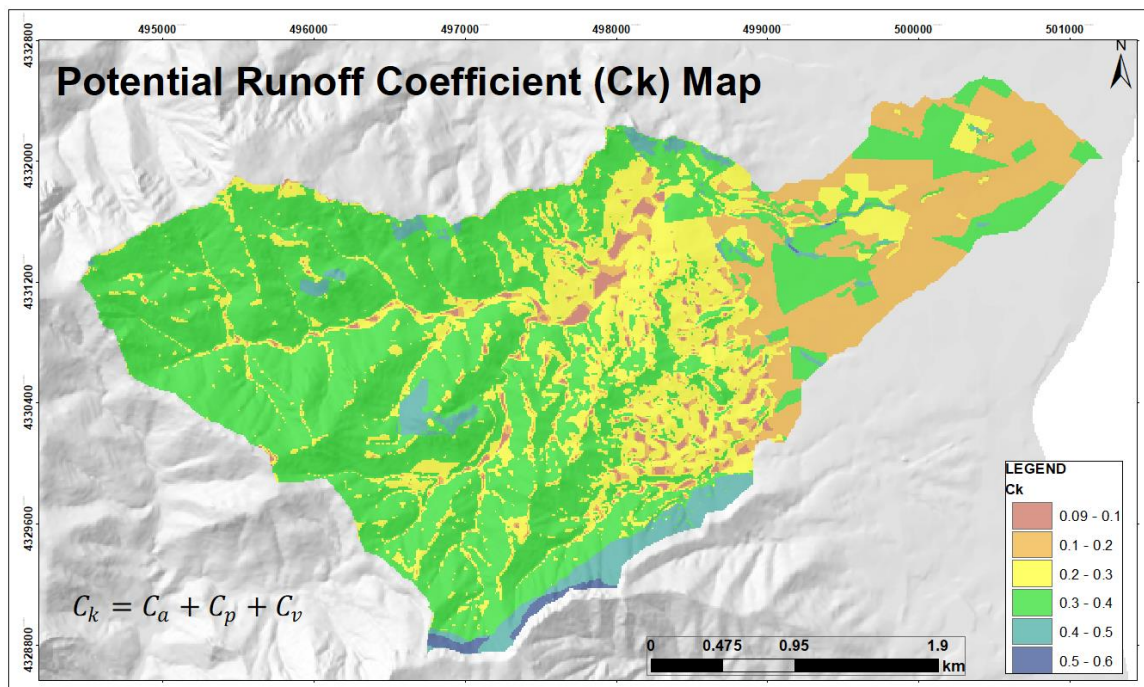


Figure 109 Annual potential runoff coefficient map.

5.2.10 Mean Annual Potential Effective infiltration calculated from the Water Balance

The precipitation and the evapotranspiration mean values and maps used for the water balance were those obtained from the linear regression interpolation and the Turc-Santoro equation, respectively.

The runoff map obtained using the annual potential runoff coefficient is shown in Figure 110. The mean annual potential runoff map shows that the annual potential runoff decreases fast with elevation and is very low and uniform in the coastal plain. The highest potential runoff values in the basin are in the east and south limits and in the spots where there is grazing land. The valleys of the tributaries in the upper and middle basin have lower potential runoff than in the area around them.

The mean annual potential effective infiltration ($I_{e_{Ap}}$) obtained subtracting the PET_A and the R_{Ap} of the P_A ($I_e = P - ET - R$) is shown in the map (Figure 111). The $I_{e_{Ap}}$ decreases with the elevation it has its maximum values in the eastern limit of the basin and the minimum values in the coastal plain. The valleys of the main stream and tributaries have higher values of infiltration than the area surrounding them.

The mean value of the annual runoff map is 39.43 mm. While the mean value of the mean annual potential effective infiltration map is 97.81 mm (Table 61).

Table 61 Statistics for the mean annual potential runoff and mean annual potential effective infiltration maps in the RMO basin. The last four columns compare the mean values obtained from linear regression and unique value.

From precipitation and temperature interpolated with linear regression					Unique value
Parameter	Min	Max	SD	Mean	Capoterra 1
Mean annual potential runoff (mm)	6.69	168.98	24.82	39.43	27.75
Mean annual potential effective infiltration (mm)	27.44	335.86	44.45	97.81	53.25

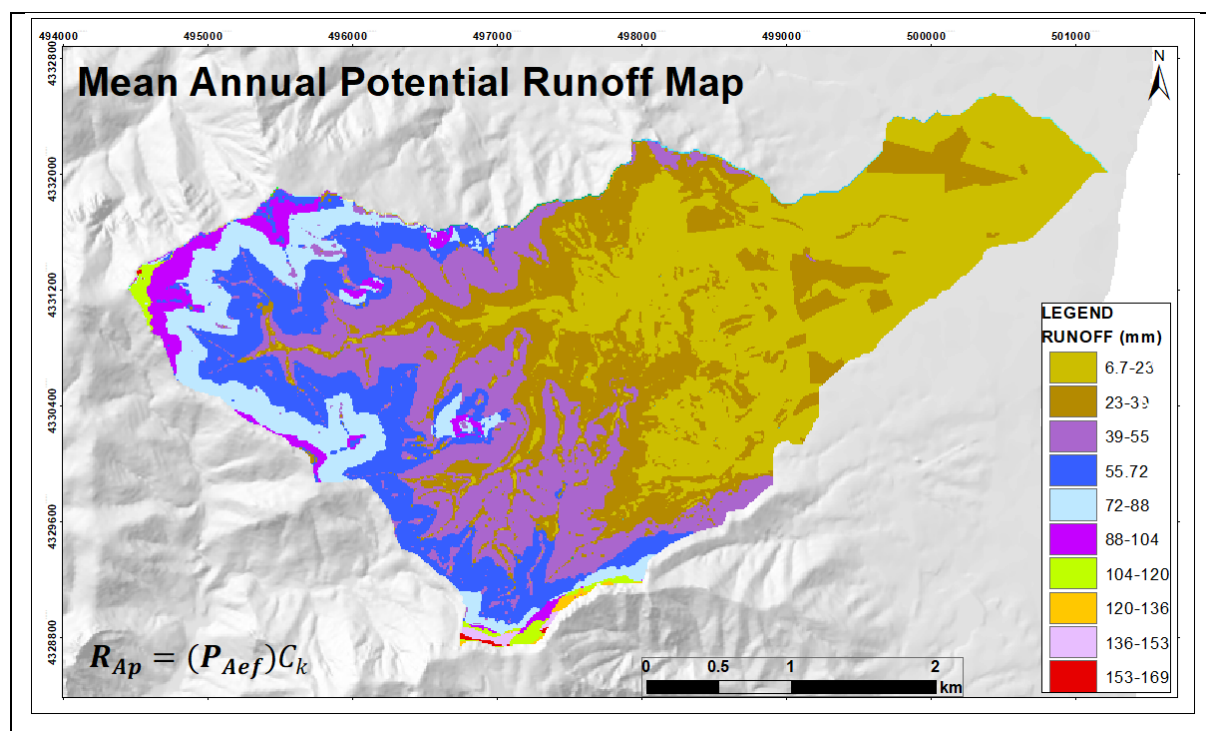


Figure 110 Mean annual potential runoff map

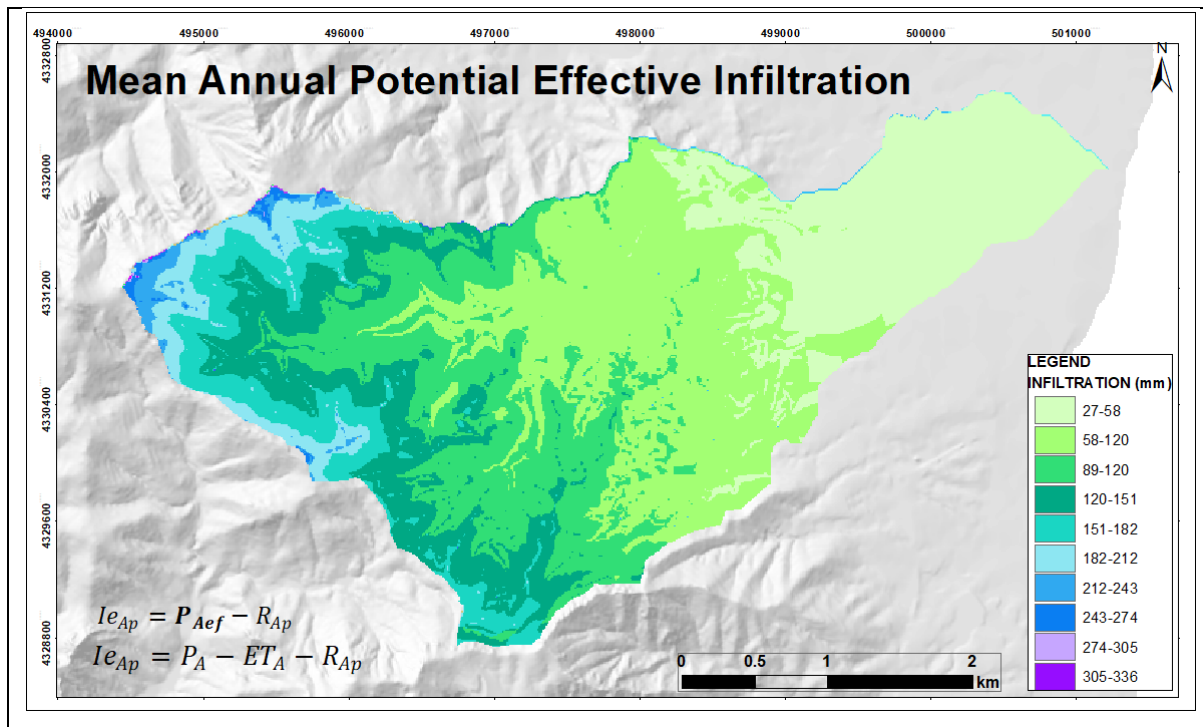


Figure 111 Mean annual potential effective Infiltration map

5.2.11 Streamflow

The flow measurement has allowed realising the behaviour of the stream along the river basin and how it changes in time.

The physiographic indirect method to estimate the mean annual potential runoff was applied for the whole basin and also to smaller sections corresponding with the flow measurement stations to look for correspondence between the indirect and direct method (Table 62). However, the values measured are low compared with the estimated ones. Unfortunately, the flow measuring during 2015, 2016 and 2017 was compromised by the low precipitation. Therefore the use of this data may only be indicative of the behaviour but not useful to estimate quantitative values.

The percentage deviation (PD, Equation 36) between the C_k and C_s for the watersheds is between -22% and 96%. The C_p and the DP was not evaluated for the final section of the river (RMO9, RMO10 and RMO11) because that area was problematic to measure.

Equation 36

$$PD = (C_k - C_s / C_s) * 100$$

In general terms, the discharge increases downstream and grows immediately after a precipitation event. However, the tendency has variations along the basin Table 62. At some stations, the flow decreases, and it increases again in the next station. It is more frequent to find water flowing where the streambed is on rock than in alluvial deposit. When the stream water flows out of the mountain area to the floodplain the discharge tends to decrease, being zero (when the general flow is low) in the bridge on the road Cagliari-Pula (station RMO9).

Table 62 Evaluation of potential runoff coefficient calculated with indirect physiographic method and runoff coefficient calculated with the measured runoff and precipitation in sub-basins.

stations	Average streamflow (m ³ /s)	Area at closure section (m ²)	Runoff Calculated from streamflow (mm)	P_A from linear regression 2015-2016 (mm)	Runoff coefficient $C_s = R_A/P_A$	Potential Runoff coefficient C_k	Percentage deviation C_s and C_k
LFd01	0.004900	618380	143.763	710.171	0.202	0.3010	48.680
RMO01	0.021418	1442903	269.326	694.266	0.388	0.3014	-22.310
RMO02	0.011278	1936755	105.658	675.663	0.156	0.3019	93.089
RMO03	0.019303	2744492	127.612	659.600	0.193	0.3010	55.568
RMO05	0.020671	3798433	107.427	629.263	0.171	0.3010	76.299
RMO06	0.022490	6171543	104.666	607.777	0.172	0.2953	71.483
RMO07	0.035601	7018166	101.801	590.858	0.172	0.2885	67.466
RMO08	0.039377	8019872	83.016	569.200	0.146	0.2867	96.569

Figure 112 Figure 112 Graphic showing the discharge behaviour along the river in October and November of 2015. shows the flow measured in eleven station along the river Masoni Ollastru from the river source to the mouth (Table 63). The streamflow shows tendency to increase downstream, but it decreases from station RMO6 on 8th and 23rd of October and from station RMO8 on 13th of October. The flow also decreased in Stations RMO3a and RMO3 on 6th, 13th and 23rd of October. On 9th and 10th of October rained 32 and 25 mm. The streamflow measured on 13th of October increased respect to the two previous measurement on October. The streamflow decreased to the levels of 6th and 8th on 23rd of October. The stream flow measure in November was lower than that measured in October that is consequent with the precipitation (Figure 113, Figure 114 and Figure 115).

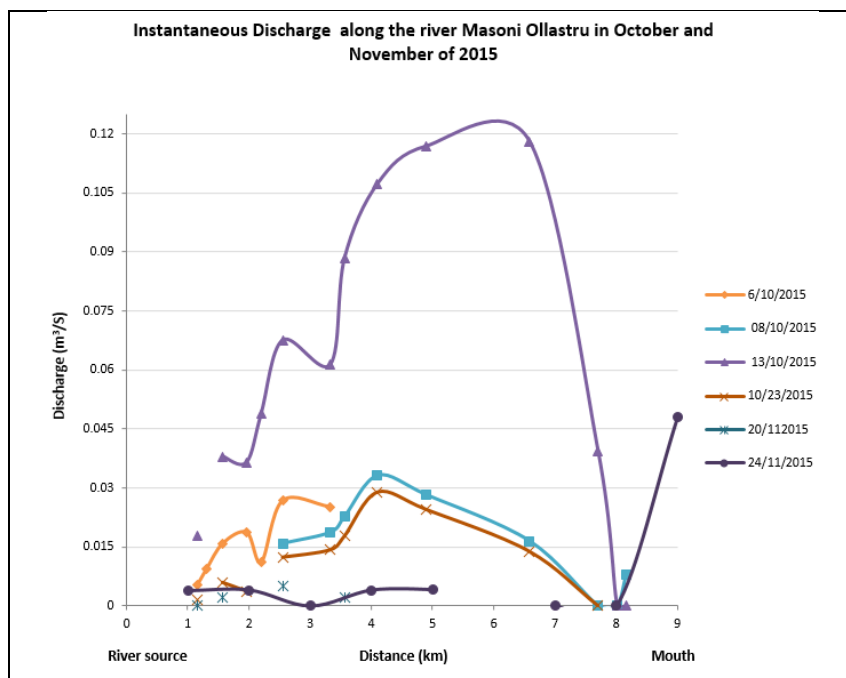


Figure 112 Graphic showing the discharge behaviour along the river in October and November of 2015.

Table 63 Streamflow measured in 12 stations in October and November of 2015 and characteristics of the area of the station.

Station	Distance from river source (km)	Elevation (MASL)	Riverbed material	Geol. Unit
Alft1	1.15	300	Sediments+bedrock	U.I. Santa Barbara
RMO1a	1.3	245	Sediments	U.I. Villacidro
RMO1	1.57	239	Sediments	Alluvial Deposits
RMO2	1.96	201	Sediments	
RMO3a	2.2	170	Sediments +bedrock	
RMO3	2.55	160	Bedrock	
RMO4	3.33	116	Bedrock	
RMO5	3.56	106	Sediments	
RMO6	4.1	84	Sediments	
RMO7	4.89	59	Bedrock	
RMO8	6.58	16	Sediments	Terrace alluvial deposits
RMO9	7.7	3	Artificial Channel	Alluvial Deposits
RMO10	8.01	1		Coastal sediments
RMO11	8.16	0	Sandy beach	Coastal sediments
measurements				

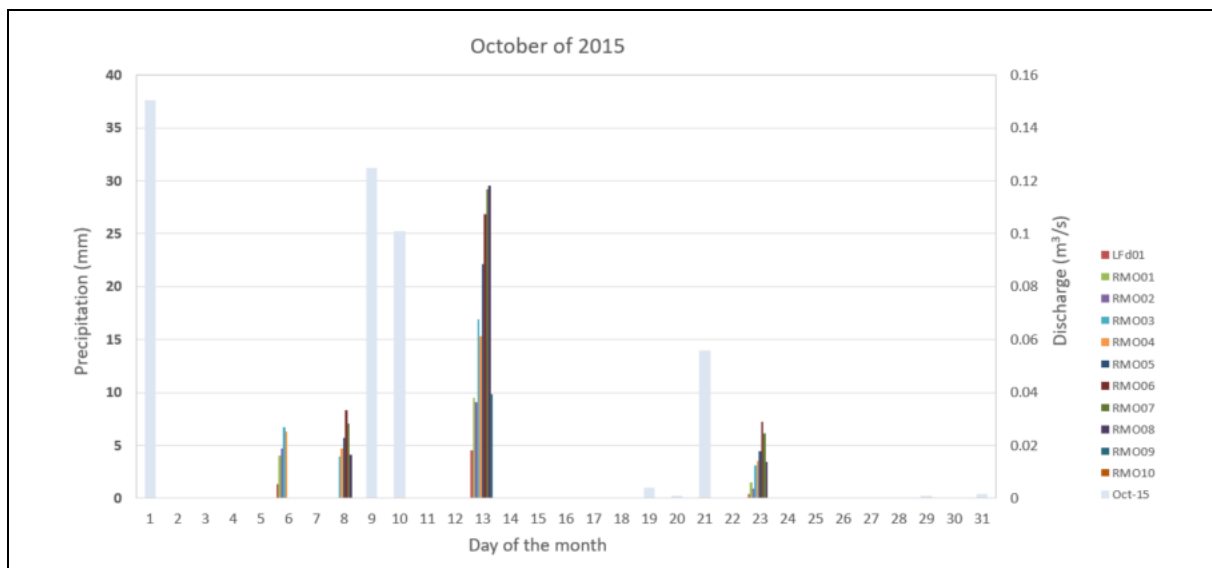


Figure 113 Graphic showing the discharge and the precipitation along the river in on October of 2015

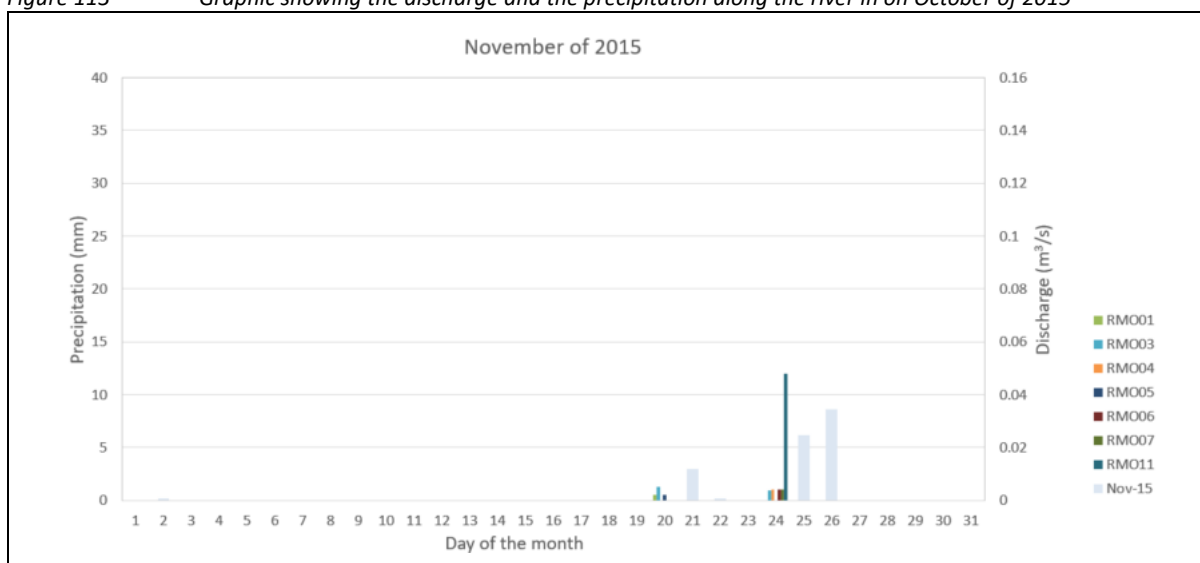


Figure 114 Graphic showing the discharge and the precipitation along the river in on November of 2015

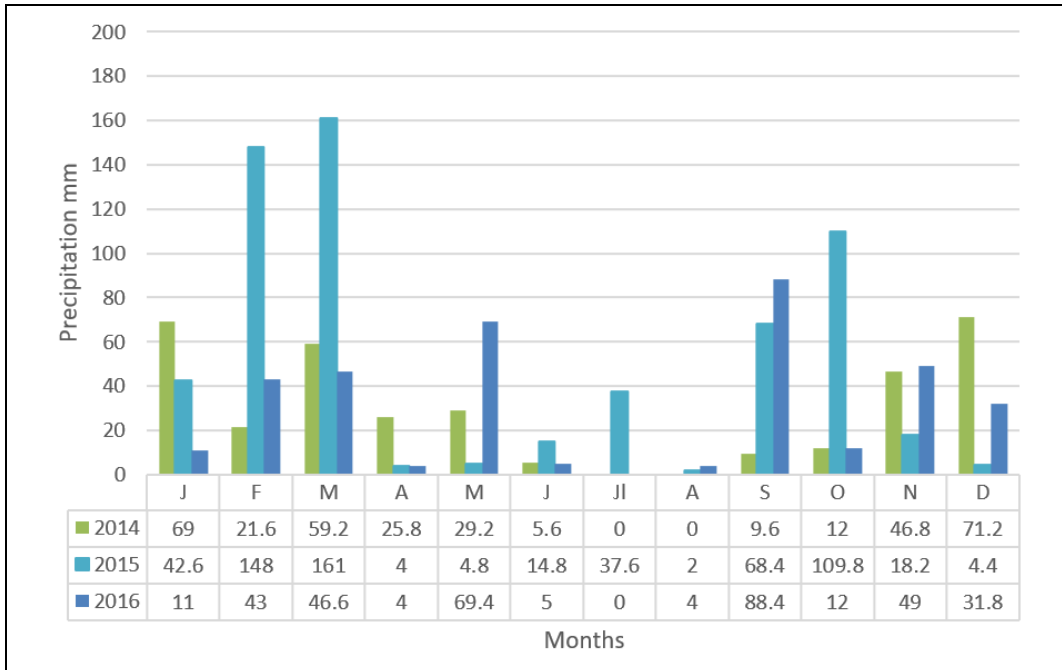


Figure 115 Precipitation in the Capoterra station for the last three years. The current year has been drier, which is reflected in the stream flow of the Masoni Ollastru River.

6 DISCUSSION

The primary objective of this study was to characterise the fracture network to estimate the permeability values in the granitic recharge area of the Masoni Ollastru river basin. In addition, parameters of the water budget were estimated indirectly given that the studied basin is ungauged, to evaluate the hydrogeological potential.

In this study, the values of permeability were calculated applying the continuum approach and the cubic law. It varied in a range of 10^{-8} to 10^{-2} m/s (§5.1.4). These values are in agreement with those reported for fractured granitic rocks: 10^{-8} to 10^{-4} m/s (Freeze and Cherry 1979).

The higher values in the MORB (10^{-4} to 10^{-2} m/s) respond to the wide opening of the aperture in the surface due to exogenous factor (see § 4.2.1). Tensile aperture by the toppling of blocks in valley walls, weathering and erosion were the main processes affecting the aperture. The aperture of the open fractures ranges between 0.4 mm to 30 mm, and 40% is concentrated below 5.2mm. However, as discussed in § 5.1.3, 40 % of the fractures is closed. As the sub-vertical sets have the widest aperture, they contribute more to the permeability. No preferential orientation trend was observed in the sets with wider aperture, although, in six stations the set with wider aperture has more or less the same trend than the slope face. The analysis of the fractures showed that those with dip below 70° have aperture lower than 10mm. While the aperture of the fractures dipping over 70° are mainly below 20mm but can reach higher values.

The flow direction would be mainly influenced by the more frequent and persistent fractures (§2.2.6) that can be classified into sub-vertical (main trends NW-SE, NE-SW and E-W) and sub horizontal. Among them, the fractures trending NE-SW and E-W are more persistent, then they could dominate the flow direction.

The Villacidro and Santa Barbara Intrusive Units can be treated as a single hydrogeological unit as fractures have the same density and the preferential directions (NW-SE, NE-SW and E-W). In contrast, fractures in metasedimentary Formation Pala Manna are less or less evident, and common sets are E-W and N-S.

The areas close to the faults and dykes are more affected by fractures, and the pattern is more heterogeneous. Therefore, the permeability in these areas can be effective.

The map of lineaments density shows higher density in the granitic formations, in the north of the basin, in the elevated areas and near some dykes and faults. The map of the density of intersections of lineaments shows the same trend of density than the lineaments density map.

Although the accuracy and quality of the final DEM were satisfactory (§ 4.2.2), the interpretation of the digital stereo-pairs was negatively affected by the uneven density of the vegetation, sharp relief, shadows and low resolution of the images. These resulted in an overestimation of low length lineaments, due to the difficulty to follow the full trace of a fracture where the vegetation was dense. Nevertheless, the multiscale approach consisting in the integration of data collected in the field with those collected remotely helped to

decrease the uncertainties and limitations, leading to more reliable and representative fractures characterisation.

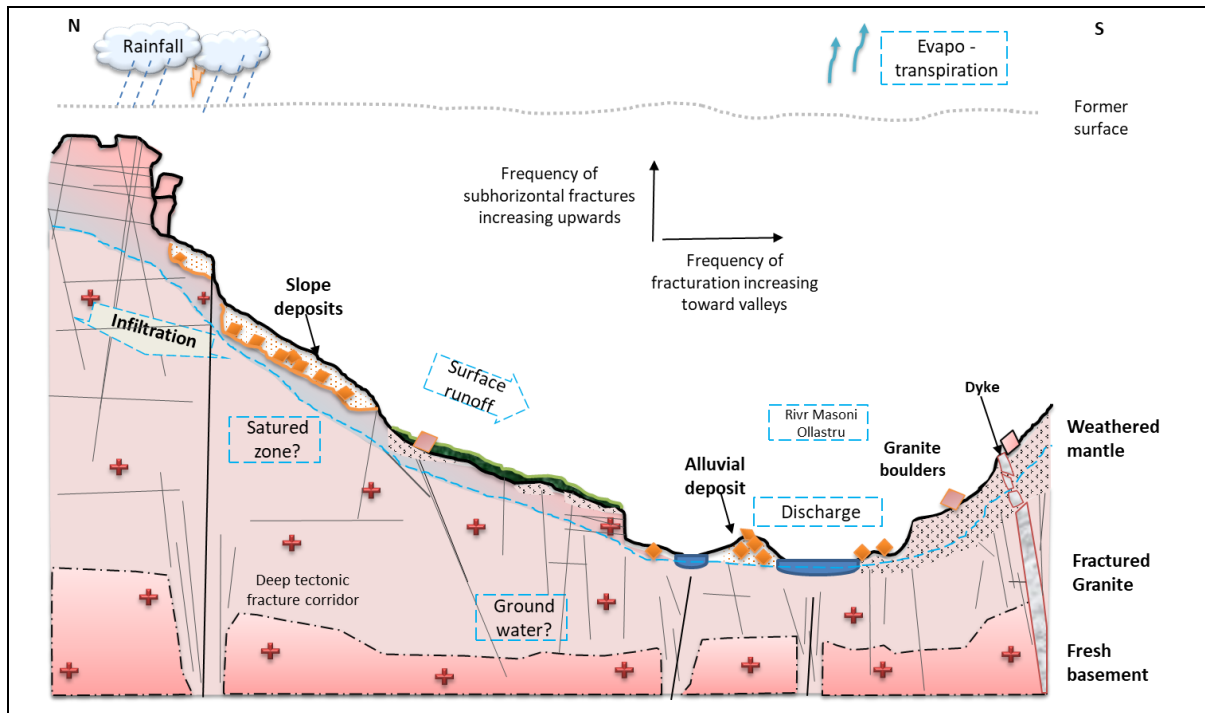


Figure 116 Schematic transversal profile oriented N-S in the mountainous granitic area in MORB showing the hypothesis of the fracture distribution and the possible hydrogeological zonation in the granitic.

According to the available data, in this study, a conceptual hydrogeological model of the granitic aquifer in the MORB has been proposed (Figure 116). For this purpose two different scenarios have been evaluated: the first one concerns a stratiform aquifer in the paleo-weathering profile of the granites (see § 2.1.2 and Figure 3); the second one regards valley incision by differential erosion determined by structural features (fractures density) (Le Coeur, 2014). A possible integration of these models can be adapted to the physiographic conditions of the MORB.

The presence of a stratiform aquifer with a sub-horizontal fissured layer or sub-vertical fissured layers were analysed because the biotitic leucomonzogranite of the Villacidro intrusive Unit and the monzogranite of the Santa Barbara Intrusive Unit exhibit sub-horizontal and sub-vertical fractures. The model of a stratiform aquifer in the granite weathering profile envisages a thick layer of unconsolidated alterite above fissured granite, which is not present in the MORB. In the granites in the south of Sardinia, the abrupt relief and deep valleys and the occurrence of a thin layer of saprolite indicate that the erosion of the granitic bodies is in an advanced stage. Probably, the weathering profile has developed, but the erosion could have removed the unconsolidated layer of alterite and excavated the granite in the weaker zones. Indeed, the study area is located in the western shoulder of the Campidano graben, the most extensional structure in South Sardinia (Casula *et al.* 2001; Cocco *et al.* 2013), that testifies the occurrence of a recent uplift (after Pliocene time) which produced and high relief energy. Some features related to an uplift are also detectable in MORB, as the occurrence of some hanging valleys and possibly fault scarps.

Sub-horizontal fractures are present all along the basin, although, most of the time, the fractures are closed, or their aperture is below 1 mm (mean aperture of 0.125 mm - § 5.1.3).

According to this model, the frequency of the sub horizontal fractures should increase upwards. In MORB the mean spacing of sub horizontal fractures decreases with elevation, therefore the frequency shows a tendency to increase with elevation. Furthermore, near the river bed, the aperture of sub-horizontal fractures seems to be wider than away from the river, probably because they are more affected by erosion. The aperture of the fractures in the stations facing the north, east and west is lower than the aperture for station facing southeast, south and southwest. The slopes facing south are less vegetated and steeper, then more susceptible to erosion, than the slope facing the north. The second scenario is based on the erosional processes that excavate the valleys and morphological depressions in the granite, where the frequency of fractures is higher. For this purposes, the frequency of the fractures was evaluated regarding the position with the valley. It was found that the frequency of the sub-vertical sets is higher in the slopes facing S, SE and E, in the north and the centre of the basin. The aperture does not change with elevation neither between different formations. Spacing of all the fractures is mainly between 0.1 and 1 m. The spacing between fractures dipping below 40° is mainly around 0.3 m and for the fractures dipping over 60° is more concentrated around 0.15 m.

From results discussed in § 5.1.4, the permeability in the shallower granite is about 10^{-3} m/s.

According to the conceptual model, it is expected that it decreases in depth. This was also observed in the adjacent basin of Rio Pula, where the permeability estimated from a well was 10^{-8} m/s (Barrocu 2007).

The evaluation of the water budget allowed to estimate the mean annual potential runoff and mean annual potential effective infiltration of all MORB. The meteorological data obtained from linear regression of the precipitation and temperature against elevation (§5.2.2 and §5.2.3) gave a spatial distribution appropriate to the real data measured. Therefore, the topography would exert a wide control on the remaining water that flows as runoff or that infiltrates.

The range of aridity index (I_a) in the MORB is between 10.5 and 24.6. The climate in the MORB was classified using de aridity index and De Martonne (1926) classification (seven classes) into:

- Area between sea level and 480 MASL is classified as semi-dry ($10 \leq I_a < 20$),
- Area above 480 MASL is classified as Mediterranean ($20 \leq I_a < 24$) and
- A very small area (20m wide, 220 m long) in the highest point (670 MASL) of the basin has semi-humid climate ($24 \leq I_a < 28$).

However, the indirect physiographic method used to estimate the potential runoff coefficient classifies the whole basin into one class: $I_a < 25$. In that way, the C_k was calculated assuming a homogeneous climatic class. Therefore, the potential runoff coefficient spatial variation is controlled only by the slope, land cover and permeability. Given that the evaluation of the permeability of the granitic aquifer resulted in a wide range between 10^{-8} to 10^{-2} m/s and the high spatial variability, the mean value of permeability of the granitic aquifer (3.5×10^{-3} m/s) was assumed for the granitic watershed and also a unique permeability coefficient (C_p) (§ 5.2.8). Thus, the spatial variation of C_k is more dependent on land cover and slope (§ 5.2.9). It would be desirable to evaluated the C_k taking into account spatial variation of permeability in

granitic aquifer. However, it would require a better understanding of the variation of permeability with depth, which is unknown at the present state of the work, giving the lack of direct measurement.

The percentage deviation (PD) between C_s and C_k was high. As it was observed by Ghiglieri et al. (2014) the PD was as high as 63%, but for most of the evaluated basins it was below 30%. It would be convenient to identify the causes of the variation of the validity of the method in Sardinia. However, the C_s was influenced by the variability of the discharge that can be influenced as well by the instrumental error.

The maps of mean annual potential runoff and mean annual potential effective infiltration evidence the control that the elevation exerts on the water areal distribution in the system (§ 5.2.10). In lowlands, where the alluvial aquifer with good permeability (10^{-4} m/s, see § 4.3.7) outcrops, most of the precipitation (479 to 510 mm) is lost like evapotranspiration (421 to 450 mm), resulting in an effective precipitation around 60 mm. Otherwise, in highlands, effective precipitation is higher (up to 380 mm) due to the high precipitation (550mm to 974mm) and lower evapotranspiration (450 mm to 594mm). Therefore, in lowlands almost all effective precipitation infiltrates (more than 60%), while in highlands most of effective precipitation flows like surface runoff (up to 60%). However, higher availability of water in the highlands results in a significant amount of infiltration in absolute value, although for small areas confined at highest altitudes.

Estimating the water budget, especially the mean annual potential effective infiltration, in the granitic area gave an idea of the role and relevance of the granitic aquifer in MORB. As seen before, the higher levels of water available for infiltration are located in the more elevated zones of the basin. According to the values of permeability calculated in surface in the MORB and the fact that the surface water is rapidly absorbed in fractures zones granitic aquifers in Sardinia (Barrocu 2007), such water could be responsible for recharging the granitic aquifer and, partially, for recharging the alluvial aquifer in the coastal plain. The lineaments trending NE-SW and ENE-WSW, almost parallel to the direction of the axis of the basin are the most persistent and continuous (§5.1.1). Those fractures could be helping to transmit the water from the granitic aquifer to the alluvial aquifers in the east. This hypothesis is consequent with the work of Balia et al. (2007) who observed a W-E gradient in the productive alluvial aquifers in the coastal plain of Capoterra. Also, Sciabicca (1994), concluded that the alluvial aquifers are mainly recharged laterally by the fractured granite. However, the lack of wells in the study area to perform piezometric surveys, does not allow confirming this hypothesis. Building some observation wells could be a follow up of the study to validate the conceptual model.

7 CONCLUSION

- The results showed the validity of a multiphase methodology with a multiscale approach to propose a hydrogeological conceptual model in a hard rock aquifer. The use of geomechanical survey and photogeology decreased the uncertainties and limitations in characterizing fractures network.
- The high permeability calculated using the cubic law is highly conditioned by the fractures aperture. As the fractures are open mainly on the surface, because of alteration and low confining stress condition, the resulting permeability is overestimate if referred to the whole aquifer. In fact, the apertures of fractures decrease in depth, consequently the permeability.
- The model of the fissured layer can be applied, given the fracture distribution and the geological context. The model regarding the selective erosion controlled by structural features is consequent with the fracture density and the geomorphology seen in the valley.
- Furthermore, the sub vertical fractures can act as the path of infiltration of meteoric water and the sub horizontal fractures interconnect the fracture network enhancing the circulation. The high density of sub horizontal fracture in the ridges and the higher density of sub vertical fractures in the valleys should give a staggered flow path dominated by horizontal flow uphill and by vertical flow downhill. The fractures in the valley and in the fault zone could be feeding the groundwater in depth.
- Regarding the water budget, the results demonstrate that the precipitation and temperature can be correlated with the elevation to achieve a good representation of their real areal distribution.
- The parameters of the hydrological cycle are dependent on morphology and land use.
- The understanding of recharge, circulation and continuity of the granitic aquifer in depth is limited by lack of direct measurements.
- The annual potential runoff coefficient, mean annual potential runoff and mean annual potential effective infiltration estimated indirectly can be used as a qualitative representation and a validation with available data would be advisable.
- The assumptions regarding the circulation between aquifers are based in considerations of shallow flow that should be supported by a further understanding of the groundwater.

8 REFERENCES

Allen, R. G., Pereira, L. S., Raes, D., and Smith, M. (1998). Crop evapotranspiration-Guidelines for computing crop water requirements-FAO Irrigation and drainage paper 56. FAO, Rome, 300(9), D05109.

Allmendinger, R. W., Cardozo, N., and Fisher, D. M. (2011). Structural geology algorithms: Vectors and tensors. Cambridge University Press.

Atkinson, L. C. (2000). The role and mitigation of groundwater in slope stability. *Slope Stability in Surface Mining*, 427-434.

Balia, R., Ardaù, F., Barrocu, G., Gavaudo, E., and Ranieri, G. (2009). Assessment of the Capoterra coastal plain (southern Sardinia, Italy) by means of hydrogeological and geophysical studies. *Hydrogeology journal*, 17(4), 981-997.

Banfield, J.F., and Eggleton, R.A. (1990). Analytical transmission electron micro-scope studies of plagioclase, muscovite, and K-feldspar weathering. *Clays Clay Minerals*, 38, 71–89.

Barazzuoli, P., Izzo, S., Menicori, P., Micheluccini, M., and Salleolini, M. (1989). A new practical aid to regional hydrogeologic planning: the runoff coefficient map. *Environmental Management*, 13(5), 613-622

Barca, S., Serri, R., Rizzo, R., Forci, A., Calzia, P., and Pertusati, P. C. (2009). Note Illustrative della Carta Geologica d'Italia alla scala 1: 50.000, Foglio 565, Capoterra. ISPRA, Sardegna, Italy.

Barrocu, G. (1971, October). Idrogeologia sotterranea dei graniti cataclastici della valle del Rio San Gerolamo fra Monte su Sinzuru e Monte Pauliara (Capoterra-Sardegna Meridionale)[Underground hydrogeology of the cataclastic granites of the Rio San Gerolamo valley, between Monte su Sinzuru and Monte Pauliara (Capoterra-southern Sardinia)]. Proceedings of the Symposium Internazionale sulle acque sotterranee nelle rocce cristalline, Cagliari, 25-26.

Barrocu, G., Sciabica, M.G., Uras, G., Cortis, A., Vernier, E. (1997, November) Saltwater intrusion and artificial recharge modelling in the coastal aquifer system of Capoterra (Southern Sardinia). In Proceedings of the Conference on Water Problems in the Mediterranean Countries, Nicosia, 17–21.

Barrocu, G. (2007). Hydrogeology of granite rocks in Sardinia. In: Krasny J., and Sharp J.M. (Eds), *Groundwater in fractured rocks*. Taylor & Francis, London, 33-44.

Barton, N., and Choubey, V. (1977). The shear strength of rock joints in theory and practice. *Rock mechanics*, 10(1-2), 1-54.

Barton, N. (1982). Modelling rock joint behaviour from in situ block tests: implications for nuclear waste repository design. Terra Tek, Inc., Salt Lake City, UT (USA). (No. ONWI-308).

Barton, N., Bandis, S., and Bakhtar, K. (1985, June). Strength, deformation and conductivity coupling of rock joints. In *International Journal of Rock Mechanics and Mining Sciences and Geomechanics Abstracts*, Pergamon, 22 (3), 121-140).

Barton, N. (1988). Some aspects of rock joint behaviour under dynamic conditions. *Secondo ciclo di conferenze di Meccanica e Ingegneria delle Rocce*, Torino, 17, 1-14.

- Beer, A. J., Stead, D., and Coggan, J. S. (2002). Technical note estimation of the joint roughness coefficient (JRC) by visual comparison. *Rock mechanics and rock engineering*, 35(1), 65-74.
- Beven, K. J. (2011). *Rainfall-runoff modelling: the primer*. John Wiley & Sons, 449 p.
- Bieniawski, Z. T. (1984). *Rock mechanics design in mining and tunneling*. A.A. Balkema, Rotterdam, 272 p.
- Bieniawski, Z. T. (1989). *Engineering rock mass classifications: a complete manual for engineers and geologists in mining, civil, and petroleum engineering*. John Wiley & Sons, 251 p.
- Bidgoli, M. N., and Jing, L. (2015). Water pressure effects on strength and deformability of fractured rocks under low confining pressures. *Rock Mechanics and Rock Engineering*, 48(3), 971-985.
- Black, P. E. (1997). Watershed functions. *Journal of the American Water Resources Association* 33(10), 1–11.
- Blöschl, G. (Ed.). (2013). *Runoff prediction in ungauged basins: synthesis across processes, places and scales*. Cambridge University Press.
- Bossard, M., Feranec, J., Otahel, J., and Steenmans, C. (2000). *The revised and supplemented Corine land cover nomenclature*. European Environment Agency, Copenhagen K.
- Boulos, M. N. K., and Robinson, L. R. (2009). Web GIS in practice VII: stereoscopic 3-D solutions for online maps and virtual globes. *International Journal of Health Geographics*, 2009, 8(1), 1-12. <https://doi.org/10.1186/1476-072X-8-59>
- Boutt, D. F., Diggins, P., and Mabee, S. (2010). A field study (Massachusetts, USA) of the factors controlling the depth of groundwater flow systems in crystalline fractured-rock terrain. *Hydrogeology Journal*, 18(8), 1839-1854.
- Bouwer, H. (1978). *Groundwater hydrology*. McGraw-Hill Book, New York, 480p.
- Brugioni, M., Consumi, F., Mazzanti, B., Menduni, G., and Montini, G. (2008). Determinazione dell'infiltrazione efficace alla scala di bacino finalizzata alla individuazione delle aree a diversa disponibilità di risorse idriche sotterranee. *Atti del simposio "Stato del territorio e delle risorse naturali in Toscana, 23-25 ottobre 2008"*, Ordine dei Geologi della Toscana, Firenze 2008.
- Bucher, K., and Stober, I. (2000). The composition of groundwater in the continental crystalline crust. In *Hydrogeology of crystalline rocks*. Springer, Dordrecht. 141-175
- Cardozo, N., and Allmendinger, R. W. (2013). Spherical projections with OSXStereonet. *Computers and Geosciences*, 51, 193-205.
- Carmignani, L. (2001). *Memorie descrittive della carta geologica d'Italia (Vol. 60)*. Italy. Servizio geologico nazionale.
- Casula, G., Cherchi, A., Montadert, L., Murru, M., and Sarria, E. (2001). The Cenozoic graben system of Sardinia (Italy): geodynamic evolution from new seismic and field data. *Marine and Petroleum Geology*, 18(7), 863-888.
- Chilton, P. J., and Foster, S. S. D. (1995). Hydrogeological characterisation and water-supply potential of basement aquifers in tropical Africa. *Hydrogeology Journal*, 3(1), 36-49.

- Cocco F., Funedda A., Patacca E., and Scandone P. (2013). Plio-Pleistocene extensional tectonics in the Campidano graben (SW Sardinia, Italy): preliminary note. *Rendiconti Online Società Geologica Italiana*, 2013,29, 31-34.
- Courtois, N., Lachassagne, P., Wyns, R., Blanchin, R., Bougaïré, F. D., Somé, S., and Tapsoba, A. (2010). Large-Scale Mapping of Hard-Rock Aquifer Properties Applied to Burkina Faso. *Groundwater*, 48(2), 269-283.
- Costantini, E. A., Fantappiè, M., and L'Abate, G. (2013). Climate and pedoclimate of Italy. In *The soils of Italy*. Springer, Dordrecht, 19-37
- Cuccuru, S., Naitza, S., Secchi, F., Puccini, A., Casini, L., Pavanetto, P., and Oggiano, G. (2016). Structural and metallogenic map of late Variscan Arbus Pluton (SW Sardinia, Italy). *Journal of Maps*, 12(5), 860-865.
- Cundall, P. A. (1988, June). Formulation of a three-dimensional distinct element model—Part I. A scheme to detect and represent contacts in a system composed of many polyhedral blocks. In *International Journal of Rock Mechanics and Mining Sciences and Geomechanics Abstracts*. Pergamon, 25(3), 107-116.
- Dardashti, A. F., and Ajalloeian, R. (2015). Evaluation of hydraulic aperture of the joints of Behesht Abad Dam foundation, Iran. *Open Journal of Geology*, 5(6), 375.
- Davis, S. N., and DeWiest, R. J. (1966). *Hydrogeology* (No. 551.49 D3).
- Day-Lewis, F. D., Hsieh, P. A., and Gorelick, S. M. (2000). Identifying fracture-zone geometry using simulated annealing and hydraulic-connection data. *Water Resources Research*, 36(7), 1707-1721.
- Dearman, W. R. (2013). *Engineering geological mapping*. Elsevier, 396p.
- Delitala, A., Cesari, D., Chessa, P. A., and Ward, M. N. (2000). Precipitation over Sardinia (Italy) during the 1946–1993 rainy seasons and associated large-scale climate variations. *International Journal of Climatology*, 20(5), 519-541.
- De Martonne, E. (1926). L'indice d'aridité. *Bulletin de l'Association de géographes français*. 3(9), 3-5.
- Detto, M., Montaldo, N., Albertson, J. D., Mancini, M., and Katul, G. (2006). Soil moisture and vegetation controls on evapotranspiration in a heterogeneous Mediterranean ecosystem on Sardinia, Italy. *Water Resources Research*, 42, W08419, doi:10.1029/2005WR004693.
- Devia, G. K., Ganasri, B. P., and Dwarakish, G. S. (2015). A review on hydrological models. *Aquatic Procedia*, 4, 1001-1007.
- Dewandel, B., Lachassagne, P., Wyns, R., Maréchal, J. C., and Krishnamurthy, N. S. (2006). A generalized 3-D geological and hydrogeological conceptual model of granite aquifers controlled by single or multiphase weathering. *Journal of Hydrology*, 330(1-2), 260-284.
- Díaz Delgado, C., Esteller Alberich, M. V., and López-Vera, F. (2006). Recursos Hídricos: Conceptos básicos y estudios de caso en Iberoamérica. *Red Iberoamericana de Potabilización y Depuración del Agua*, Centro Interamericano de Recursos de Agua, Facultad de Ingeniería, Universidad Autónoma del Estado de México (México) y Piriguazú ediciones (Uruguay)
- Dobesch, H., Dumolard, P., and Dyras, I. (Eds.). (2013). *Spatial interpolation for climate data: the use of GIS in climatology and meteorology*. John Wiley & Sons.

- Dyras, I., and Ustrnul, Z. (2007). The spatial analysis of the selected meteorological fields in the example of Poland. In *Spatial interpolation for climate data: the use of GIS in climatology and meteorology*. John Wiley & Sons. 87-96
- Elkhoury, J. E., Brodsky, E. E., and Agnew, D. C. (2006). Seismic waves increase permeability. *Nature*, Nature Publishing Group, 441(7097), 1135.
- Farina, D., and Gaspari, A. (1990, August). Application of the Kennesey method for the determination of the runoff coefficient and evaluation of aquifer recharge in mountain regions. In *Proceedings of the Symposium on Improved Methods of Hydrological Measurements in Mountain Areas and the Symposium on Quantitative and Qualitative Water Cycle Aspects in Heterogeneous Basins*. 553-556.
- Farmin, R. (1937). Hypogene exfoliation in rock masses. *Journal of Geology*, 45, 625–635.
- Feng, X., Vico, G., and Porporato, A. (2012). On the effects of seasonality on soil water balance and plant growth. *Water Resources Research*, 48, W05543, doi:10.1029/2011WR011263.
- Fossen, H. (2016). *Structural geology*. Cambridge University Press, 509p, doi:10.1017/CBO9780511777806.
- Freeze, R. A., and Cherry, J. A. (1979). *Groundwater*. Englewood Cliffs, NJ: Prentice-Hall Inc, 604p.
- Ghiglieri, G., Carletti, A., and Pittalis, D. (2014). Runoff coefficient and average yearly natural aquifer recharge assessment by physiography-based indirect methods for the island of Sardinia (Italy) and its NW area (Nurra). *Journal of hydrology*, 519, 1779-1791.
- Gillespie, M. R., Barnes, R. P., and Milodowski, A. E. (2011). British Geological Survey scheme for classifying discontinuities and fillings. British Geological Survey.
- Gillespie, P. A., Howard, C. B., Walsh, J. J., and Watterson, J. (1993). Measurement and characterisation of spatial distributions of fractures. *Tectonophysics*, 226(1-4), 113-141.
- Gilli, É., Mangan, C., and Mudry, J. (2012). *Hydrogeology: objectives, methods, applications*. CRC Press, 365p.
- Goovaerts, P. (2000). Geostatistical approaches for incorporating elevation into the spatial interpolation of rainfall. *Journal of Hydrology*, 228(1-2), 113-129.
- Grillone, G., Baiamonte, G., and D'Asaro, F. (2014). Empirical determination of the average annual runoff coefficient in the Mediterranean area. *American Journal of Applied Sciences*, 11(1), 89-95. doi:10.3844/ajassp.2014.89.95
- Guglielmi, Y., Cappa, F., and Binet, S. (2005). Coupling between hydrogeology and deformation of mountainous rock slopes: Insights from La Clapière area (Southern Alps, France). *Comptes Rendus Geoscience*, 337(13), 1154-1163.
- Guillou-Frottier L., Beauvais A., Wyns R., Bailly L., Augé T., Audion A.S. (2015). Formation of corrugations during weathering of ultramafic rocks. In *Actes de la Conférences « Aquifères de socle: le point sur les concepts et les applications opérationnelles»*. In 20èmes Journées techniques du Comité Français d'Hydrogéologie de l'Association Internationale des Hydrogéologues. 11-13 Juin 2015, Auditorium ICES, La Roche-sur-Yon, Vendée, France, 8 p
- Hakami, E. (1995). Aperture distribution of rock fractures. Doctoral dissertation, Department of civil and Environmental Engineering, Royal Institute of Technology. Stockholm.

- Hardin, E., Barton, N., Lingle, D., Board, M., and Voegele, M. (1982). Heated flatjack test series to measure the thermomechanical and transport properties of in situ rock masses (heated block test) (No. ONWI-260). Terra Tek, Inc., Salt Lake City, UT (USA).
- Hill, S. M., Ollier, C. D., and Joyce, E. B. (1995). Mesozoic deep weathering and erosion-an example from Wilsons promontory, Australia. *Zeitschrift fur Geomorphologie*, 39(3), 331-339.
- Hoek, E., and Bray, J. D. (1981). *Rock slope engineering*. CRC Press
- Holmes, R. M., and Robertson, G. W. (1959). A modulated soil moisture budget. Plant Research Institute, Research Branch, Canada Department of Agriculture.
- Holzhausen, G.R., (1989). Origin of sheet structure, 1. Morphology and boundary conditions. *Engineering Geology*, 27(1-4), 225-278.
- Hsieh, P. A., and Shapiro, A. M. (1996). Hydraulic characteristics of fractured bedrock underlying the FSE well field at the Mirror Lake site, Grafton County, New Hampshire. In US Geol. Surv. Toxic Substances Hydrol. Progr., Proc. Tech. Mtg., Colorado Springs, CO. 20–24 Sept. 1993. USGS, Reston, VA. Water-Resour. Invest. Rep. 94-4015.
- Hudson, J. A., and Priest, S. D. (1979, December). Discontinuities and rock mass geometry. In *International Journal of Rock Mechanics and Mining Sciences and Geomechanics Abstracts*. Pergamon, 16(6), 339-362.
- Hudson, J. A., and Priest, S. D. (1983, April). Discontinuity frequency in rock masses. In *International Journal of Rock Mechanics and Mining Sciences and Geomechanics Abstracts* Pergamon, 20(2), 73-89.
- International Society for Rock Mechanics (ISRM) (1981) *Suggested Methods for the Quantitative Description of Discontinuities in Rock Masses* (ed. E. T. Brown). Pergamon Press, Oxford, UK, 211 p.
- Jahns, R. H. (1943). Sheet structure in granites: its origin and use as a measure of glacial erosion in New England. *The Journal of Geology*, 51(2), 71-98
- Kalinin, G. P., (1971): *Global Hydrology*. Israel Program for Scientific Translations, 309 pp.
- Kelkar, S., WoldeGabriel, G., and Rehfeldt, K. (2016). Lessons learned from the pioneering hot dry rock project at Fenton Hill, USA. *Geothermics*, 63, 5-14.
- Kennessey B., (1930). Lefolyasi tènnyezok ès retencick. *Vizugy, Kuziemények*.
- Király, L. (1969). Statistical analysis of fractures (orientation and density). *Geologische Rundschau*, 59(1), 125-151.
- Király, L. (1971). Groundwater flow in heterogeneous, anisotropic fractured media: A simple two-dimensional electric analogue. *Journal of Hydrology*, 12(3), 255-261.
- Lachassagne, P., Wyns, R., and Dewandel, B. (2011). The fracture permeability of hard rock aquifers is due neither to tectonics, nor to unloading, but to weathering processes. *Terra Nova*, 23(3), 145-161.
- Lachassagne, P., Dewandel, B., and Wyns, R. (2014). The conceptual model of weathered hard rock aquifers and its practical applications. In *Fractured Rock Hydrogeology*, 13-46.

- Le Borgne, T., Bour, O., Paillet, F. L., and Caudal, J. P. (2006). Assessment of preferential flow path connectivity and hydraulic properties at single-borehole and cross-borehole scales in a fractured aquifer. *Journal of Hydrology*, 328(1-2), 347-359.
- Le Borgne, T., Paillet, F., Bour, O., and Caudal, J. P. (2006a). Cross-borehole flowmeter tests for transient heads in heterogeneous Aquifers. *Groundwater*, 44(3), 444-452.
- Le Borgne, T., Bour, O., Riley, M. S., Gouze, P., Pezard, P. A., Belghoul, A., and Isakov, E. (2007). Comparison of alternative methodologies for identifying and characterizing preferential flow paths in heterogeneous aquifers. *Journal of Hydrology*, 345(3-4), 134-148.
- Le Coeur, C. (2014). Scenic Granitic Landscapes of Corsica. In *Landscapes and Landforms of France*. Springer, Dordrecht, 241-249
- Lin, L., Lin, H., and Xu, Y. (2014). Characterisation of fracture network and groundwater preferential flow path in the Table Mountain Group (TMG) sandstones, South Africa. *Water SA*, 40(2), 263-272
- Linsley, R. K., Kohler, M. A., and Paulhus, J. (1958). *Hydrology for engineers*. McGraw-Hill, 333p
- Lisle, R. J., and Leyshon, P. R. (2004). *Stereographic projection techniques for geologists and civil engineers*. Cambridge University Press, 112p.
- Lobina, M. F. (2010). Piano di indagine preliminare. Comune di Capoterra - Provincia di Cagliari, sistemazione idraulica del Rio San Girolamo-Masone Ollastu ed interventi di ricostruzione delle opere pubbliche danneggiate nella località Poggio dei Pini ed altre frazioni studio.
- López-Moreno, J. I., Hess, T. M., and White, S. M. (2009). Estimation of reference evapotranspiration in a mountainous mediterranean site using the Penman-Monteith equation with limited meteorological data. *Pirineos*, 164, 7-31.
- Mabee, S. B., Curry, P. J., and Hardcastle, K. C. (2002). Correlation of lineaments to ground water inflows in a bedrock tunnel. *Groundwater*, 40(1), 37-43.
- Mahmoud, S. H., Mohammad, F. S., and Alazba, A. A. (2014). Determination of potential runoff coefficient for Al-Baha Region, Saudi Arabia using GIS. *Arabian Journal of Geosciences*, 7(5), 2041-2057.
- Manda, A. K., Mabee, S. B., Boutt, D. F., and Cooke, M. L. (2013). A method of estimating bulk potential permeability in fractured-rock aquifers using field-derived fracture data and type curves. *Hydrogeology Journal*, 21(2), 357-369.
- Mandl, G. (2005). *Rock joints*. Berlin: Springer. <https://doi.org/10.1007/b137623>
- Marrett, R. and Allmendinger, R.W., (1991). Estimates of strain due to brittle faulting: sampling of fault populations. *Journal of Structural Geology*. Elsevier, 13(6), 735-738.
- Mauldon, M., and Dershowitz, W. (2000). A multi-dimensional system of fracture abundance measures. In *Geological Society of America Abstracts with Programs*, 32(7).
- Mazza, R., La Vigna, F., and Alimonti, C. (2014). Evaluating the available regional groundwater resources using the distributed hydrogeological budget. *Water Resources Management*, 28(3), 749-765.
- McCuen, R. H. (1998). *Hydrologic design and analysis*. Prince Hall, New Jersey, 814p.

- McDonnell, J. J., Sivapalan, M., Vaché, K., Dunn, S., Grant, G., Haggerty, R., Hinz, C., Hooper, R., Kirchner, J., Roderik, M. L., Selker, J., and Weiler, M. (2007). Moving beyond heterogeneity and process complexity: A new vision for watershed hydrology. *Water Resources Research*, 43, W07301, doi:10.1029/2006WR005467.
- McMahon, T. A., Finlayson, B. L., Haines, A. T., and Srikanthan, R. (1992). *Global runoff: continental comparisons of annual flows and peak discharges*. Catena Verlag, Cremlingen-Destedt, Germany, 166p.
- Michel, J. P., and Fairbridge, R. W. (1992). *Dictionary of Earth Sciences: English-French/French-English*.
- Milly, P. C. D., and Dunne, K. A. (2002). Macroscale water fluxes 2. Water and energy supply control of their interannual variability. *Water Resources Research*, 38(10).
- Milne, D., Germain, P., and Potvin, Y., (1992). Measurement of Rock Mass Properties for Mine Design. In *Proceedings of the ISRM-Eurock Symposium on Rock Characterization*, A.A. Balkema Publishers, Chester, England.
- Müller, L. (1963). "Der Felsbau, 1. Band, Theoretischer Teil, Felsbau über Tage 1. Teil." Ester band, Enke, 624p.
- Nielsen, K. A. (2007). *Fractured Aquifers-Formation evaluation by well testing*. Trafford Publishing, Victoria, 229p.
- NVIDIA. (2012). C. U. D. A C best practices guide. NVIDIA, Santa Clara, CA. <http://docs.nvidia.com/cuda/cuda-c-best-practices-guide/index.html>
- Oldekop, E. (1911). About evapotranspiration in riverine basins (in Russian). Jurjev (Tartu)
- Olsson, R., and Barton, N. (2001). An improved model for hydromechanical coupling during shearing of rock joints. *International Journal of Rock Mechanics and Mining Sciences*, 38(3), 317-329.
- Ollier, C. D. (1988). The regolith in Australia. *Earth-Science Reviews*, 25(5-6), 355-361.
- Pahl, P. J. (1981, June). Estimating the mean length of discontinuity traces. In *International Journal of Rock Mechanics and Mining Sciences and Geomechanics Abstracts*. Pergamon, 18 (3), 221-228.
- Paillet, F. L., Hess, A. E., Cheng, C. H., and Hardin, E. (1987). Characterization of fracture permeability with high-resolution vertical flow measurements during borehole pumping. *Groundwater*, 25(1), 28-40.
- Paillet, F., and Duncanson, R. (1994). Comparison of Drilling Reports and Detailed Geophysical Analysis of Ground-Water Production in Bedrock Wells. *Groundwater*, 32(2), 200-206.
- Pala A (1983) Studio geoidrologico della piana di Capoterra (Sardegna Meridionale) [Hydrogeological study of the Capoterra plain (southern Sardinia)]. *Rendiconti Seminario Facoltà Science University of Cagliari* 53, 171–196.
- Palmström, A. (1996). Characterizing rock masses by the R_{Mi} for use in practical rock engineering: Part 1: The development of the Rock Mass index (R_{Mi}). *Tunnelling and underground space technology*, 11(2), 175-188.
- Palmström, A., Sharma, V. I., and Saxena, K. (2001). Measurement and characterization of rock mass jointing. In-situ characterization of rocks. Balkema Publishers, 49-97.

- Palmström, A. (2015, January). Joint characteristics Retrieved . <http://www.rockmass.net/>
- Pantelidis, L. (2009). Rock slope stability assessment through rock mass classification systems. *International Journal of Rock Mechanics and Mining Sciences*, 46(2), 315-325.
- Penman, H. L. (1948, April). Natural evaporation from open water, bare soil and grass. In *Proceedings of the Royal Society A Lond.* , 193(1032), 120-145. <https://doi.org/10.1098/rspa.1948.0037>.
- Perdigao, A., Jochum, A., Calera, A., Pessanha, L., Chinita, A., and Maia, J. (2007). A tool for the integrated use of remote sensing with ground truth data: DEMETER project, in *spatial interpolation for climate data: The use of GIS in climatology and meteorology* (eds H. Dobesch, P. Dumolard and I. Dyras), ISTE, London, UK, 243-252.
- Piteau, D. R. (1970). Geological factors significant to the stability of slopes cut in rock. *South African Institute of Mining and Metallurgy*.
- Pollard, D., Aydin, A., (1988). Progress in understanding jointing over the past century. *Geological Society of America Bulletin* 100, 1181–1204.
- Price, M. (2013). *Introducing groundwater*. Publisher Nelson Thornes, 270p.
- Priest, S. D., and Hudson, J. A. (1976, May). Discontinuity spacings in rock. In *International Journal of Rock Mechanics and Mining Sciences and Geomechanics Abstracts*. Pergamon. 13(5), 135-148.
- Priest, S. D., and Hudson, J. A. (1981, June). Estimation of discontinuity spacing and trace length using scanline surveys. In *International Journal of Rock Mechanics and Mining Sciences and Geomechanics Abstracts*. Pergamon.18 (3), 183-197.
- Rana, G., and Katerji, N. (2000). Measurement and estimation of actual evapotranspiration in the field under Mediterranean climate: a review. *European Journal of Agronomy*, 13(2-3), 125-153.
- Rantz, S. E. (1982). *Measurement and computation of streamflow: Vol. 1. Measurement of stage and discharge; Vol. 2. Computation of discharge*. US Geological Survey Water Supply Paper, 2175, 681.
- RESMAR, Rete di tutela ambientale nello spazio maritime. (2013). *Un modello di indagine per la caratterizzazione e la gestione di un bacino idrografico a rischio alluvione*.
- Romana, M. R. (1995). A geomechanical classification for slopes: slope mass rating. In *Rock Testing and Site Characterization*, 575-600.
- Rong, G., Peng, J., Wang, X., Liu, G., and Hou, D. (2013). Permeability tensor and representative elementary volume of fractured rock masses. *Hydrogeology Journal*, 21(7), 1655-1671.
- Sánchez-Toribio, M. I. (1992). Métodos para el estudio de la evaporación y evapotranspiración. *Sociedad Española de Geomorfología*.
- Santoro, M. (1970). *Sulla applicabilità della formula di Turc per il calcolo della evapotraspirazione effettiva in Sicilia*. Istituto di Idraulica della Università di Palermo.
- Sasvári, Á., Baharev, A. (2014). SG2PS (structural geology to postscript converter) – A graphical solution for brittle structural data evaluation and paleostress calculation. *Computers & Geosciences*, 66, 81-93.

<https://doi.org/10.1016/j.cageo.2013.12.010>.

Sciabica MG (1994). Validazione dei modelli concettuali e matematici degli acquiferi con i dati idrogeologici ed idrogeochimici delle reti di monitoraggio [Conceptual and mathematical aquifer model validation by means of hydrogeological and hydro-chemical monitoring network data]. PhD Thesis, Central National Library of Florence, Italy, online catalogue code BN 97-724T.

Shapiro, A.M., (2002). Fractured-rock aquifers: understanding an increasingly important source of water: U.S. Geological Survey, Fact Sheet 112-02, 2 p.

Sharp, J. M. (Ed.). (2014). Fractured rock hydrogeology. CRC Press.

Shaw, R. (1997). Variations in sub-tropical deep weathering profiles over the Kowloon Granite, Hong Kong. *Journal of the Geological Society*, 154(6), 1077-1085.

Singhal, B. B. S., and Gupta, R. P. (2010). Applied hydrogeology of fractured rocks. Springer Science and Business Media.

Sluiter, R. (2009). Interpolation methods for climate data literature review, KNMI, De Bilt, official website.

Soil Survey Staff. (1998). Keys to soil taxonomy 8th Edition. United States Departments of Agriculture, Natural Resources conservation Service, Washington D. C., 326p.

Snow, D. T., (1969). Anisotropic permeability of fractured media: *Water Resources Research.*, 5 (6), 1273–1289.

Spadoni, M., Brilli, M., Giustini, F., and Petitta, M. (2010). Using GIS for modelling the impact of current climate trend on the recharge area of the S. Susanna spring (central Apennines, Italy). *Hydrological Processes*, 24(1), 50-64.

Spreen, W. C. (1947). A determination of the effect of topography upon precipitation. *Eos, Transactions American Geophysical Union*, 28(2), 285-290.

Szentimrey, T., Bihari, Z., and Szalai, S. (2007). Comparison of geostatistical and meteorological interpolation methods (what is what?). *Spatial interpolation for climate data: the use of GIS in climatology and meteorology*, 45-56.

Tabios, G. Q., and Salas, J. D. (1985). A comparative analysis of techniques for spatial interpolation of precipitation. *JAWRA Journal of the American Water Resources Association*, 21(3), 365-380.

Taylor, G., and Eggleton, R. A. (2001). *Regolith geology and geomorphology*. John Wiley & Sons.

Terzaghi, R. D. (1965). Sources of error in joint surveys. *Geotechnique*, 15(3), 287-304.

Thornthwaite, C. W. (1948). An approach toward a rational classification of climate. *Geographical Review*, 38(1), 55-94.

Turc, L. (1954). Calcul du bilan de l'eau évaluation en fonction des précipitations et des températures. *IAHS Publ*, 37, 88-200.

Tveito, O. E. (2007). The developments in spatialization of meteorological and climatological elements. *Spatial interpolation for climate data: the use of GIS in climatology and meteorology*, 73-86.

- Twidale, C. R. (2012). Granite landforms. Elsevier.
- UNEP (United Nations Environment Programme) (1992). World atlas of desertification. Edited by N. Middleton and DSG Thomas. Edward Arnold, London.
- United States Department of Agriculture. (2012). "Chapter 4 Engineering Classification of Rock Materials." In National Engineering Handbook, U.S. Department of Agriculture (USDA).
- Wagener, T., Sivapalan, M., Troch, P., and Woods, R. (2007). Catchment classification and hydrologic similarity. *Geography compass*, 1(4), 901-931.
- Walsh, J.J., Watterson, J. and Yielding, G., (1991). The importance of small-scale faulting in regional extension. *Nature*, 351: 391-393.
- Wang, C. Y., and Manga, M. (2010). Hydrologic responses to earthquakes and a general metric. *Geofluids*, 10(1-2), 206-216.
- Witherspoon, P. A., Wang, J. S., Iwai, K., and Gale, J. E. (1980). Validity of cubic law for fluid flow in a deformable rock fracture. *Water resources research*, 16(6), 1016-1024.
- Wright, E. P. and Burgess, W. G. (eds), (1992), *Hydrogeology of Crystalline Basement Aquifers in Africa*. Geological Society Special Publication, 66, 1-27.
- Wyllie, D. C., and Mah, C. (2004). *Rock slope engineering*. CRC Press.
- Wyns R. (2002). Climat, eustatisme, tectonique: quels contrôles pour l'altération continentale? Exemple des séquences d'altération cénozoïques en France. *Bull. Inf. Géol. Bass. Paris*, 39, (2), 5-16.
- Wyns R., Baltassat J.M., Lachassagne P., Legchenko A.V., Vairon J., and Mathieu F. (2003). Application of nuclear magnetic resonance soundings to groundwater reserves mapping in weathered basement rocks (Brittany, France). *Bulletin de la Société Géologique de France*.
- Wyns, R., Gandolfi, J. M., Damy, P. C., Touchard, F., Saplaïroles, M., Monod, B., and Ricordel-Prognon, C. (2010, September). Exploring groundwater in weathered crystalline basement areas: a method integrating geomorphologic, geologic and geophysical approach. In XXXVIII International Association of Hydrogeologist Congress. University of Silesia Press 2010. 2067-2071.
- Wyns, R., Dewandel, B., and Lachassagne, P. (2015) Origine de la fracturation des aquifères de socle: quels sont les facteurs qui contrôlent les propriétés de l'horizon fissuré?. Vingtièmes journées techniques du Comité Français d'Hydrogéologie de l'Association Internationale des Hydrogéologues. *Aquifères de socle: le point sur les concepts et les applications opérationnelles* » La Roche-sur-Yon, juin 2015.
- Yielding, G., Walsh, J.J. and Watterson, J. (1992). The prediction of small-scale faulting in reservoirs. *First Break*, 10: 449-460.
- Zhang, X., Sanderson, D. J., Harkness, R. M., and Last, N. C. (1996, January). Evaluation of the 2-D permeability tensor for fractured rock masses. In *International Journal of Rock Mechanics and Mining Sciences and Geomechanics Abstracts*. Pergamon. 33(1), 17-37.
- Zimmerman, R. W., and Bodvarsson, G. S. (1996). Hydraulic conductivity of rock fractures. *Transport in porous media*, 23(1), 1-30.

Online references

- Regione Sardegna.
<http://www.regione.sardegna.it/j/v/25?s=131338&v=2&c=5650&t=1>
- Istituto Superiore per la Protezione e la Ricerca Ambientale (ISPRA).
<http://www.acq.isprambiente.it/pluter/>
- Centro di Documentazione dei Bacini Idrografici (CEDOC)
<http://www.sardegnaicedoc.it/idrografico/stazioni/>
- Sardegna Geoportale.
<http://www.sardegnageoportale.it/navigatori/sardegnamappe/>
- ERDAS® Intergraph Geospatial (2013). Imagine Huntsville, AL:.,
http://www.intergraph.com/about_us/default.aspx.
- ArcGIS. A quick tour of geoprocessing tool references
<http://desktop.arcgis.com/en/arcmap/10.3/main/tools/a-quick-tour-of-geoprocessing-tool-references.htm>